SANDIA REPORT
SAND94-0472/1 • UC-721
Unlimited Release
Printed August 1997

Porosity, Single-Phase Permeability, and Capillary Pressure Data from Preliminary Laboratory Experiments on Selected Samples from Marker Bed 139 at the Waste Isolation Pilot Plant

Volume 1 of 3: Main Report, Appendix A

Susan M. Howarth, Tracy Christian-Frear

Prepared by
Sandia National Laboratories
Albuquerque, New Mexico 87185 and Livermore, California 94550

Sandia is a multiprogram laboratory operated by Sandia Corporation, a Lockheed Martin Company, for the United States Department of Energy under Contract DE-AC04-94AL85000.

Sandia National Laboratories

Issued by Sandia National Laboratories, operated for the United States Department of Energy by Sandia Corporation.

Available to DOE and DOE contractors from
Office of Scientific and Technical Information
P.O. Box 62
Oak Ridge, TN 37831

Prices available from (615) 576-8401, FTS 626-8401

Available to the public from
National Technical Information Service
U.S. Department of Commerce
5285 Port Royal Rd
Springfield, VA 22161

NTIS price codes
Printed copy: A13
Microfiche copy: A01

SAND94-0472/1
Unlimited Release
Printed August 1997

Distribution
Category UC-721

Porosity, Single-Phase Permeability, and Capillary Pressure Data from Preliminary Laboratory Experiments on Selected Samples from Marker Bed 139 at the Waste Isolation Pilot Plant

Volume 1 of 3: Main Report, Appendix A

Susan M. Howarth
Tracy Christian-Frear

Geohydrology Department 6115
Sandia National Laboratories
Albuquerque, NM 87185

ABSTRACT

Three groups of core samples from Marker Bed 139 of the Salado Formation at the Waste Isolation Pilot Plant (WIPP) were analyzed to provide data to support the development of numerical models used to predict the long-term hydrologic and structural response of the WIPP repository. These laboratory experiments, part of the FY93 Experimental Scoping Activities of the Salado Two-Phase Flow Laboratory Program, were designed to (1) generate WIPP-specific porosity and single-phase permeability data, (2) provide information needed to design and implement planned tests to measure two-phase flow properties, including threshold pressure, capillary pressure, and relative permeability, and (3) evaluate the suitability of using analog correlations for the Salado Formation to assess the long-term performance of the WIPP. This report contains a description of the borehole core samples, the core preparation techniques used, sample sizes, testing procedures, test conditions, and results of porosity and single-phase permeability tests performed at three laboratories: TerraTek, Inc. (Salt Lake City, UT), RE/SPEC, Inc. (Rapid City, SD), and Core Laboratories–Special Core Analysis Laboratory (Carrollton, TX) for Rock Physics Associates. In addition, this report contains the only WIPP-specific two-phase-flow capillary-pressure data for twelve core samples.

The WIPP-specific data generated in this laboratory study and in WIPP field-test programs and information from suitable analogs will form the basis for specification of single- and two-phase flow parameters for anhydrite marker beds for WIPP performance assessment calculations.

ACKNOWLEDGMENTS

The authors thank Joanne Fredrich (formerly with TerraTek, Inc., now with Sandia National Laboratories), Nancy Brodsky (formerly with RE/SPEC, Inc., now with Sandia National Laboratories), and Joel Walls of Rock Physics Associates for their contributions to this work. We also thank Rick Beauheim, Kurt Larson, and Peter Davies for their thorough review and thoughtful comments on this report. The authors also thank Sally Woerner, Tina Johnson, and Rick Bower of Tech Reps, Inc. for their help with the figures, tables, and technical editing.

TABLE OF CONTENTS

TABLE OF CONTENTS (Continued)

APPENDICES

LIST OF FIGURES

LIST OF FIGURES (Continued)

LIST OF FIGURES (Continued)

LIST OF TABLES

1.0 SUMMARY

Three groups of core samples from Marker Bed 139 (MB139) of the Salado Formation at the Waste Isolation Pilot Plant (WIPP) were analyzed to provide data to support development of the numerical models that are used to predict the long-term hydrological and structural response of the WIPP repository. These laboratory experiments, part of the FY93 Experimental Scoping Activities of the Salado Two-Phase Flow Laboratory Program, were designed to (1) generate WIPP-specific porosity and single-phase permeability data, (2) provide information needed to design test equipment and implement planned tests to measure two-phase flow properties including threshold pressure, capillary pressure, and relative permeability, and (3) evaluate the suitability of using analog correlations for the Salado Formation to assess the long-term performance of the WIPP. This report contains a description of the borehole core samples, the core preparation techniques, sample sizes, testing procedures, test conditions, and the results of porosity and single-phase permeability tests performed at three laboratories: RE/SPEC, Inc. (Rapid City, SD), TerraTek, Inc. (Salt Lake City, UT), and Core Laboratories—Special Core Analysis Laboratory (Carrollton, TX) for Rock Physics Associates. In addition, this report contains the only WIPP-specific two-phase flow data that exist; capillary pressure data for twelve core samples are included. The type and number of tests performed at each laboratory are summarized in Table 1 at the end of this section.

This report is intended to present the data collected during the Experimental Scoping Activities portion of the Salado Two-Phase Flow Laboratory Program. The WIPP-specific data generated in this laboratory study, combined with WIPP field-test programs and information from suitable analogs, will form the basis for specification of single- and two-phase flow parameters for WIPP Performance Assessment (PA) calculations. A separate document is planned that will contain recommendations for single- and two-phase flow parameters for anhydrite marker beds for the WIPP PA calculations.

The effective porosity of 42 samples tested ranged from 0.4 to 2.7%; total porosity of three samples ranged from 0.4 to 1.6%. Results of tests to determine the magnitude of the difference between total and effective porosity for specific samples were inconclusive. A slight reduction in effective porosity was observed when increasing confining stress was applied to a sample. Gas permeability ranged from a minimum of 5.0×10^{-20} m^2 at 10 MPa net effective stress to a maximum of 8.3×10^{-16} m^2 at 2 MPa net effective stress. Permeability decreased as net effective stress was increased, and an increasing gas permeability trend occurred with increasing effective porosity.

The simulated MB139 brine was found unsuitable for liquid flow tests on MB139 core samples; it caused dissolution of test specimens, resulting in order-of-magnitude increases in permeability. Liquid permeability measurements performed using odorless mineral spirits (OMS) agreed well with Klinkenberg-corrected gas permeability.

Air-brine threshold pressures determined from the mercury injection capillary pressure tests ranged from 0.33 to 0.78 MPa (48 to 113 psi). Air-brine threshold pressures from the centrifuge capillary pressure test could not be determined exactly. Residual liquid saturation ranged from 0.8 to 17.4%. The threshold pressure results from cores tested in this study are within the range that would be predicted from the Davies' (1991) correlation for anhydrite.

Table 1. Summary of Successful Preliminary Laboratory Tests Performed

Laboratory	RE/SPEC	TerraTek	Core Laboratories	Total
Total Porosity	0	3	0	3
Effective Porosity	0	14	28	42
Gas Permeability	2	6	23	31
Liquid Permeability	2	3	0	5
Capillary Pressure Centrifuge	0	0	6	6
Capillary Pressure Mercury Injection	0	0	6	6
Petrography XRD	9	6	15	30
Petrography Thin Sections	9	6	15	30

2.0 INTRODUCTION AND FRAMEWORK FOR INVESTIGATION

2.1 Background

The WIPP is the U.S. Department of Energy's (DOE's) planned repository for transuranic (TRU) waste generated by United States defense programs. This underground research and development effort is generating the technology base for the safe disposal of TRU waste in bedded salt. The Salado Formation was chosen for the repository in part because of salt's very low permeability and its natural ability to creep under the effects of stress, ultimately encapsulating and isolating the waste.

The Salado Formation consists of thick halite layers with interbeds of minerals such as clay and anhydrite, as shown in Figure 1. The polycrystalline Salado salt and anhydrite layers contain small quantities of brine in intragranular fluid inclusions and as intergranular (pore) fluid. It is important to quantify the amount of brine in the Salado Formation and to determine its mobility and flow properties because the accumulation and subsequent migration of significant quantities of brine in the repository might lead to problems that affect the salt's ability to isolate waste.

Salado rock and flow parameters describe its ability to transmit and store fluids. Permeability data from in situ tests indicate that the anhydrite and impure halite interbeds within the Salado Formation have higher permeability, by 1 to 2 orders of magnitude, than the pure halite intervals (Beauheim et al., 1991; 1993). Numerical flow simulations and sensitivity analyses show that the anhydrite interbeds could be the primary flow path for brine moving into the repository and the path for waste-generated gas and contaminated brine flowing outward into the formation (Davies et al., 1991). Thus the role of the anhydrite interbeds in the long-term hydrological response of the WIPP facility has become an issue that involves the initial state of the material, the mechanism(s) and potential for brine and gas flow in the material, and the influence of excavation-induced and/or gas-pressure-induced damage on these flow parameters.

About 45 siliceous or sulfatic laterally continuous units exist within the Salado Formation; these include Marker Bed 138 and MB139, which are in the vicinity of the repository horizon (Borns, 1985). MB139, an approximately 1-m thick anhydrite interbed that lies approximately 1 m below the planned waste storage rooms, is a potential gas and brine flow path. Although permeability values of 5×10^{-17} to 8×10^{-20} m^2 have been inferred from in situ borehole tests in MB139 (Beauheim et al., 1991; 1993), laboratory examination and testing of the anhydrite interbed material have been extremely limited until this study.

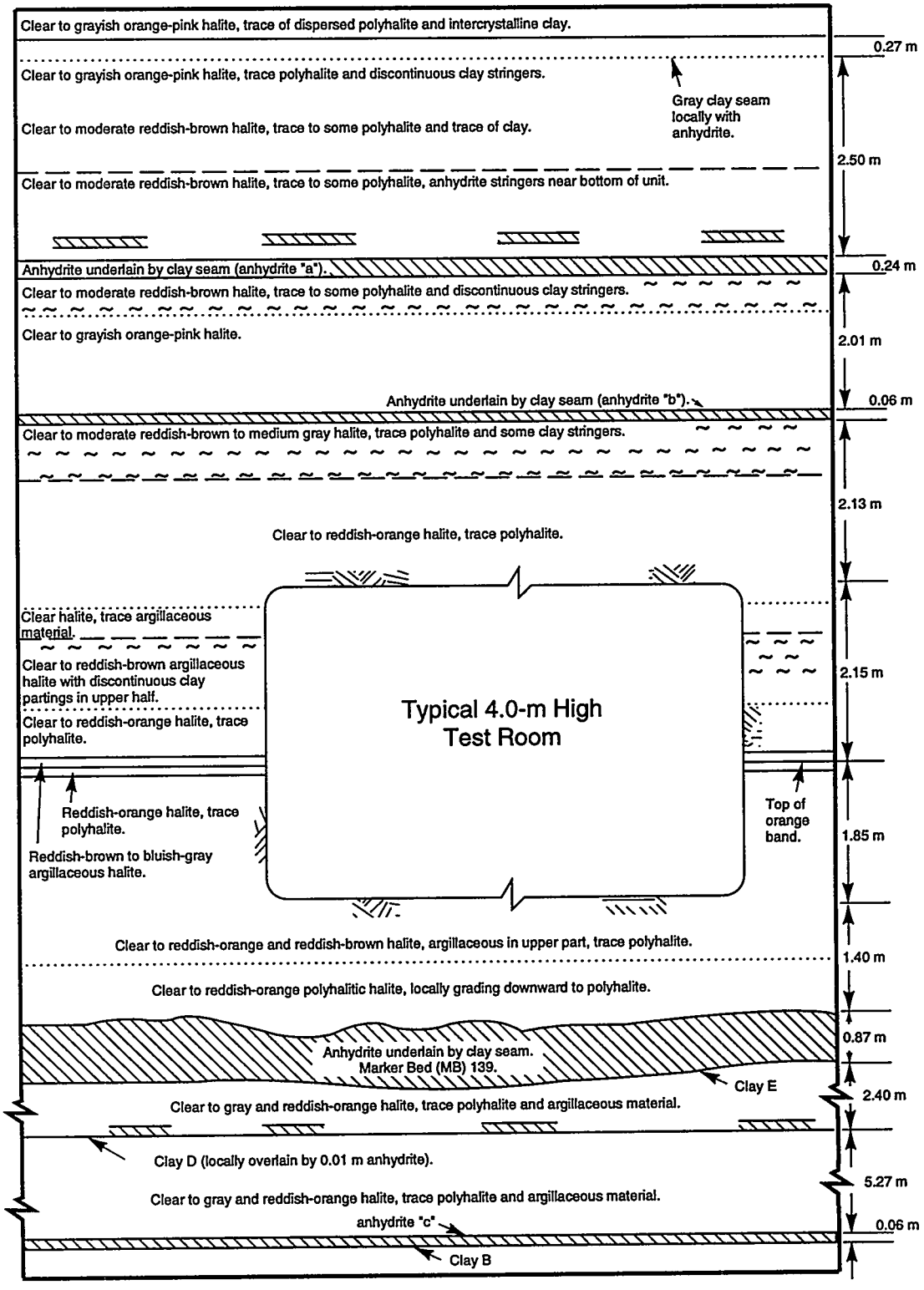

Figure 1. Stratigraphy of the Salado Formation in the vicinity of the WIPP underground excavations.

2.2 Marker Bed 139 Description

Within the Salado Formation, MB139 is one of 45 siliceous or sulfatic units that are traceable in the repository subsurface for several kilometers but may not be recognizable in every borehole. The approximately 0.4- to 1.25-m thick unit is located approximately 1 m below the planned repository interval, as shown in Figure 1. The bed is described as a microcrystalline anhydrite with moderate reddish orange/brown to light and medium grey coloring. As further described by Borns (1985) and Fredrich and Zeuch (1996), MB139 exhibits an undulatory upper surface with vertical amplitudes of approximately 0.5 m (20 in.) and wave lengths of about 0.6 to 1.8 m (2 to 6 ft). A "swallowtail" pattern, consisting of halite growths within the anhydrite, is common in the upper part of the marker bed. Locally, hairline, clay-filled low-angle fractures are located in the lower part of the unit. A thin halite layer is commonly found close to the lower contact, and clay "E" is situated at the base of the unit.

Borns (1985) studied core taken from five 10-cm (4-in.) boreholes drilled from Room 4 at the WIPP; MB139 was then mesoscopically divided into five stratigraphic zones. Zone I, termed the Upper Contact Zone, was described as the "upper contact, clay layer with inter-layered halite, polyhalite and clay, clusters of halite crystals; contact with Zone II is sharp where defined by clay seam." Zone II, termed the Massive Polyhalitic Anhydrite, was described as "polyhalitic anhydrite with patches of relict anhydrite, convolute stylolites, swallowtail growth structures." Zone III, termed the Mixed Anhydrite and Polyhalitic Anhydrite, was described as containing "equal proportions relict anhydrite and polyhalitic anhydrite, commonly fissile, numerous sub-horizontal fractures, which are partially filled with halite." Zone IV, termed the Laminated Anhydrite with Halite, was described as "inter-layered halite and anhydrite; anhydrite shows pull-apart structures, layering is sub-horizontal." Zone V, termed the Lower Contact Zone, was described as the "lower contact zone, clay layer; the lower boundary of the clay is undulatory where clay infills embayments in lower surface; these structures do not reflect structures in zones above." An idealized core section on which the five zones are identified and described is shown in Figure 2.

2.3 Salado Two-Phase Flow Laboratory Program–Preliminary Laboratory Experiments

The tests reported here were part of preliminary experimental activities of the Salado Two-Phase Flow Laboratory Program as described in Howarth (1993). As shown in Figure 3, these preliminary measurements (anhydrite) experiments are an integral part of the Salado

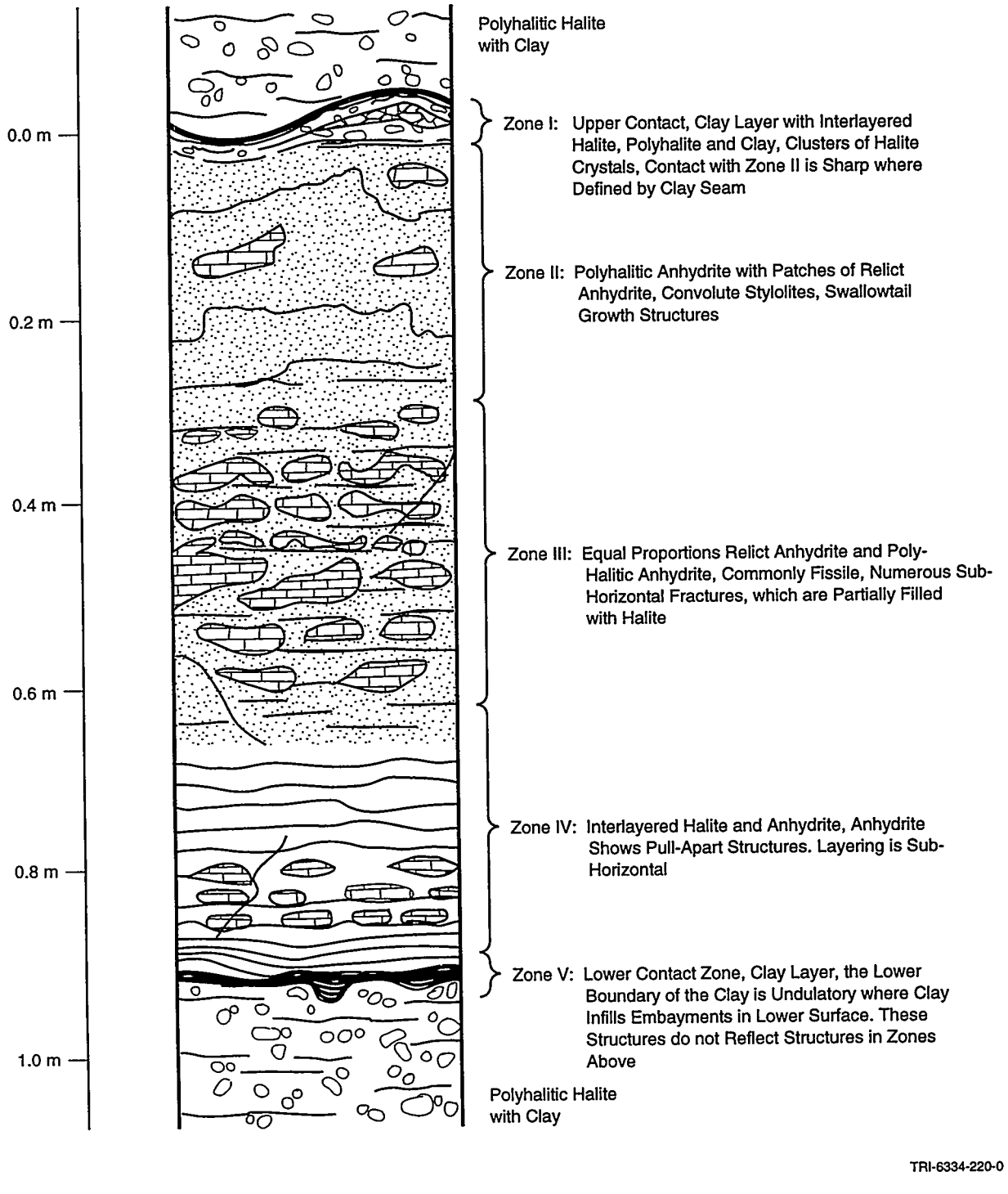

Figure 2. The five zones of MB139, shown in an idealized core section (after Borns, 1985).

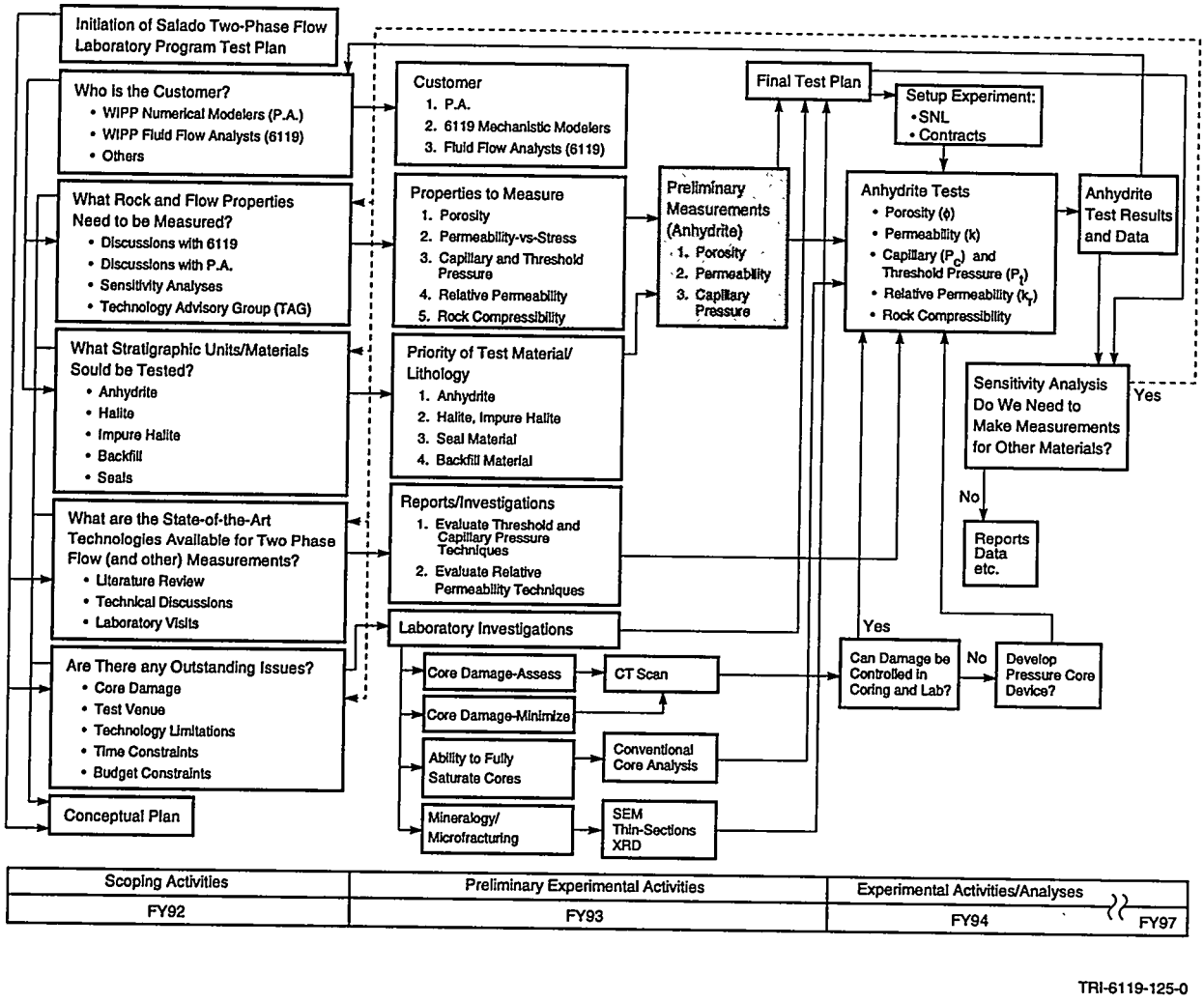

Figure 3. Salado Two-Phase Flow Laboratory Program roadmap (Howarth, 1993).

Two-Phase Flow Program. The preliminary laboratory test matrix was designed to provide a wide variety of information regarding the rock and flow properties of MB139, including total and effective porosity, gas and liquid permeability, permeability anisotropy, and mercury injection and centrifuge capillary pressure. Porosity and permeability tests were performed under various stress conditions to evaluate stress sensitivity. In addition, the suitability of using a synthetic brine for liquid permeability tests and the compositional and hydrological heterogeneity of MB139 were investigated.

Porosity and gas permeability are two fundamental, measurable rock properties. Simple methods exist to measure these rock properties. Ultimately, developing relationships between the more difficult-to-measure properties and effective porosity and/or gas permeability is desirable. Therefore, when possible, effective porosity and/or gas permeability measurements were made on all core samples tested within the scope of the preliminary laboratory experiments. In addition, specimens were categorized according to Borns' (1985) stratigraphic zone classification system to assess whether correlations between stratigraphic zone and porosity and/or permeability exist within MB139.

Standard petrographic analysis, including x-ray diffraction (XRD) and scanning electron microscopy (SEM), was used to describe the mineral composition. This analysis consists of a description of the assemblage of each sample, which includes a modal analysis of the phases present, a description of primary (growth fabrics, reworking, etc.) and secondary (replacement mineral growth, overprinting, relic minerals, fracture infilling, etc.) textures, and a description of fracture or pore systems present and observed. Section 3 contains a brief summary of the petrographic analysis preformed in conjunction with the porosity, permeability, and capillary pressure tests. Details of these and other petrographic analyses performed as part of the Salado Two-Phase Flow Laboratory Program are found in Holcomb et al. (1995) and Fredrich and Zeuch (1996).

2.4 Net Effective Stress

Measurements of effective porosity and permeability were performed while confining pressure, and in some cases pore pressure, was applied to the test specimen. As described in Howarth (1993), the effective stress law is used to describe the appropriate stress state of a rock by defining a relationship between internal pore pressure, P_p, and confining stress, σ, for any given material property or process. A generalized effective stress law is presented in Equation 1.

$$P = G(\sigma - \alpha P_p) \quad (1)$$

The classic definition for net effective stress, σ', is shown in Equation 2 (Warpinski and Teufel, 1992).

$$\sigma' = \sigma - P_p \quad (2)$$

For Equations 1 and 2:

P	=	the specific material property or process (i.e., permeability, deformation, rock compressibility, or capillary pressure)
G	=	generalized function which describes the effect of stress on the property or process
σ	=	external confining stress on the sample (for hydrostatic conditions, $\sigma = P_{conf}$)
P_{conf}	=	confining pressure
P_p	=	pore pressure
α	=	poroelastic parameter that relates stress and pore pressure
σ'	=	net effective stress.

The classic definition for net effective stress is the effective stress law when $\alpha = 1.0$. In this definition, the net effective stress is given by $\sigma - P_p$, and σ is assumed to be constant, thereby resulting in a linear effective stress law. This definition, widely used in soil and hard rock analysis, is used to quantify the stress state imposed on test specimens analyzed for this report. In all cases where confining pressure was applied to test specimens for this study, the applied confining stress, P_{conf}, was hydrostatic. Therefore the net effective stress, σ', is defined by Equation 3 for this report. Further investigation of the net effective stress law for these tests was beyond the scope of this study.

$$\sigma' = P_{conf} - P_p \quad (3)$$

2.5 Report Organization

The following sections present the results of measured rock and flow properties from the preliminary laboratory experiments. In addition to summarizing the petrographic analyses, Section 3 describes the test specimens and details of the borehole cores from which

the test specimens were taken. Section 4 contains a description of the porosity and grain density test methods, procedures, and results. Similarly, Section 5 describes the single-phase gas and liquid permeability test methods, procedures, and results. A description of the capillary pressure test methods, procedures, and results, including threshold pressure, is found in Section 6. Relationships between measured parameters are found in Section 7. Conclusions are found in Section 8, and Section 9 contains recommendations. Section 10 contains the references. Results of the petrographic analyses are reported in a separate document (Fredrich and Zeuch, 1996).

The unabridged final data and analysis reports from Rock Physics Associates (incorporating data from Core Laboratories in Carrollton, TX), RE/SPEC, and TerraTek are included in Appendices A, B, and C, respectively. In some instances, inconsistencies remain between the raw data and/or calculated values from test laboratory notebooks and worksheets and the data reported in the final data and analysis reports exist. Therefore an errata sheet that identifies inconsistencies is included at the beginning of each appendix. Copies of the laboratory notebooks/worksheets are retained in the Sandia WIPP Central Files (SWCF) records center.

3.0 MARKER BED 139 TEST SPECIMENS

3.1 Test Specimen Selection

The intent of the test specimen selection process was to select groups of cores that represent a distribution of MB139 physical textures. However, only Borns' (1985) stratigraphic Zones II, III, and IV were recovered in their entirety from all holes during the coring process. In most cases, the whole cores broke during coring or recovery. Breaks occurred at the upper and lower contact zones (Zones I and V, respectively), and a specimen could not be cut from either the Zone I or Zone V remaining whole cores. In these cases, there appeared to be pre-existing fractures at the contact zones, consistent with observations of stress-sensitive fracturing along marker bed contacts in the vicinity of older excavated rooms. In other cases, the contact zone was so thin that a truly representative test specimen of Zone I or V could not be cut. Because of the different composition of Zones I and V and the possible existence of pre-existing fractures, the flow properties for Zones I and V might vary from the more intact portions of MB139.

To obtain samples that would withstand the core preparation and finishing process, test samples were cut from competent portions of the borehole core (also referred to here as whole core). The test specimens were cut from whole core taken from six underground boreholes at the WIPP: E1X07, E1X08, E1X10, E1X11, P3X10, and P3X11. Locations of the six boreholes are shown in Figure 4, together with locations of the cores studied by Holcomb et al. (1995) and Borns (1985). Table 2 is a cross-reference guide that contains borehole coordinates and elevation from mean sea level (MSL).

Tables 3a, 3b, and 3c summarize information about each specimen, including designation of the laboratory that performed the tests, the borehole number from which the specimen was taken, the sample number at the test laboratory, zone classification, depth (from borehole collar) at which the specimen was cut from the whole core, specimen bulk volume, flow direction (with respect to the bedding plane) during permeability testing, and grain density. Tables 3a, 3b, and 3c contain information from Core Laboratories, RE/SPEC, and TerraTek, respectively. Porosity, permeability, and threshold pressure test results and anhydrite content for each core are presented in Tables 3a, 3b, and 3c and are discussed in Sections 4, 5 and 6, respectively. Zone classifications were determined during consultation with D. J. Borns and were based on review of photographs showing the locations where test specimens were extracted from whole cores.

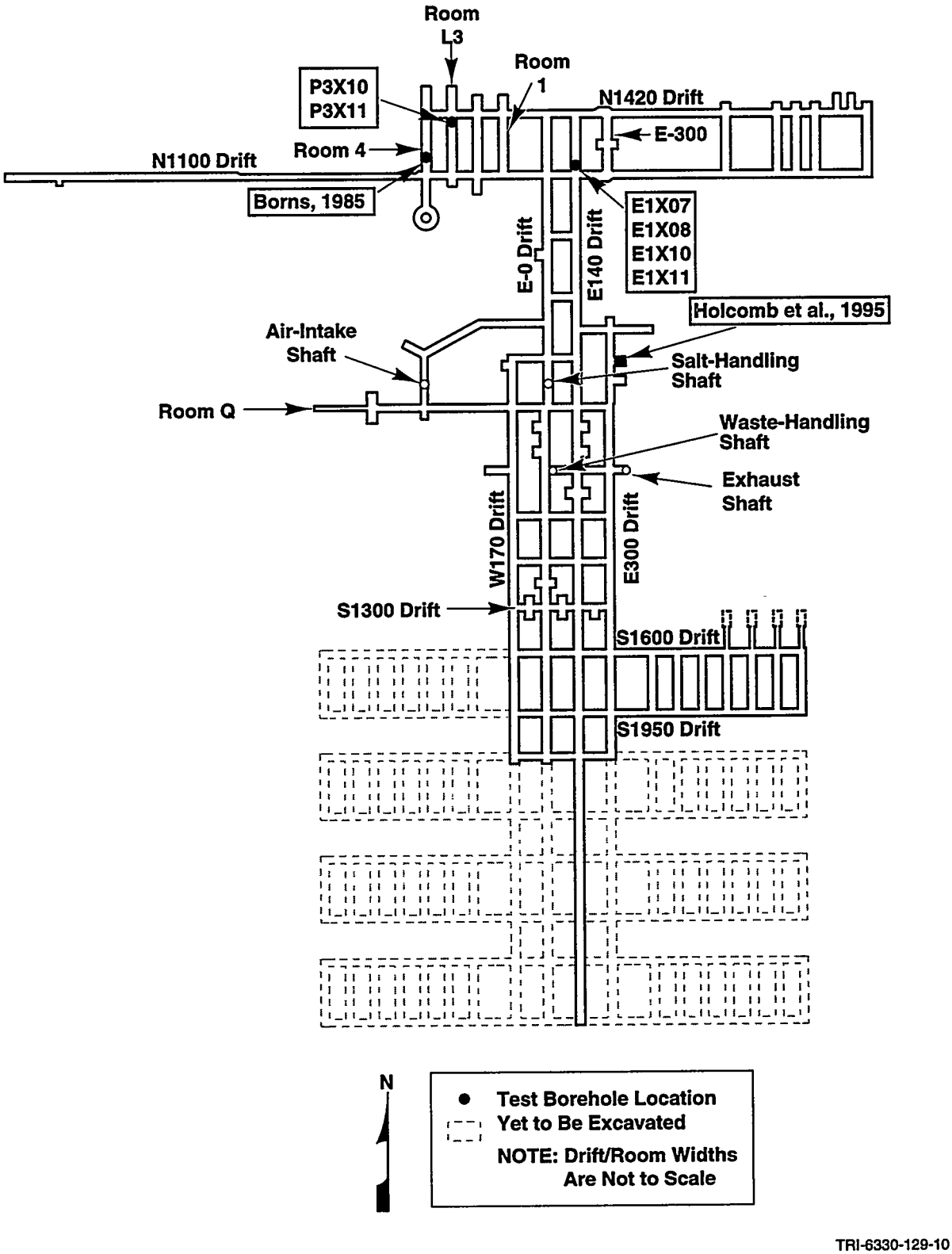

Figure 4. Location of boreholes for test specimens.

Table 2. Borehole Locations

Borehole Number	Borehole Coordinate North (ft)*	Borehole Coordinate East (ft)**	Borehole Elevation at Collar (ft MSL)
E1X07	10830.61	7064.48	1302.46
E1X08	10998.45	7064.97	1303.09
E1X10	10992.22	7064.80	1303.12
E1X11	10988.49	7065.02	1303.14
P3X10	11103.34	6385.30	1297.27
P3X11	11101.62	6385.46	1297.26

* To convert this coordinate to the New Mexico State Plane Coordinate System (Gonzales, 1989), add 490,000.00 to the coordinate value given here. For example, the north coordinate of E1X07 is 500,830.61 in the New Mexico State Plane Coordinate System.

** To convert this coordinate to the New Mexico State Plane Coordinate System (Gonzales, 1989), add 660,000.00 to the coordinate value given here. For example, the east coordinate of E1X07 is 667,064.48 in the New Mexico State Plane Coordinate System.

Table 3a. Detailed Summary of Information for Each Test Sample at Core Laboratories

Lab	Bore Hole No.	Sample No.	Zone	Depth (feet)	Flow Dir.	Bulk Vol (cc)	*Grain Den. (g/cc)	Effective Porosity			** Gas Permeability			Anhydrite Cont.		Thres. Press.	Res. Brine Sat.
								3.4 MPa (%)	6 MPa (%)	10 MPa (%)	3.4 MPa (m^2)	6 MPa (m^2)	10 MPa (m^2)	XRD (wt%)	TS (vol%)	140 d (MPa)	(%)
CL	E1X10	1	2	4.5	H	11.88	2.64	0.60									
CL	E1X10	2	2	4.5	H	10.7	2.59	0.80	0.70		6.50e-19	4.60e-19	2.30e-19	80	82		
CL	E1X10	3	2	5	H			0.60									
CL	E1X10	4	2	5	H	12.69	2.62	0.90	0.90		1.30e-18	8.80e-19	6.50e-19	73	72		
CL	E1X10	5	3	5.25	H	12.45	2.62	0.70	0.60		5.10e-19	3.80e-19	1.80e-19	56	67	0.541	7.26
CL	E1X10	6	3	5.25	H	12.43	2.62	0.70			5.80e-19	3.00e-19	5.00e-20				
CL	E1X10	7	3	5.25	V	12.65	2.95	1.10	1.00		9.50e-19	5.50e-19		99	99	0.78	6.99
CL	E1X10	8	3	5.25	V	12.98	2.95	1.10	1.00		8.20e-19	4.90e-19	1.40e-19				
CL	E1X10	9	3	5.5	H	12.65	2.85	0.90			4.70e-19			92	93		
CL	E1X10	10	3	5.5	H	12.65	2.94	1.00			1.10e-18	1.80e-19					
CL	E1X10	11	3	5.75	H	12.53	2.89	1.70	1.70	1.60	1.80e-18	1.60e-18	1.10e-18	93	95	0.45	17.4
CL	E1X10	12	3	5.75	H	12.93	2.92	1.40	1.30		1.40e-18	1.00e-18	7.30e-19				
CL	E1X10	13	3	5.75	V	12.7	2.96	1.60	1.50	1.50	1.60e-18	3.10e-19		97	82	0.753	10.86
CL	E1X10	14	3	5.75	V	10.78	2.95	1.20	1.10		6.10e-19	3.10e-19	1.70e-19				
CL	E1X10	15	4	6.25	V	12.6	2.96	1.00	0.90		5.90e-19	1.30e-19	6.40e-20	96	100		
CL	E1X10	16	4	6.25	V	12.37	2.96	0.60									
CL	E1X11	17	2	4.5	H	11.38	2.63	0.80			4.00e-19	3.40e-19	1.00e-19	54	60		
CL	E1X11	18	2	4.5	H	11.88	2.63	1.80									
CL	E1X11	19	3	4.75	H	12.91	2.72	0.90			4.70e-19	3.20e-19	1.00e-19	68	71		
CL	E1X11	20	3	4.75	H	12.83	2.79	0.90	0.80		3.90e-19						
CL	E1X11	21	3	5	H	12.04	2.82	1.10	1.00		7.70e-19	5.70e-19	2.60e-19	66	64	0.329	0.78
CL	E1X11	22	3	5	H	12.29	2.69	1.40	1.30		1.50e-18	8.40e-19					
CL	E1X11	23	3	5.25	H	12.62	2.65	2.10			1.30e-18	5.90e-19		54	69	0.397	6.88
CL	E1X11	24	3	5.25	H	12.2	2.67	1.40	1.40		1.50e-18	5.70e-19					
CL	E1X11	25	3	5.25	V	13	2.61	0.90	0.80		2.00e-18	5.60e-19	2.90e-19	69	83		
CL	E1X11	26	3	5.25	V	12.93	2.74	1.60			2.20e-18	7.50e-19	3.30e-19				
CL	E1X11	27	4	5.75	H	12.72	2.75	1.60	1.40	1.20				85	44		
CL	E1X11	28	4	5.75	H	13.67	2.91										
CL	E1X11	29	4	5.75	V	12.69	2.96	0.80									
CL	E1X11	30	4	5.75	V	12.72	2.96	1.00			1.50e-18	5.90e-19		99	100		

* Grain densities from effective grain volume measurements.

** Pressure values are net effective stress; gas permeabilities are Klinkenberg corrected.

Table 3b. Detailed Summary of Information for Each Test Sample at RE/SPEC Inc.

Lab	Bore Hole No.	Sample No.	Zone	Depth (feet)	Flow Dir.	Bulk Vol (cc)	*Grain Den. (g/cc)	Permeability (pressure values are net effective stress)						Anhydrite Content	
								Gas (Klinkenberg Corrected)			Liquid **				
								1.6 MPa (m^2)	5.6 MPa (m^2)	9.6 MPa (m^2)	1.6 MPa (m^2)	5.6 MPa (m^2)	9.6 MPa (m^2)	XRD (wt%)	TS (vol%)
RS	P3X11	5-2-SP1	2	5.50	H	823.5		3.20e-18	1.70e-18	1.40e-18	5.30e-17				
RS	P3X11	5-2-SP1T	2	5.50	H	12.62	2.73							18	
RS	P3X11	5-2-SP1B	2	5.50	H	13.97	2.73							6	
RS	P3X10	6-SP2	3	5.70	H	820.5									
RS	P3X10	6-SP2T	3	5.70	H	14.59	2.69							55	
RS	P3X10	6-SP2B	3	5.70	H	13.19	2.57							45	
RS	P3X11	5-3-SP3	4	7.05	H	813.00		1.60e-17	8.90e-18	5.10e-18	7.90e-17	4.30e-17	2.60e-17		
RS	P3X11	5-3-SP3T	4	7.05	H	14.97	2.53							55	
RS	P3X11	5-3-SP3B	4	7.05	H	17.88	2.70							59	
RS	P3X11	5-3-2-TS1-1	3	5.93	H										70
RS	P3X11	5-3-2-TS1-2	3	5.93	V										46
RS	P3X11	5-3-2-TS1-3	3	5.93	V										49
RS	P3X11	5-3-2-TS1-4	3	5.93	V									60	
RS	P3X10	5-3-2-TS2-1	2	5.28	H										68
RS	P3X10	5-3-2-TS2-2	2	5.28	V										43
RS	P3X10	5-3-2-TS2-3	2	5.28	V										58
RS	P3X10	5-3-2-TS2-4	2	5.28	V									47	
RS	P3X11	6-TS3-1	4	7.60	H										96
RS	P3X11	6-TS3-2	4	7.60	V										90
RS	P3X11	6-TS3-3	4	7.60	V										67
RS	P3X11	6-TS3-4	4	7.60	V									72	

* Grain densities from effective grain volume measurements.

** All liquid permeabilities are scoping calculations.

Table 3c. Detailed Summary of Information for Each Test Sample at TerraTek, Inc.

Lab	Bore Hole No.	Sample No.	Zone	Depth (feet)	Flow Dir.	Bulk Vol (cc)	* Grain Den. (g/cc)	Porosity		Permeability (pressure values are net effective stress)						Anhydrite Content	
								Total	Eff.	Gas (Klinkenberg Corrected)			Liquid**			XRD	TS
									0 MPa	2 MPa	6 MPa	10 MPa	2 MPa	6 MPa	10 MPa		
								(%)	(%)	(m^2)	(m^2)	(m^2)	(m^2)	(m^2)	(m^2)	(wt%)	(vol%)
TT	E1X08	A	2	3.82	H	822.8	2.65		1.90	8.20e-18	5.70e-18	5.00e-18	6.70e-18	5.70e-18	5.30e-18		
TT	E1X08	B	3	4.66	H	776.8	2.60		0.50	1.30e-17	7.40e-18	4.60e-18					
TT	E1X08	C	4	5.53	H	819.6	2.72		1.00	4.60e-18	2.60e-18	2.00e-18	3.60e-18	2.40e-18	1.80e-18		
TT	E1X08	EP1	2	3.57	H	83.47	2.56	1.40	1.30								
TT	E1X08	EP2	3	4.4	H	84.39	2.66		0.80								
TT	E1X08	EP3	3	5.12	H	83.54	2.58	0.40	0.40								
TT	E1X08	EP4	4	5.93	H	83.35	2.88	1.60	1.60								
TT	E1X08	PX1	2	4.07												70	6
TT	E1X08	PX2	3	4.93												32	62
TT	E1X08	PX3	4	5.78												98	80
TT	E1X07	D	2	4.32	H	803.8	2.71		0.70	1.50e-19	5.90e-20	5.50e-20					
TT	E1X07	E	3	4.82	H	843.1	2.71		1.50	8.30e-16	3.00e-16	1.50e-16					
TT	E1X07	F	4	5.38	H	815.3	2.88		1.00	1.10e-18	6.90e-19	5.70e-19	1.10e-18	6.10e-19	5.10e-19		
TT	E1X07	EP5	2	4.07	H	84.85	2.64		1.90								
TT	E1X07	EP6	2	4.57	H	84.04	2.70		2.70								
TT	E1X07	EP7	3	5.07	H	83.73	2.80		0.60								
TT	E1X07	EP8	4	5.66	H	84.52	2.75		1.60								
TT	E1X07	PX4	2	4.07												7	50
TT	E1X07	PX5	3	5.07												62	66
TT	E1X07	PX6	4	5.8												81	82

* Grain densities from effective grain volume measurements.

** All liquid permeabilities are scoping calculations.

3.2 Test Specimen Preparation and Description

All test specimens used in this study were taken from 10- or 15.2-cm (4- or 6-in.) diameter core drilled through MB139 from six different underground locations. All samples were cut and prepared according to SNL-approved procedures. Prior to the tests conducted at RE/SPEC and TerraTek, the mineralogical composition of the test samples was uncertain and there was concern that some clays might be present. Because overdrying of clays can cause increases in porosity and permeability that are not indicative of natural, in situ conditions (Bush and Jenkins, 1970), the specimens at TerraTek and RE/SPEC were dried under controlled temperature and humidity conditions (65° C and 45% humidity). Subsequent compositional analysis at TerraTek and RE/SPEC revealed that clays were not present in measurable quantities; therefore Core Laboratories personnel were instructed to dry their specimens in a vacuum oven at 104° C until the weight stabilized to within 0.001 gram over a 24-hour period.

Figure 5 is a flow diagram that shows the tests performed on the specimens. As previously stated, developing relationships between the more difficult-to-measure properties and effective porosity and/or gas permeability was desired, so, when possible, effective porosity and/or gas permeability measurements were made on all core samples tested within the scope of this program. Table 4 contains a summary of the results of x-ray diffraction (XRD) and thin-section petrographical analysis performed on samples from the six boreholes. The list of "other" minerals included carbonate (predominately magnesite), polyhalite, carbon, or pyrite. RE/SPEC and TerraTek both analyzed for polyhalite, a dominant constituent in five of the twelve samples analyzed by these two laboratories, but Core Laboratories did not. (Note that RE/SPEC subcontracted petrographic work to the South Dakota School of Mines, Core Laboratories subcontracted to Omni Laboratories, and TerraTek subcontracted some analysis to the University of Utah and performed the remainder in house.) Details of the petrographic analysis are contained in Fredrich and Zeuch (1996).

Table 4. Summary of Petrographic Analysis Results

Mineral	XRD (Mean Weight %)	Thin Section (Mean Volume %)
Anhydrite	65	70
Other	35	30

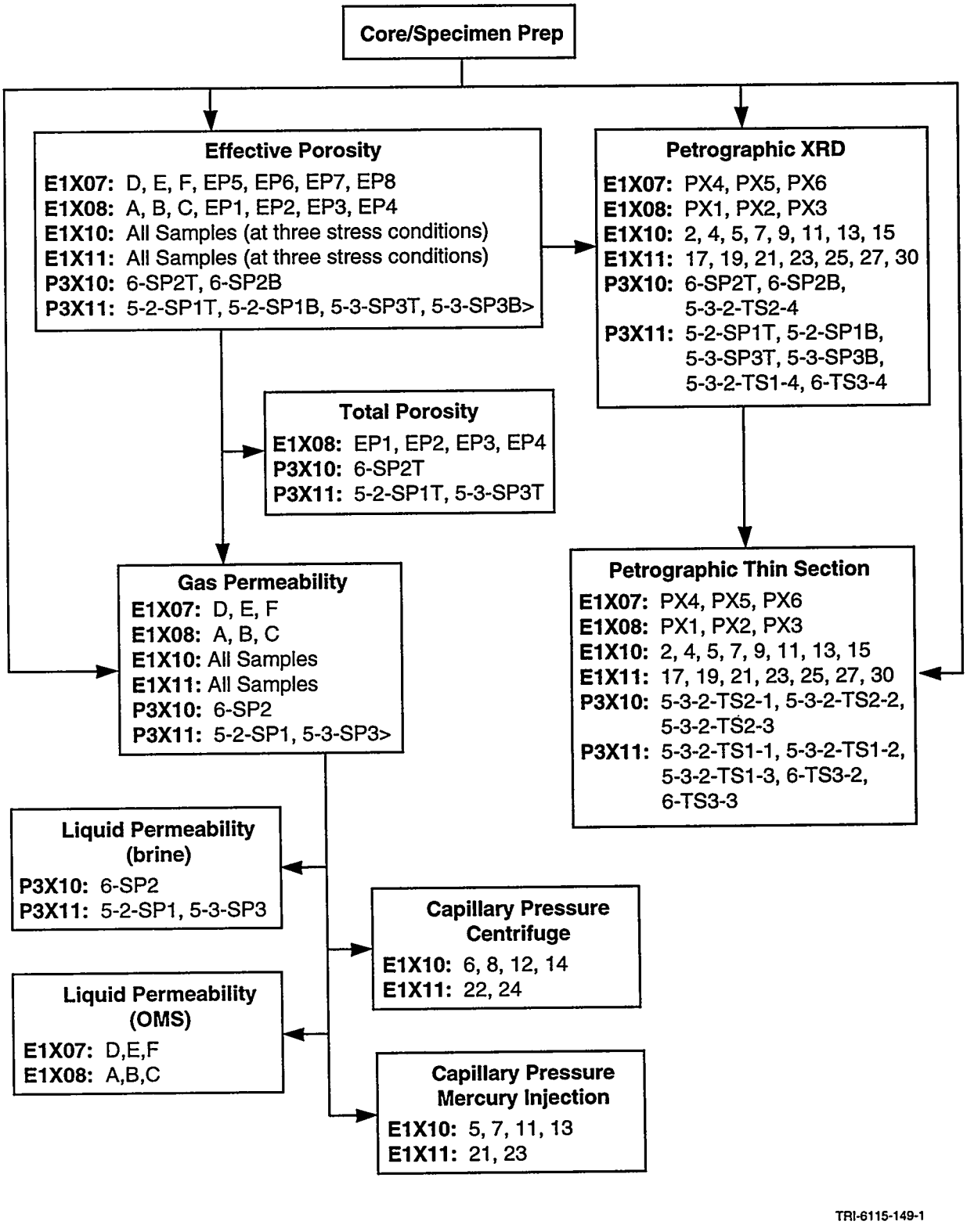

Figure 5. Flow diagram for tests performed on Marker Bed 139 specimens.

4.0 POROSITY

Porosity is a measure of the void space or storage capacity of a rock. Effective porosity is the ratio of the interconnected pore volume to bulk volume. Total porosity is the ratio of interconnected and non-interconnected pore space to bulk volume. A summary of the results of total and effective porosity tests is given in Tables 3a, 3b, and 3c. Results of effective and total porosity tests are presented and discussed below. Successful measurements of both total and effective porosity were made on three MB139 samples by TerraTek. Effective porosity was measured on an additional 42 samples. RE/SPEC porosity measurements could not be qualified as required by SNL WIPP Quality Assurance procedures and thus are not included here. In most cases, a particular core specimen subsequently underwent such additional testing as gas or liquid permeability, capillary pressure, or petrography upon completion of effective porosity tests, as shown in Figure 5.

4.1 Effective Porosity

Effective porosity was successfully measured on 28 specimens at Core Laboratories and 14 specimens at TerraTek, Inc. The data are shown in Tables 3a, 3b, and 3c.

4.1.1 Test Procedures

Effective porosity was determined at Core Laboratories under the direction of Rock Physics Associates using the CMS 300 system, which directly measures pore volume using the Boyle's law helium expansion technique and the autoporosimeter to measure grain volume. As shown in Table 3a, effective porosity was measured while the samples were subject to 3.4, 6.0, and 10.0 MPa net effective stress. Details regarding test procedures at Core Laboratories are found in Appendix A.

Effective porosity was determined at TerraTek using Archimedes' principle to determine bulk volume and a porosimeter (using the Boyle's Law helium expansion technique) to measure grain volume. The specimens were not subject to confining stress during the tests. Details regarding test procedures at TerraTek are found in Appendix C.

4.1.2 Histograms and Probability Distributions

Effective porosity was successfully measured on 42 specimens; 14 at TerraTek under

zero confining stress (zero net effective stress) conditions, and 28 at Core Laboratories under three stress conditions. Effective porosity for zero confining stress ranged from 0.4 to 2.7% with a mean of 1.2% and is shown as a histogram in Figure 6a and as a cumulative frequency in Figure 6b.

Effective porosity was measured on 28 cores at a net effective stress of 3.4 MPa. Effective porosity ranged from 0.6 to 2.1% with a mean of 1.1%. The porosity data for the specimens tested under 3.4 MPa net effective stress are shown as a histogram in Figure 7a and as a probability distribution in Figure 7b. Effective porosity was successfully measured on 16 of the 28 specimens under a net effective stress of 6.0 MPa. At 6.0 MPa net effective stress, effective porosity ranged from 0.6 to 1.7 % with a mean of 1.1%. The porosity data for the specimens tested under 6.0 MPa net effective stress are shown as a histogram in Figure 8a and as a probability distribution in Figure 8b. Effective porosity was successfully measured on three of the 16 specimens, previously tested under 3.4 and 6.0 MPa net effective stress conditions, at a net effective stress of 10.0 MPa. At 10.0 MPa net effective stress, effective porosity ranged from 1.2 to 1.6% with a mean of 1.5%. The porosity data for the specimens tested under 10.0 MPa net effective stress are shown as a histogram in Figure 9a and as a cumulative frequency in Figure 9b.

Table 5 summarizes the effective porosity data for all net effective stress conditions. All porosity measurements ranged between 0.4 and 2.7%, independent of confining stress conditions. The effect of stress on effective porosity is discussed in Section 4.1.3.

Table 5. Summary of Effective Porosity Data Results

	Porosity				
	Total	Effective			
		0 MPa	3.4 MPa	6 MPa	10 MPa
	(%)	(%)	(%)	(%)	(%)
Minimum	0.4	0.4	0.6	0.6	1.2
Maximum	1.6	2.7	2.1	1.7	1.6
Sum	3.4	17.4	31.4	17.3	4.4
Points	3	14	28	16	3
Mean	1.1	1.2	1.1	1.1	1.5
Median	1.4	1.2	1	1.0	1.5
Std. Deviation	0.63	0.66	0.4	0.32	0.20
Variance	0.4	0.44	0.16	0.10	0.04

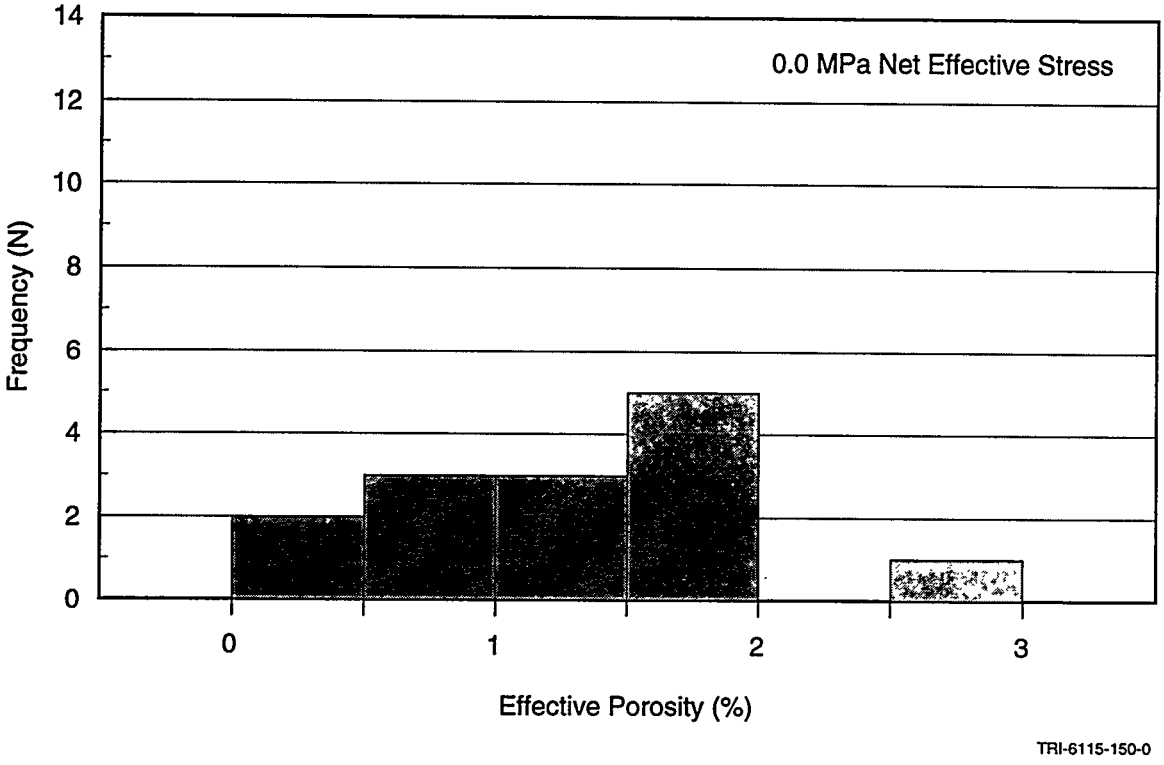

Figure 6a. Effective porosity at 0.0 MPa net effective stress histogram.

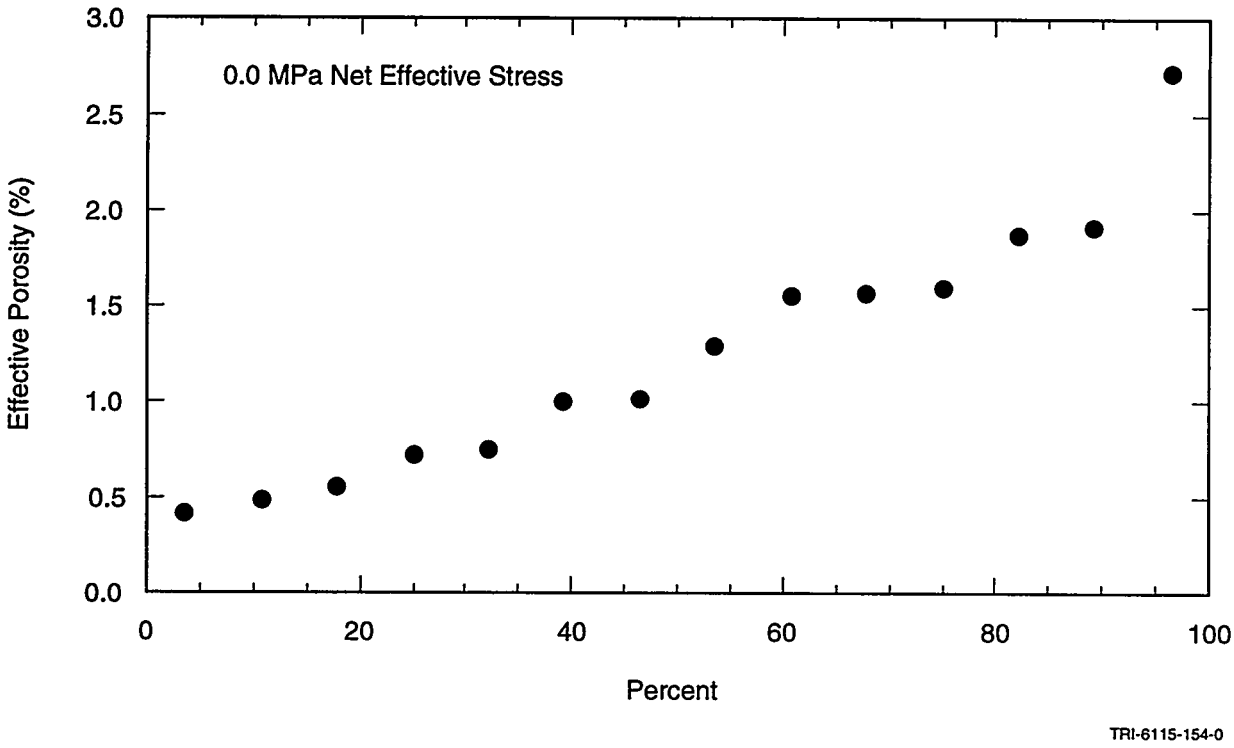

Figure 6b. Effective porosity at 0.0 MPa net effective stress cumulative frequency plot.

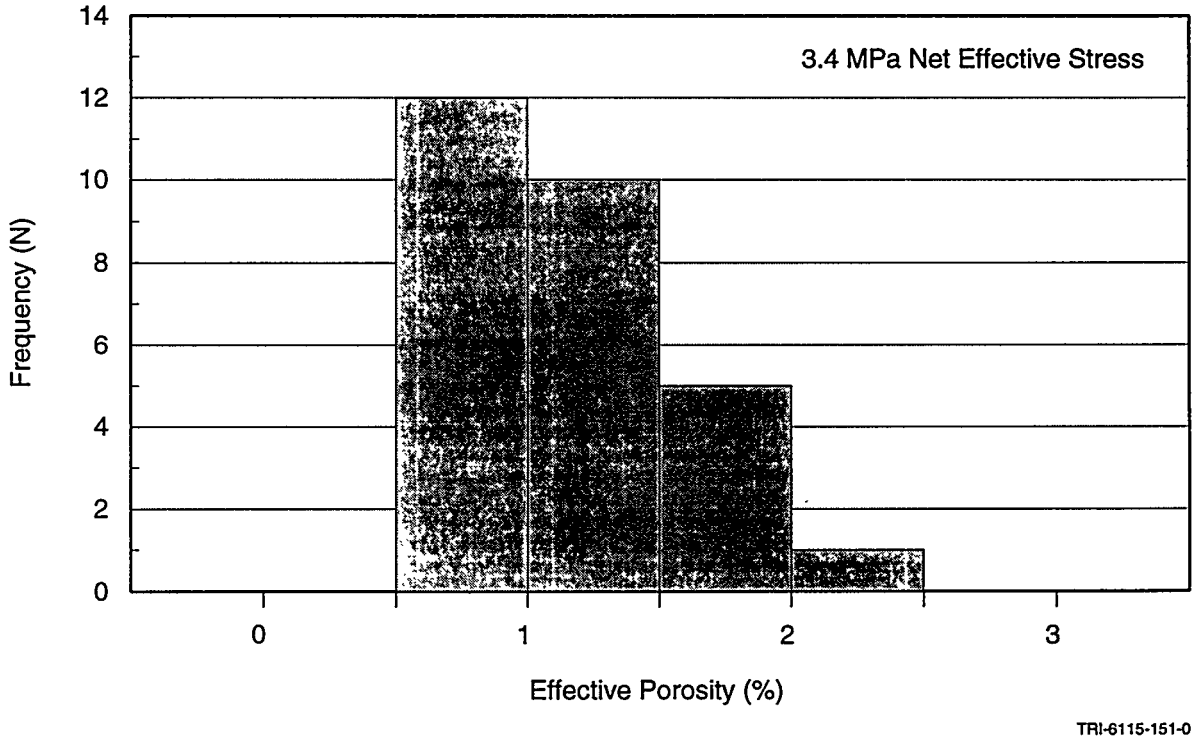

Figure 7a. Effective porosity at 3.4 MPa net effective stress histogram.

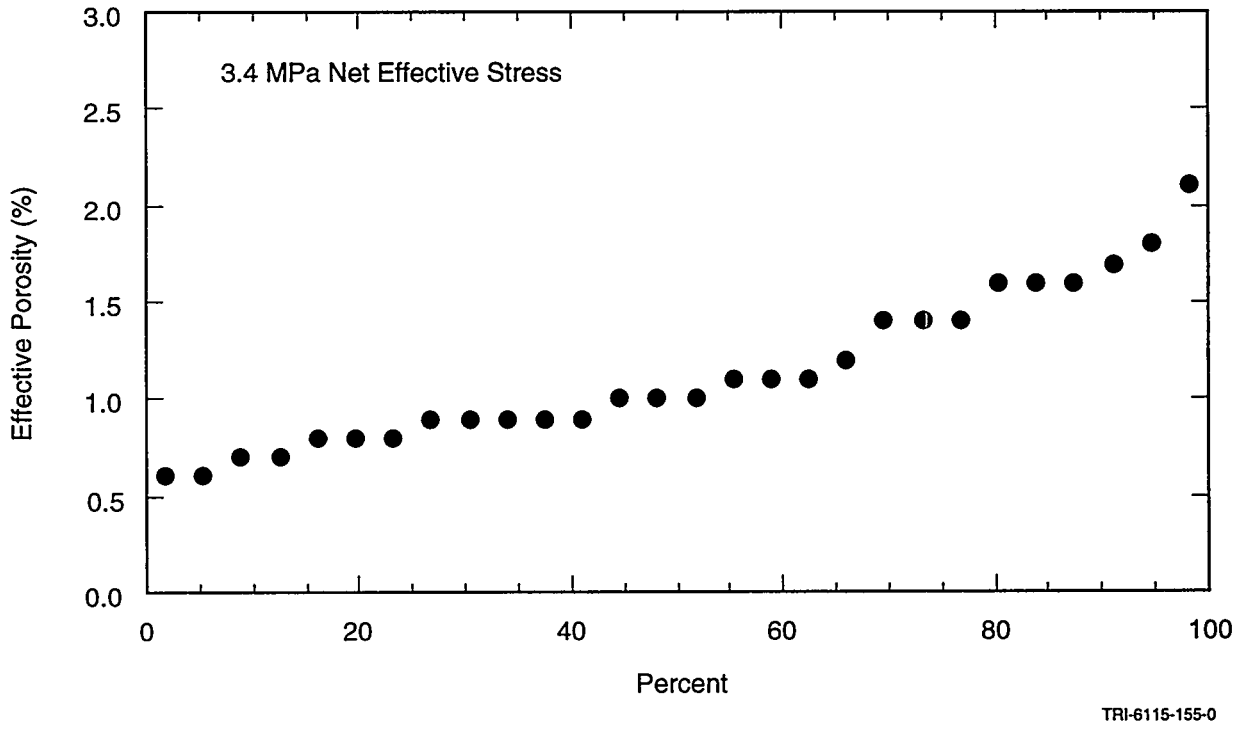

Figure 7b. Effective porosity at 3.4 MPa net effective stress cumulative frequency plot.

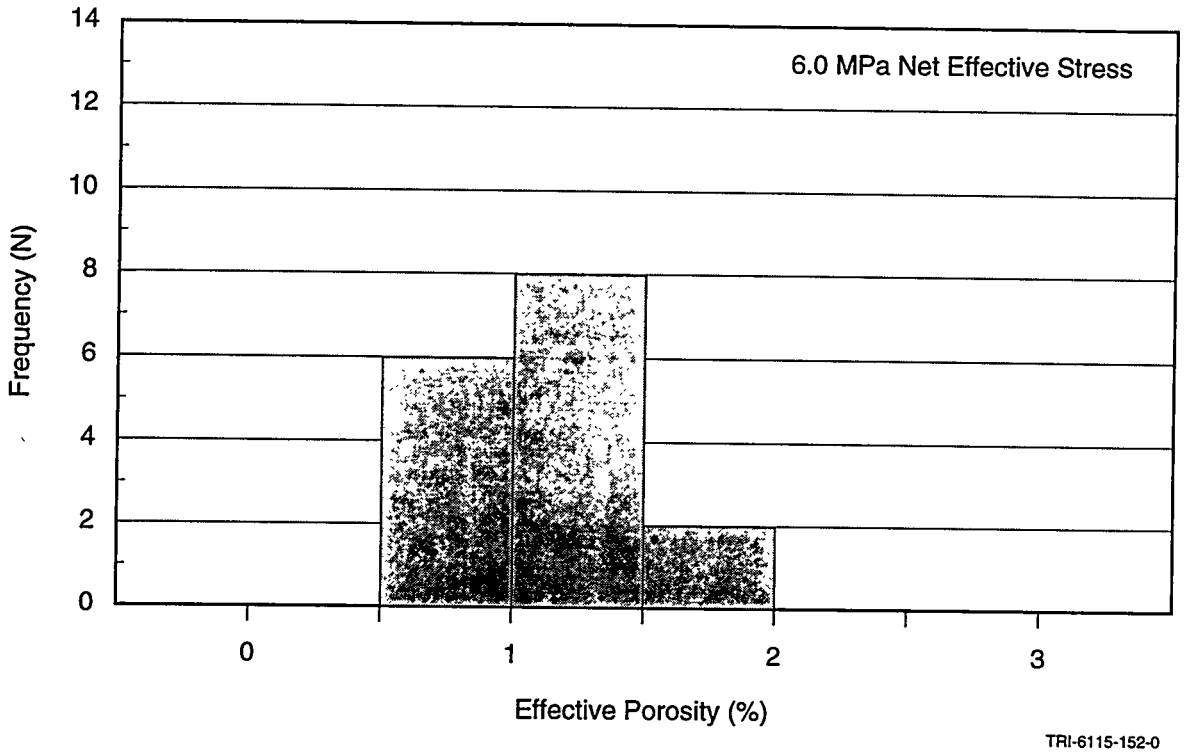

Figure 8a. Effective porosity at 6.0 MPa net effective stress histogram.

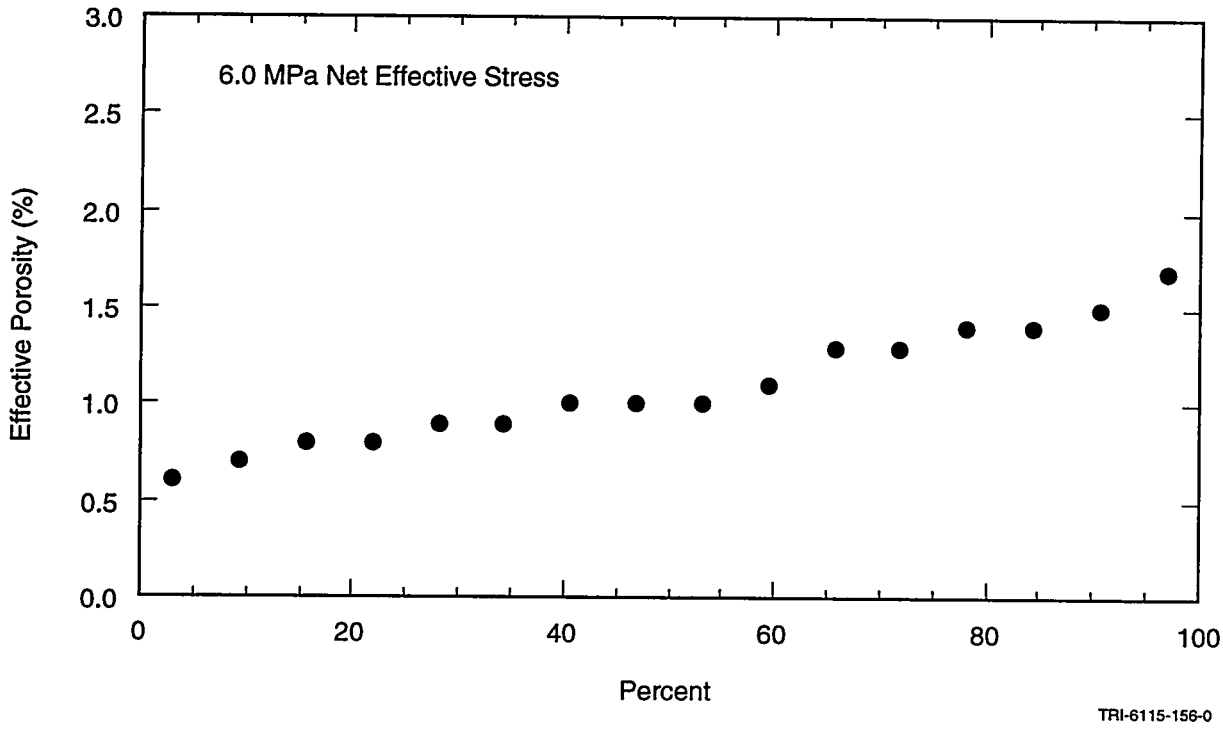

Figure 8b. Effective porosity at 6.0 MPa net effective stress cumulative frequency plot.

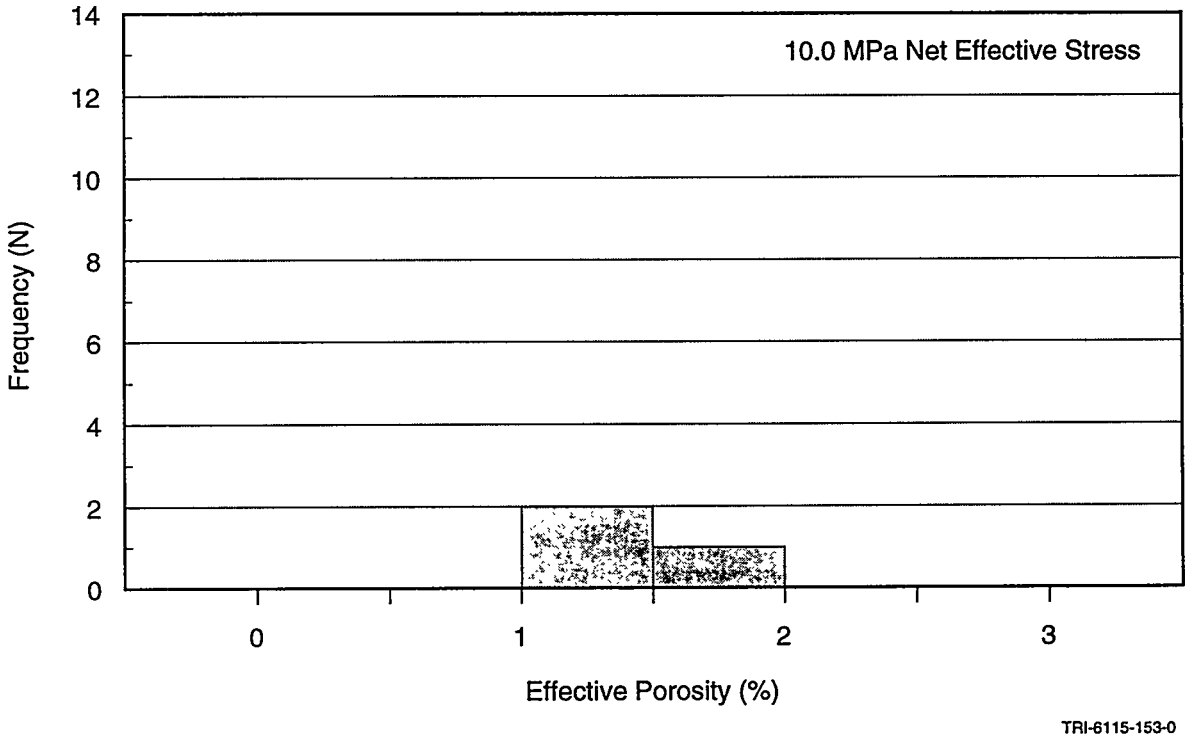

Figure 9a. Effective porosity at 10.0 MPa net effective stress histogram.

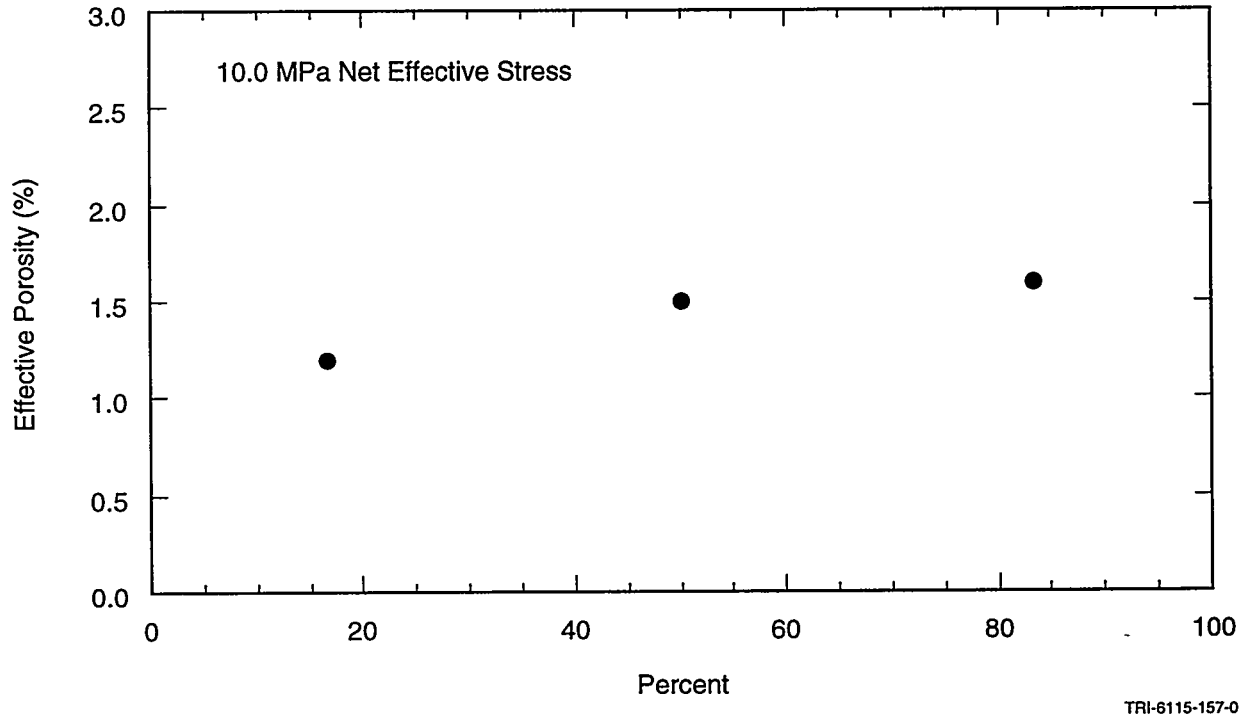

Figure 9b. Effective porosity at 10.0 MPa net effective stress cumulative frequency plot.

4.1.3 Effect of Stress on Effective Porosity

Twenty-eight specimens were tested under different hydrostatic confining stress conditions. Effective porosity was successfully measured on all 28 specimens at a net effective stress of 3.4 MPa, on 16 of the 28 specimens at a net effective stress of 6.0 MPa, and on three of the 16 specimens at a net effective stress of 10.0 MPa. Figure 10 shows the effective porosity versus net effective stress for all samples tested at TerraTek and Core Laboratories. The graph shows the range of measured effective porosity values at each net effective stress and the mean effective porosity at each net effective stress. Note that these data are for two different sets of cores: (1) the specimens tested at TerraTek at 0.0 MPa, and (2) the specimens tested at Core Laboratories at 3.4, 6.0, and 10.0 MPa. None of the specimens tested at TerraTek is included in the set of cores tested at Core Laboratories.

Increasing the net effective stress on the specimens caused the porosity either to remain constant or to decrease. This trend is illustrated in Figure 10 for the three Core Laboratories' specimens, Samples 11, 13, and 27, for which effective porosity was successfully measured at 3.4, 6.0, and 10.0 MPa net effective stress conditions. The decrease in porosity corresponding to an increase in net effective stress from one stress level to the next was ≤ 0.1 porosity units for all specimens except for Sample 27. For Sample 27, the effective porosity decreased by 0.2 porosity units when the net effective stress was increased from 3.4 to 6.0 MPa and by 0.2 porosity units when the net effective stress was increased from 6.0 MPa to 10.0 MPa.

4.1.4 Relationship between Zone Classification and Effective Porosity

The core samples were classified according to the five stratigraphic zones described in Section 3.2. Zone classifications for core samples are listed in Tables 3a, 3b, and 3c. The data are shown in Figure 11. Specimens were cut only from Zones II, III, and IV. Zones I and V, the upper and lower contact zones, respectively, are thin compared to Zones II, III, and IV. Also, because of the presence of clay interlayers, Zones I and V fracture during the coring process; therefore intact specimens could not be cut from within those sections of whole core.

As Figure 11 shows, the range of effective porosity values is largest for Zone II cores and smallest for Zone IV cores; a slight trend suggests that Zone III has lower effective porosity than Zones II and IV. However, insufficient data exist to draw definitive conclusions regarding correlations between Borns' (1985) MB139 stratigraphic zone

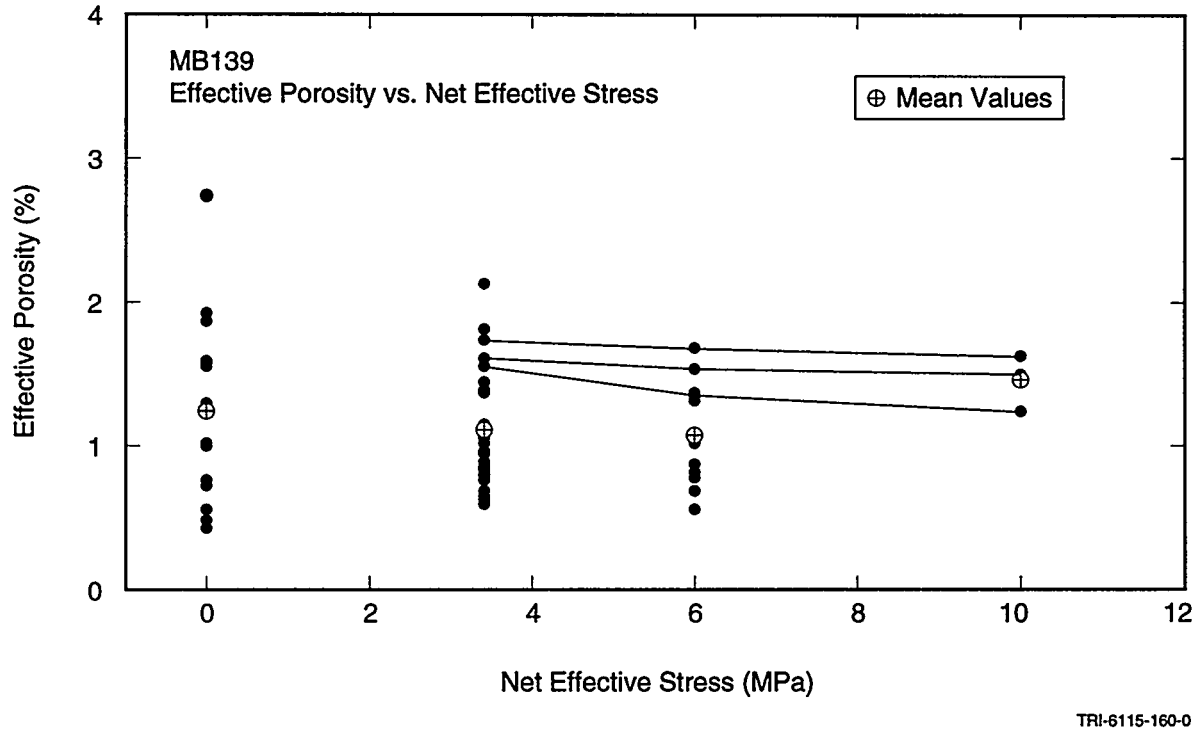

Figure 10. Effective porosity versus net effective stress.

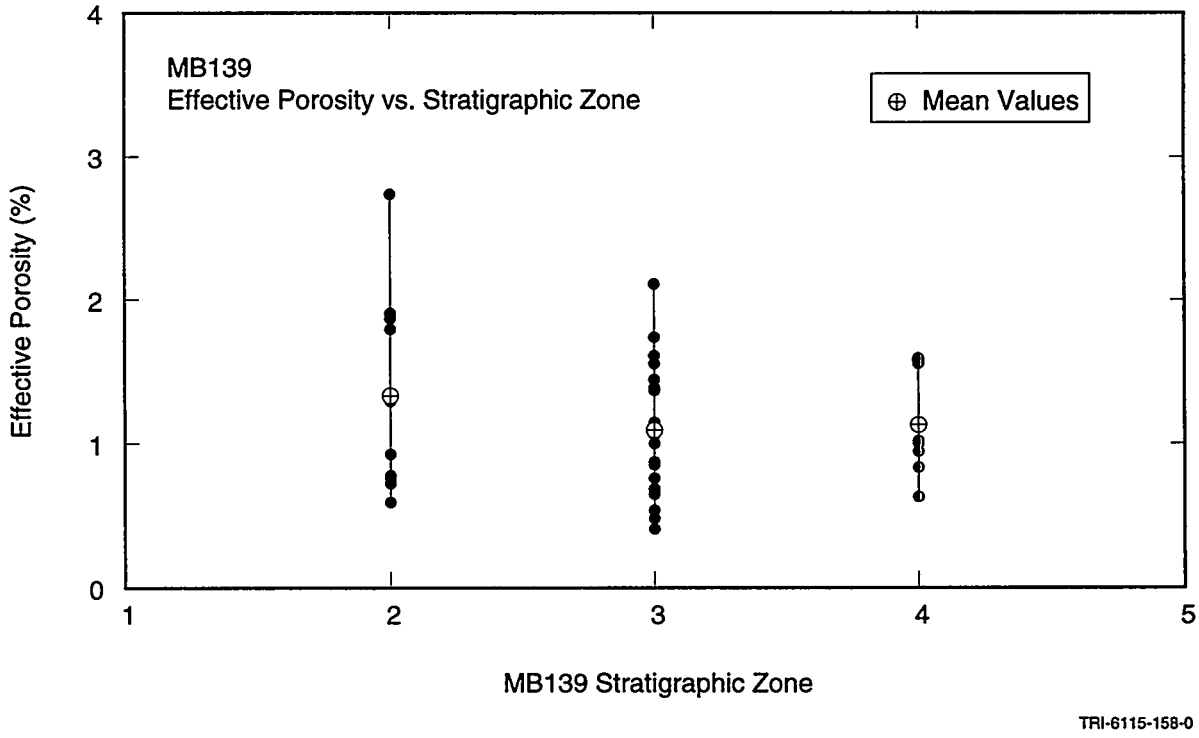

Figure 11. Effective porosity versus Marker Bed 139 stratigraphic zone.

classifications and effective porosity. The properties of Zones I and V are expected to be more representative of fractured rock and therefore likely to have greater porosity than Zones II, III, or IV.

4.2 Total Porosity

The total porosity data are summarized in Table 3c and discussed in the following sections. Because of the small number of total porosity data points generated, a sufficient data base from which to develop significant trends does not exist.

4.2.1 Test Procedures

Total (interconnected plus non-interconnected) porosity was measured on four specimens at TerraTek. The specimens were not subject to confining stress during these tests. Of the four tests performed, only three are considered to have produced useable data because significant portions of Sample EP2 were lost during the pulverization process. The effective porosity of each of these samples was measured prior to measuring total porosity. Total porosity was determined at TerraTek by powdering the test specimens and determining the grain density. Details regarding the test procedures are found in Appendix C.

4.2.2 Histograms and Probability Distribution

Total porosity was successfully measured at TerraTek on three samples for which effective porosity was also measured. Total porosity values ranged from 0.4 to 1.6%, with a mean of 1.1%. The total porosity data are shown as a histogram in Figure 12a and as a probability distribution in Figure 12b.

4.2.3 Relationship between Total and Effective Porosity

Figure 13 illustrates the relationship between total and effective porosity for the three samples on which both tests were performed. As expected, total porosity is greater or equal to effective porosity for all three samples. Note however that in Sample EP1, for which total porosity was greater than effective porosity, the difference was less than the corresponding experimental error (see Tables 6 and 7 of Appendix C). Sufficient data do not presently exist to draw definitive conclusions regarding correlations between total and effective porosity.

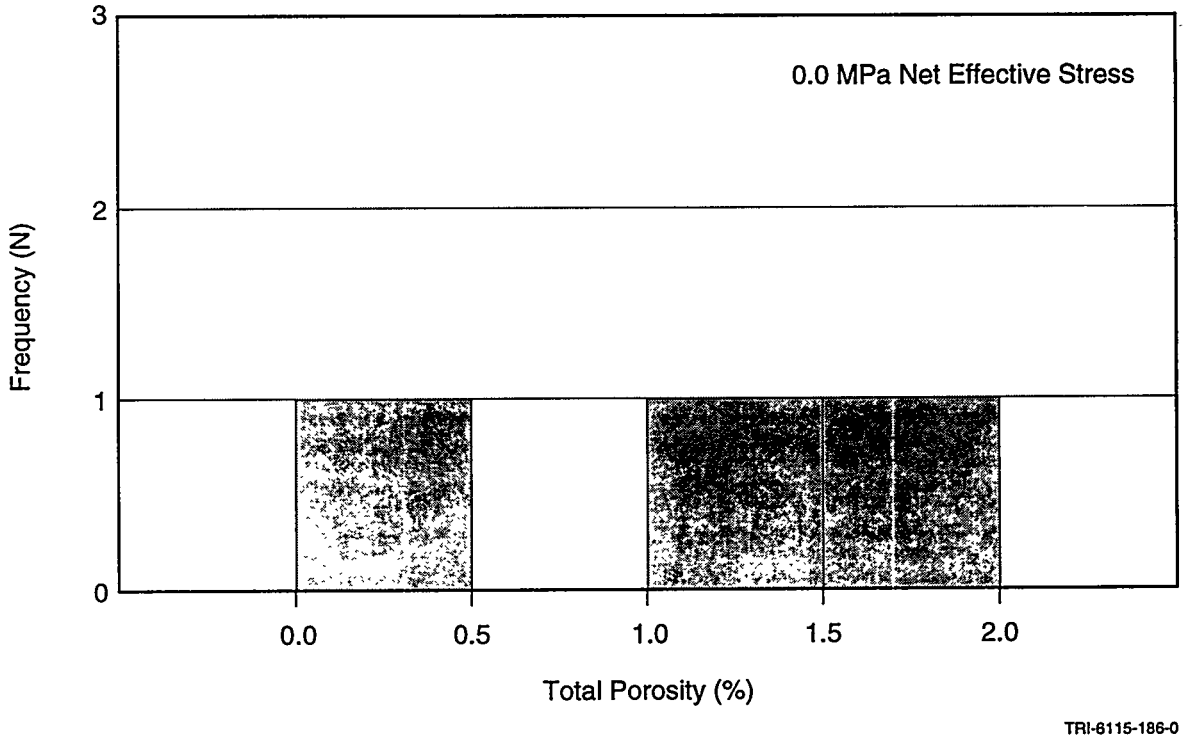

Figure 12a. Total porosity histogram.

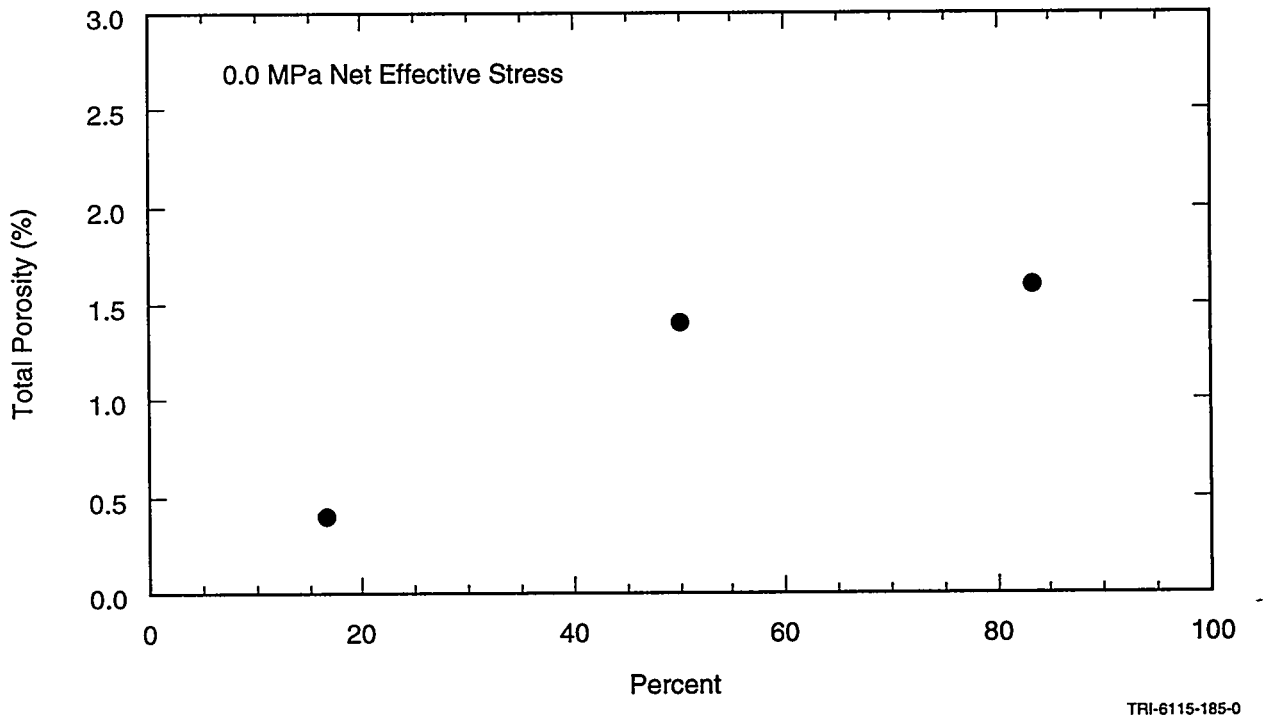

Figure 12b. Total porosity cumulative frequency plot.

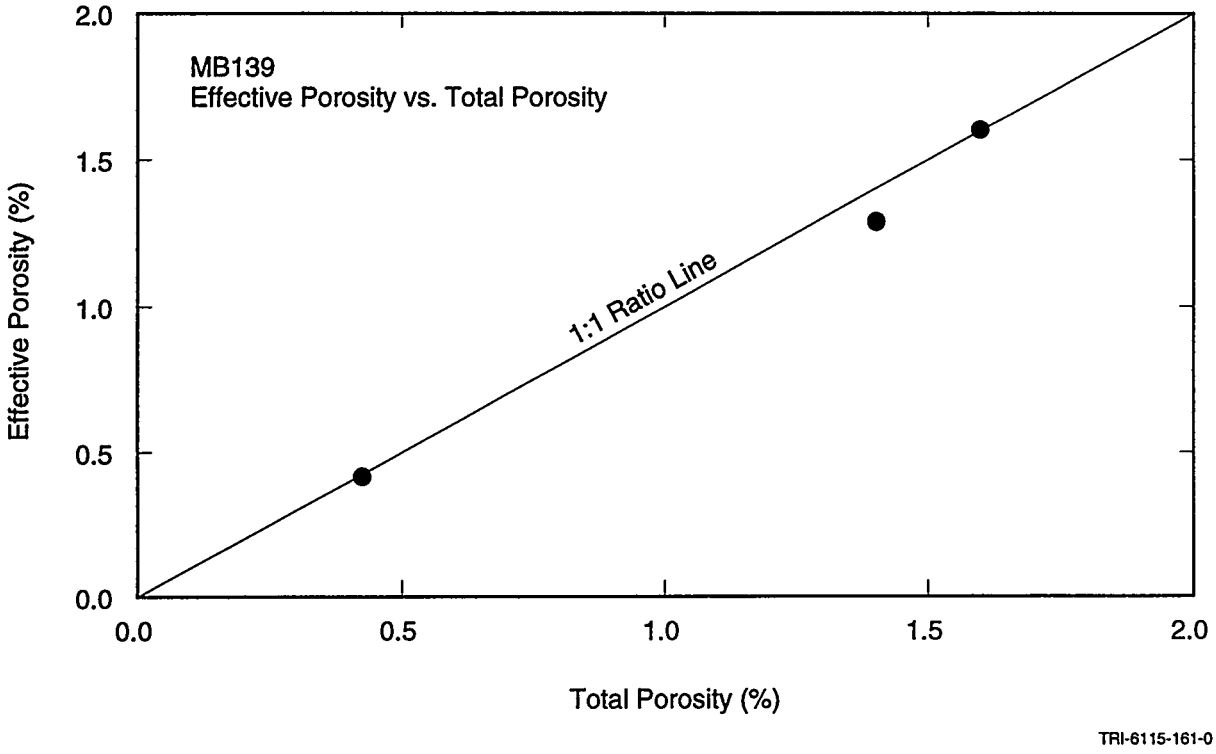

Figure 13. Effective porosity versus total porosity.

4.2.4 Relationship between Zone Classification and Total Porosity

The three total porosity specimens were classified according to the five MB139 stratigraphic zones described in Section 3.2. Zone classification for each specimen is listed in Table 3, and the data, are shown in Figure 14. Total porosity was measured only on specimens cut from Zones II, III, and IV. As Figure 14 shows, the data suggest that Zone III has lower total porosity than Zones II and IV. However, at this time insufficient data exist from which to draw definitive conclusions regarding correlations between Borns' (1985) MB139 stratigraphic zone classifications and total or effective porosity.

4.3 Grain Density

4.3.1 Test Procedures

Grain density was calculated for 49 cores by dividing the weight of the dry specimen by the grain volume measured using a porosimeter and the Boyle's law helium expansion technique. As shown in Table 3, the grain density values ranged from 2.53 to 2.96 g/cm^3,

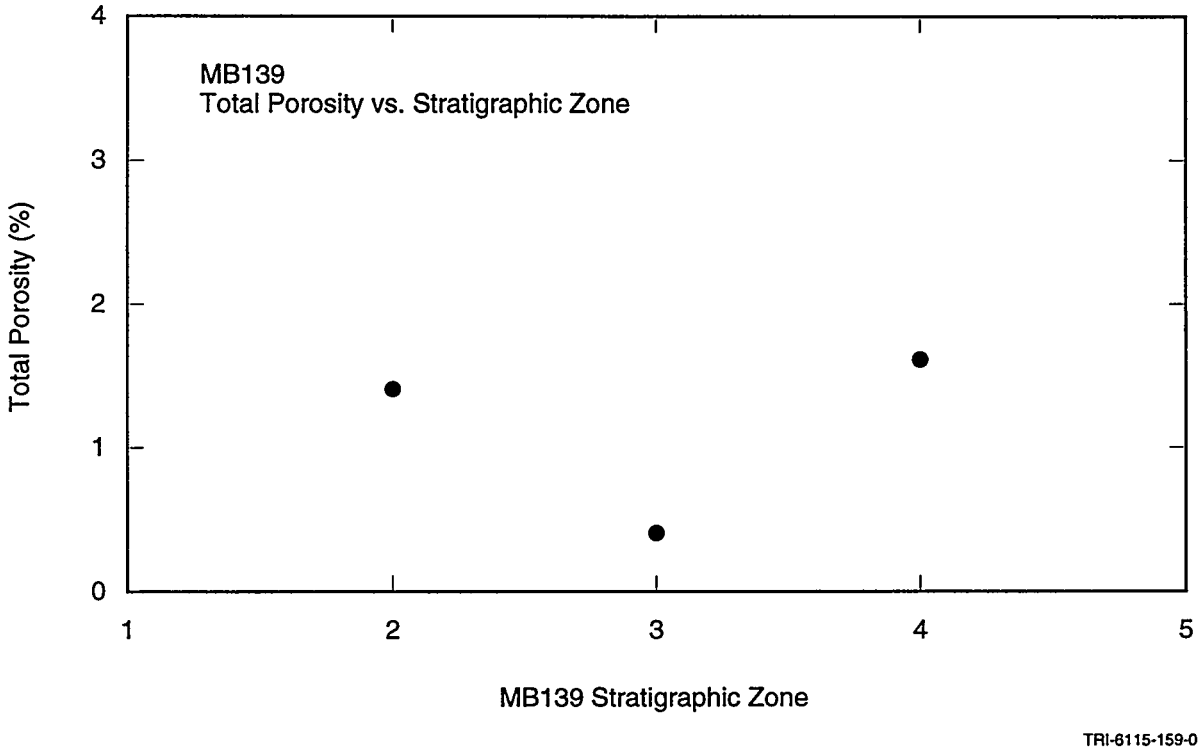

Figure 14. Total porosity versus Marker Bed 139 stratigraphic zone.

with a mean of 2.75 g/cm^3. The specific gravity of pure anhydrite is 2.89 to 2.98 g/cm^3, and these results illustrate the wide variability in anhydrite content within MB139.

4.3.2 Histogram and Probability Distribution

Distributions of grain density data are shown as a histogram in Figure 15a and as a cumulative frequency plot in Figure 15b. As Figure 15a illustrates, the marker bed exhibits a bimodal distribution of grain density. Approximately 75% of the samples are composed of anhydrite and other minerals, and approximately 25% are nearly pure anhydrite.

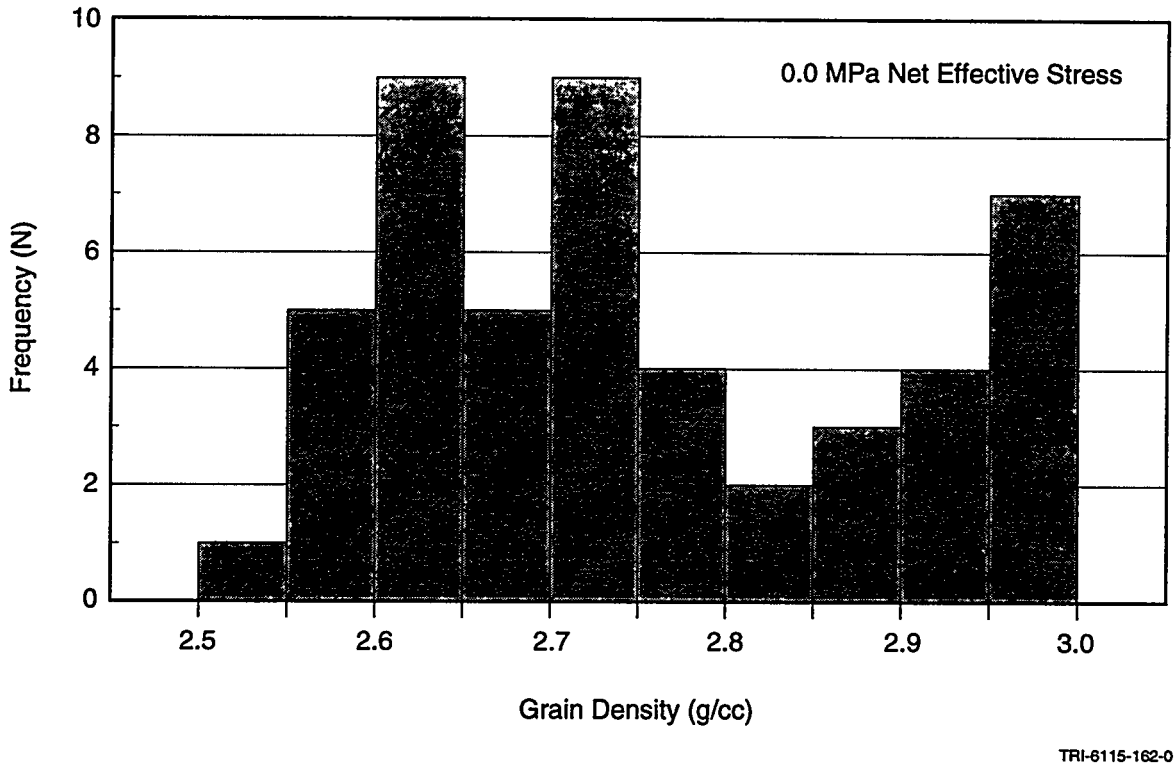

Figure 15a. Grain density histogram.

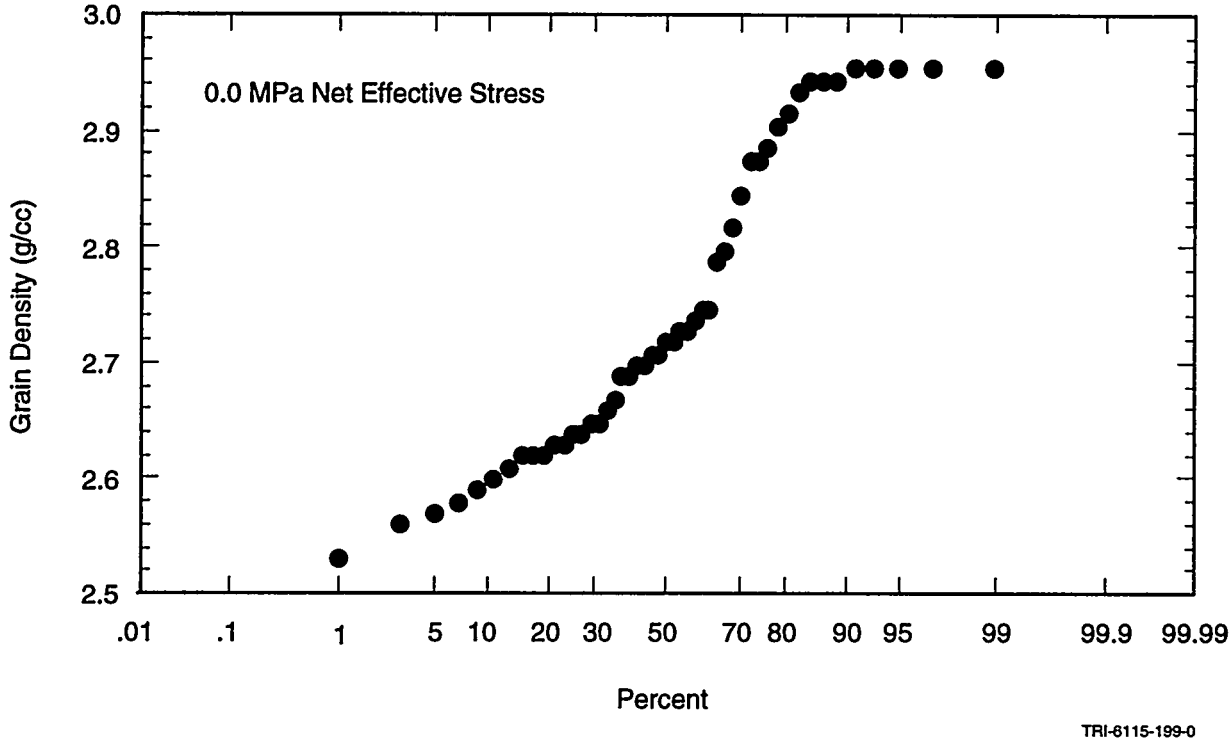

Figure 15b. Normalized grain density cumulative frequency plot.

5.0 PERMEABILITY

The permeability test matrix was designed to provide MB139 permeability data, to investigate the effects of confining stress on gas and liquid permeability and possible differences between horizontal and vertical (with respect to the bedding plane) gas permeability, and to assess the suitability of using synthetic MB139 brine versus a known nonreactive liquid for liquid permeability tests. Gas permeability was measured using the steady-state method on 39 specimens at the three test laboratories. Successful gas permeability measurements including correction for gas-slippage effects were made on 31 specimens. Successful liquid permeability measurements were conducted on five of the 31 specimens.

The results of the gas and liquid permeability tests performed under various net effective stress conditions are summarized in Tables 3a, 3b, and 3c. Twenty-three successful measurements were made on the 29 tested specimens, which were cut and oriented so that the flow direction was parallel to the bedding plane to measure horizontal permeability. Eight successful measurements were made on ten specimens, which were cut and oriented so that the flow direction was perpendicular to the bedding plane to measure vertical permeability. Five successful liquid permeability tests were conducted. Three specimens were tested at TerraTek using odorless mineral spirits (OMS) as the saturant; three specimens were tested at RE/SPEC, producing two successful tests, using a simulated MB139 brine as the saturant.

5.1 Test Procedures

5.1.1 Single-Phase Gas Permeability

The test matrix for each test laboratory was designed to measure permeability at three different suites of net effective stress. The values of 2, 6, and 10 MPa were chosen to represent a wide range of in situ stress conditions, assuming that the MB139 specimens obey the classical net effective stress law described in Section 2.4 of this report. (For example, the 2 MPa value reflects conditions where the difference between the lithostatic and the pore pressures is 2 MPa.)

RE/SPEC was the first laboratory to perform permeability tests on the MB139 samples. Significant uncertainty existed on the range of gas permeability values expected and on the appropriate values of pore pressure and confining pressure to be applied.

Therefore permeability tests were conducted at RE/SPEC at 2, 6, and 10 MPa confining pressure with 0.4, 0.7, and 1.0 MPa inlet pore pressure and 0.1 MPa outlet pore pressure at each confining pressure step. To ensure reproducible results, each test was repeated twice at each inlet pore pressure.

To provide data comparable to that from the other laboratories, the net effective stress was calculated at each confining pressure from the average pore pressure, as shown in Equation 4, using the raw RE/SPEC data contained in Appendix B. For example, for the tests performed at 2 MPa confining pressure, the average pore pressures were 0.25 MPa, 0.4 MPa, and 0.55 MPa. The average pore pressure for this suite, 0.4 MPa [i.e., (0.25 MPa + 0.4 MPa + 0.7 MPa)/3], was then calculated. Using the confining pressure and the average pore pressure, the net effective stress, 1.6 MPa [i.e., (2.0 MPa - 0.4 MPa)] was determined. This method was repeated for the 6.0 and 10.0 MPa confining pressure data, and the corresponding permeability results for RE/SPEC are presented in Table 3b at 1.6, 5.6, and 9.6 MPa net effective stress. Results from RE/SPEC indicated that permeability measurements can be made at specified effective stress. Therefore the net effective stresses chosen for subsequent tests were 2, 6, and 10 MPa.

$$P_p = (P_{inlet} + P_{outlet}) / 2 \quad (4)$$

Because of equipment limitations at Core Laboratories, the lowest net effective stress that could be imposed on the cores was 3.4 MPa; therefore permeability was measured at 3.4, 6.0, and 10.0 MPa at this test facility. TerraTek performed permeability tests at the three specified net effective stress values of 2.0, 6.0, and 10.0 MPa. In some cases, equipment resolution capabilities were exceeded at Core Laboratories, which precluded completion of tests at higher net effective stress conditions.

Ten of the specimens tested at Core Laboratories were cut perpendicular to the bedding plane of MB139. The other 20 Core Laboratories specimens and all specimens tested at RE/SPEC and TerraTek were cut parallel to the MB139 bedding plane. In the general discussion of gas and liquid permeability test results, the results are presented independent of flow orientation with respect to bedding plane. Section 5.2.4 contains a comparison of gas permeability results related to flow orientation.

The test conditions and procedures used at Core Laboratories, RE/SPEC, and TerraTek are described in detail in Appendices A, B, and C, respectively.

5.1.2 Single-Phase Liquid Permeability

Single-phase, steady-state liquid permeability was measured for five specimens at three net effective stress conditions: three at TerraTek at 2.0, 6.0, and 10.0 MPa net effective stress; two at RE/SPEC at 1.6, 5.6, and 9.6 MPa net effective stress. Prior to the liquid permeability tests, gas permeability was measured on each specimen so that direct comparisons could be made between the liquid permeability and the Klinkenberg-corrected gas permeability: the measured liquid permeability should be equal to the Klinkenberg-corrected gas permeability (Klinkenberg, 1941).

To address concerns about the possibility of brine composition affecting the permeability of a test specimen (e.g., causing local dissolution of the specimen), liquid permeability tests were performed at TerraTek using odorless mineral spirits (OMS), a non-reactive liquid. These tests were performed at RE/SPEC using a simulated MB139 brine, SB-139-95B. This brine was formulated according to the recipe contained in Appendix D.

5.2 Test Results

5.2.1 Single-Phase Gas Permeability

The results of the Klinkenberg-corrected, single-phase gas permeability measurements are detailed in Tables 3a, 3b, and 3c and summarized in Tables 6a and 6b. All gas permeability data presented in Tables 3a, 3b, and 3c have been rigorously verified and are considered "good" data. Explanation and discussion of data excluded from Tables 3a, 3b, and 3c are found at the beginning of Appendix A, B, or C for Core Laboratories, RE/SPEC, or TerraTek, respectively.

For simplicity, in Table 6b the results for gas permeability tests performed at 1.6, 2.0, and 3.4 MPa are grouped together and in this discussion are referred to as the 2 MPa data. Similarly, the 5.6 and 6.0 MPa data are combined and referred to as the 6 MPa data, and the 9.6 and 10.0 MPa data are combined and referred to as the 10 MPa data. Gas permeability ranged from a minimum of 1.5×10^{-19} m^2 to a maximum of 8.3×10^{-16} m^2 for the 2 MPa tests, 5.9×10^{-20} m^2 to 3.0×10^{-16} m^2 for the 6 MPa tests, and, 5.0×10^{-20} m^2 to 1.5×10^{-16} m^2 for the 10 MPa tests. The high permeability of Sample E, tested at TerraTek, appears to be an anomaly. It is not known whether the core was damaged or its high permeability occurred naturally. The log of gas permeability values are also summarized in Table 6b.

5.2.1.1 Histograms and Probability Distributions

The histogram and associated cumulative frequency plots for the 2, 6, and 10 MPa data are shown in Figures 16, 17, and 18, respectively. The permeability distribution appears to be log normal. A log-normal distribution is expected because permeability depends on pore-size distribution, and pore-size distribution is typically log-normal for rocks (Freeze, 1975).

Table 6a. Summary of Gas Permeability Data Results

	Gas Permeability (Klinkenberg Corrected)						
	1.6 MPa (m^2)	2 MPa (m^2)	3.4 MPa (m^2)	5.6 MPa (m^2)	6 MPa (m^2)	9.6 MPa (m^2)	10 MPa (m^2)
Minimum	3.2×10^{-18}	1.5×10^{-19}	3.9×10^{-19}	1.7×10^{-18}	5.9×10^{-20}	1.4×10^{-18}	5.0×10^{-20}
Maximum	1.6×10^{-17}	8.3×10^{-16}	2.2×10^{-18}	8.9×10^{-18}	3.0×10^{-16}	5.1×10^{-18}	1.5×10^{-16}
Sum	1.9×10^{-17}	8.5×10^{-16}	2.4×10^{-17}	1.1×10^{-17}	3.3×10^{-16}	6.5×10^{-18}	1.7×10^{-16}
Points	2	6	23	2	27	2	20
Mean	9.7×10^{-18}	1.4×10^{-16}	1.1×10^{-18}	5.3×10^{-18}	1.2×10^{-17}	3.2×10^{-18}	8.5×10^{-18}
Median	9.7×10^{-18}	6.4×10^{-18}	9.5×10^{-19}	5.3×10^{-18}	5.7×10^{-19}	3.2×10^{-18}	2.8×10^{-19}
Std. Deviation	9.1×10^{-18}	3.4×10^{-16}	5.5×10^{-19}	5.1×10^{-18}	5.8×10^{-17}	2.7×10^{-18}	3.4×10^{-17}
Variance	8.3×10^{-35}	1.1×10^{-31}	3.0×10^{-37}	2.6×10^{-35}	3.4×10^{-33}	7.1×10^{-36}	1.2×10^{-33}

Table 6b. Statistical Summary of Gas Permeability and Log of Gas Permeability (Klinkenberg Corrected)

	Gas Permeability			Log (Gas Permeability)		
	2 MPa (m^2)	6 MPa (m^2)	10 MPa (m^2)	2 MPa (m^2)	6 MPa (m^2)	10 MPa (m^2)
Minimum	1.5×10^{-19}	5.9×10^{-20}	5.0×10^{-20}	-18.84	-19.23	-19.30
Maximum	8.3×10^{-16}	3.0×10^{-16}	1.5×10^{-16}	-15.08	-15.52	-15.82
Sum	9.0×10^{-16}	3.4×10^{-16}	1.8×10^{-16}	-552.29	-524.43	-402.17
Points	31	29	22	31	29	22
Mean	2.9×10^{-17}	1.2×10^{-17}	8.0×10^{-18}	-17.82	-18.08	-18.28
Median	1.3×10^{-18}	5.7×10^{-19}	3.1×10^{-19}	-17.89	-18.24	-18.51
Std. Deviation	1.5×10^{-16}	5.6×10^{-17}	3.2×10^{-17}	0.67	0.69	0.83
Variance	2.2×10^{-32}	3.2×10^{-33}	1.1×10^{-33}	0.45	0.48	0.69

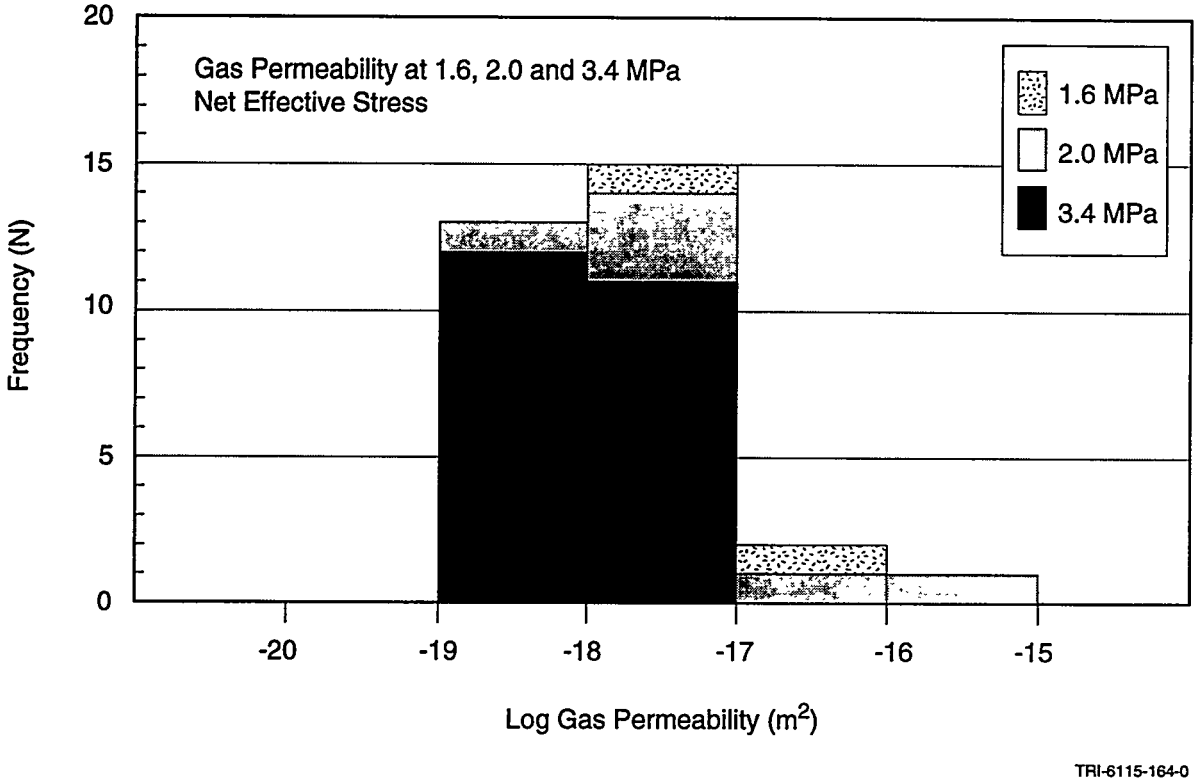

Figure 16a. Gas permeability histogram for 1.6, 2.0, and 3.4 MPa net effective stress.

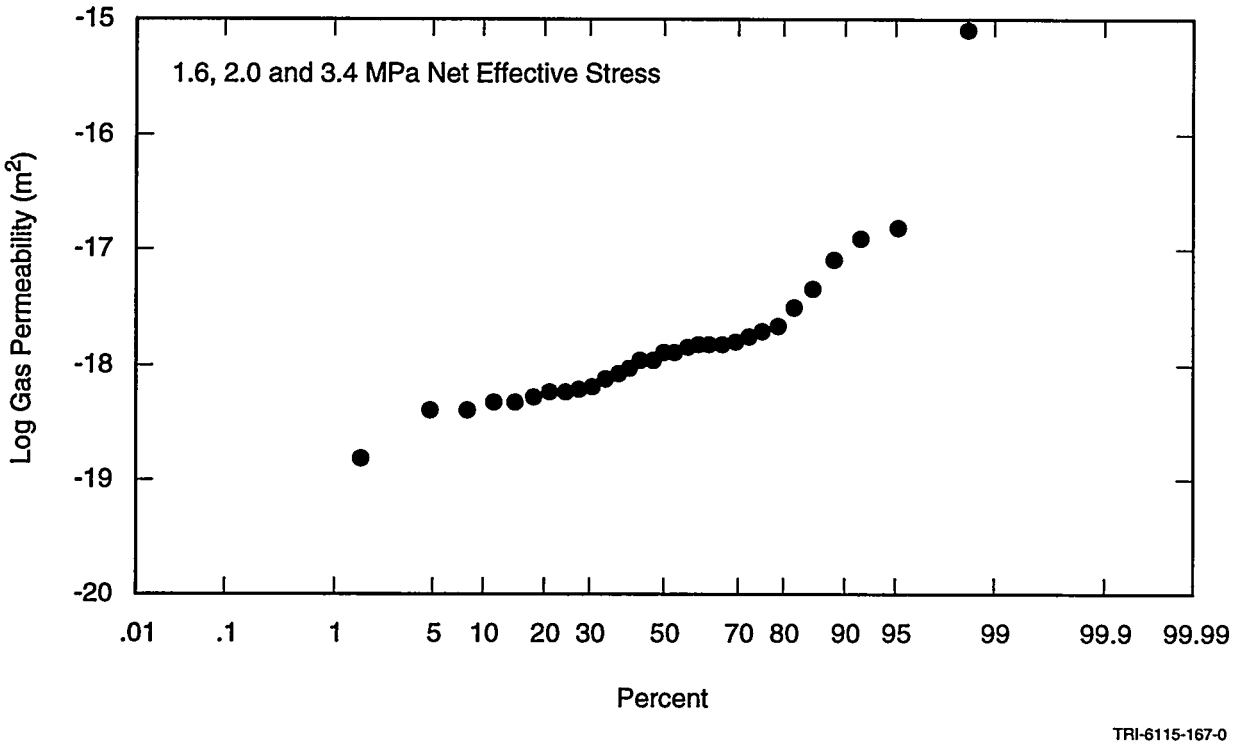

Figure 16b. Normalized cumulative frequency plot for 1.6, 2.0, and 3.4 MPa net effective stress.

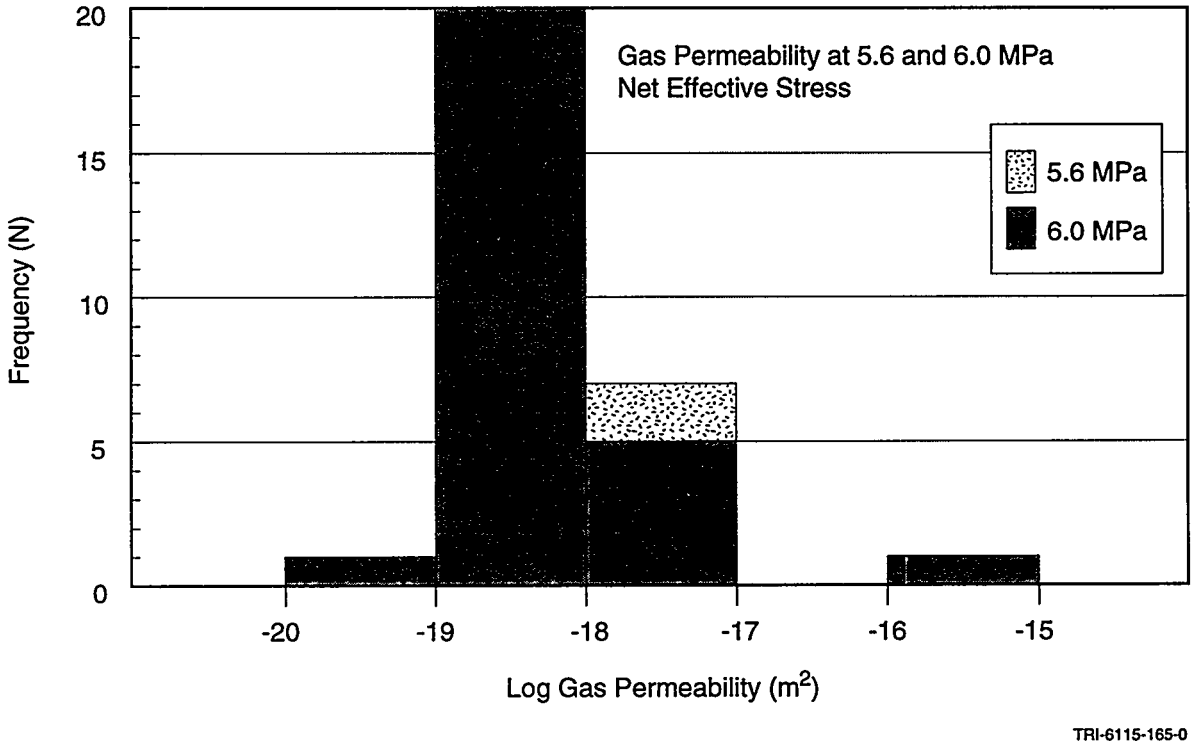

Figure 17a. Gas permeability histogram for 5.6 and 6.0 MPa net effective stress.

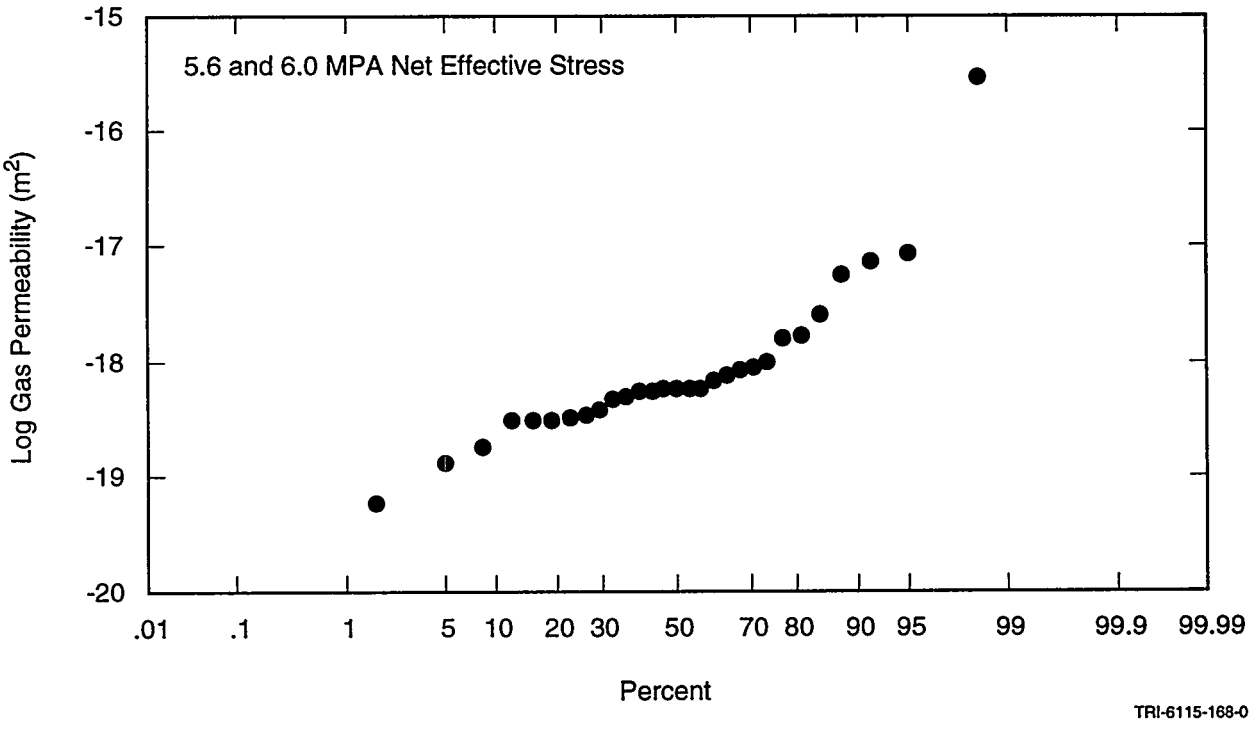

Figure 17b. Normalized cumulative frequency plot for 5.6 and 6.0 MPa net effective stress.

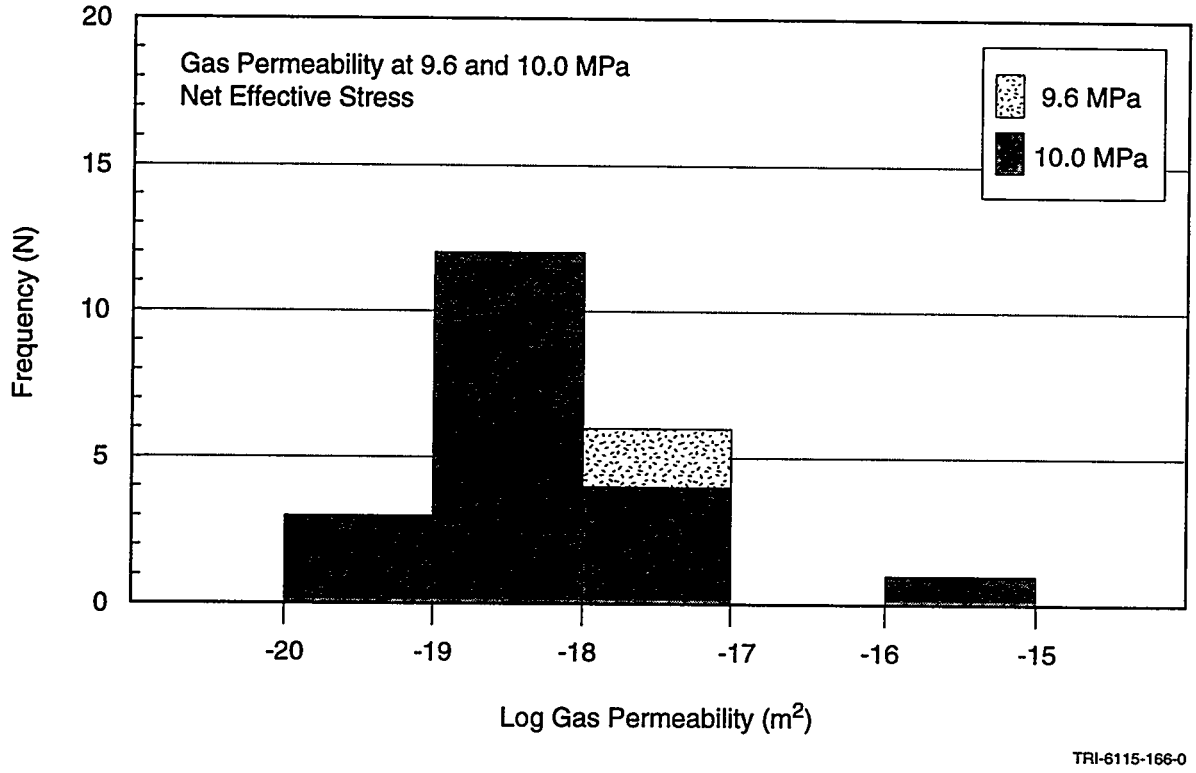

Figure 18a. Gas permeability histogram for 9.6 and 10.0 MPa net effective stress.

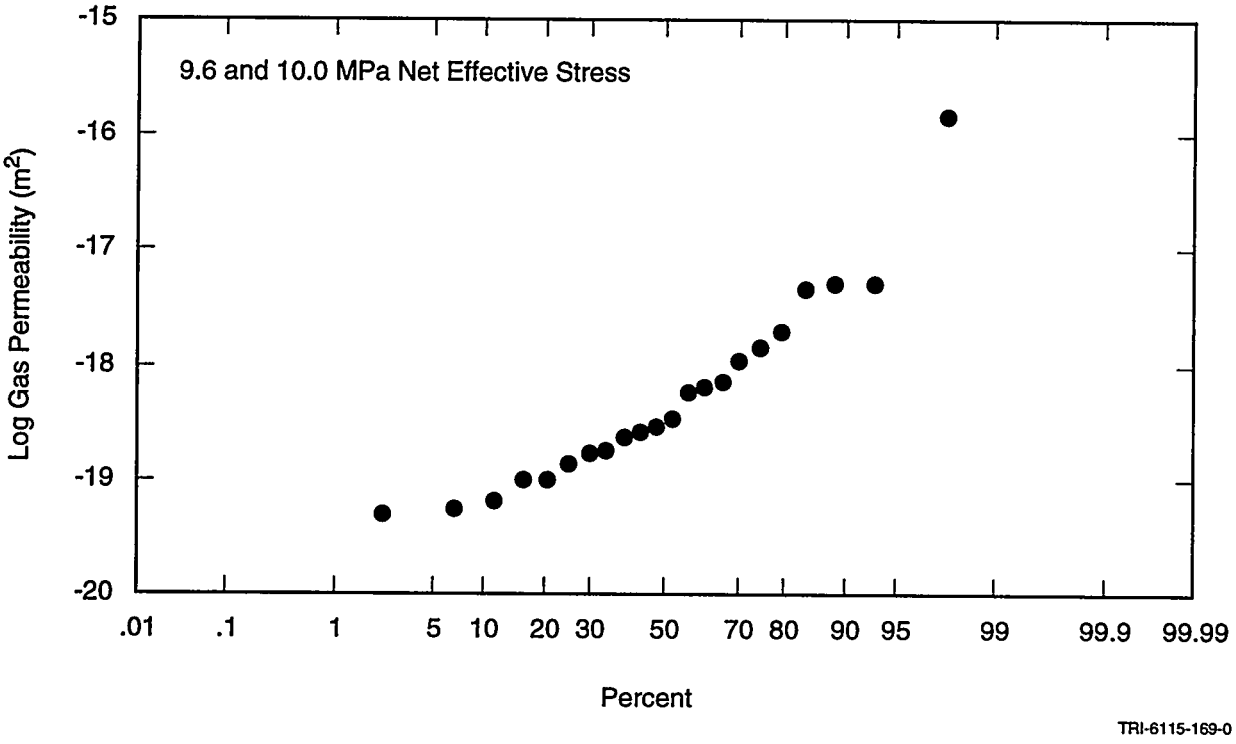

Figure 18b. Normalized cumulative frequency plot for 9.6 and 10.0 MPa net effective stress.

5.2.1.2 Relationship between Zone Classification and Gas Permeability

Figure 19 shows a plot used to evaluate gas permeability for the 2 MPa data among MB139 Stratigraphic Zones II, III, and IV. The results are summarized in Table 7. No specimens were cut from Zones I or V. No definitive distribution is evident from the gas permeability data; however, the data suggest that the permeability of Zone IV is slightly higher than Zones II and III, if the anomalously high permeability data from TerraTek's Sample E are excluded. The flow properties of Zones I and V are expected to be more representative of fractured rock and are therefore likely to have greater permeability than Zones II, III, or IV.

Table 7. Summary of Gas Permeability Data Results by Zone at 2 MPa Net Effective Stress

Zone	Number of Data Points	Minimum Permeability (m^2)	Maximum Permeability (m^2)	Median Permeability (m^2)
II	6	5.9×10^{-20}	5.7×10^{-18}	9.6×10^{-19}
III	20	3.9×10^{-19}	3.0×10^{-16}	1.2×10^{-18}
IV	5	5.9×10^{-19}	8.9×10^{-18}	1.5×10^{-18}

5.2.1.3 Relationship between Confining Stress and Gas Permeability

Gas permeability tests were successfully conducted on 31 specimens under hydrostatic confining stress conditions. Gas permeability was successfully measured on 31 specimens at the 2 MPa net effective stress level, on 29 of the 31 specimens at the 6 MPa net effective stress level, and on 22 of 29 specimens at the 10 MPa net effective stress level.

Figure 20 is a graph showing Klinkenberg-corrected gas permeability versus net effective stress for 31 specimens. The graph shows the range of measured gas permeability values at each net effective stress and the median gas permeability at each net effective stress. The near-horizontal lines on Figure 20 connect the gas permeability data for some specimens. Attempts were made at each test laboratory to measure gas permeability at three net effective stresses. In some cases, however, equipment resolution capabilities were exceeded at Core Laboratories, precluding the completion of tests at higher net effective stress conditions.

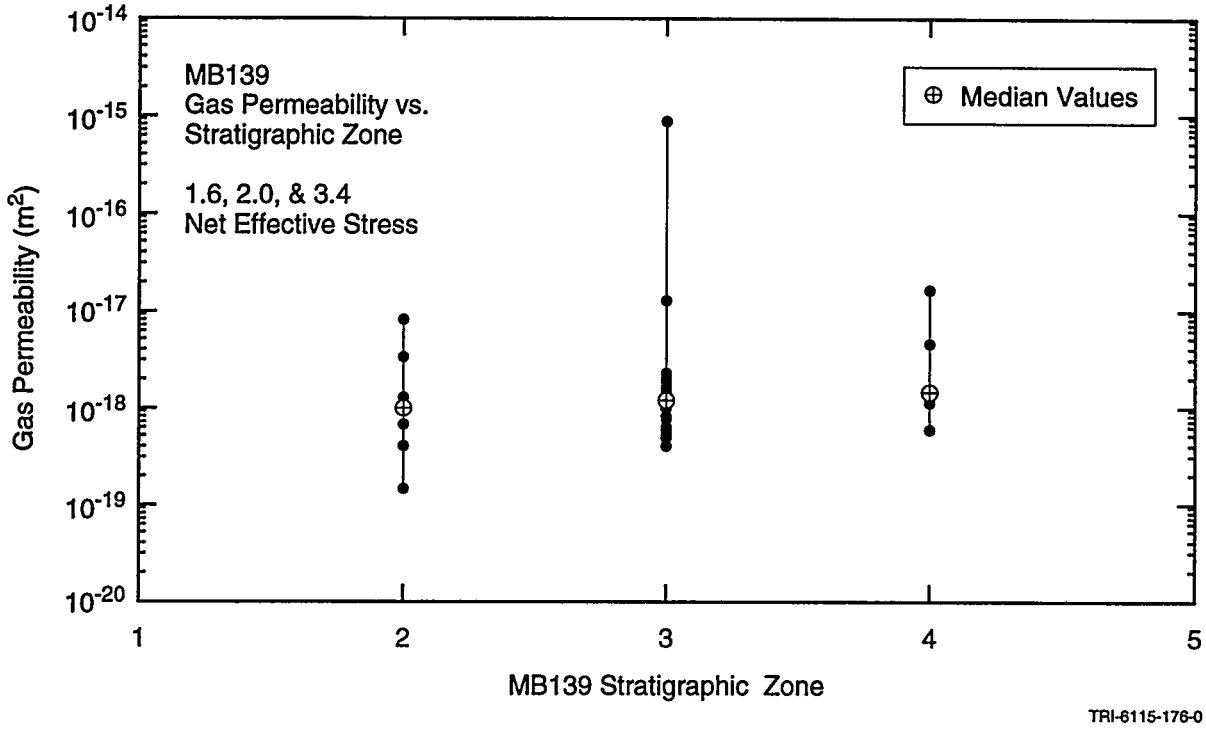

Figure 19. Gas permeability versus Marker Bed 139 stratigraphic zone.

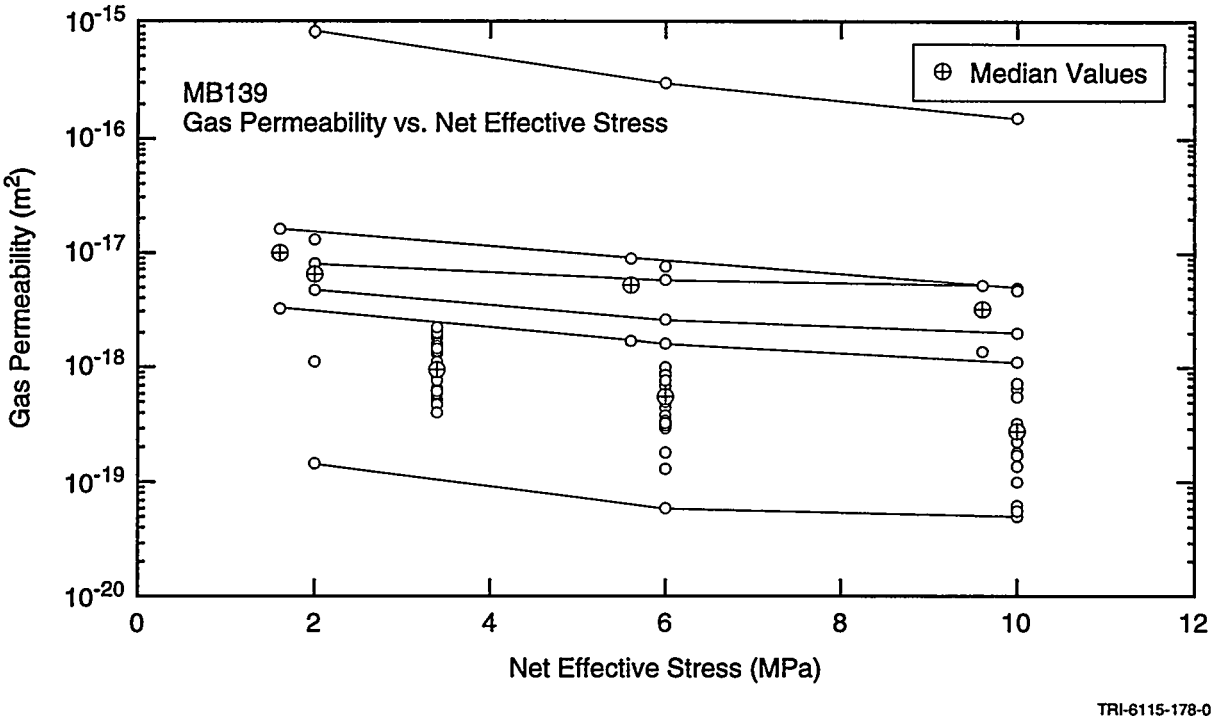

Figure 20. Gas permeability versus net effective stress.

Increasing the net effective stress on a specimen caused the gas permeability to decrease in all cases. The decrease in Klinkenberg-corrected gas permeability corresponding to an increase in net effective stress from 2 to 10 MPa ranged from a factor of 1.6 to 11.6, with a mean of 4.0.

5.2.2 Single-Phase Liquid Permeability

Single-phase, steady-state liquid permeability was measured for five specimens: three at TerraTek and two at RE/SPEC. Prior to the liquid permeability tests, gas permeability was measured for each specimen so that direct comparisons could be made between the liquid permeability and the Klinkenberg-corrected gas permeability: the measured liquid permeability should equal the Klinkenberg-corrected gas permeability (Klinkenberg, 1941). Results of the liquid permeability tests are summarized in Tables 3b and 3c.

Liquid permeability tests were designed to be conducted using the steady-state method with fully saturated test specimens. However, both test laboratories reported difficulties related to saturating the test specimens. RE/SPEC observed during the saturation process that noticeable dissolution of both specimens occurred, indicating that brine composition was not compatible with the rock. A careful review of the raw TerraTek liquid permeability data showed that only "preliminary" data were included; in some cases, it was reported that specimens were over 100% saturated with OMS, which is not possible. Therefore the liquid permeability data reported here should be considered only as "scoping data." Although the liquid permeability data provide useful information for designing and implementing future liquid and relative permeability tests, the data do not meet applicable quality standards necessary for use within the WIPP Performance Assessment (PA) program.

5.2.2.1 Histograms and Probability Distributions

Results of single-phase liquid permeability measurements performed at RE/SPEC and TerraTek are shown in Tables 3b and 3c and summarized in Table 8. RE/SPEC measured liquid permeability for two specimens at 1.6 MPa net effective stress but was able to measure liquid permeability on only one core at 5.6 and 9.6 MPa net effective stress because of mechanical failure. TerraTek measured liquid permeability for all three samples at 2.0, 6.0, and 10.0 MPa net effective stress. Measured liquid permeabilities ranged from a minimum of 5.1×10^{-19} m^2 to a maximum of 7.9×10^{-17} m^2 at the lower net effective stress levels. The lowest measured permeability of 5.1×10^{-19} m^2 was at 10.0 MPa net effective stress.

Table 8. Summary of Liquid Permeability Data Results

	Liquid Permeability					
	1.6 MPa (m^2)	2 MPa (m^2)	5.6 MPa (m^2)	6 MPa (m^2)	9.6 MPa (m^2)	10 MPa (m^2)
Minimum	5.3×10^{-17}	1.1×10^{-18}	4.3×10^{-17}	6.1×10^{-19}	2.6×10^{-17}	5.1×10^{-19}
Maximum	7.9×10^{-17}	6.7×10^{-18}	4.3×10^{-17}	5.7×10^{-18}	2.6×10^{-17}	5.3×10^{-18}
Sum	1.3×10^{-16}	1.1×10^{-17}	4.3×10^{-17}	8.7×10^{-18}	2.6×10^{-17}	7.6×10^{-18}
Points	2	3	1	3	1	3
Mean	6.6×10^{-17}	3.8×10^{-18}	4.3×10^{-17}	2.9×10^{-18}	2.6×10^{-17}	2.5×10^{-18}
Median	6.6×10^{-17}	3.6×10^{-18}	4.3×10^{-17}	2.4×10^{-18}	2.6×10^{-17}	1.8×10^{-18}
Std. Deviation	1.8×10^{-17}	2.8×10^{-18}		2.6×10^{-18}		2.5×10^{-18}
Variance	3.4×10^{-34}	7.9×10^{-36}		6.6×10^{-36}		6.1×10^{-36}

The histogram and associated cumulative frequency plots for the 2, 6, and 10 MPa data are shown in Figures 21, 22, and 23, respectively. The permeability distribution appears to be log normal. A log-normal distribution is expected because permeability depends on pore-size distribution, and pore-size distribution is typically log-normal for rocks (Freeze, 1975).

5.2.2.2 Relationship between Zone Classification and Liquid Permeability

A plot of liquid permeability for the 2 MPa data among MB139 Stratigraphic Zones II and IV is shown in Figure 24. No specimens were cut from Zones I or V, and no successful measurements were made from Zone III.

Zone II permeabilities for net effective stress at 2 MPa ranged from 6.7×10^{-18} to 5.3×10^{-17} m^2 with a median value of 3×10^{-17} m^2. Zone IV permeabilities ranged from 1.1×10^{-18} to 7.9×10^{-17} m^2 with a median value of 3.6×10^{-18} m^2. There are not sufficient data from which to draw conclusions regarding liquid permeability distribution within the MB139 zones.

5.2.2.3 Relationship between Confining Stress and Liquid Permeability

Figure 25 is a graph showing liquid permeability versus net effective stress for the five specimens. The graph shows the range of measured liquid permeability values at each net effective stress. The line on Figure 25 shows the general trend of the gas permeability data for the four specimens measured at three different net effective stresses.

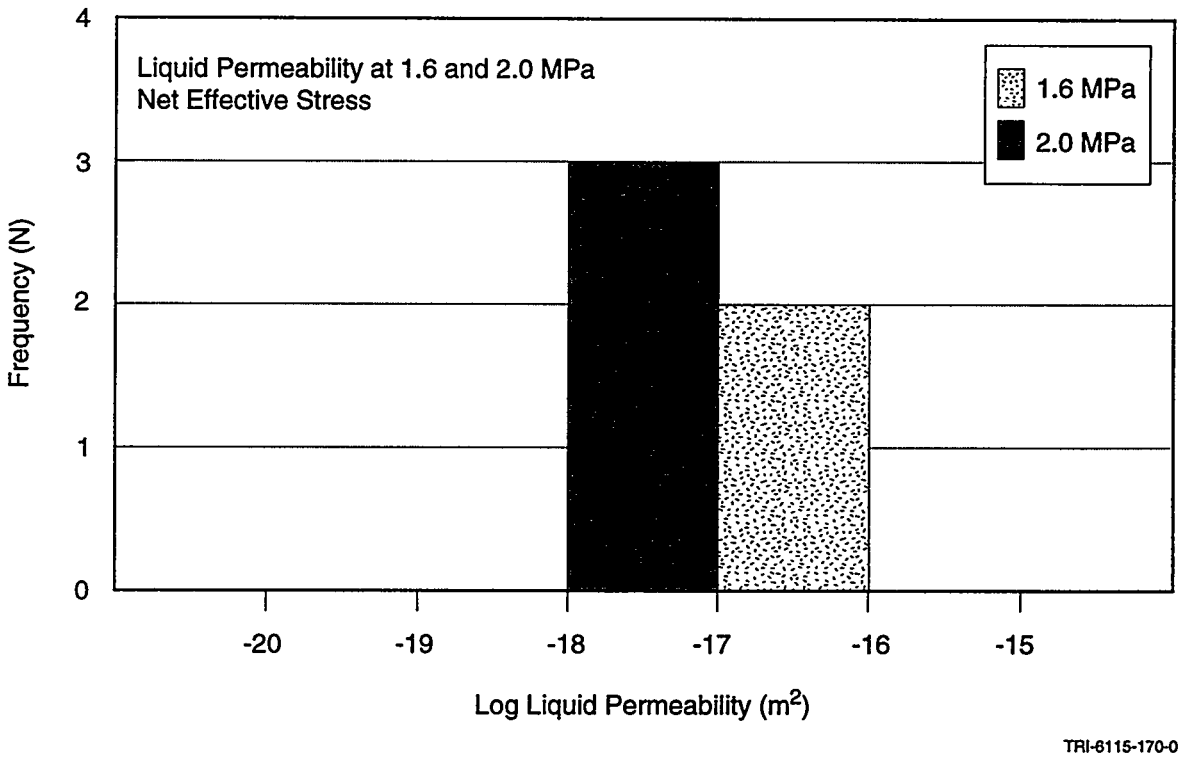

Figure 21a. Liquid permeability histogram for 1.6 and 2.0 MPa net confining stress.

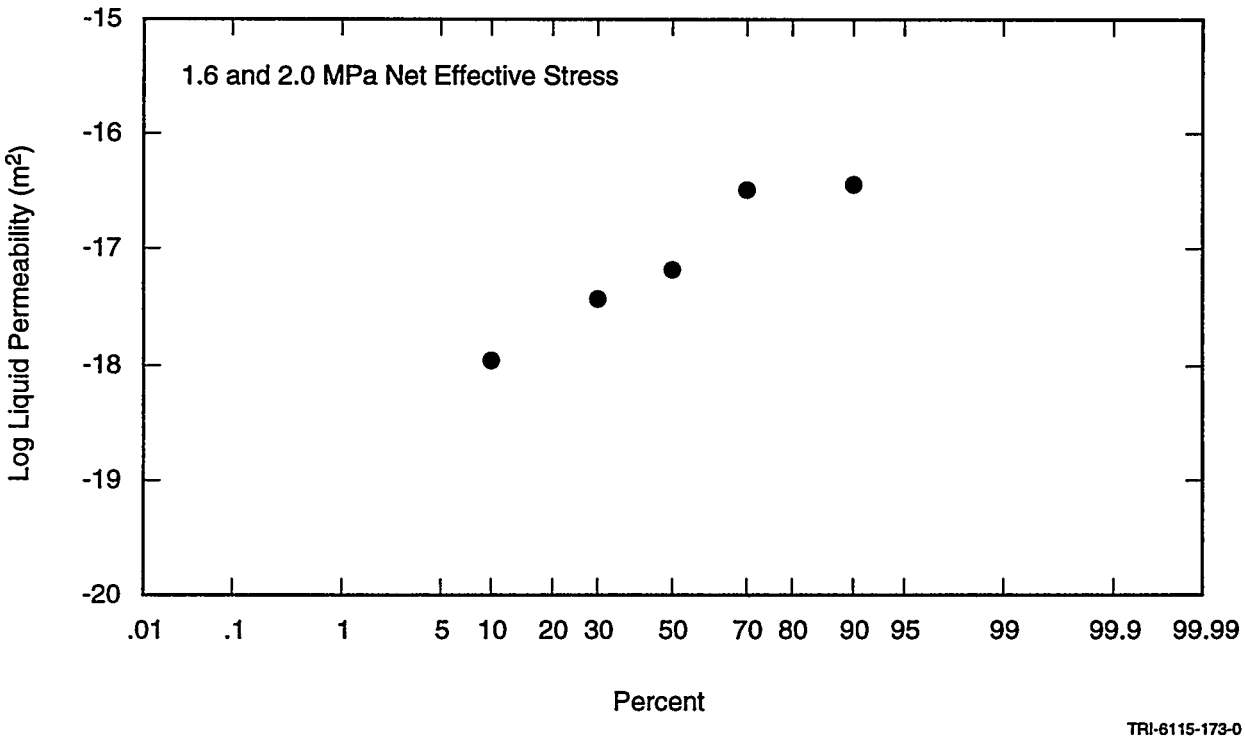

Figure 21b. Normalized cumulative frequency plot for 1.6 and 2.0 MPa net effective stress.

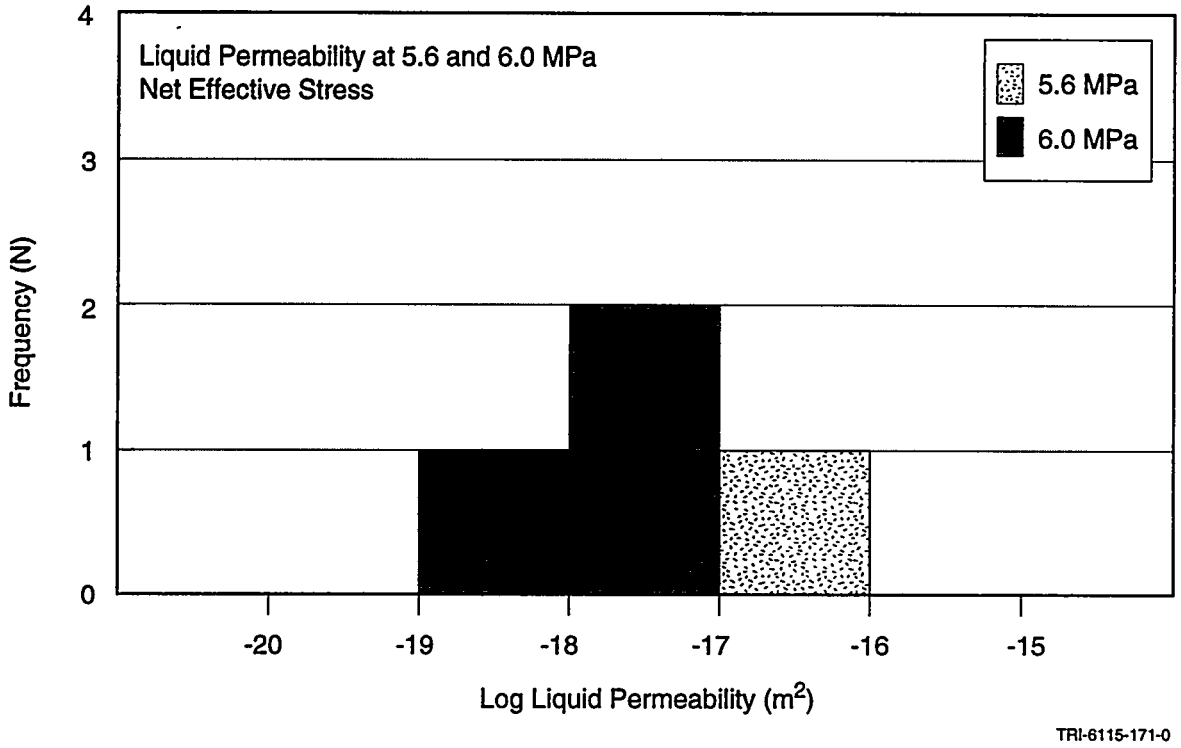

Figure 22a. Liquid permeability histogram for 5.6 and 6.0 MPa net confining stress.

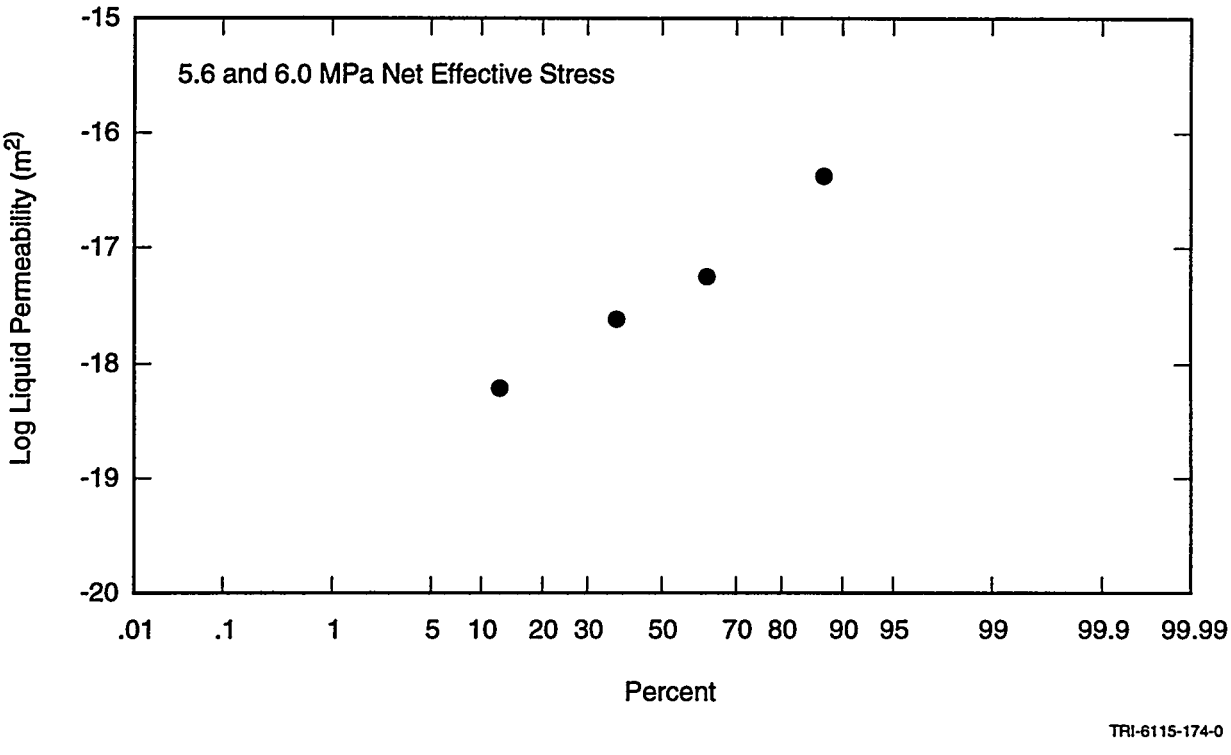

Figure 22b. Normalized cumulative frequency plot for 5.6 and 6.0 MPa net effective stress.

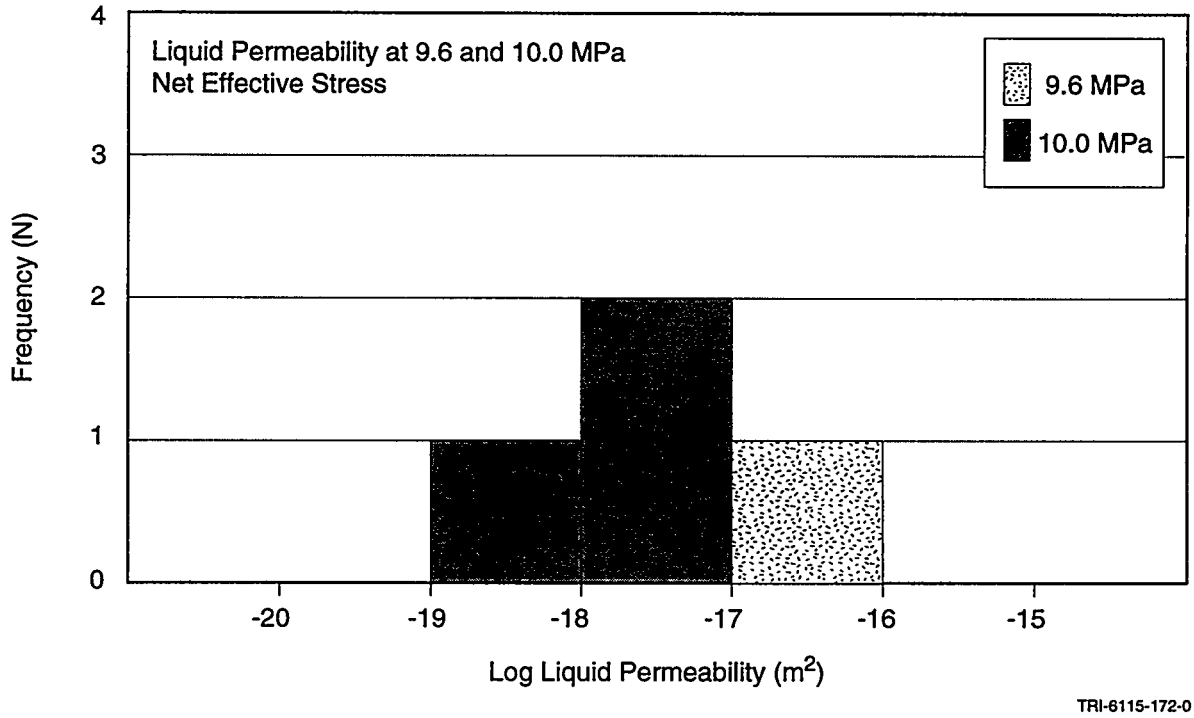

Figure 23a. Liquid permeability histogram for 9.6 and 10.0 MPa net confining stress.

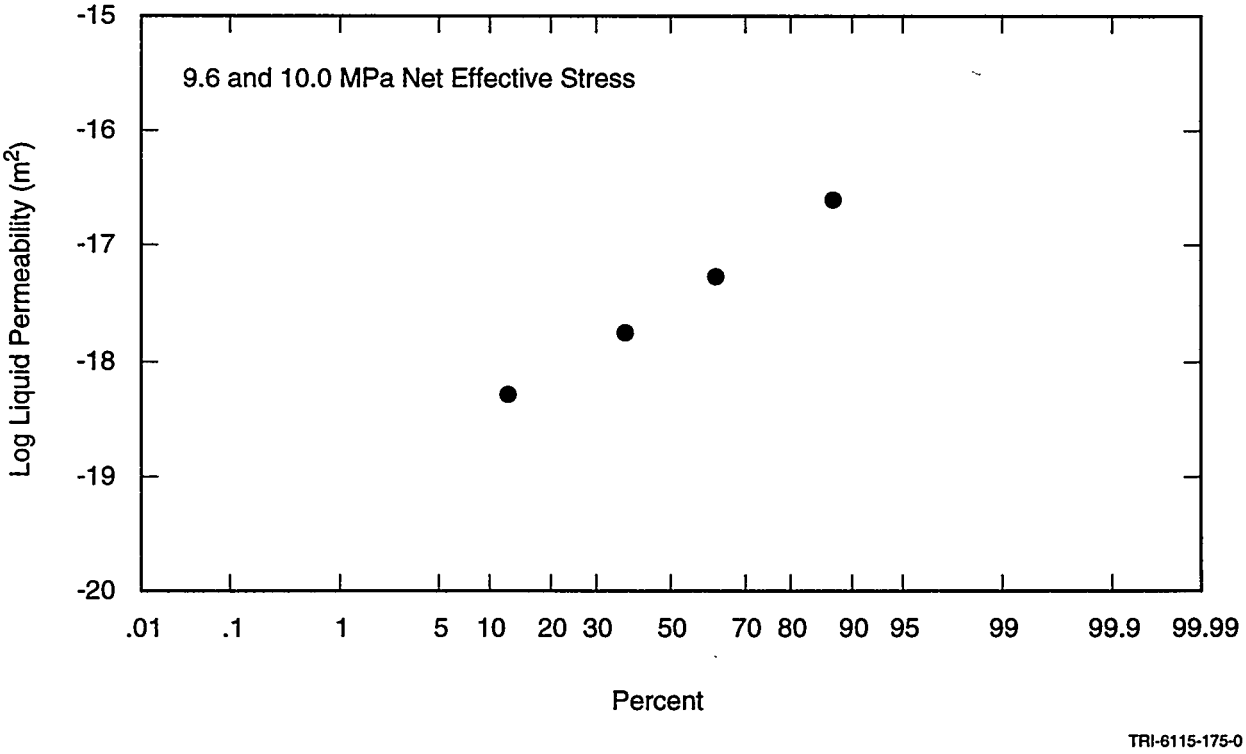

Figure 23b. Normalized cumulative frequency plot for 9.6 and 10.0 MPa net effective stress.

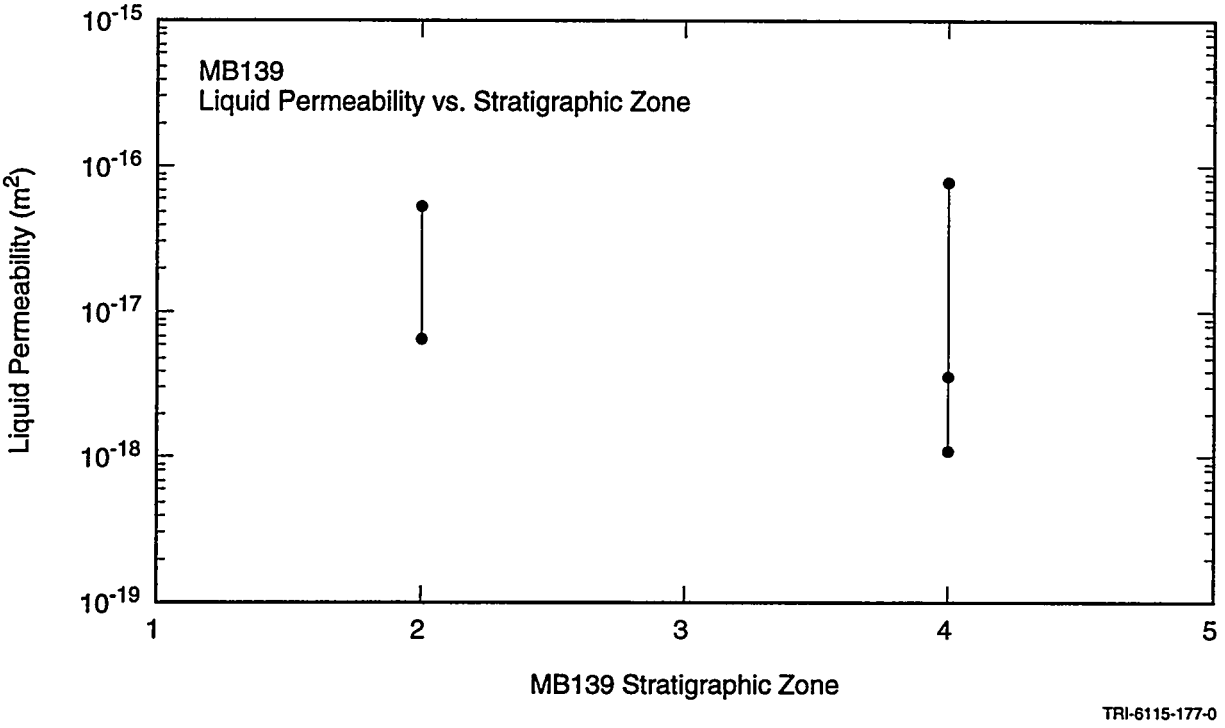

Figure 24. Liquid permeability versus Marker Bed 139 stratigraphic zone.

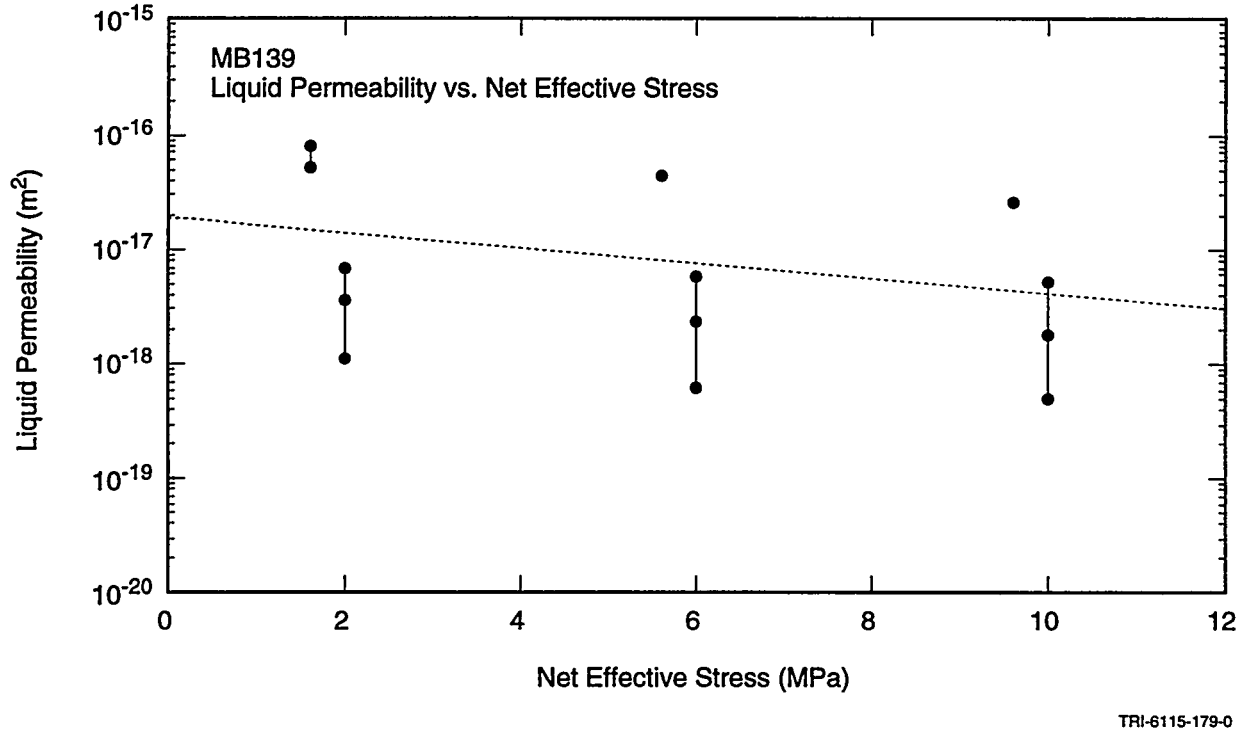

Figure 25. Liquid permeability versus net effective stress.

As expected, liquid permeability decreases as the net effective pressure is increased. The range of the magnitude of permeability decrease with an 8.0 MPa increase in net effective stress is less than for the gas permeability samples. However, at this time there are insufficient data from which to draw definitive conclusions regarding the decrease in liquid permeability with increasing net effective stress.

5.2.3 Comparison of Gas and Liquid Permeability

Figure 26 shows a plot of liquid permeability versus Klinkenberg-corrected gas permeability for the five cores for which gas and liquid permeability were measured. As expected, the liquid permeability measurements made with OMS show a nearly one-to-one agreement with the Klinkenberg-corrected gas-measured permeabilities. However, liquid permeability measurements performed with brine as the saturant show a significant difference from the gas permeability measurements. The significantly higher liquid permeabilities of the brine-saturated specimens were most likely caused by dissolution of the specimen, which resulted in an increase in the interconnected pathways.

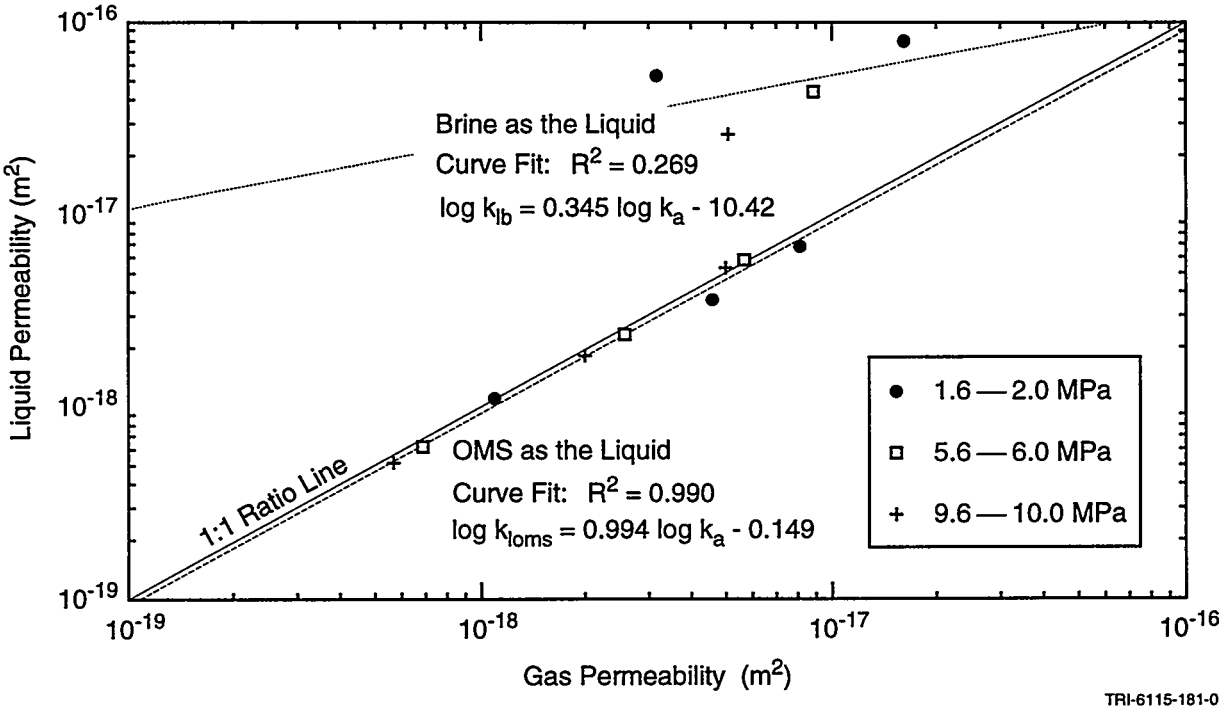

Figure 26. Liquid permeability versus gas permeability.

5.2.4 Comparison of Vertical and Horizontal Permeability

To evaluate anisotropy within the marker bed, Core Laboratories cut specimens from the same depth from whole cores oriented parallel and perpendicular to the bedding plane of MB139. The flow direction orientation with respect to the MB139 bedding plane is shown in Tables 3a, 3b, and 3c for each specimen. The "H" designates horizontal flow (i.e., flow parallel to the bedding plane), and the "V" designates vertical flow (i.e., flow perpendicular to the bedding plane).

Figure 27 shows a cross-plot of vertical and horizontal permeability made at 3.4 MPa net effective stress for six pairs of specimens that were drilled at Core Laboratories. The pairings were as follows: E1X10 Samples 5 and 7, E1X10 Samples 6 and 8, E1X10 Samples 11 and 13, E1X10 Samples 12 and 14, E1X11 Samples 23 and 25, and E1X11 Samples 24 and 26. Figure 27 shows the measurements with a one-to-one ratio line indicating where the data would fall if the horizontal and vertical permeabilities were the same. The limited data results suggest that anisotropy in MB139 is not apparent; horizontal and vertical permeability are the same, within experimental error parameters.

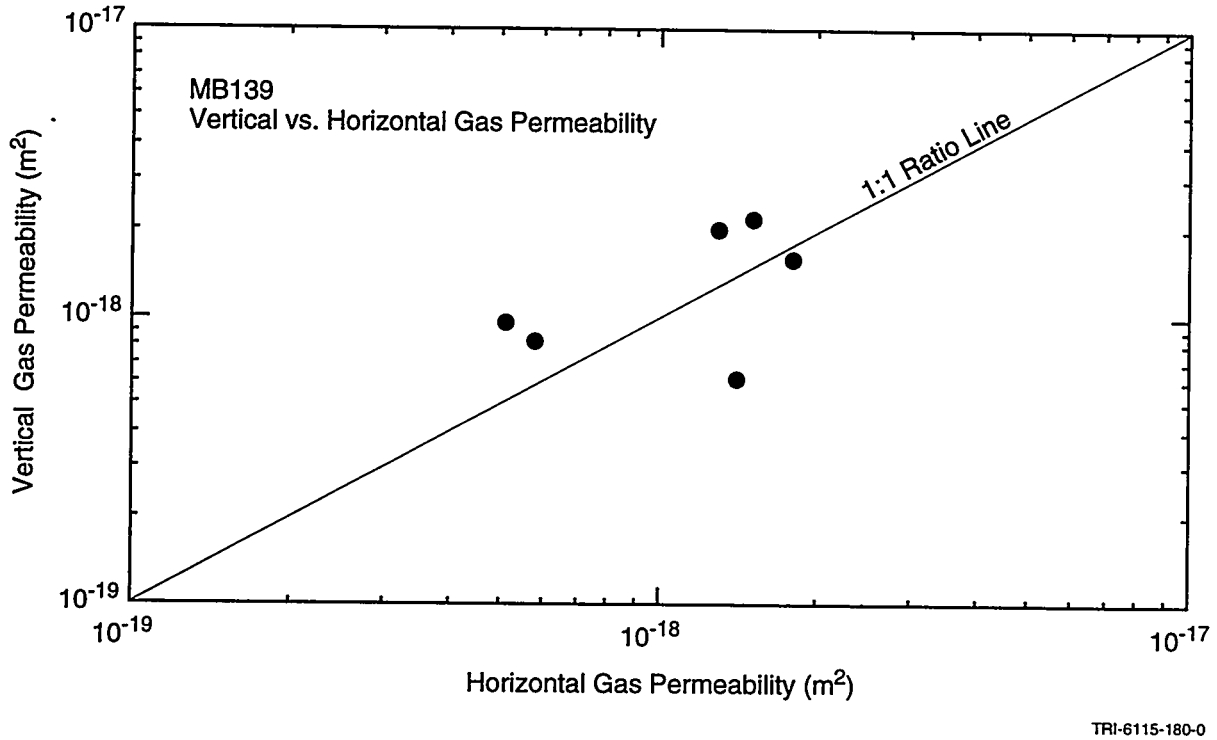

Figure 27. Gas vertical permeability versus horizontal permeability.

6.0 CAPILLARY PRESSURE

This report contains the only WIPP-specific two-phase flow data that exist. Capillary pressure tests were performed on twelve cores from the Core Laboratories' set of 2.5-cm (1-in.)-diameter specimens using the centrifuge and mercury injection techniques. The objective of the capillary pressure tests was to use two conventional oil and gas laboratory techniques (high-speed centrifuge and mercury injection), assess whether either was applicable for MB139 samples, and compare the results from the two techniques. Six pairs of specimens with comparable orientation, depth, porosity, and permeability values were selected from the Core Laboratories specimens. One specimen from each pair underwent centrifuge capillary pressure tests and the other specimen underwent mercury injection capillary pressure tests. Neither the centrifuge nor the mercury injection tests were performed under confining stress.

Details about the test procedures, raw data, and analysis are presented in Appendix A. Because this is the only report containing the results of two-phase flow tests on Salado rock, this section is more detailed than the previous sections in which the single-phase data were presented. This section contains the raw data converted from test conditions to repository conditions and presents the data in tabular and graphic formats. This section also contains comparisons of data from the two techniques from adjacent core samples, compilation of the data generated by each technique, and compilation of the results from all twelve tests.

6.1 Test Procedures

Using x-ray photos, quantitative x-ray diffraction data, and porosity and permeability data, six pairs of specimens used in the capillary pressure tests were selected from the 30 specimens tested at Core Laboratories. Two characteristics comprised the selection criteria: (1) adequate permeability and porosity for testing, and (2) same orientation, depth, and reasonable similarity between the two samples in each pair as evidenced from the x-ray photos, diffraction data, and porosity and permeability data. The six selected pairs were: Samples 5 and 6; 7 and 8; 11 and 12; 13 and 14; 21 and 22; and 23 and 24. After selection, axial x-ray computer tomography (CT) slices were made at two orientations on each core to provide additional evidence for comparison purposes. The odd-numbered core from each pair was tested using the mercury injection method; the even-numbered core was tested using the centrifuge.

6.1.1 Centrifuge Tests

A high-speed centrifuge was used to determine the drainage capillary pressure curves for six samples using decane (a non-reactive hydrocarbon) to pressures up to about 3.45 MPa (500 psi). The centrifuge method is nondestructive, yields reproducible results, and can provide data for both drainage and imbibition curves. During a drainage test (non-wetting phase [gas] displacing wetting phase [liquid]), a core is fully saturated with the liquid and placed on a semipermeable membrane inside a centrifuge rotor's coreholder. A low rotation rate is selected, and the core is spun. The high acceleration rate increases the force field on the fluids, in effect subjecting the core to an increased gravitational field (Bass, 1987). The volume of liquid is measured as the core is rotated until the volume of expelled liquid is constant. An average value of brine saturation is calculated using a method such as that of Hassler and Brunner (1945) for the core at each rotation rate, and the rotation speed is converted into force units in the center of the sample. A higher rotation rate is selected, and the steps are repeated. If the test system has different surface tension behavior than in situ, the results are converted using standard correction factors.

Decane was chosen as the wetting phase fluid for the centrifuge tests because it is available in a very pure form, will not react with water-soluble minerals found in the specimens, and has a well-documented surface tension (24 dynes/cm at 25°C). The dry samples were fully saturated with 99%-pure decane, then placed in a high-speed centrifuge with calibrated collection tubes located below each sample. The decane volume in the collection tubes was read manually using a strobe light synchronized to the speed of the spinning rotor. These tests were performed at ambient temperature and at zero confining stress.

The equilibrium time between speed changes was at least 24 hours. Collection tubes had an original volume of 1 cm^3 and were subdivided into 0.025 cm^3 divisions, readable to 0.01 cm^3. Because the porosity of the specimens was very low and greater volume resolution was desired, small Plexiglass rods with cross-sectional areas approximately half that of the collection tubes were inserted in the collection tubes. This ballast volume reduced the volume resolution to approximately 0.0125 per division, readable to 0.005 cm^3.

The Hassler-Brunner (1945) and the Rajan (1986) methods were used to reduce the data and generate the capillary pressure curves from the produced volume and rotation speed data. Correction factors were then applied to the reduced data to correct from the decane-air test conditions to the desired brine-air in situ conditions.

6.1.2 Mercury Injection Tests

With the mercury injection method, a dry core sample is submersed in a chamber containing mercury and then evacuated. Volumes of mercury, a non-wetting liquid, are then incrementally forced into the core under pressure. The volume of mercury injected at each pressure is used to determine the non-wetting phase saturation, and the process is repeated until the entire capillary pressure curve is obtained (Bass, 1987). Because a mercury-air system is used, the mercury surface tension behavior is converted to that of the in situ fluids. This is a destructive method for determining capillary pressure.

The test system used at Core Laboratories measured the volume injected at each pressure from 0 to 345 MPa (0 to 50,000 psi). This test was destructive to the samples; the mercury-filled samples were discarded after the tests. Tests were conducted by an automated system that recorded all data on a computer data logger. Data reduction was performed using software provided by the manufacturer of the two-sample Micromeritics Autopore II 9220, which is a standard machine for testing porous ceramics, rocks, and similar materials.

6.2 Test Results

Conversion of capillary pressure data from one fluid system to another (e.g., air-decane to air-brine or air-mercury to air-brine) is performed using the following equation as described in Section 4.5 of Appendix A.

$$P_{c2} = P_{c1}\left(\frac{T_2 \cos\phi_2}{T_1 \cos\phi_1}\right) \tag{5}$$

where

P_c = capillary pressure
T = surface tension
ϕ = contact angle at the fluid/solid interface (subscripts refer to the different fluid systems).

Table 9 contains the values for surface tensions and contact angles used in this study. As described in Appendix A, to convert air-decane capillary pressure to that of an air-brine system, air-decane capillary pressure is multiplied by 3. Similarly, to convert air-mercury capillary pressure to that of an air-brine system, air-mercury capillary pressure is multiplied by 5.2 or 6.7, depending on whether 140° or 180° is used for the contact angle conversion.

Table 9. Capillary Pressure Conversion Constants Used in this Study

Fluid System	Surface Tension (T) (dynes/cm)	Contact Angle (ϕ) (degrees)
air-decane	24	0
air-brine	72	0
air-mercury	485	140 or 180

6.2.1 Centrifuge Tests

The results of the centrifuge capillary pressure tests, converted from the air-decane test conditions to the WIPP in situ air-brine conditions, are presented in Table 10. Data were reduced using the Hassler-Brunner method (Hassler and Brunner, 1945). The initial pressure plotted for each of the six samples is 0.0345 MPa (5 psi), which corresponds to a rotation speed of 1,720 rpm; the final pressure for each specimen was 4.48 MPa (650 psi), which corresponds to a rotation speed of 17,660 rpm. The initial rotation speed was selected because high threshold entry pressures were expected; the final rotation speed was a function of equipment limitations.

Table 10. Summary of Centrifuge Capillary Pressure Data

Capillary Pressure (MPa)	Capillary Pressure (psi)	Sample 6 Brine Saturation (%)	Sample 8 Brine Saturation (%)	Sample 12 Brine Saturation (%)	Sample 14 Brine Saturation (%)	Sample 22 Brine Saturation (%)	Sample 24 Brine Saturation (%)
0.10	15	95.2	86.9	91.5	85.2	90.7	94.4
0.21	30	88.7	86.4	88.6	85.1	90.1	90.5
0.52	75	82.0	84.6	81.8	84.5	87.0	78.5
1.03	150	70.3	80.5	70.2	82.3	76.2	61.9
2.07	300	45.5	68.3	42.0	73.6	46.5	40.2
4.14	600	20.7	32.1	21.4	48.6	30.1	25.9
8.28	1200	13.0	17.8	13.0	45.1	20.8	24.0
13.45	1950	11.1	10.7	10.6	44.5	17.6	23.6

The Hassler-Brunner method was used because it is applicable when the samples are small enough that the ratio of distance from centrifuge axis to top end of the sample divided by the distance from the centrifuge axis to bottom end of sample is greater than 0.7 (for details see Appendix A, page 6). This condition was met for all samples tested at Core Laboratories using the centrifuge. The results from the Hassler-Brunner method were compared to the results from the Rajan method (Rajan, 1986). The differences between the calculated end face saturations were typically less than 1% of the pore volume measured at 3.45 MPa (500 psi) net effective stress using the CMS-300 test apparatus.

The decane (oil) saturation at 0.0345 MPa (5 psi) capillary pressure ranged from approximately 85 to 95% for the six samples. Therefore the threshold entry pressure was less than 0.0345 MPa (5 psi). Residual liquid saturations at 4.48 MPa (650 psi) ranged from approximately 11 to 45%. Based on the general shape of the centrifuge capillary pressure curves, exhibiting a concave downward shape (or "knee") at 80 to 905 liquid saturation, a bimodal or multimodal pore size distribution is suggested. Except for Sample 14, the relatively low final liquid saturations suggest that these specimens did not contain significant microporosity. The centrifuge capillary pressure curves for Samples 6, 8, 12, 14, 22, and 24 are presented in Figures 28a through f, respectively. All data presented in these figures were converted from the air-decane test conditions to the air-brine system to represent in situ WIPP conditions.

6.2.2 Mercury Injection Tests

Results of the mercury injection capillary pressure tests are presented in Tables 11a through f for Samples 5, 7, 11, 13, 21, and 23, respectively. Each table presents the mercury-air test conditions data corrected to the air-brine system representing the in situ WIPP conditions. The data were corrected using both the 140° and 180° contract angles as recommended by Good and Mikhail (1981), and both sets of results are included in each table for comparison. Pore volumes for the mercury injection specimens were measured using the CMS-300 at 3.45 MPa (500 psi) net effective stress, consistent with the centrifuge pore volumes. The starting pressure for the mercury injection was about 0.010 MPa (1.5 psi), and the final pressure was approximately 345 MPa (50,000 psi), which results in a complete capillary pressure curve from 100% wetting-phase saturation to a residual wetting-phase saturation.

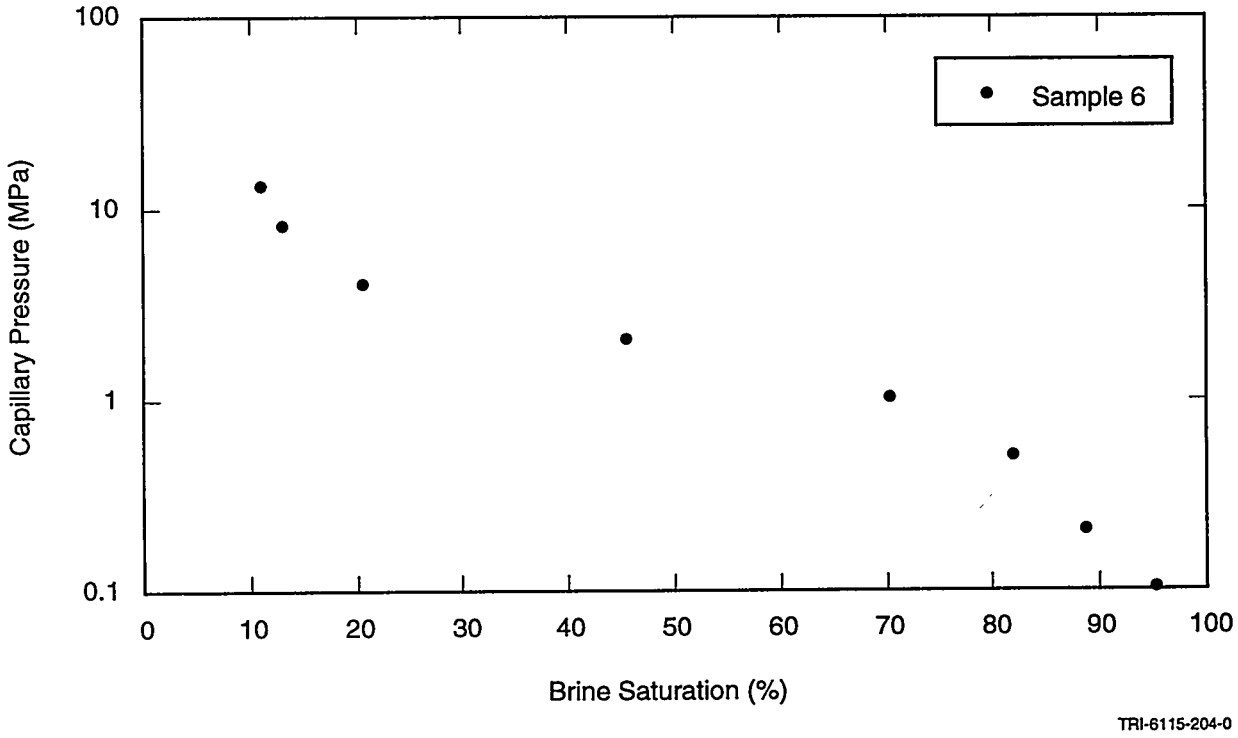

Figure 28a. Centrifuge capillary pressure versus brine saturation: Sample 6.

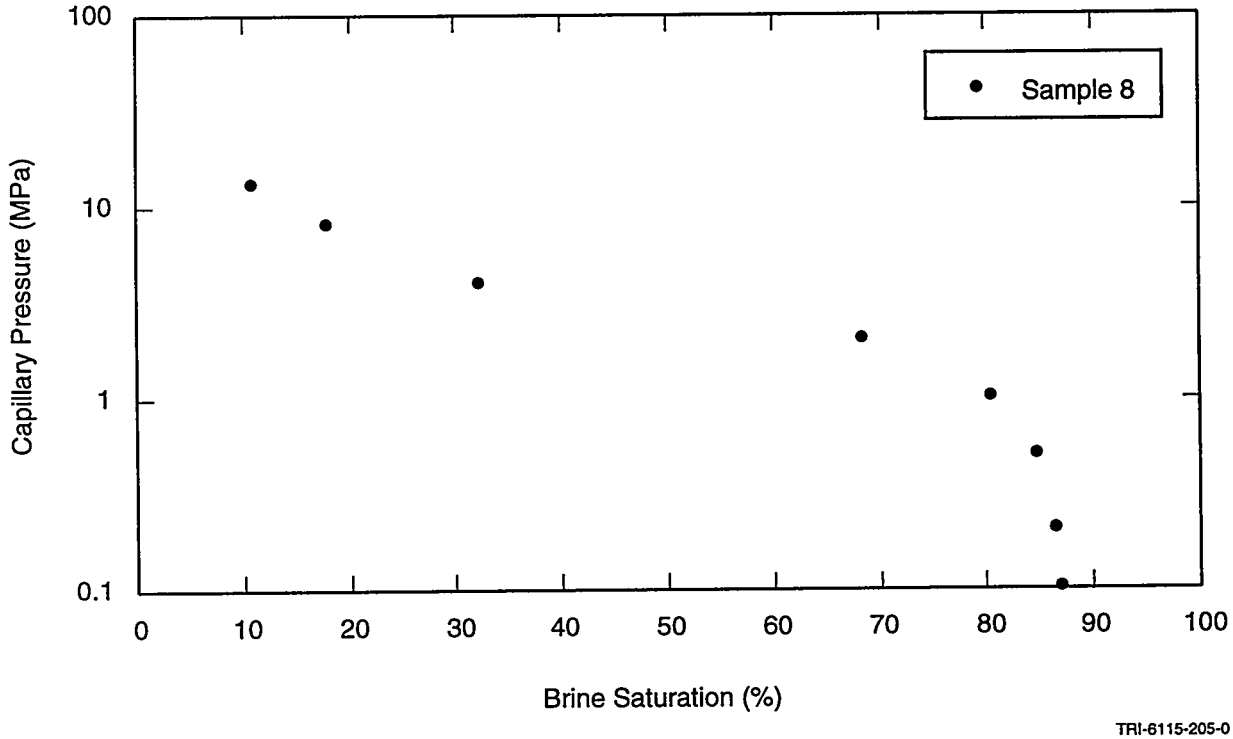

Figure 28b. Centrifuge capillary pressure versus brine saturation: Sample 8.

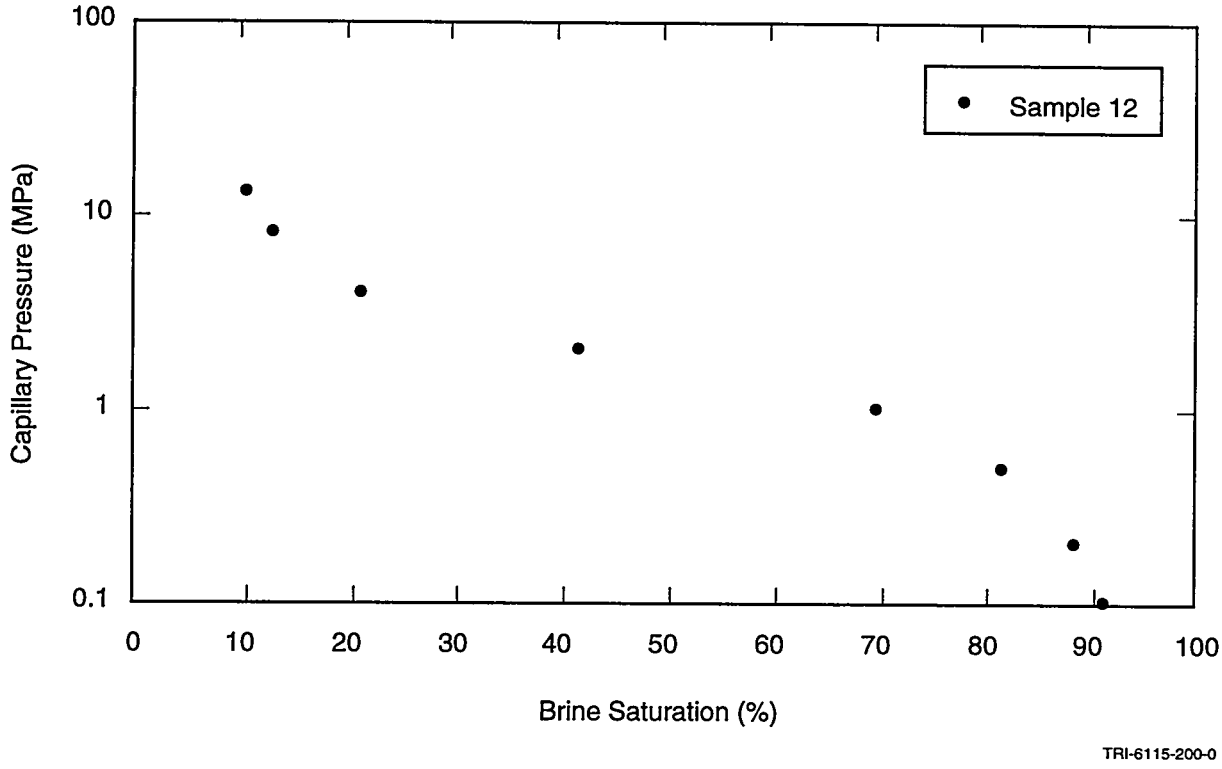

Figure 28c. Centrifuge capillary pressure versus brine saturation: Sample 12.

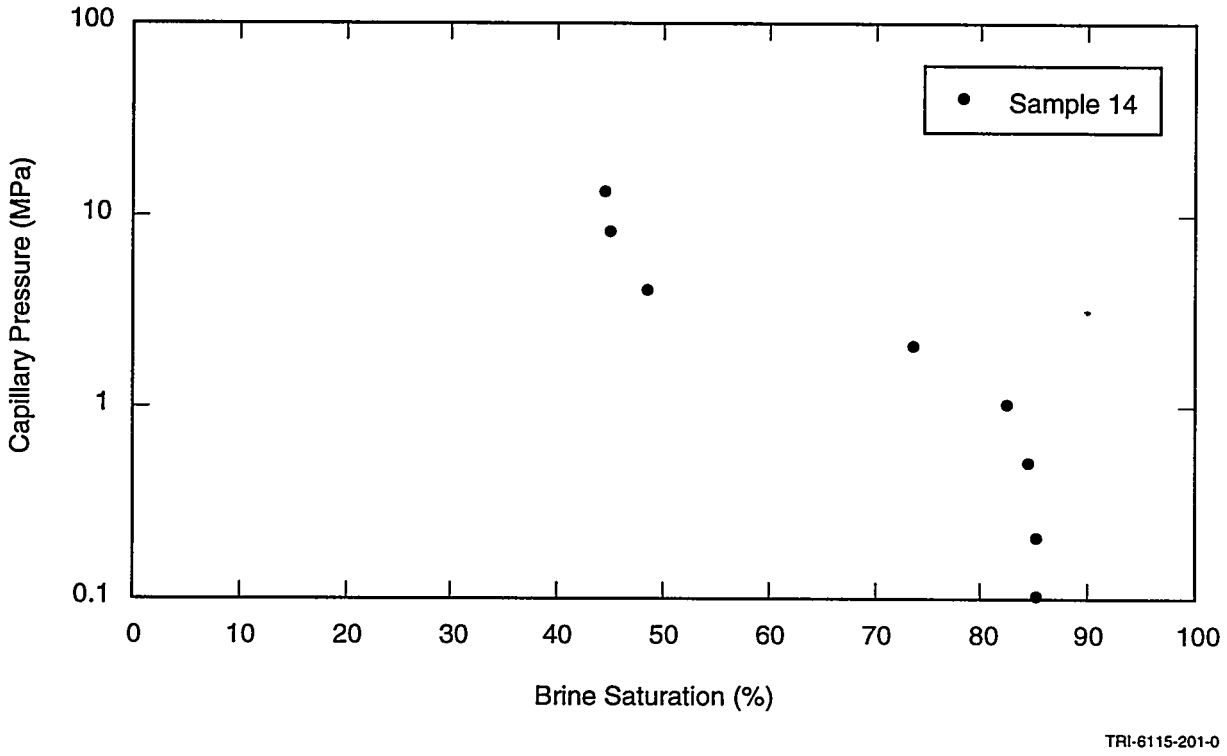

Figure 28d. Centrifuge capillary pressure versus brine saturation: Sample 14.

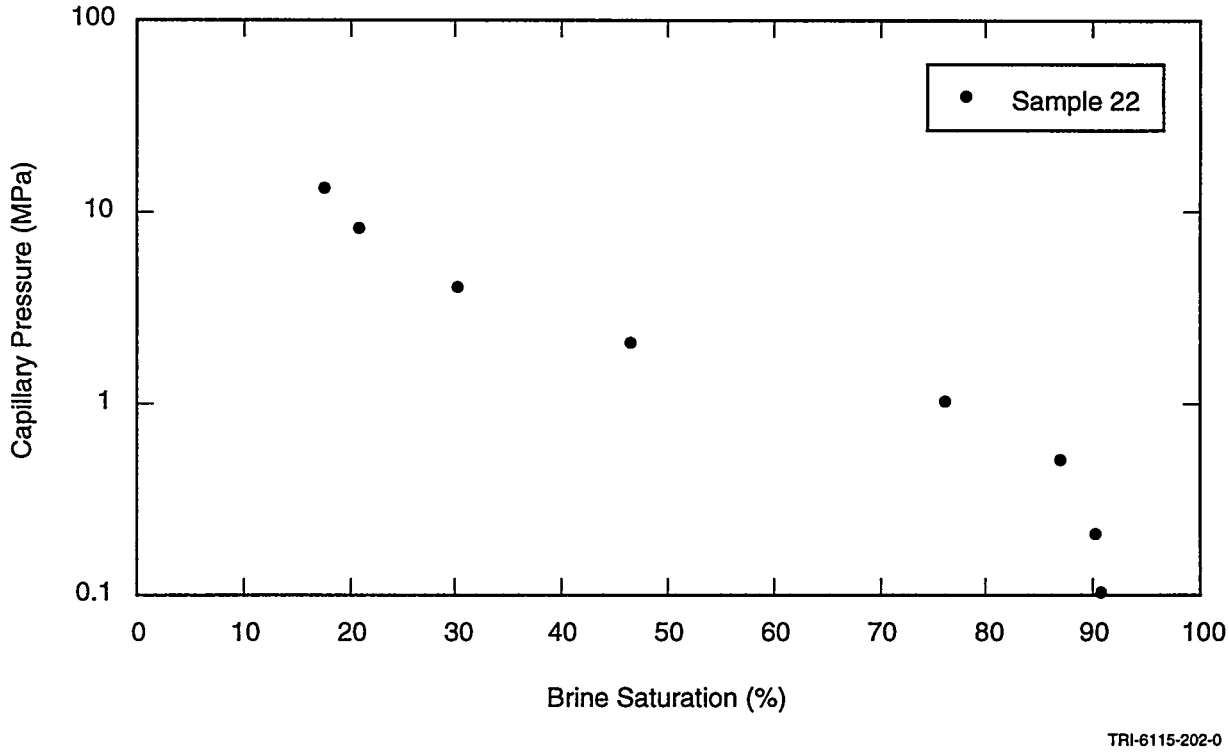

Figure 28e. Centrifuge capillary pressure versus brine saturation: Sample 22.

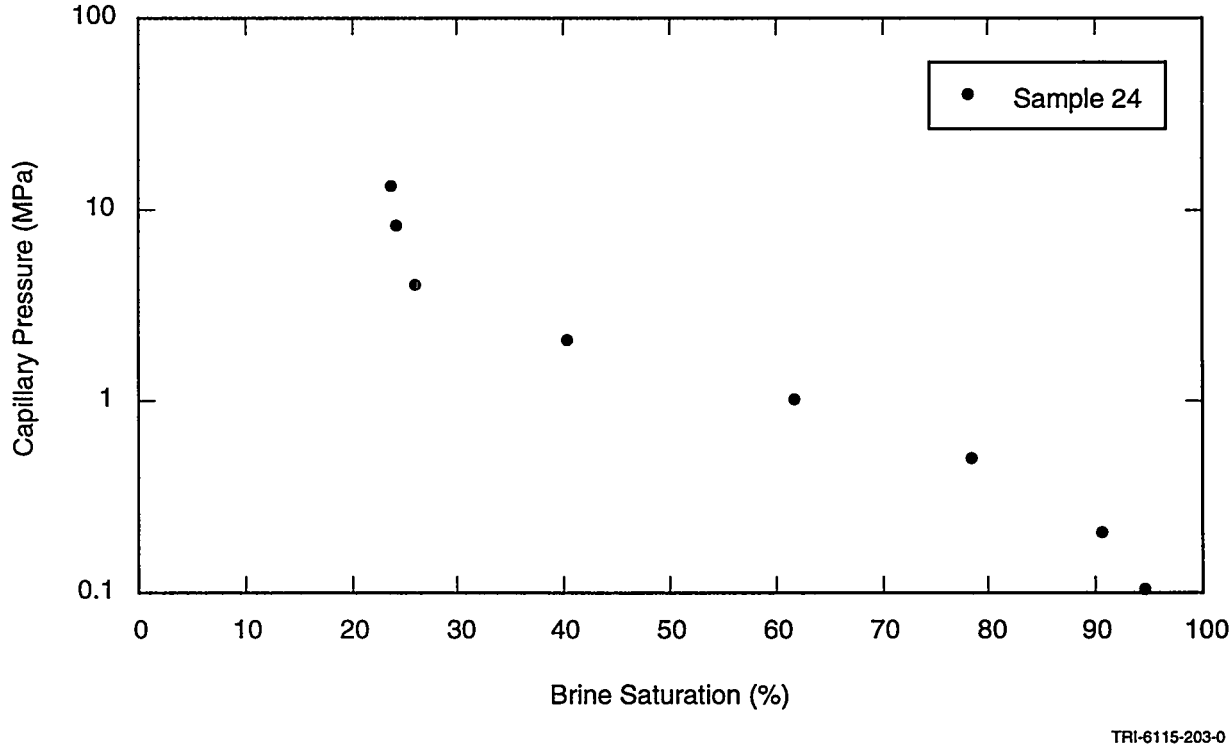

Figure 28f. Centrifuge capillary pressure versus brine saturation: Sample 24.

Table 11a. Mercury Injection Capillary Pressure Data for Sample 5

Brine Saturation	140° Contact Angle Capillary Pressure		180° Contact Angle Capillary Pressure	
(%)	(MPa)	(psi)	(MPa)	(psi)
100	0.002	0.3	0.002	0.23
100	0.004	0.58	0.003	0.44
100	0.008	1.2	0.006	0.89
100 *	0.012	1.7 *	0.009	1.3 *
96	0.016	2.3	0.012	1.8
96	0.024	3.5	0.019	2.7
92	0.033	4.8	0.026	3.7
92	0.047	6.8	0.036	5.2
88	0.06	8.7	0.046	6.7
88	0.076	11	0.057	8.2
88	0.097	14	0.076	11
88	0.131	19	0.1	15
84	0.017	24	0.12	18
84	0.21	31	0.17	24
84	0.24	35	0.19	27
84	0.27	39	0.21	30
80	0.41	59	0.31	45
80	0.53	77	0.41	59
76	0.67	97	0.51	74
68	1	145	0.77	111
60	1.3	193	1	148
56	1.7	243	1.3	186
44.1	2.1	311	1.6	238
40.1	2.7	387	2	296
40.1	3.3	484	2.6	371
36.1	4.7	676	3.6	518
36.1	5.7	825	4.4	632
32.1	6.7	968	5.1	742
28.1	9.3	1351	7.1	1035
28.1	13.3	1931	10.2	1479
24.1	16.7	2416	12.8	1850
16.1	20	2897	15.3	2219
12.1	26.6	3860	20.4	2957
12.1	33.3	4830	25.5	3700
12.1	40	5795	30.6	4440
8.1	46.7	6765	35.7	5182
8.1	53.3	7725	40.8	5917
8.1	60	8708	46	6671
8.1	66.5	9643	50.9	7387

* Threshold entry pressures and residual brine saturations.

Table 11b. Mercury Injection Capillary Pressure Data for Sample 7

Brine Saturation	140° Contact Angle Capillary Pressure		180° Contact Angle Capillary Pressure		Brine Saturation	140° Contact Angle Capillary Pressure		180° Contact Angle Capillary Pressure	
(%)	(MPa)	(psi)	(MPa)	(psi)	(%)	(MPa)	(psi)	(MPa)	(psi)
100	0.004	0.58	0.003	0.45	45.4	5.7	823	4.4	631
100	0.008	1.2	0.006	0.89	40.3	6.7	965	5.1	739
100 *	0.012	1.7 *	0.009	1.3 *	35.1	9.3	1354	7.2	1037
97.4	0.016	2.3	0.012	1.8	29.9	13.3	1933	10.2	1481
97.4	0.024	3.5	0.019	2.7	24.7	16.6	2411	12.7	1847
94.8	0.033	4.8	0.026	3.7	19.5	20	2894	15.3	2217
92.2	0.047	6.8	0.036	5.2	14.3	26.7	3864	20.4	2960
92.2	0.06	8.7	0.046	6.7	14.3	33.3	4825	25.5	3696
92.2	0.076	11	0.057	8.2	14.3	40	5790	30.6	4435
89.6	0.103	15	0.076	11	11.7	46.6	6758	35.7	5177
89.6	0.14	20	0.1	15	11.7	53.3	7723	40.8	5916
87	0.17	24	0.13	19	11.7	60	8705	46	6668
87	0.21	31	0.17	24	11.7	66.8	9683	51.2	7417
87	0.24	35	0.19	27					
87	0.27	39	0.21	30					
84.4	0.4	58	0.31	45					
81.8	0.54	78	0.41	60					
79.2	0.67	97	0.51	74					
76.6	1	146	0.77	112					
74	1.3	195	1	149					
71.4	1.7	241	1.3	185					
66.2	2.1	310	1.6	237					
61	2.7	386	2	296					
55.8	3.3	483	2.6	370					

* Threshold entry pressures and residual brine saturations.

Table 11c. Mercury Injection Capillary Pressure Data for Sample 11

Brine Saturation	140° Contact Angle Capillary Pressure		180° Contact Angle Capillary Pressure	
(%)	(MPa)	(psi)	(MPa)	(psi)
100	0.004	0.58	0.003	0.44
100	0.008	1.2	0.006	0.89
100	0.012	1.7	0.009	1.3
100 *	0.016	2.3 *	0.012	1.8 *
98.4	0.024	3.5	0.019	2.7
98.4	0.033	4.8	0.026	3.7
96.8	0.047	6.8	0.036	5.2
96.8	0.060	8.7	0.046	6.7
96.8	0.076	11	0.057	8.2
96.8	0.10	15	0.08	11
96.8	0.13	19	0.10	15
96.8	0.17	24	0.12	18
95.2	0.21	31	0.17	24
93.6	0.24	35	0.19	27
92.1	0.27	39	0.21	30
85.7	0.41	59	0.31	45
80.9	0.53	77	0.41	59
79.3	0.67	97	0.51	74
72.9	1.0	145	0.8	111
66.5	1.3	193	1.0	148
61.8	1.7	242	1.3	186
57	2.1	311	1.6	238
50.6	2.7	387	2.0	296
41	3.3	484	2.6	371
37.9	5.7	824	4.4	632
36.3	6.7	968	5.1	742
33.1	9.3	1351	7.1	1035
29.9	13.3	1931	10.2	1479
28.3	16.7	2415	12.8	1850
28.3	20.0	2897	15.3	2219
26.7	26.6	3860	20.4	2957
25.1	33.3	4830	25.5	3700
23.5	40.0	5795	30.6	4439
23.5	46.7	6765	35.7	5182
23.5	53.3	7725	40.8	5917
23.5	60.1	8708	46.0	6671
23.5	66.5	9643	50.9	7387

* Threshold entry pressures and residual brine saturations.

Table 11d. Mercury Injection Capillary Pressure Data for Sample 13

Brine Saturation	140° Contact Angle Capillary Pressure		180° Contact Angle Capillary Pressure	
(%)	(MPa)	(psi)	(MPa)	(psi)
100 *	0.004	0.58*	0.003	0.45 *
98.2	0.008	1.2	0.006	0.89
96.4	0.012	1.7	0.009	1.3
96.4	0.016	2.3	0.012	1.8
96.4	0.024	3.5	0.019	2.7
92.7	0.033	4.8	0.026	3.7
92.7	0.047	6.8	0.036	5.2
92.7	0.060	8.7	0.046	6.7
90.9	0.08	11	0.057	8.2
90.9	0.10	15	0.08	11
90.9	0.13	19	0.10	15
90.9	0.17	24	0.13	19
87.3	0.21	31	0.17	24
85.5	0.24	35	0.19	27
85.5	0.27	39	0.21	30
78.2	0.40	58	0.30	44
76.4	0.53	77	0.41	59
74.6	0.66	96	0.51	74
70.9	1.0	145	0.8	111
65.5	1.3	193	1.0	148
61.8	1.7	241	1.3	185
58.2	2.1	309	1.6	236
49.1	2.7	386	2.0	296
40	4.7	677	3.6	519
40	5.7	823	4.4	631
36.4	6.7	967	5.1	741
32.8	9.3	1351	7.1	1035
29.2	13.3	1932	10.2	1480
25.5	16.7	2418	12.8	1852
20.1	20.0	2896	15.3	2218
20.1	26.6	3863	20.4	2959
16.4	33.3	4826	25.5	3697
16.4	40.0	5794	30.6	4439
16.4	46.6	6750	35.7	5171
14.6	53.2	7718	40.8	5912
14.6	60.0	8705	46.0	6669
14.6	66.5	9649	51.0	7392

* Threshold entry pressures and residual brine saturations.

Table 11e. Mercury Injection Capillary Pressure Data for Sample 21

Brine Saturation	140° Contact Angle Capillary Pressure		180° Contact Angle Capillary Pressure	
(%)	(MPa)	(psi)	(MPa)	(psi)
100	0.004	0.58	0.003	0.45
100 *	0.008	1.2 *	0.006	0.89 *
97.4	0.012	1.7	0.009	1.3
97.4	0.016	2.3	0.012	1.8
94.9	0.024	3.5	0.019	2.7
94.9	0.033	4.8	0.026	3.7
94.9	0.046	6.7	0.036	5.2
94.9	0.060	8.7	0.046	6.7
94.9	0.076	11	0.057	8.2
94.9	0.10	15	0.08	11
92.3	0.13	19	0.10	15
92.3	0.17	24	0.13	19
92.3	0.21	31	0.17	24
92.3	0.24	35	0.19	27
92.3	0.27	39	0.21	30
87.3	0.40	58	0.30	44
82.2	0.54	78	0.41	59
77.1	0.66	96	0.51	74
64.3	1.0	145	0.8	111
56.7	1.3	193	1.0	148
51.6	1.7	241	1.3	185
44	2.1	309	1.6	236
33.8	2.7	386	2.0	296
28.7	4.7	677	3.6	519
26.2	5.7	823	4.4	631
26.2	6.7	967	5.1	741
21.1	9.3	1351	7.1	1035
18.5	13.3	1932	10.2	1480
16	16.7	2418	12.8	1852
13.4	20.0	2896	15.3	2218
10.9	26.6	3863	20.4	2959
10.9	33.3	4827	25.5	3698
10.9	40.0	5794	30.6	4439
8.3	46.6	6750	35.7	5171
8.3	53.2	7718	40.8	5912
8.3	60.0	8705	46.0	6669
8.3	66.5	9649	51.0	7392

* Threshold entry pressures and residual brine saturations.

Table 11f. Mercury Injection Capillary Pressure Data for Sample 23

Brine Saturation	140° Contact Angle Capillary Pressure		180° Contact Angle Capillary Pressure		Brine Saturation	140° Contact Angle Capillary Pressure		180° Contact Angle Capillary Pressure	
(%)	(MPa)	(psi)	(MPa)	(psi)	(%)	(MPa)	(psi)	(MPa)	(psi)
100	0.004	0.58	0.003	0.45	19.4	3.3	483	2.6	370
100 *	0.008	1.2 *	0.006	0.89 *	13.2	4.7	677	3.6	518
97.5	0.012	1.7	0.009	1.3	11.9	5.7	823	4.3	630
97.5	0.016	2.3	0.012	1.8	10.7	6.6	964	5.1	739
97.5	0.024	3.5	0.019	2.7	10.7	9.3	1353	7.2	1037
96.3	0.033	4.8	0.026	3.7	10.7	13.3	1933	10.2	1481
93.8	0.047	6.8	0.036	5.2	9.4	16.6	2411	12.7	1847
93.8	0.060	8.7	0.046	6.7	9.4	20.0	2894	15.3	2217
93.8	0.08	11	0.057	8.2	9.4	26.6	3864	20.4	2960
93.8	0.10	15	0.08	11	8.2	33.3	4825	25.5	3696
92.5	0.14	20	0.10	15	8.2	39.9	5789	30.6	4435
92.5	0.17	24	0.12	18	8.2	46.6	6758	35.7	5177
91.3	0.21	31	0.17	24	8.2	53.3	7723	40.8	5916
91.3	0.24	35	0.19	27	8.2	60.0	8704	46.0	6668
90.1	0.27	39	0.21	30	8.2	66.8	9682	51.2	7417
87.6	0.40	58	0.31	45					
80.1	0.54	78	0.41	60					
73.9	0.67	97	0.51	74					
61.5	1.0	146	0.8	112					
51.6	1.3	195	1.0	149					
44.2	1.7	241	1.3	185					
34.2	2.1	309	1.6	237					

* Threshold entry pressures and residual brine saturations.

6.2.3 Comparison of Results from Centrifuge and Mercury Injection Tests

Figures 29 through 34 show the comparisons of capillary pressure results for the six pairs of core samples. The top graphs (a) of Figures 29 through 34 show the air-brine (converted) centrifuge data plotted with the 140° contact angle air-brine (converted) mercury injection data. The bottom graphs (b) show the same air-brine (converted) centrifuge data plotted with the 180° contact angle air-brine (converted) mercury injection data. The difference in the capillary pressure results, when converted to an air-brine system using 140°or 180° for the contact angle, is not significant.

Figure 35 is a plot of all the air-brine (converted) centrifuge capillary pressure data, and Figure 36 is a plot of all the air-brine (converted) mercury injection capillary pressure data using a contact angle of 140°. Figure 37 is a Cartesian plot of all the capillary pressure data from Figures 35 and 36, and Figure 38 is a log-linear plot of the same data.

The mercury injection method has the advantage of producing capillary pressure data over the full saturation range, but it is a slow method and tests cannot be performed under confining stress conditions. In addition, the mercury injection method is destructive and no further tests can be performed on the cores. The faster centrifuge method was unable to capture the high brine saturation data because of equipment hardware constraints that precluded the use of very low spin rates. Although these centrifuge capillary pressure tests were performed using an apparatus that could not impose confining stress on samples, newer generation centrifuges are now available that can test cores under prespecified stress conditions. Both the mercury injection and centrifuge test apparatus have sample size limitations, which currently allow only small specimens to be tested.

6.3 Determination of Threshold Pressure

As described by Davies (1991), some investigators define threshold pressure as the capillary pressure associated with first penetration of a nonwetting phase into the largest pores near the surface of the medium. Others define threshold pressure as the capillary pressure associated with the incipient development of a continuum of the nonwetting phase through a pore network, providing gas pathways not only through relatively large pores, but also through necks between pores. Defining threshold pressure as corresponding to first penetration of a nonwetting phase into the largest pores near the surface of the medium means that threshold pressure is equal to the capillary pressure at a brine saturation of 1.0.

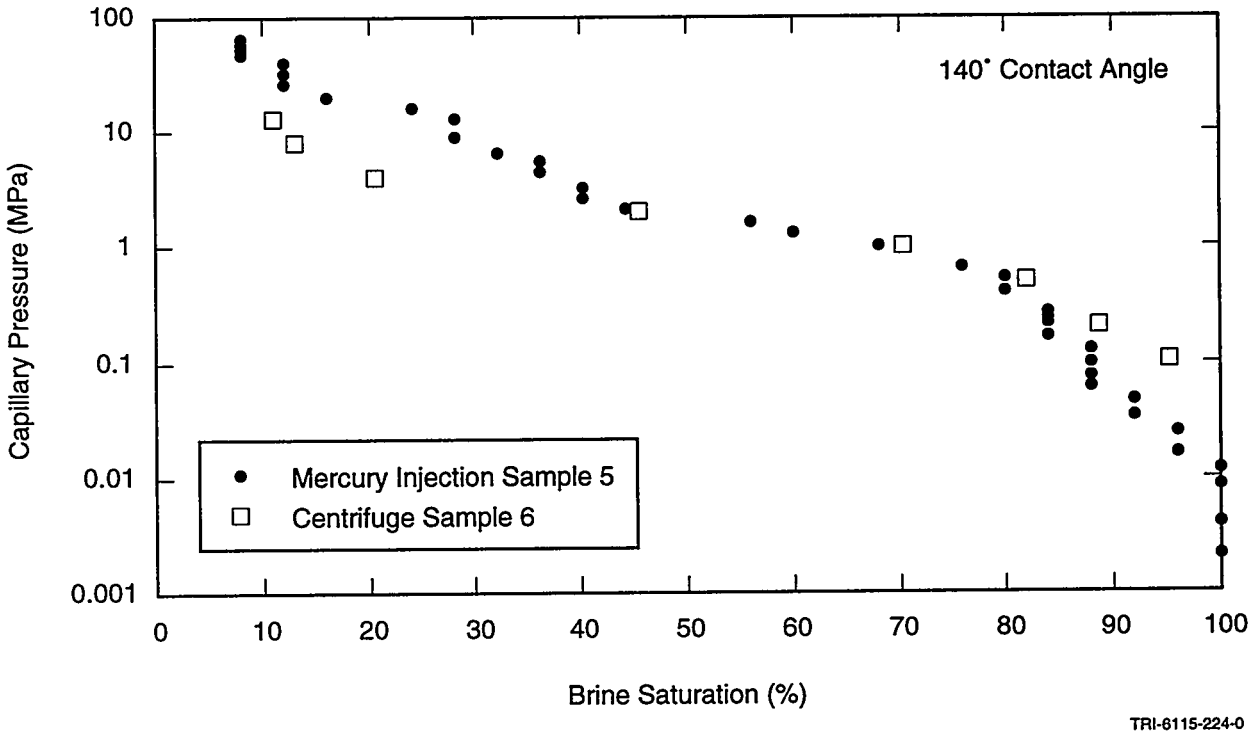

Figure 29a. Comparison of centrifuge and mercury injection capillary pressure: Samples 5 and 6, 140° contact angle.

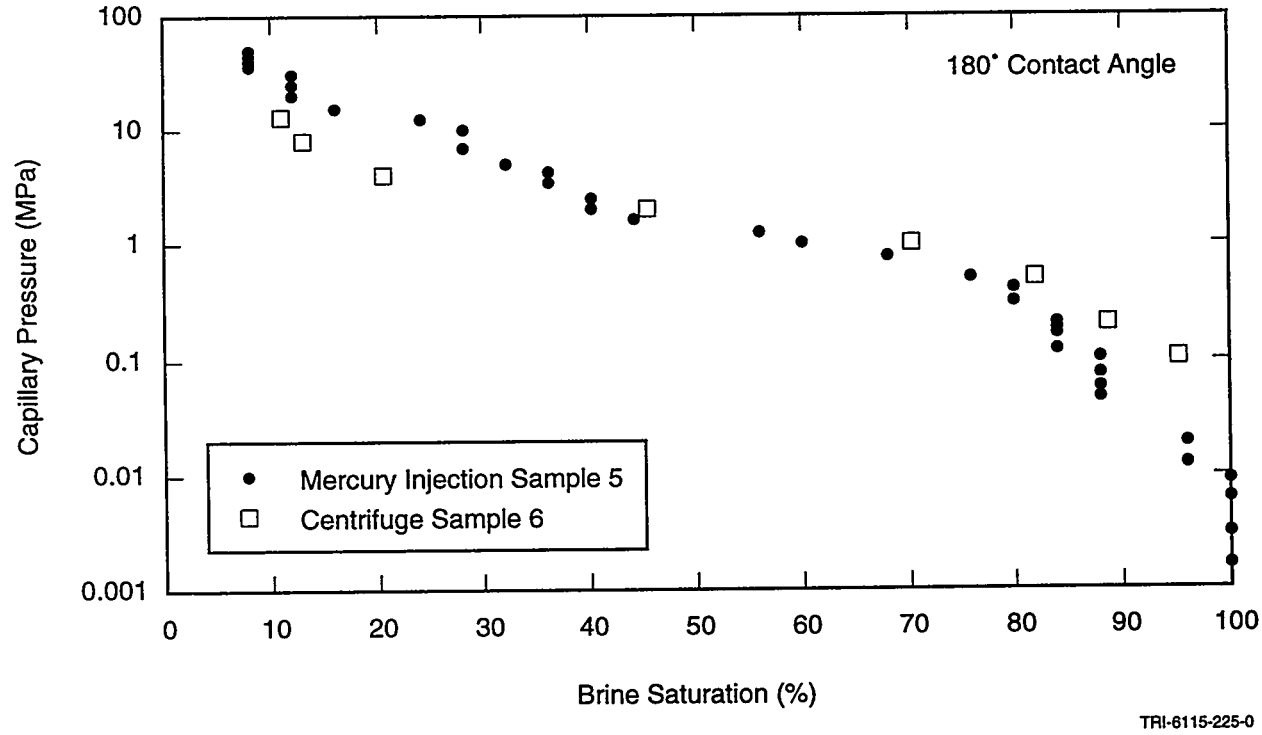

Figure 29b. Comparison of centrifuge and mercury injection capillary pressure: Samples 5 and 6, 180° contact angle.

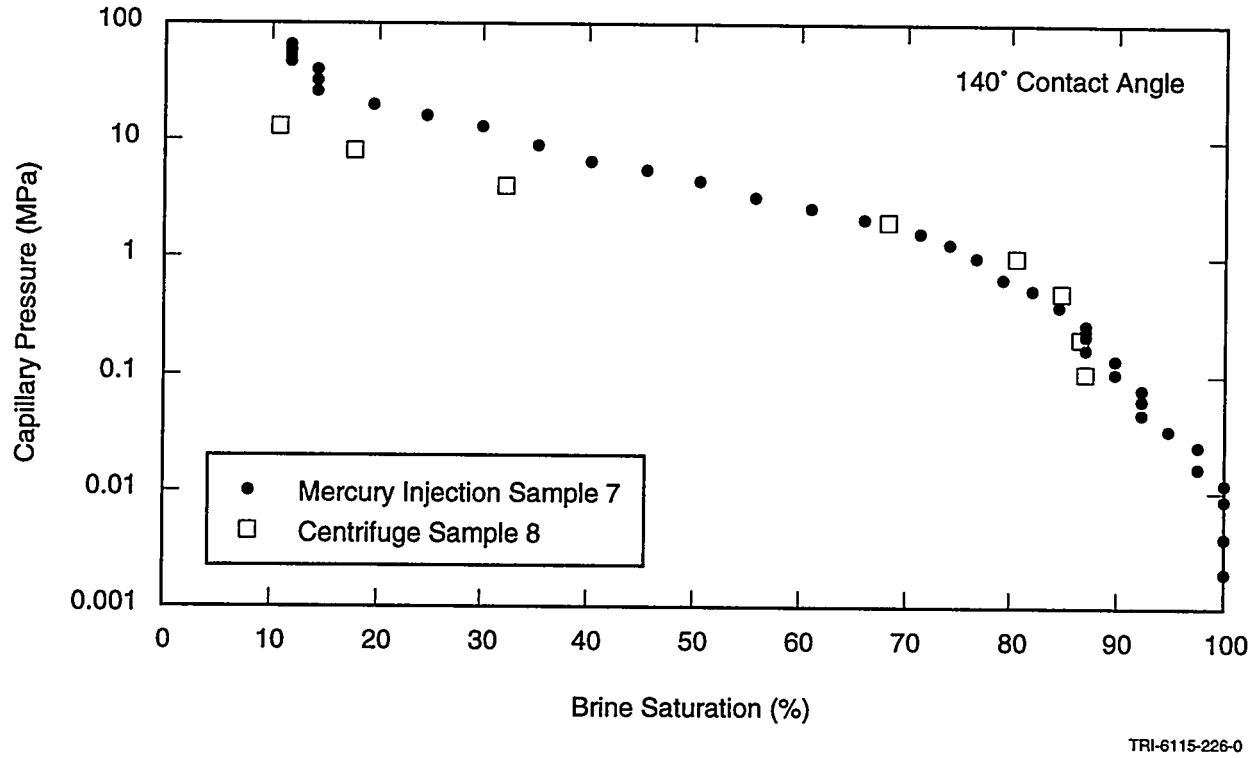

Figure 30a. Comparison of centrifuge and mercury injection capillary pressure: Samples 7 and 8, 140° contact angle.

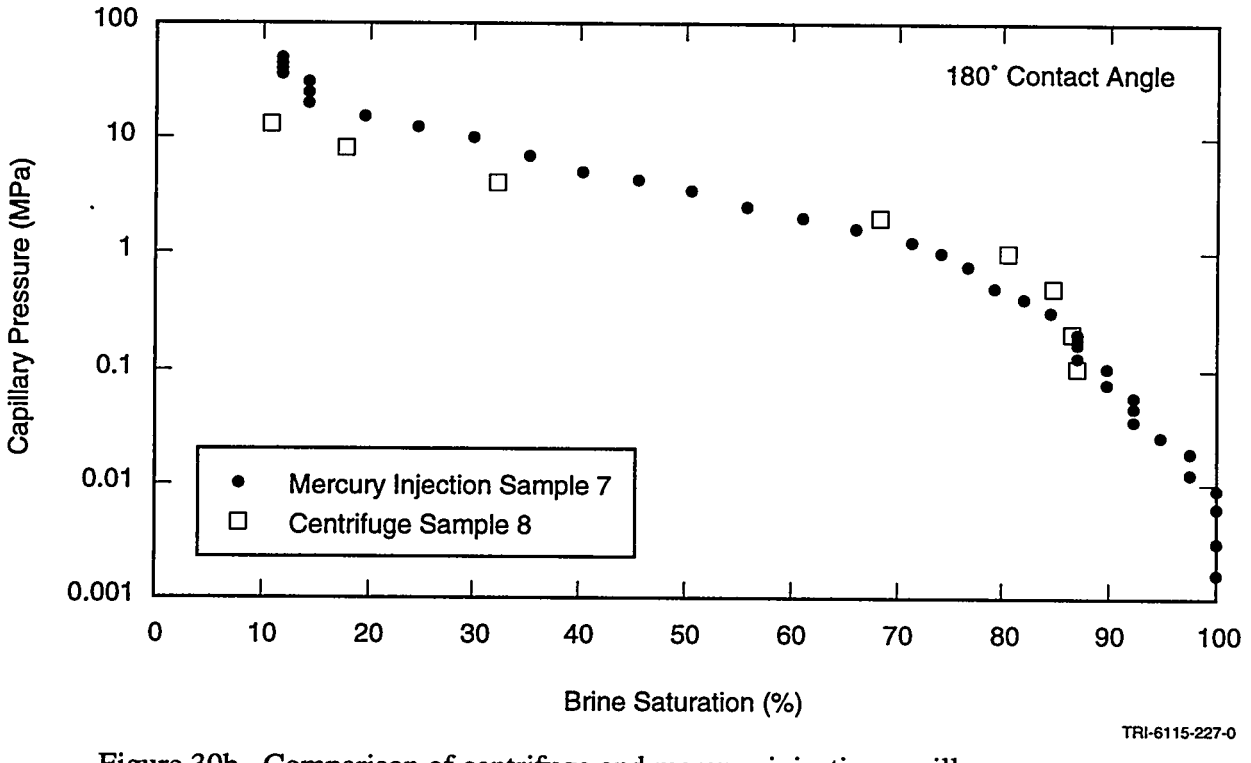

Figure 30b. Comparison of centrifuge and mercury injection capillary pressure: Samples 7 and 8, 180° contact angle.

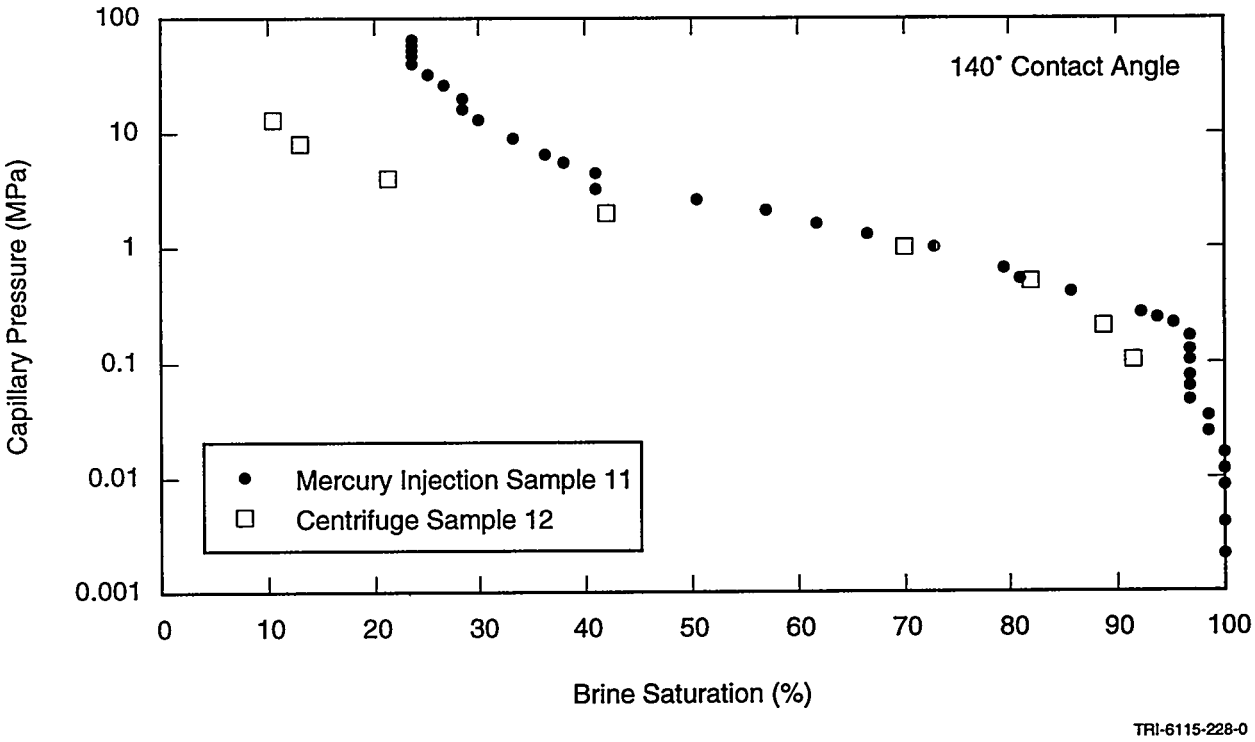

Figure 31a. Comparison of centrifuge and mercury injection capillary pressure: Samples 11 and 12, 140° contact angle.

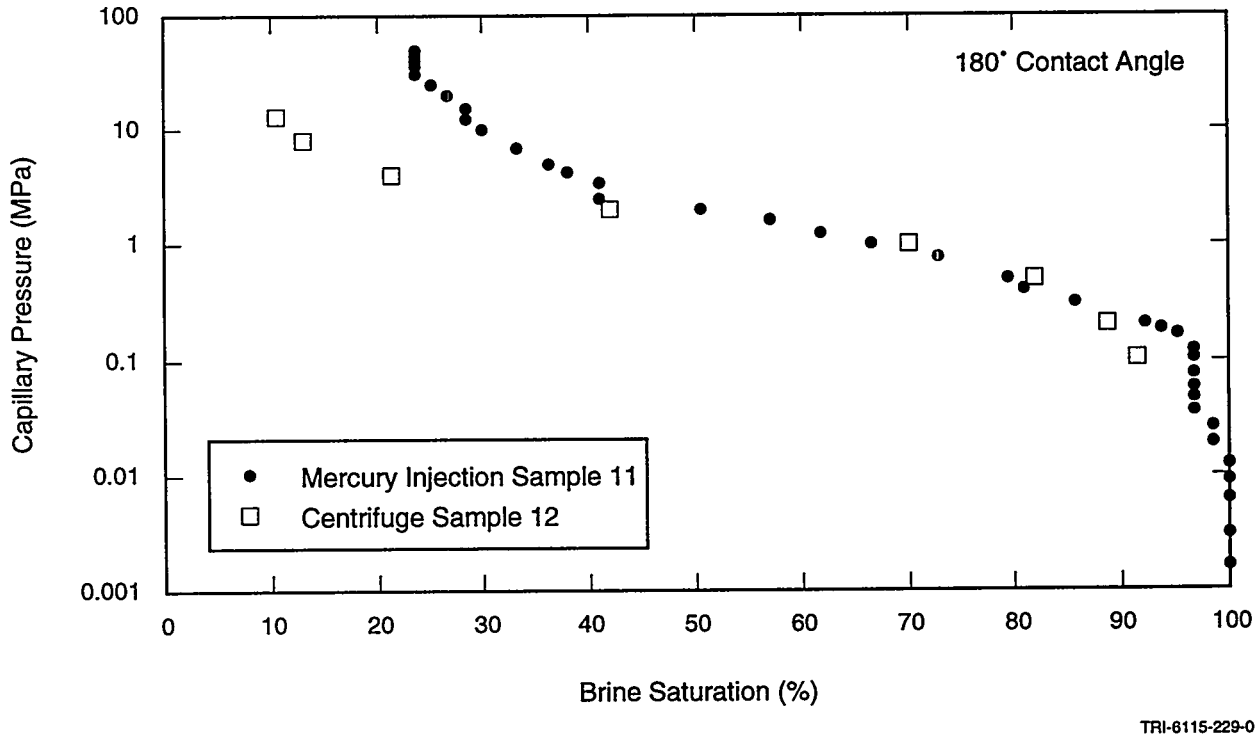

Figure 31b. Comparison of centrifuge and mercury injection capillary pressure: Samples 11 and 12, 180° contact angle.

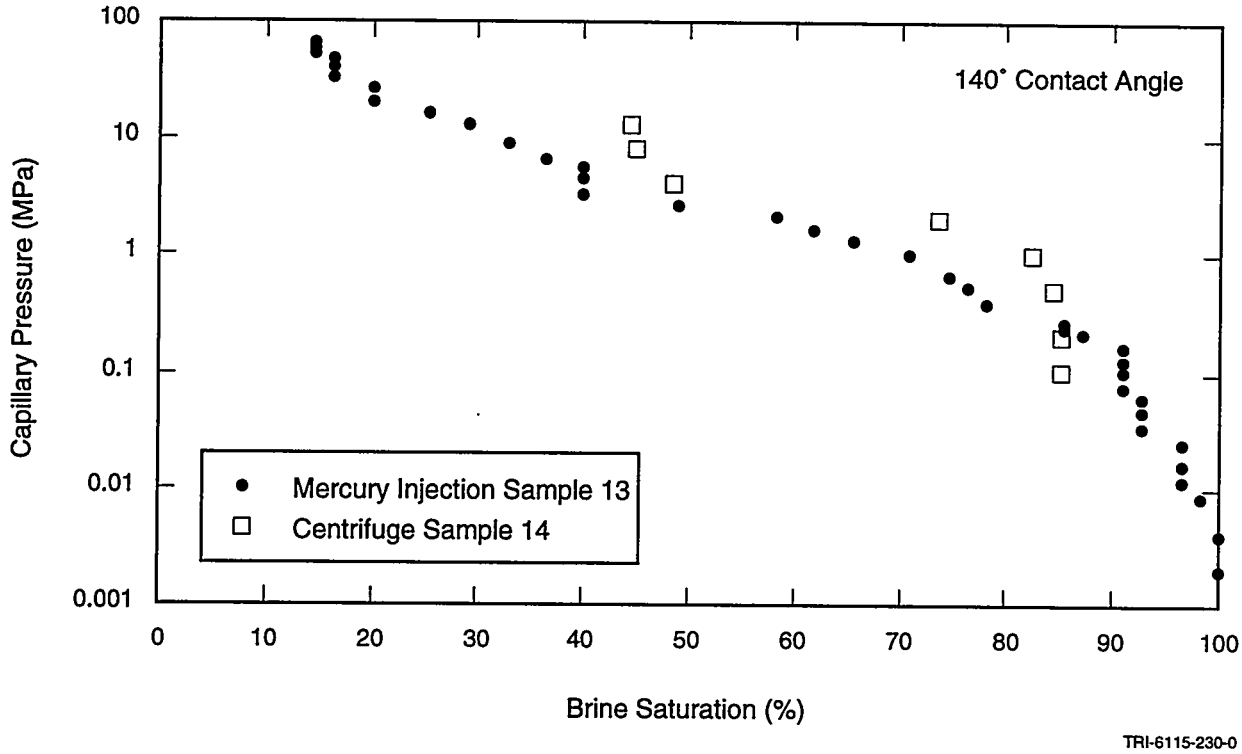

Figure 32a. Comparison of centrifuge and mercury injection capillary pressure: Samples 13 and 14, 140° contact angle.

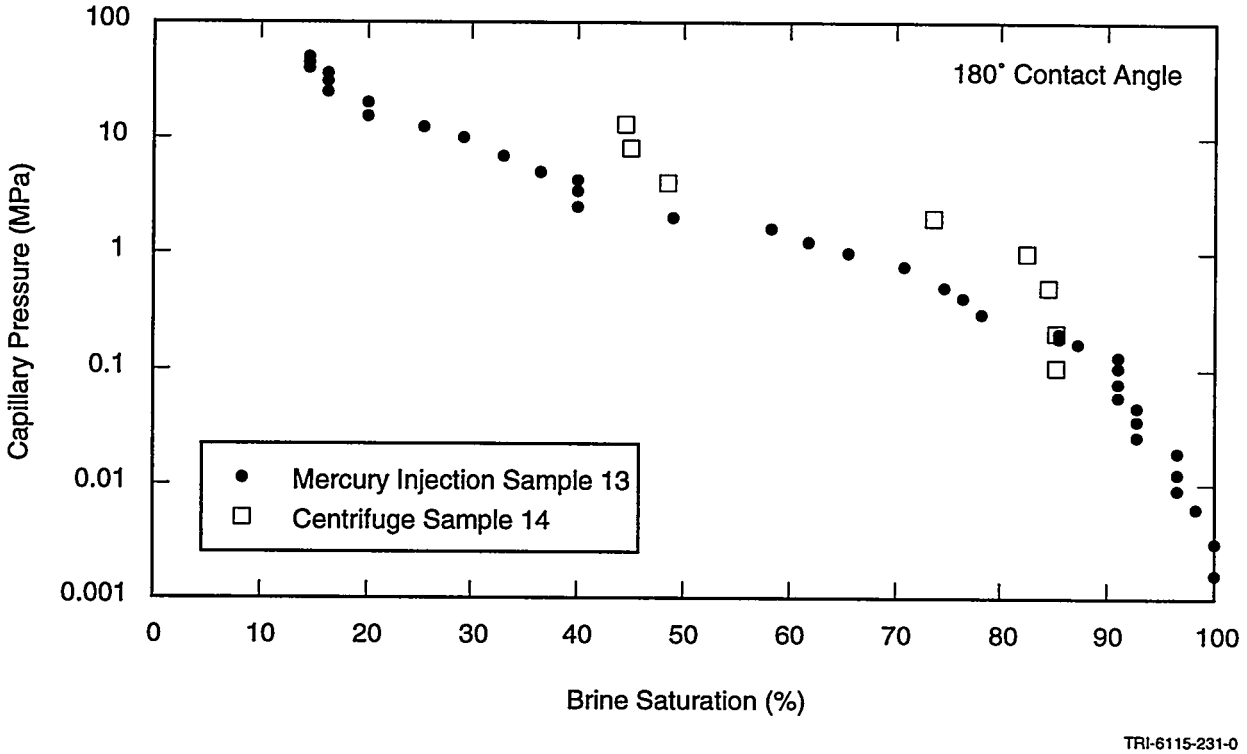

Figure 32b. Comparison of centrifuge and mercury injection capillary pressure: Samples 13 and 14, 180° contact angle.

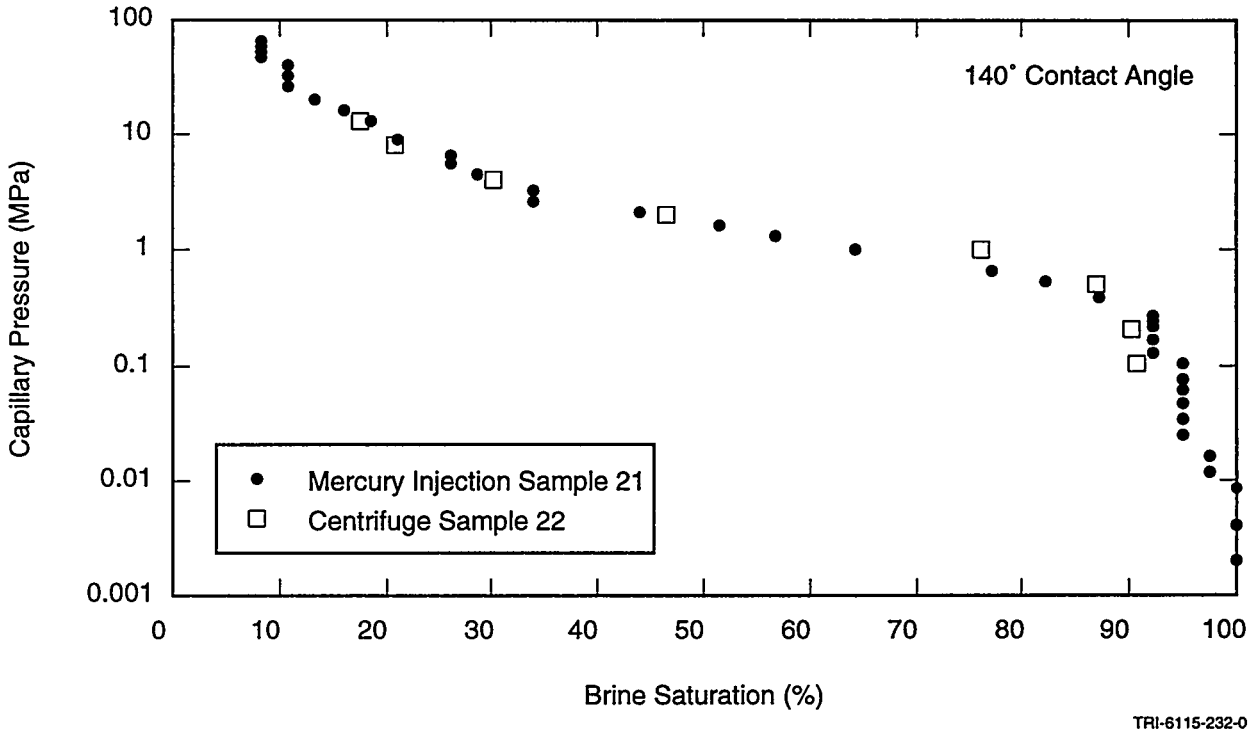

Figure 33a. Comparison of centrifuge and mercury injection capillary pressure: Samples 21 and 22, 140° contact angle.

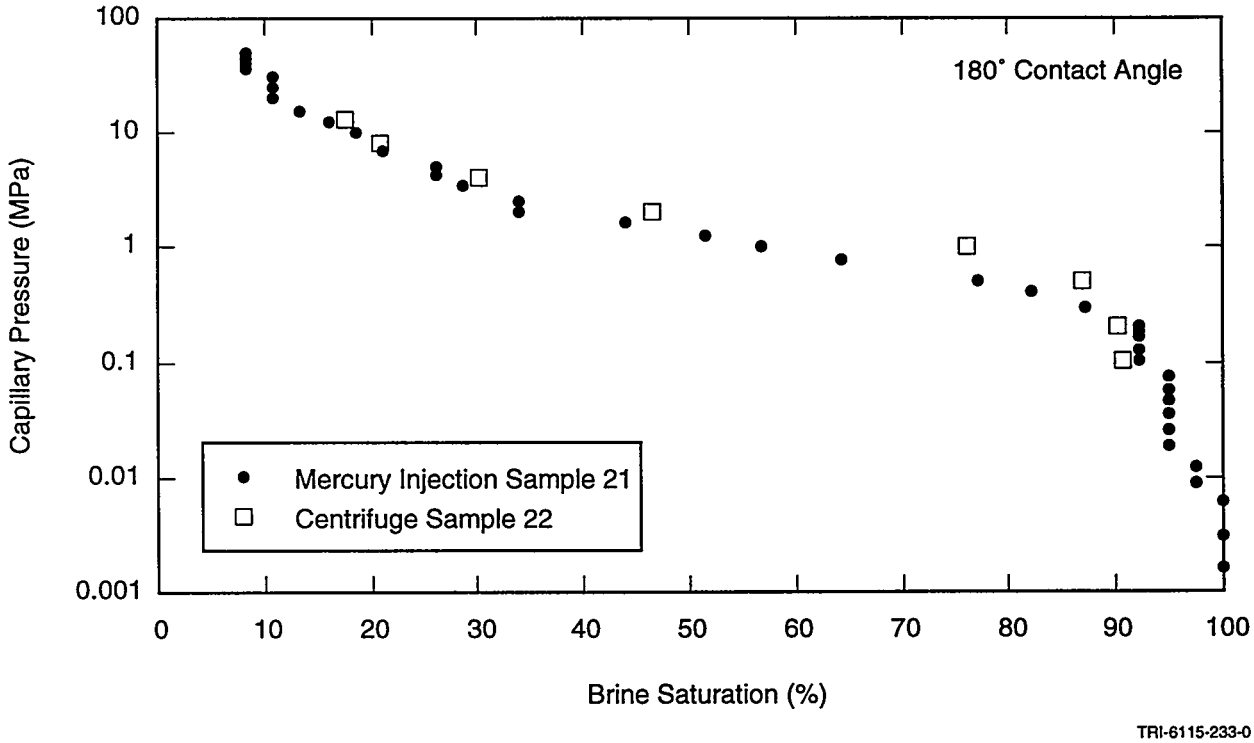

Figure 33b. Comparison of centrifuge and mercury injection capillary pressure: Samples 21 and 22, 180° contact angle.

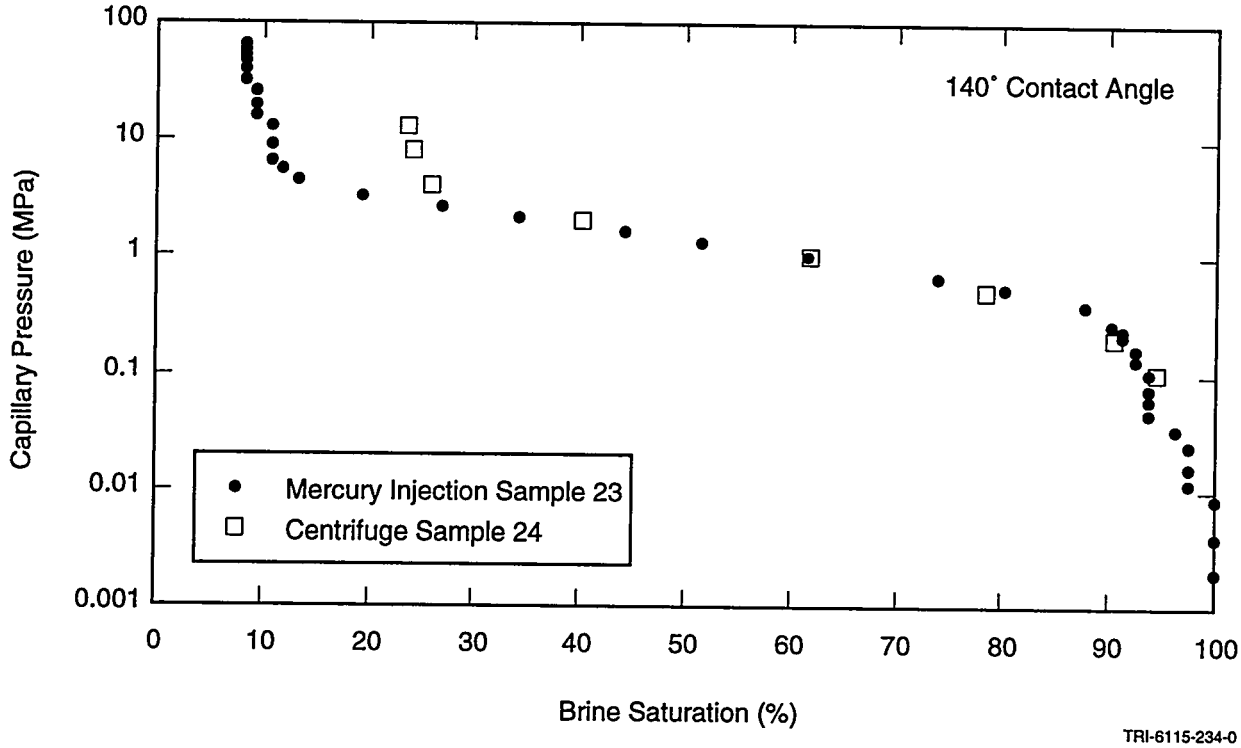

Figure 34a. Comparison of centrifuge and mercury injection capillary pressure: Samples 23 and 24, 140° contact angle.

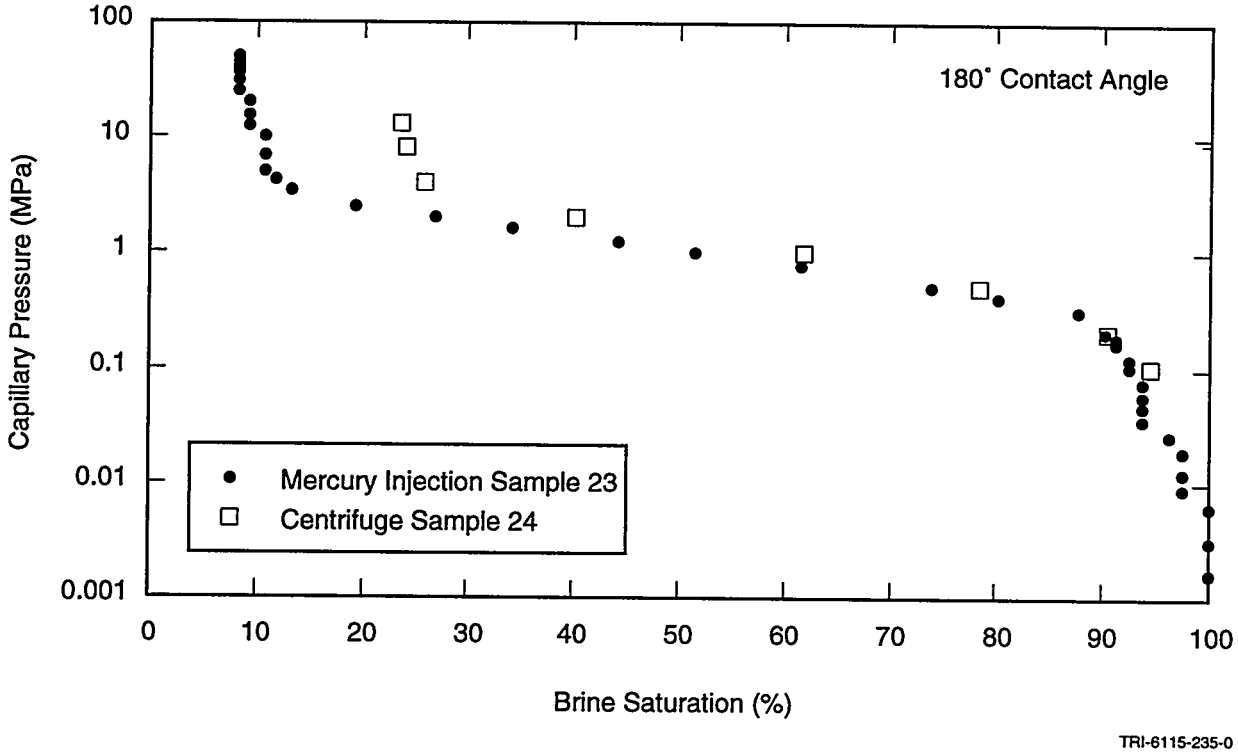

Figure 34b. Comparison of centrifuge and mercury injection capillary pressure: Samples 23 and 24, 180° contact angle.

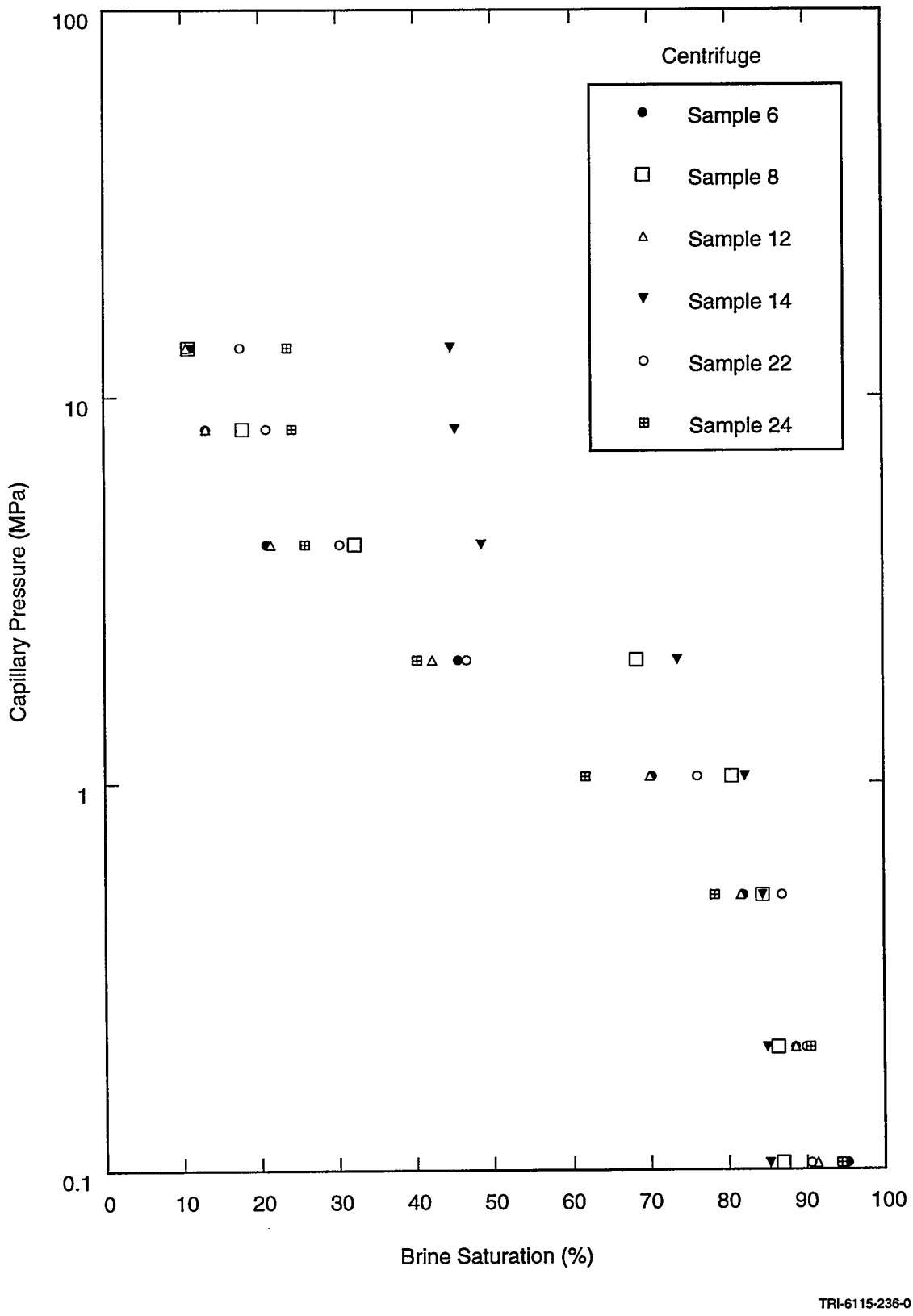

Figure 35. Centrifuge capillary pressure data versus brine saturation: all samples (log-linear).

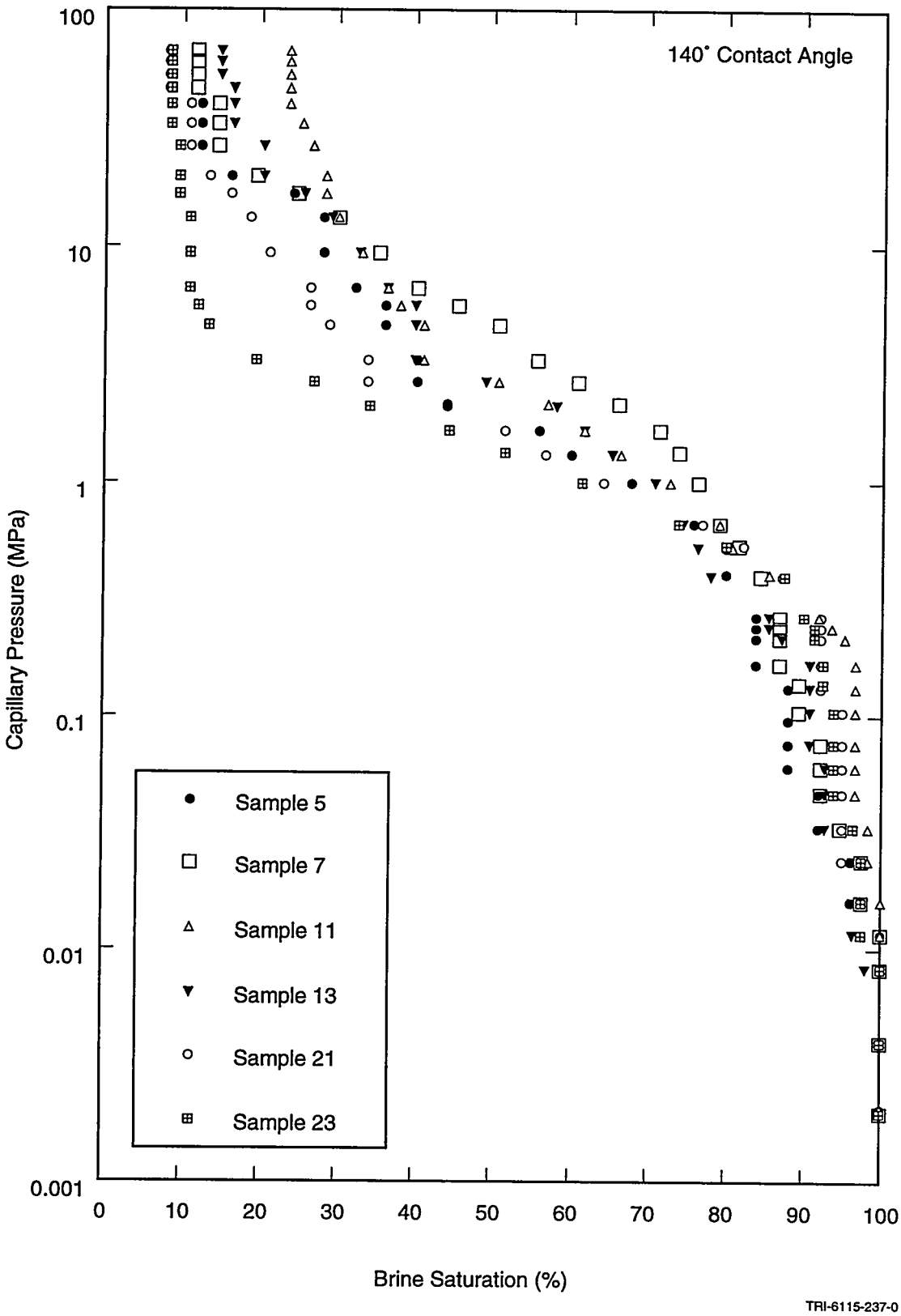

Figure 36. Mercury injection capillary pressure data versus brine saturation: all samples (log-linear).

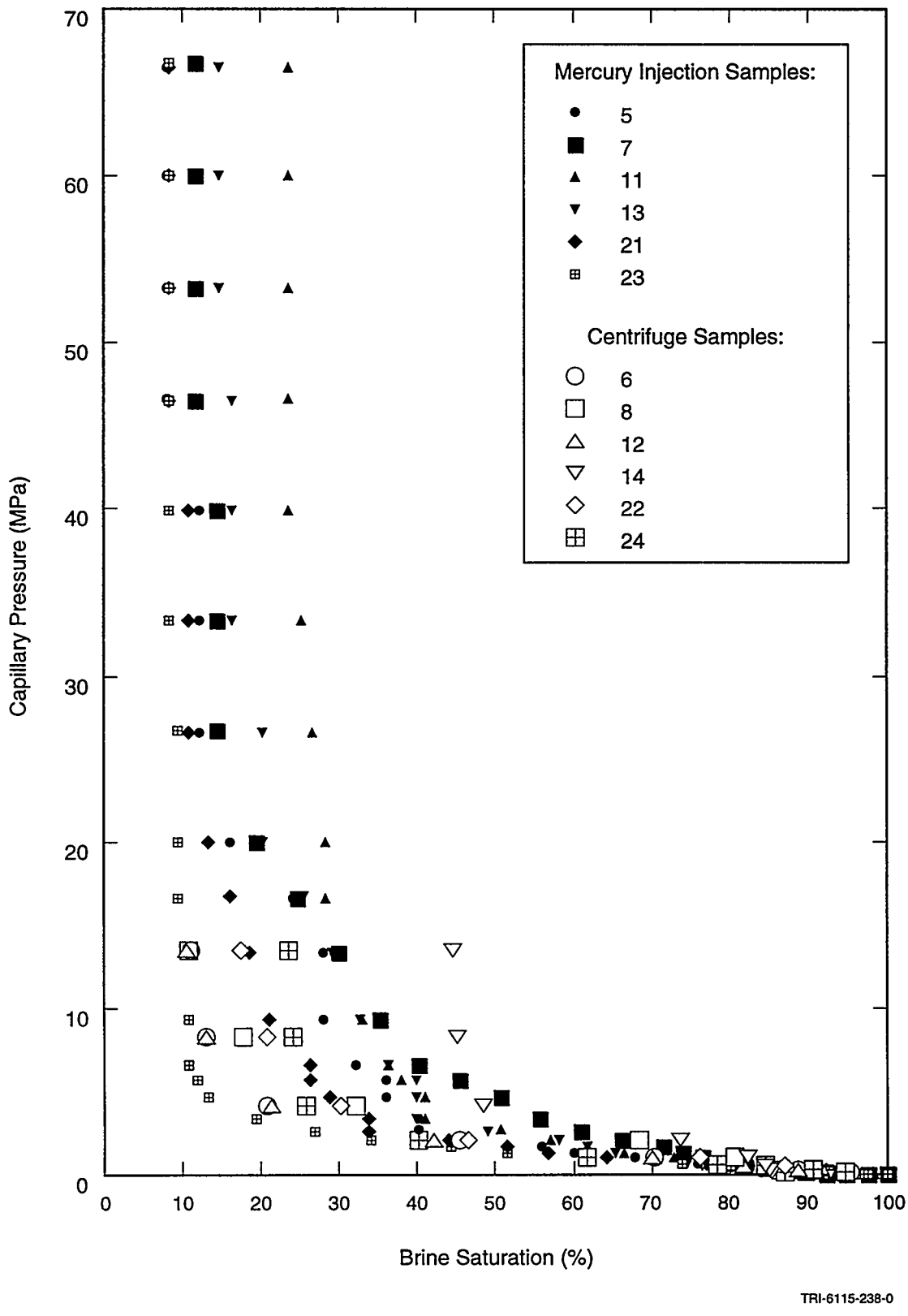

Figure 37. Capillary pressure data: all samples (Cartesian).

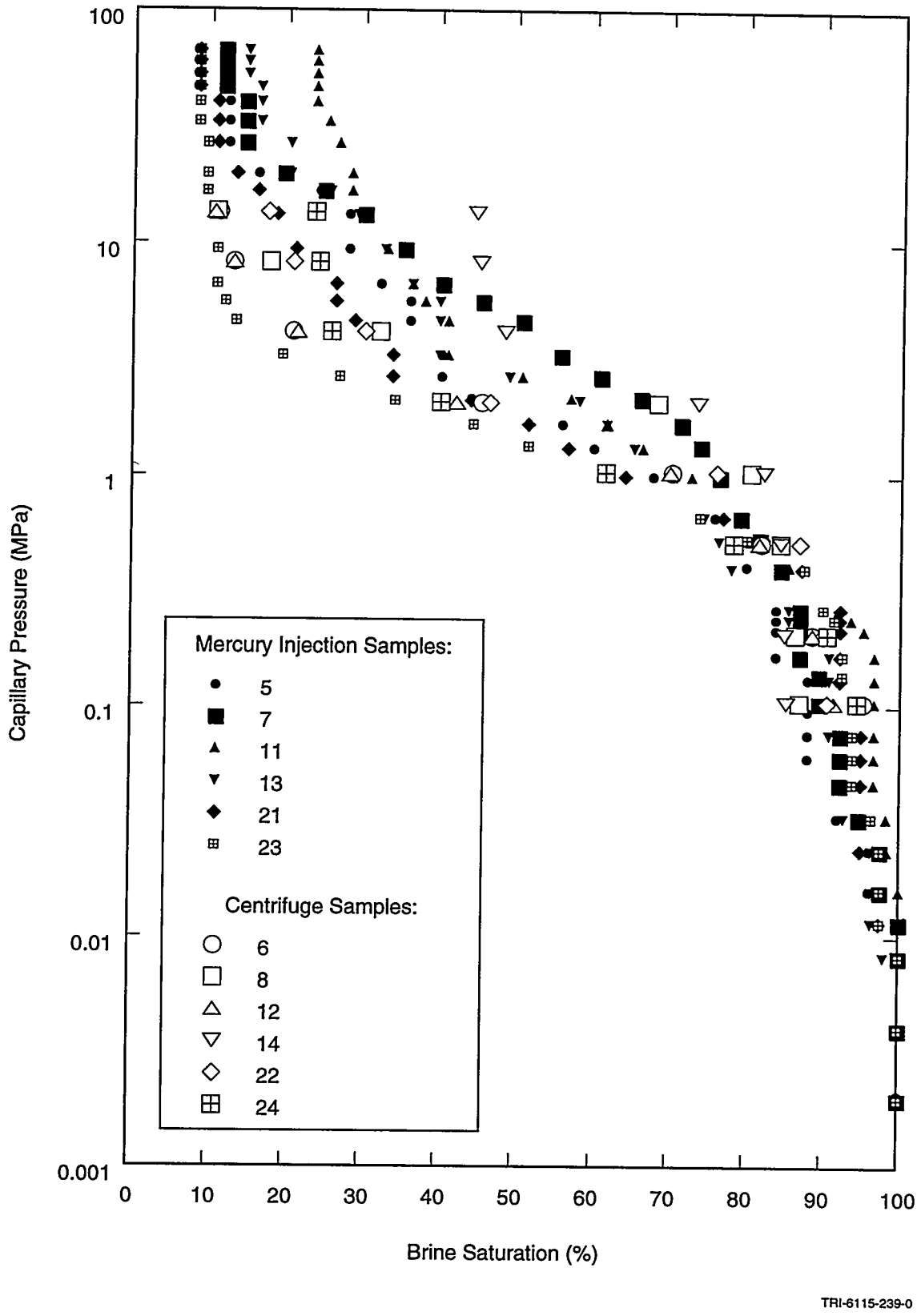

Figure 38. Capillary pressure data: all samples (log-linear).

Defining threshold pressure as corresponding to the incipient formation of a continuum of the nonwetting phase through the pore network means that threshold pressure is equal to the capillary pressure at a saturation equal to the critical gas saturation. In other words, threshold pressure is equal to the capillary pressure at which the relative permeability to the gas phase begins to rise from its zero value, corresponding to the incipient development of interconnected gas flow paths through the pore network.

The present study is concerned with quantifying the potential for flow of waste-generated gas outward from the WIPP repository. This process will likely require that outward flowing gas penetrate and establish a gas-filled network of flow paths in the surrounding formation. Therefore the term gas threshold displacement pressure, shortened here to *threshold pressure*, will be defined as the pressure associated with the incipient formation of a continuous network of gas flow paths. The pressure corresponding to the initial penetration of the nonwetting phase (gas) into the largest pores near the surface of the medium will be termed the *gas entry pressure* in this report.

Table 12 contains a summary of the two-phase flow data for the mercury injection cores, including sample number, effective permeability, gas entry pressure, threshold pressure residual fluid saturations, and the Brooks and Corey Lambda parameter. The gas entry pressures reported in Table 12 are taken from the 140° contact angle corrected data reported in Tables 11a through 11f as the capillary pressure at the last 100% wetting-phase saturation. Likewise the residual brine saturations reported in Table 12 are also taken from the data reported in Tables 11a through 11f as the brine saturation value.

Table 12. Summary of Two-Phase Flow Data Results for Mercury Injection Cores

Sample Number	Permeability (m^2) 3.4 MPa Net Effective Stress	Gas Entry Pressure (psi/MPa) 140° Contact Angle	Gas Entry Pressure (psi/MPa) 180° Contact Angle	Residual Brine Saturation (%)	Threshold Pressure (psi/MPa) 140° Contact Angle	Residual Liquid Saturation (%)	Residual Gas Saturation (%)	Lambda
5	5.1×10^{-19}	1.7/0.012	1.3/0.009	8.1	78/0.54	7.3	11.6	0.655
7	9.5×10^{-19}	1.7/0.012	1.3/0.009	11.7	113/0.78	7.0	7.8	0.664
11	1.8×10^{-18}	2.3/0.016	1.8/0.012	23.5	65/0.45	17.4	1.4	0.558
13	1.6×10^{-18}	0.6/0.004	0.5/0.003	14.6	109/0.75	10.9	19.7	0.652
21	7.7×10^{-19}	1.2/0.008	0.9/0.006	8.3	48/0.33	0.8	2.5	0.491
23	1.3×10^{-18}	1.2/0.008	0.9/0.006	8.2	58/0.40	6.8	3.2	0.842

The values for threshold pressure, residual liquid saturation, residual gas saturation, and lambda reported in Table 12 were derived using an iterative trail-and-error solution technique documented in Appendix E. These values are consistent with the Brooks and Corey and the van Genuchten-Parker definitions.

6.4 Comparison of MB139 Mercury Injection Capillary Pressure Data to Brooks-Corey and van Genuchten Correlations

Figure 39 presents a plot of the six mercury injection capillary pressure curves (corrected using a 140° contact angle) shown in Figure 36 with the Mixed Brooks and Corey (see Appendix F) and van Genuchten correlations used in WIPP Performance Assessment (PA) calculations of 1992. The values for input parameters for these correlations are the median values for anhydrite used in the 1992 WIPP PA (Sandia WIPP Project, 1992) and are shown on Figure 32. The van Genuchten correlation shows a better fit to general shape of the capillary pressure curves, especially in the high brine-saturation region of the graph, than does the Mixed Brooks and Corey correlation. However, values from the high brine-saturation region approach experimental resolution. Therefore, the use of one correlation over the other cannot be recommended.

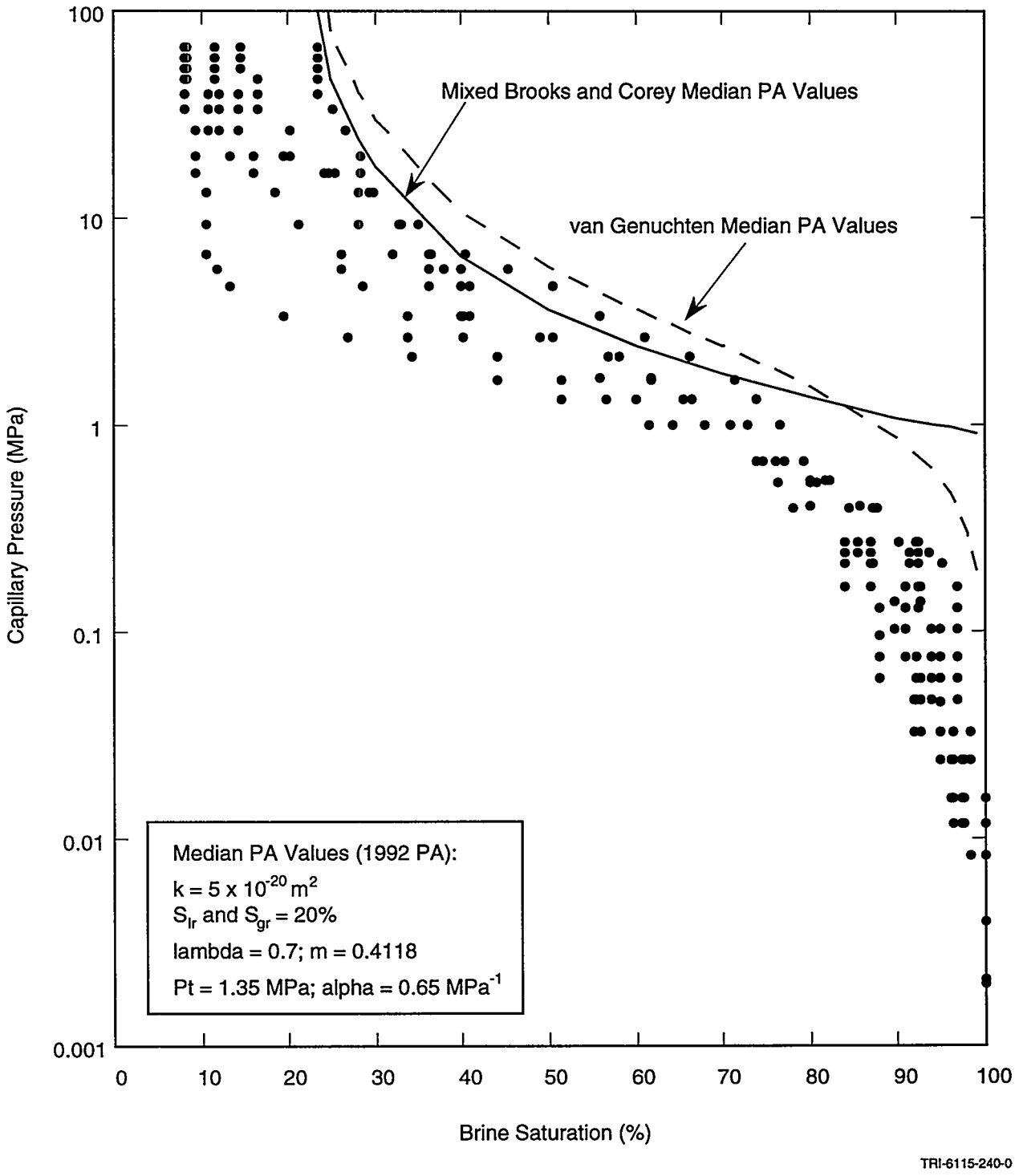

Figure 39. Comparison of measured MB139 mercury injection capillary pressure data (140° contact angle) to median parameter values used in determining the two-phase flow capillary pressure curve in performance assessment.

7.0 RELATIONSHIPS BETWEEN MEASURED PARAMETERS

7.1 Single-Phase Gas Permeability versus Porosity and Grain Density

Figures 40 and 41 are log-linear cross-plots of gas permeability versus effective porosity and grain density, respectively. As illustrated in Figure 40, there is a trend of increasing Klinkenberg-corrected gas permeability, k_g, with increasing effective porosity, ϕ_{eff}, as described by Equation 6.

$$\log k_g = -0.416\phi_{eff} - 18.59 \quad (6)$$

No apparent correlation exists between the gas permeability and grain density, as illustrated by the gas permeability versus grain density cross-plot in Figure 31. Sufficient data were not available to determine if a relationship existed between total and effective porosity or between total porosity and single-phase gas permeability.

7.2 Single-Phase Gas Permeability versus Threshold Pressure

Figure 42 is a cross-plot of air-brine threshold pressure versus Klinkenberg-corrected gas permeability. The results from cores tested in this study are shown with the Davies' (1991) correlation for all rock and for anhydrite. The Davies' (1991) correlation for all rock types, Equation 7, relates threshold pressure, P_t, to intrinsic permeability, k.

$$P_t(MPa) = 5.6 \times 10^{-7}[k\,(m)^2]^{-0.346} \quad (7)$$

This correlation, used in the 1992 WIPP PA calculations, was developed prior to the initiation of the Salado Two-Phase Flow Program using data from a variety of consolidated rock lithologies including carbonate, anhydrite, shale, and sandstone. The Davies' correlation was considered the best available analog-based correlation for relating intrinsic permeability to threshold pressure, and uncertainties regarding its applicability to the Salado provided the impetus for this work.

The Davies' (1991) correlation for anhydrite appears to be adequate for relating threshold pressure and permeability for anhydrite, based on the tests conducted for this study.

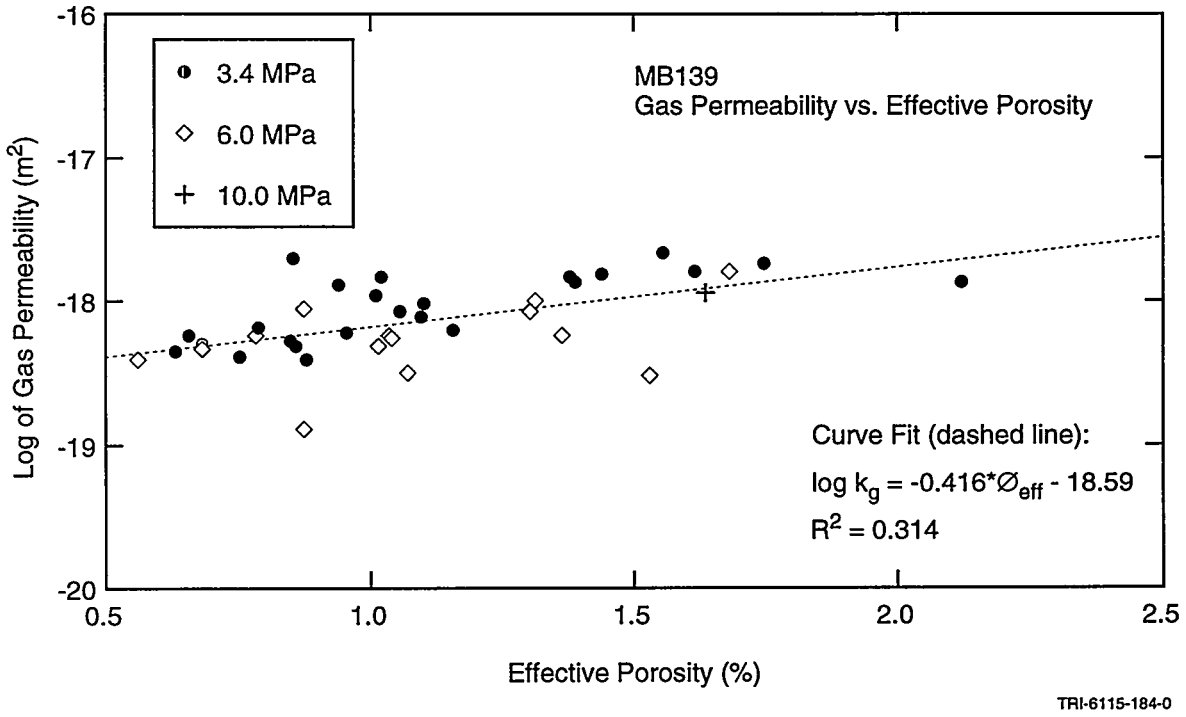

Figure 40. Gas permeability versus effective porosity.

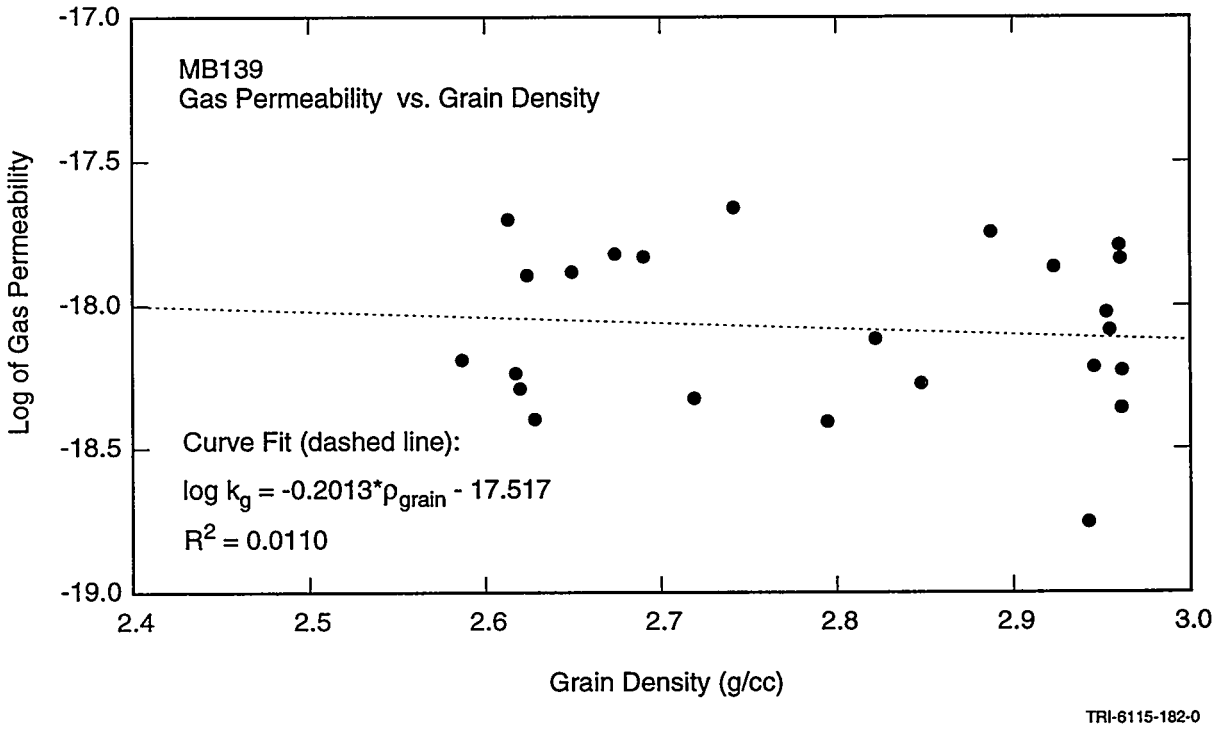

Figure 41. Gas permeability versus grain density.

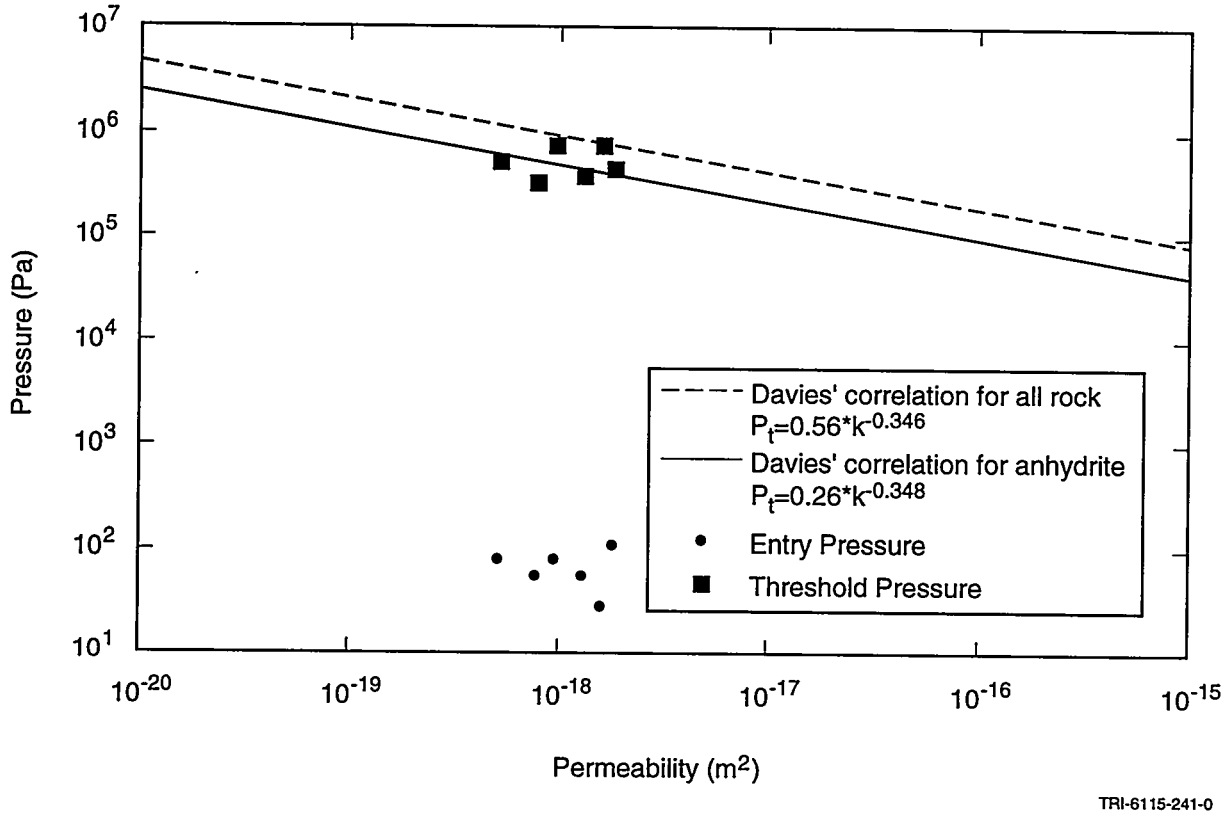

Figure 42. Comparison of measured MB139 gas threshold entry pressure to Davies (1991) correlation.

8.0 CONCLUSIONS

The laboratory experiments and results reported here comprise the Preliminary Measurements (Anhydrite) portion of the Preliminary Experimental Activities of the Salado Two-Phase Flow Laboratory Program. These measurements were made to (1) generate WIPP-specific porosity and single-phase permeability data; (2) provide information needed to design test equipment and implement planned tests to measure two-phase flow properties, including relative permeability, threshold pressure, and capillary pressure; and (3) evaluate the suitability of using analog correlations for the Salado Formation to assess the long-term performance of the WIPP. Section 8.1 summarizes conclusions about the measurement of porosity and single-phase permeability of WIPP-specific material (anhydrite), Section 8.2 summarizes information from these tests that will be used for designing and implementing the two-phase flow tests, and Section 8.3 summarizes conclusions regarding the suitability of using analog correlations for the anhydrite marker beds in WIPP PA calculations.

8.1 WIPP-Specific Porosity and Single-Phase Permeability Measurements

8.1.1 Porosity

Effective porosity, measured on 42 samples, ranged from 0.4 to 2.7%; total porosity, measured on three of the 42 samples, ranged from 0.4 to 1.6%. The magnitude of difference between total and effective porosity could not be determined because of the limited amount of data and experimental error.

A slight reduction in effective porosity occurred when increasing confining stress was applied to a sample. In general, Zone III samples exhibited slightly higher effective porosity than Zone II and IV samples; no porosity measurements were made in Zone I or V rock. Because of the presence of pre-existing fractures in Zones I and V and/or differences in composition between Zones I and V and Zones II, III, and IV, the porosity of Zones I and V is expected to be more representative of fractured rock and therefore is likely to be higher than the rock recovered from Zones II, III, and IV.

8.1.2 Permeability

Gas permeability ranged from a minimum of 5.0×10^{-20} m^2 at 10 MPa net effective stress to a maximum of 8.3×10^{-16} m^2 at 2 MPa net effective stress. For all specimens tested,

permeability decreased as net effective stress was increased. Differences between vertical and horizontal permeability were within experimental error bounds. In general, Zone IV samples exhibited slightly higher permeability than Zone II and III samples; no permeability measurements were made in Zone I or V rock. Because of the presence of pre-existing fractures in Zones I and V and/or differences in composition between Zones I and V and that of Zones II, III, and IV, the permeability of Zones I and V is expected to be more representative of fractured rock and therefore higher than rock recovered from Zones II, III, and IV.

The relationship between effective porosity and gas permeability was linear; however, insufficient total-porosity data were available to define a relationship between total porosity and gas permeability. No trend existed between gas permeability and grain density, nor between gas permeability and threshold pressure resulting from the mercury injection capillary pressure tests.

8.2 Application of Test Results for Design and Implementation of Two-Phase Flow Tests

The design and implementation of a test program and development of experimental apparatus for measuring two-phase flow properties is highly dependent on the expected magnitude and range of single-phase flow properties (Christiansen and Howarth, 1995). The porosity of MB139 is very low, especially compared to sandstones and other rocks for which flow properties are routinely measured. Because capillary pressure and relative permeability are directly related to saturation and therefore to porosity and pore volume, accurate porosity measurements are essential. The Boyle's law helium expansion technique was used to measure porosity for this study and yielded acceptable results.

The gas and liquid permeability tests reported here were successfully performed using the steady-state technique when a non-reactive fluid was used. The magnitude and range of intrinsic permeability results from these tests also support the use of transient methods that would decrease the amount of time necessary for each test.

The simulated MB139 brine (recipe found in Appendix D) is not suitable for liquid flow tests on MB139 core samples. Dissolution of specimens which resulted in order-of-magnitude increases in permeability occurred when the simulated MB139 brine recipe was used. Liquid permeability measurements performed using odorless mineral spirits (OMS) agreed well with Klinkenberg-corrected gas permeability. Liquid permeability measurements

performed using the simulated MB139 brine did not agree with Klinkenberg-corrected gas permeability.

Both the centrifuge and mercury injection methods were suitable for measuring capillary pressure on samples from MB139. Although the decane-air centrifuge data and the mercury-air mercury injection data must be converted to air-brine data, introducing possible error, the air-brine corrected capillary pressure for tests conducted using the mercury injection technique agreed well for 140° and 180° contact angles, especially at higher wetting-phase saturations. Either the Hassler-Brunner or Rajan data reduction method for determining end face saturations for capillary pressure curves for centrifuge data could be used; no significant difference existed in the calculated capillary pressure because the sample lengths were short.

Air-brine threshold pressures determined from the mercury injection test results ranged from 0.33 to 0.78 MPa (48 to 113 psi). Air-brine gas entry pressures could not be determined exactly from the centrifuge capillary pressure test data. Residual liquid saturation results determined from the mercury injection technique ranged from 0.8 to 17.4%. The residual liquid saturations determined from the centrifuge tests should not be used in WIPP PA calculations because centrifuge hardware limitations precluded tests at sufficiently high spin rates to define the residual liquid saturations properly.

8.3 Suitability Using Analog Correlations for WIPP PA Calculations

As shown in Figure 42, the air-brine threshold pressure versus Klinkenberg-corrected gas permeability data from measurements made in this study are within an acceptable range that would be predicted from the Davies' (1991) anhydrite correlation; this correlation appears to be adequate for relating threshold pressure and permeability for Salado anhydrite.

The capillary pressure and threshold pressure data measured on MB139 samples do not match the characteristic curves that result from the Brooks and Corey or van Genuchten correlations, as shown in Figure 29. The general shape of the van Genuchten capillary pressure characteristic curve is similar to that of the actual MB139 capillary pressure curves. However, values from the high brine-saturation region approach experimental resolution. Therefore, the use of one correlation over the other cannot be recommended.

9.0 RECOMMENDATIONS

Based on the preliminary tests and results summarized in this report, the recommendations in Sections 9.1 and 9.2 should be considered in the development of future test programs and experimental procedures. Section 9.3 contains recommendations and considerations that should be made regarding the compilation and development of a technical basis for specification of single- and two-phase flow parameters for WIPP PA calculations.

9.1 WIPP-Specific Porosity and Single-Phase Permeability Measurements

- The net effective stress law should be determined for MB139. MB139 permeability and porosity tests should be performed under appropriate confining stress conditions.
- Anisotropy in permeability of MB139 should be investigated further.
- Porosity and single-phase permeability should be measured on core specimens from Zones I and V of MB139 to determine the flow properties of those zones.

9.2 Application of Test Results for Design and Implementation of Two-Phase Flow Tests

- If capillary pressure is measured using a centrifuge, the selected system must be one that can accommodate sufficiently slow spin rates such that the threshold entry pressure could be determined.
- Capillary pressure should be measured on MB139 samples using apparatus that allows confining stress to be exerted on samples during the test to verify the estimated effect of stress on threshold entry pressures and capillary pressure characteristic curves for MB139 samples.
- The simulated MB139 brine (recipe found in Appendix D) should not be used for flow tests on MB139 core-scale specimens.
- Both the centrifuge and mercury injection methods were suitable for testing samples from MB139; however, only small samples can be tested using existing hardware at commercial laboratories. The porous plate method should also be investigated for use in measuring threshold and capillary pressure of MB139 rocks because larger, more representative samples could be tested and WIPP-specific brines and appropriate gas could be used.

9.3 Technical Basis for Specification of Single- and Two-Phase Flow Parameters for PA Calculations

The development of parameter distributions for single- and two-phase anhydrite marker bed flow properties for WIPP PA calculations should be based on three sets of data/information: (1) the WIPP-specific, laboratory-generated data presented in this report, (2) WIPP-specific, in situ permeability and threshold pressure test-data, (3) non-WIPP-specific tests performed on analogous materials reported in the literature. The value of the data/information with associated limitations and uncertainties must be considered in the development of distributions for permeability, porosity, and two-phase flow parameters, as outlined below.

- WIPP-specific, laboratory-generated single- and two-phase data:

  Value of data/information: measurement of total and effective porosity and liquid and gas permeability under three stress conditions and capillary and threshold pressure on specimens from MB139; control of pore pressure and confining stress; control of saturation; documentation of quality control for all tests.

  Sources of uncertainty and limitations: tests performed on small, core-sized specimens; no tests on samples from Zones I or V; cores taken from only three underground locations; all cores taken from MB139.

- WIPP-specific, in situ permeability and threshold pressure test-data:

  Value of data/information: tests performed in situ; test performed over full-thickness of marker beds; more than one anhydrite marker bed tested; numerous tests performed at different underground locations; documentation of quality control for all tests.

  Sources of uncertainty and limitations: limited number of permeability and threshold pressure tests; limited knowledge of in-situ stress conditions for permeability and threshold pressure conditions; limited knowledge of in-situ saturation conditions; limited knowledge of extent of disturbance to test zone resulting from proximity of excavations.

- Non-WIPP-specific analogous materials:

  Value of data/information: available, accessible data published in technical journals and other publications for permeability and porosity.

Sources of uncertainty and limitations: unknown how well analogs represent Salado rock; unknown details regarding test conditions for permeability and threshold pressure tests, including saturation state, test fluids used, stress conditions, and corrections for gas slippage effects; uncertainty in two-phase flow tests, including effects of stress on results and extremely limited data base for two-phase flow tests in low-permeability porous media; no documentation of quality control for any tests.

10.0 REFERENCES

Amyx, J.W., D.M. Bass, Jr., and R.L. Whiting. 1960. *Petroleum Reservoir Engineering: Physical Properties*. New York, NY: McGraw-Hill, Inc.

API (American Petroleum Institute). 1956. *Recommended Practice for Determining Permeability of Porous Media.* 3rd ed. API RP 27. Washington, DC: American Petroleum Institute. (Copy on file in the Sandia WIPP Central Files, Sandia National Laboratories, Albuquerque, NM as WPO#8709.)

API (American Petroleum Institute). 1960. *Recommended Practice for Core-Analysis Procedure.* API RP 40. Washington, DC: American Petroleum Institute. (Copy on file in the Sandia WIPP Central Files, Sandia National Laboratories, Albuquerque, NM as WPO#27179.)

Basan, P., J.R. Hook, K. Hughes, J. Rathmell, and D.C. Thomas. 1988. "Measuring Porosity, Saturation and Permeability from Cores: An Appreciation of the Difficulties," *The Technical Review* (A Schlumberger Publication). Vol. 36, no. 4, 22-36. (Copy on file in the Sandia WIPP Central Files, Sandia National Laboratories, Albuquerque, NM as WPO#8521.)

Bass, D.M., Jr. 1987. "Chapter 26 Properties of Reservoir Rocks," *Petroleum Engineering Handbook.* Ed. H.B. Bradley. Richardson, TX: Society of Petroleum Engineers. (Copy of chapter on file in the Sandia WIPP Central Files, Sandia National Laboratories, Albuquerque, NM as WPO#45569.)

Beauheim, R.L., G.J. Saulnier, Jr., and J.D. Avis. 1991. *Interpretation of Brine-Permeability Tests of the Salado Formation at the Waste Isolation Pilot Plant Site: First Interim Report.* SAND90-0083. Albuquerque, NM: Sandia National Laboratories.

Beauheim, R.L., R.M. Roberts, T.F. Dale, M.D. Fort, and W.A. Stensrud. 1993. *Hydraulic Testing of Salado Formation Evaporites at the Waste Isolation Pilot Plant Site: Second Interpretive Report.* SAND92-0533. Albuquerque, NM: Sandia National Laboratories.

Borns, D.J. 1985. *Marker Bed 139: A Study of Drillcore From a Systematic Array.* SAND85-0023. Albuquerque, NM: Sandia National Laboratories.

Brace, W.F., J.B. Walsh, and W.T. Frangos. 1968. "Hydraulic Properties of Granite Under High Pressure," *Journal of Geophysical Research.* Vol. 73, no. 6, 2225-2236. (Copy on file in the Sandia WIPP Central Files, Sandia National Laboratories, Albuquerque, NM as WPO#45570.)

Brooks, R.H., and A.T. Corey. 1964. "Hydraulic Properties of Porous Media." Hydrology Paper No. 3. Fort Collins, CO: Colorado State University. (Copy on file in the Sandia WIPP Central Files, Sandia National Laboratories, Albuquerque, NM as WPO#41117.)

Bush, D.C., and R.E. Jenkins. 1970. "Proper Hydration of Clays for Rock Property Determinations," *Journal of Petroleum Technology.* Vol. 22, no. 7, 800-804. (Copy on file in the Sandia WIPP Central Files, Sandia National Laboratories, Albuquerque, NM as WPO#45572.)

Christiansen, R.L., and S.M. Howarth. 1995. *Literature Review and Recommendation of Methods for Measuring Relative Permeability of Anhydrite from the Salado Formation at the Waste Isolation Pilot Plant*. SAND93-7074. Albuquerque, NM: Sandia National Laboratories.

Davies, P.B. 1991. *Evaluation of the Role of Threshold Pressure in Controlling Flow of Waste-Generated Gas into Bedded Salt at the Waste Isolation Pilot Plant*. SAND90-3246. Albuquerque, NM: Sandia National Laboratories.

Davies, P.B., L.H. Brush, M.A. Molecke, F.T. Mendenhall, and S.W. Webb, eds. 1991. *Waste-Generated Gas at the Waste Isolation Pilot Plant: Papers Presented at the Nuclear Energy Agency Workshop on Gas Generation and Release from Radioactive Waste Repositories*. SAND91-2378. Albuquerque, NM: Sandia National Laboratories.

Davies, P.B., R.L. Beauehim, and E.D. Gorham. 1992. Appendix A. "Additional Comments on Far-Field Anhydrite Permeability Distribution in 'PA Modeling Using BRAGFLO-1992' 7-8-92 Memo by J. Schreiber," *Preliminary Performance Assessment for the Waste Isolation Pilot Plant, December 1992. Volume 3: Model Parameters*. Sandia WIPP Project. SAND92-0700/3. Albuquerque, NM: Sandia National Laboratories. A-39 through A-45.

Deal, D.E., and J.B. Case. 1987. *Brine Sampling and Evaluation Program Phase I Report.* DOE-WIPP-87-008. Carlsbad, NM: Westinghouse Electric Corporation. (Copy on file in the Sandia WIPP Central Files, Sandia National Laboratories, Albuquerque, NM as WPO#44308.)

Fatt, I., and D.H. Davis. 1952. "Technical Note 147. Reduction in Permeability with Overburden Pressure," *Petroleum Transactions, AIME*. Vol. 195, 329. (Copy on file in the Sandia WIPP Central Files, Sandia National Laboratories, Albuquerque, NM as WPO#8627.)

Fredich, J.T., and D.H. Zeuch. 1996. *Petrographic and X-Ray Diffraction Analyses of Selected Samples from Marker Bed 139 at the Waste Isolation Pilot Plant*. SAND95-1240. Albuquerque, NM: Sandia National Laboratories.

Freeman, D.L., and D.C. Bush. 1983. "Low-Permeability Laboratory Measurements by Nonsteady-State and Conventional Methods," *Society of Petroleum Engineers Journal.* Vol. 23, no. 6, 928-936. (Copy on file in the Sandia WIPP Central Files, Sandia National Laboratories, Albuquerque, NM as WPO#45575.)

Freeze, R.A. 1975. "A Stochastic-Conceptual Analysis of One-Dimensional Groundwater Flow in Nonuniform Homogeneous Media," *Water Resources Research*. Vol. 11, no. 5, 725-741. (Copy on file in the Sandia WIPP Central Files, Sandia National Laboratories, Albuquerque, NM as WPO#45948.)

Gonzales, M.M. 1989. *Compilation and Comparison of Test-Hole Location Surveys in the Vicinity of the Waste Isolation Pilot Plant Site*. SAND88-1065. Albuquerque, NM: Sandia National Laboratories.

Good, R.J., and R.S. Mikhail. 1981. "The Contact Angle in Mercury Intrusion Porosimetry," *Powder Technology*. Vol. 29, no. 1, 53-62. (Copy on file in the Sandia WIPP Central Files, Sandia National Laboratories, Albuquerque, NM as WPO#45577.)

Hassler, G.L., and E. Brunner. 1945. "Measurement of Capillary Pressures in Small Core Samples," *Petroleum Transactions, AIME*. Vol. 192, 114-123. (Copy on file in the Sandia WIPP Central Files, Sandia National Laboratories, Albuquerque, NM as WPO#27177.)

Holcomb, D.J., D.H. Zeuch, K. Morin, R. Hardy, and T.V. Tormey. 1995. *Field and Laboratory Investigations of Coring-Induced Damage in Core Recovered from Marker Bed 139 at the Waste Isolation Pilot Plant Underground Facility*. SAND94-2757. Albuquerque, NM: Sandia National Laboratories.

Howarth, S.M. 1993. *Conceptual Plan: Two-Phase Flow Laboratory Program for the Waste Isolation Pilot* Plant. SAND93-1197. Albuquerque, NM: Sandia National Laboratories.

Hsieh, P.A., J.V. Tracy, C.E. Neuzil, J.D. Bredeheoft, and S.E. Silliman. 1981. "A Transient Laboratory Method for Determining the Hydraulic Properties of 'Tight' Rocks—I. Theory," *International Journal of Rock Mechanics and Mining Sciences & Geomechanics* Abstracts. Vol. 18, no. 3, 245-252. (Copy on file in the Sandia WIPP Central Files, Sandia National Laboratories, Albuquerque, NM as WPO#45118.)

Jones, F.O., and W.W. Owens. 1980. "A Laboratory Study of Low-Permeability Gas Sands," *Journal of Petroleum Technology*. Vol. 32, no. 9, 1631-1640. (Copy on file in the Sandia WIPP Central Files, Sandia National Laboratories, Albuquerque, NM as WPO#45579.)

Keelan, D.K. 1972. "A Critical Review of Core Analysis Techniques," *The Journal of Canadian Petroleum Technology*. Vol. 11, no. 2, 42-55.

Klinkenberg, L.J. 1941. "The Permeability of Porous Media to Liquids and Gases," *API Drilling and Production Practice*. 200-213. (Copy on file in the Sandia WIPP Central Files, Sandia National Laboratories, Albuquerque, NM as WPO#8556.)

McLatchie, A.S., R.A. Hemstock, and J.W. Young. 1958. "The Effective Compressibility of Reservoir Rock and Its Effects on Permeability," *Journal of Petroleum Technology*. Vol. 10, 49-51. (Copy on file in the Sandia WIPP Central Files, Sandia National Laboratories, Albuquerque, NM as WPO#45580.)

Parker, J.C., R.J. Lenhard, and T. Kuppusamy. 1987. "A Parametric Model for Constitutive Properties Governing Multiphase Flow in Porous Media," *Water Resources Research*. Vol. 23, no. 4, 618-624. (Copy on file in the Sandia WIPP Central Files, Sandia National Laboratories, Albuquerque, NM as WPO#41124.)

Rajan, R.R. 1986. "Theoretically Correct Analytical Solution for Calculating Capillary Pressure-Saturation From Centrifuge Experiments," *Transactions of the SPWLA 27th Annual Logging Symposium, Houston, TX, June 9-13, 1986*. Houston, TX: Society of

Professional Well Log Analysts, Inc. (Copy on file in the Sandia WIPP Central Files, Sandia National Laboratories, Albuquerque, NM as WPO#45949.)

Rudd, N. 1974. "New Techniques for Threshold Pressure Determination in Gas Storage Cap Rock," *Geo-Engineering Laboratories, Inc. Tech Memo No. 6*. Chicago, IL: Institute of Gas Technology. (Copy on file in the Sandia WIPP Central Files, Sandia National Laboratories, Albuquerque, NM as WPO#8622.)

Sandia WIPP Project. 1992. *Preliminary Performance Assessment for the Waste Isolation Pilot Plant, December 1992. Volume 3: Model Parameters*. SAND92-0700/3. Albuquerque, NM: Sandia National Laboratories.

Thomas, L.K., D.L. Katz, and M.R. Tek. 1968. "Threshold Pressure Phenomena in Porous Media," *Society of Petroleum Engineers Journal*. Vol. 8, no. 2, 174-184. (Copy on file in the Sandia WIPP Central Files, Sandia National Laboratories, Albuquerque, NM as WPO#45583.)

Walls, J.D., and J.O. Amaefule. 1985. "Capillary Pressure and Permeability Relationships in Tight Gas Sands," *SPE/DOE Symposium on Low Permeability Gas Reservoirs, Denver, CO, May 19-22, 1985*. SPE/DOE 13879. Dallas, TX: Society of Petroleum Engineers. 293-302.

Warpinski, N.R., and L.W. Teufel. 1992. "Determination of the Effective Stress Law for Permeability and Deformation in Low-Permeability Rocks," *SPE Formation Evaluation*. Vol. 7, no. 2, 123-131.

Appendix A.
Data Report: Rock Physics Associates (Core Laboratories)

The following section includes Appendix A and Appendices A-A through A-C.

Appendix A

Capillary Pressure Measurements in Anhydrite Samples from MB 139

Errata Sheet

Upon review of the "raw" data, the following inconsistencies were found:

Data from sample 3 are not included in the data report because the sample was chipped and it is inconclusive if the "repair" by the laboratory was sufficient.

There are errors in Table 4.1.

1) The conversion value used to convert permeability from m^2 to Darcy was in error. The author of the report used the general conversion that a Darcy =1E-12 m^2, not the true conversion of Darcy = 9.869E-13 m^2. The original permeabilities were in m^2; thus all the permeability values are off by about 0.1%.
2) The permeability of sample 2 at 1450 psi net stress should be 0.000228, not 0.000278 md.
3) The permeability of sample 9 at 500 psi net stress should be 0.000476, not 0.000535 md.
4) The permeability of sample 16 was unable to be determined in that the Klinkenberg correction slope was negative. Thus no value should have been given.
5) The permeability of sample 17 at 500 psi net stress should be 0.000405, not 0.000407 md.

The reported capillary pressure for sample 6 shown in tabulation form on Figure 4.9 is incorrect. The correct data are contained in the text of SAND 94-0472.

The results from Appendix C of this report, *Capillary Pressure Measurements in Anhydrite Samples from MB 139,* are not included in the data report because the data were not qualified by the time of report publication. Appendix A-C data from Sample EX 10-7 5.75-5.9 should not be used because the sample was broken during testing. Errors in Appendix A-C include:

1) Second page of Section 1, first line should read "confining pressure" not "confiningressure."
2) Second page of Section 1, equation 1, the denominator should read
   "$A*(P1^2 - P2^2)$"
   not "$A*(P1^2 * P2^2)$"
3) Basic Rock Properties table, sample EX 10-6 4.50-5.1: the length should be 7.047, not 3.801.

The following modifications should be made to the references on pages A-24 and A-25 in Appendix A.

Ref. No.	Comment
2	copy of Ciftcioglu et al., 1992 on file in SWCF as WPO#45574
3	correct name for second author is "R. Angers"; copy on file in SWCF as WPO#45576
4	the existence of McCullough et al., 1944 could not be verified
5	to Thornton and Marshall, 1947 remove "the" from title; paper is available as Am Inst. of Min & Met Engrs Tech Publ 2126 (1946), 9 pp.
6	correct name for second author is "H.J. Welge"
7	Rose and Bruce, 1949 is published in *Petroleum Transactions, AIME,* Vol. 186, pp. 127-142; copy on file in SWCF as WPO#45582
8	Calhoun et al., 1949 is published in *Petroleum Transactions, AIME,* Vol. 186; copy on file in SWCF as WPO#45573
9	complete name of first author is G.L. Hassler Jr.; correct location is *Petroleum Transactions*; correct page numbers are 114-123; copy on file in SWCF as WPO#27177
10	to citation for Christiansen the word "Relationships" should be inserted after the word "Pressure" in the title; add: Vol. 7, no. 4
11	to citation for Melrose add: Vol. 29, no. 1
12	to citation for Chen et al. add: pp. 221-228
14	to citation for Purcell add: Vol. 186, pp. 39-48; copy on file in SWCF as WPO#45581
15	correct location for Melrose et al. is pp. 333-343 in *Formation Evaluation and Reservoir Geology Proceedings, SPE Annual Technical Conference and Exhibition, Dallas, TX, November 6, 1991*
16	correct title for Ward and Morrow paper is "Capillary Pressures and Gas Relative Permeabilities of Low-Permeability Sandstone"; paper presented at the *Low Permeability Gas Reservoirs Symposium*; add: pp. 321-334
17	copy of Walls and Howarth, 1993 on file in SWCF as WPO#35253
18	the existence of this Core Laboratories internal document could not be verified
19	in Rajan, 1986 the words "Pressure-Saturation" should replace the words "Pressure Curves" in the paper title; published in *Transactions of the SPWLA*; Vol. I, 18 pp.; copy on file in SWCF as WPO#45949
20	to citation for Walls and Amaefule add: pp. 293-302
21	copy of Davies, 1991 on file in SWCF as WPO#26169
22	to Good and Mikhail, 1981 add: Vol. 29, no. 1; copy on file in SWCF as WPO#45577

Final Report

Capillary Pressure Measurements in Anhydrite Samples from MB 139

Prepared By:
Rock Physics Associates
Project # 93-03

Prepared for:

Sandia National Laboratories

August, 1995

Table of Contents

Figures

Tables

Test Procedures and QA Plan: Capillary Pressure Measurements in Anhydrite

1.0 Introduction

The Waste Isolation Pilot Plant (WIPP) is designed to safely contain low-level transuranic radioactive waste. The design relies mainly on the stability and low permeability of the Salado Formation. Interbedded anhydrite layers within the Salado such as Marker Bed (MB) 139 may be more permeable than the surrounding halite and may allow gas generated from the degrading waste to escape from the underground storage rooms. The extent of this gas flow, if any, in response to an applied pressure gradient will be controlled by several factors. These include porosity, intrinsic or absolute permeability, gas-liquid capillary pressure, gas-liquid relative permeability and the degree of interconnectivity of the anhydrite pore system. This report contains the results of a preliminary experimental program to measure the porosity, gas permeability, and capillary pressure of 1 inch diameter by 1 inch long cylindrical samples from MB 139. These tests were conducted as part of the Salado Two-Phase Flow Laboratory Program by a commercial core analysis lab that specializes in testing low permeability rock . Also included is a literature review in the field of capillary pressure.

The capillary pressure tests were carried out on six pairs of samples. The pairs were chosen by a careful screening process that eliminated non-representative or highly heterogeneous samples. The screening process included visual inspection, x-ray imaging for internal irregularities, and measurements of density, porosity, and permeability. One sample from each pair was tested by the mercury injection capillary pressure method and the other was tested by the centrifuge capillary pressure method. These two methods were chosen because they are the most appropriate for low porosity and permeability samples such as the anhydrite. The results from both techniques were reasonably consistent for each pair of samples after the data was converted to an air-brine system. Two features of the data stood out. First, the threshold entry pressures were very low, typically less than 5 psi, and second, the residual wetting phase saturation was less than 30% in all cases. These characteristics would be expected of samples with much higher permeability.

Additional measurements of porosity and gas permeability at multiple confining stresses were performed. These samples were 1.5 inches in diameter and about 1 to 2 inches in length, and the results of these tests are given in Appendix A-C. Because they were not in the original sample set, and were not considered for capillary pressure testing, the results have not been included in the main body of this report. The gas permeability of these samples were not Klinkenberg corrected.

2.0 Review of Capillary Pressure Measurement Methods

The modern literature on capillary pressure measurements can be broadly divided into two groups: 1) material science and 2) oil and gas. The material science publications generally focus on determining pore size distribution of compacted powders, sintered granular materials and ceramics. The method most often used is the high pressure mercury injection technique [1,2] although the air-water dynamic expulsion method is also reported occasionally [3]. The major interests in oil and gas are determining water, oil, and gas saturations, relative permeability behavior, and pore size distribution on a variety of different rock types. The methods used are porous plate displacement, centrifuge displacement, mercury injection, and occasionally, vapor desorption. Because the petroleum publications focus on natural materials and include a wide variety of methods, we concentrated on this body of literature. This review is not exhaustive, but rather attempts to highlight important or representative publications. Each of the four primary measurement methods are discussed below, followed by the rationale for selecting the two techniques, mercury injection and centrifuge, that were used in this study.

2.1 Porous Plate Displacement

This method was discussed by McCullough, et al.[4] and several other early experimenters [5,6,7,8]. There are two major variations on the method, batch mode porous plate displacement and overburden pressure porous plate displacement. In the batch mode, several samples are placed on a large semi-permeable membrane or capillary plate that can be made of various materials (Figure 2.1). For rock sample testing, the capillary plate material is often porous ceramic, and in soil testing cellulose membranes are used. For drainage cycle testing, the sample is initially fully saturated with the wetting fluid. Each sample is weighed before it goes into the cell, and the density of the wetting and non-wetting fluids are known.

As shown in Figure 2.1, the displacing (non-wetting) fluid fills the upper part of the batch mode cell and the displaced (wetting) fluid fills the lower part of the cell. In this type of test, the non-wetting fluid is often humidified air or nitrogen. Pressure is increased on the non-wetting fluid, and when it exceeds the threshold entry pressure in one or more of the samples, wetting phase fluid begins to flow from the lower part of the cell. The actual volume of this fluid does not matter since there is no way to tell from which sample it came. However, when the fluid flow stops, it signals that all samples are at equilibrium at that pressure and can be removed from the cell for weighing. The saturation in each sample is determined gravimetrically. This process is repeated at higher and higher non-wetting injection pressures until the threshold pressure of the capillary plate is reached. Spontaneous imbibition can be achieved by reducing the injection pressure to zero and

allowing the samples to imbibe the wetting phase fluid. Usually only a small amount of fluid (5% to 10% of pore volume) will spontaneously imbibe.

More recently, porous plate capillary pressure apparatus has been adapted so that overburden or confining pressure can be applied to the sample during testing. In this configuration a sample is jacketed with an elastomeric sleeve around the sides, and two metal end caps are placed on each end of the sample. This assembly is contained within a pressure cell that permits hydrostatic or bi-axial stress to be applied to the sample. The example in Figure 2.2 shows a hydrostatic capillary pressure cell. The semi-permeable membrane or capillary plate is usually mounted on one end of the sample, and the non-wetting phase fluid is injected from the opposite end of the sample. The volume of wetting phase displaced is measured with a precision balance or in a small calibrated glass tube. This arrangement can also be equipped with an oil-wet membrane to permit both forced drainage and imbibition capillary pressure curves.

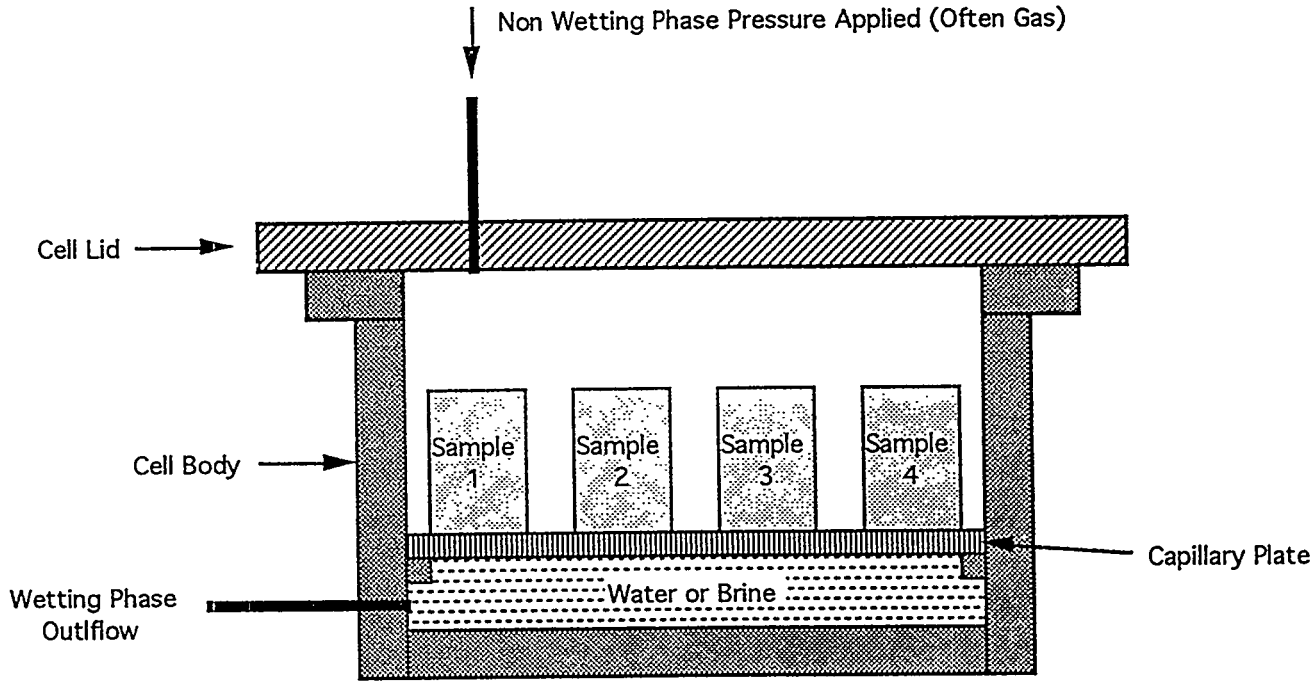

Figure 2.1: Batch Mode Capillary Pressure Cell

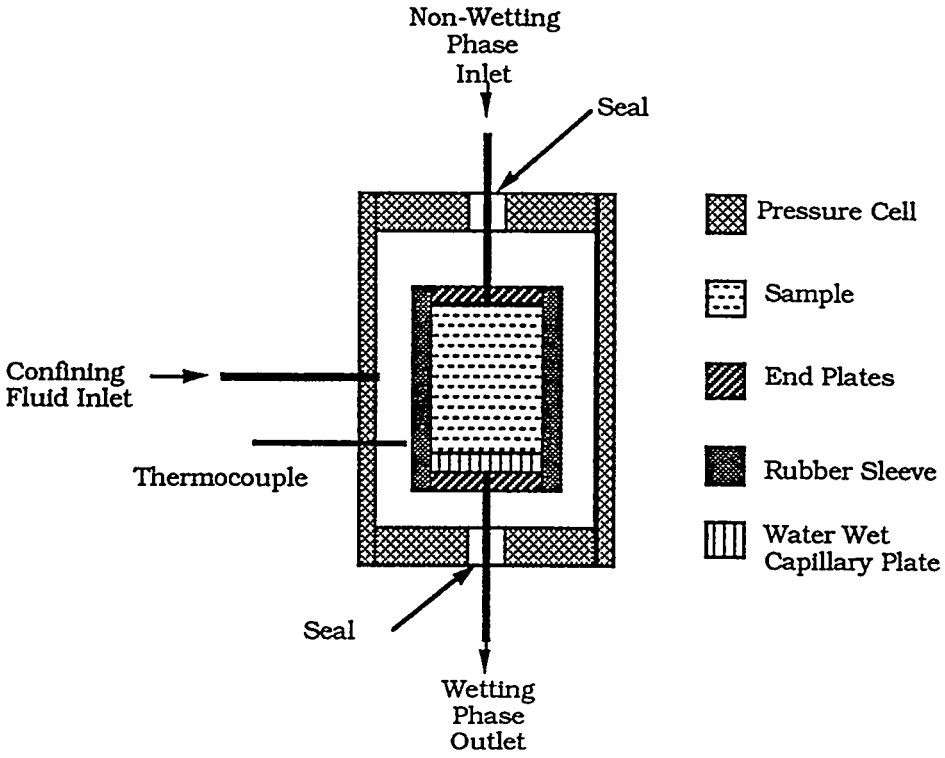

Figure 2.2: Hydrostatic Overburden Capillary Pressure Cell

2.2 Centrifuge Displacement

The centrifuge displacement technique for measuring capillary pressure has been the subject of many studies since first introduced to the petroleum industry by Hassler and Brunner[9] in 1945. This method involves placing a brine- or oil-saturated sample into a centrifuge rotor and incrementally increasing the rotational speed. A stroboscope device is used to read the volume of fluid that is displaced from the sample at each speed which is collected in a clear plastic calibrated tube (see Figure 2.3). The measured values in centrifuge displacement are centrifugal acceleration (G's) and the average saturation of the sample. The desired results are capillary pressure and the saturation at a specific location on the sample, usually the inflow face.

Converting centrifugal acceleration to pressure is straightforward, but converting average saturation to point saturation is where disagreement sometimes arises. Hassler and Brunner provided a general solution to the problem for a homogeneous sample. Their saturation equation could be solved by successive approximations, thereby achieving any desired degree of accuracy. However, in practice, most people only use the first approximation, because it is mathematically more convenient, and it is often adequate for small sample lengths (where $R_1/R_3 > 0.7$). R_1 and R_3 are the distances from the centrifuge axis to the top end of the sample and to the bottom end of the sample, respectively as shown in Figure 2.3. Therefore, this first approximation has now

become widely known as the "Hassler-Brunner solution." Review of the many responses to and revisions of the Hassler-Brunner approach are presented in several recent articles[10,11,12].

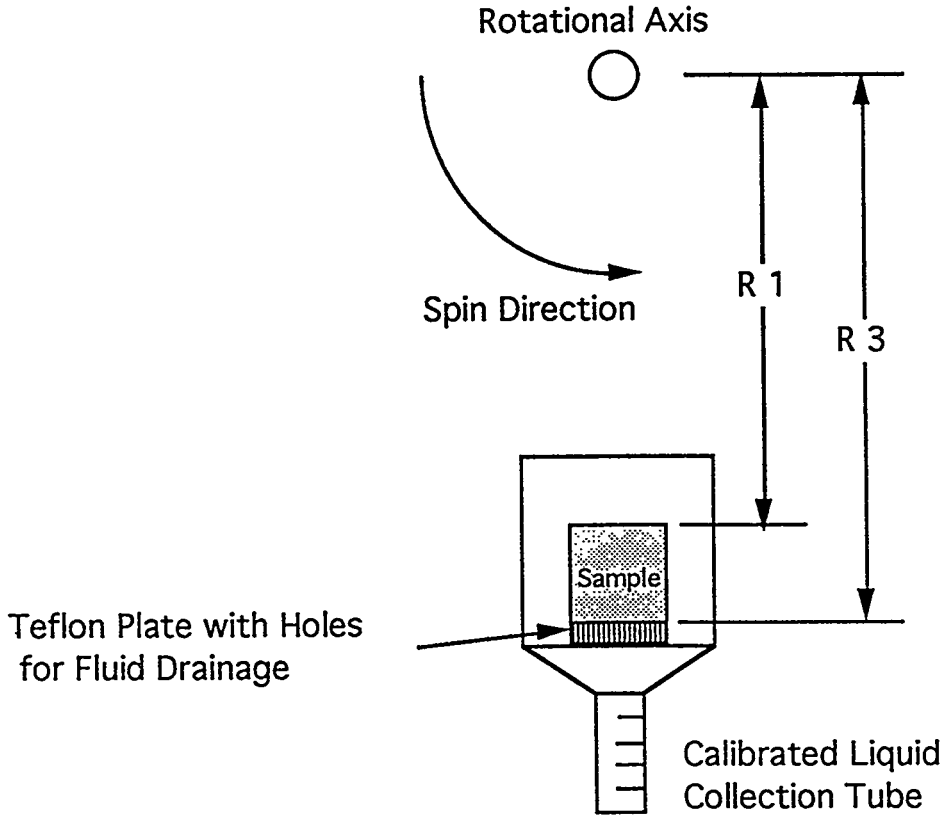

Figure 2.3: Diagram of One Arm of a Multi-Sample Centrifuge Capillary Pressure System

One advantage of the centrifuge method over porous plate methods is that it can be used to develop higher capillary pressures, and therefore results can be obtained at low wetting phase saturations. For example, using a high speed centrifuge with oil as the wetting phase and air as the non-wetting phase, it is possible to measure capillary pressures of 650 psi or more. This is very important for low permeability materials. Another advantage is that the time required for equilibrium is not as long as for porous plate methods. Omoregie[13] has shown that some porous plate tests require equilibration periods that are greater than 10 times longer than the centrifuge displacement test for the same sample.

2.3 Mercury Injection

The mercury injection method, as applied to rock samples, was first presented by Purcell[14]. The method can be used over a wide range of wetting phase saturations, from 100% to less than 10% for some rocks. Because the contact angle of mercury against solid mineral surfaces is about 140 degrees, mercury is the non-wetting phase and air is the wetting phase. A correction factor is used

to apply the air-mercury data to other fluids systems as described in Section 4.5. Current mercury injection instruments can reach up to 50,000 psi mercury pressure.

Equilibrium times are very short for this method because of the high pressures involved, and the method does not depend on displacement of the wetting phase by mass flow through the sample. As a result, mercury injection has been used extensively for characterizing the pore size distribution of sintered powders and ceramics[1,2]. Mercury injection is intended for samples that will not be seriously affected by drying or evacuation of the pore space. If hydrated clays are present, for example, the sample drying (required for mercury injection) may cause clay damage that would change the pore throat size distribution of the sample. Mercury is very useful for determining the threshold entry pressure of a sample, since the equivalent pressure required to cause mercury to enter an empty pore throat is about 5 times greater than that required for air to displace water.

2.4 Vapor Desorption

Vapor desorption is a method generally used to define the very low wetting phase saturation region of the capillary pressure curve. This portion of the curve is controlled by the smallest pore throat radii. For rock sample testing, the vapor phase is usually water, but nitrogen[15] and other gases can be used. Ward and Morrow[16] describe a typical experiment measuring water vapor desorption isotherms in low permeability sandstones. The method requires saturating a cylindrical rock sample with distilled water. The sample is then placed in a chamber with constant temperature and humidity of 99%. The sample is weighed periodically until its weight stabilizes. The relative humidity is then decreased to values of 98%, 95%, 92%, 90%, 75%, 60%, 40%, and 20%. Based on the weight of the dry sample, water saturation is calculated at each relative humidity. Ward and Morrow show that relative humidity is related to vapor pressure and vapor pressure depends on liquid/gas interface curvature. Therefore capillary pressure at each relative humidity, and water saturation, can be calculated.

2.5 Choice of Methods for this Project

Because of the low porosity and permeability of the Salado anhydrite samples, the methods that best suited testing of these samples are the mercury injection and centrifuge displacement methods. These two methods have a more rapid equilibrium process than the porous plate technique. Also, high threshold entry pressures, are expected, and these methods are the only ones that can be used if the threshold entry pressure is high. The vapor desorption method was not considered because it does not provide data near the 100% wetting phase saturation limit, and water can react with the halite in these samples.

3.0 Test Procedures

The sections below describe the test procedures that were used in this experimental project. For a description of the instrument calibration procedures, please refer to the relevant QA Plan[17] for this project.

3.1 Sample Preparation

The plug samples for these tests came from two six inch diameter whole cores E1X10 and E1X11 provided by Sandia National Laboratories. The cores were drilled downward through the Marker Bed 139 at approximately 90 degrees to the bedding planes. These cores were shipped directly to Marilyn Black, Core Analysis Supervisor, of Core Laboratories in Carrollton, TX. The samples were slabbed (cut) along their length, with the cut approximately 1/3 of the sample diameter from the outer circumference of the core (Figure 3.1). The cutting fluid for slabbing and plug cutting was Isopar, a light refined oil. This fluid was chosen because it can be easily removed from the core by standard drying procedures and because it does not react with halite, as a water based fluid might. After slabbing, both faces of the cores were photographed with white light. See Appendix A-A photographs.

Figure 3.1 shows a sketch of sample cutting locations. Horizontal (with respect to the bedding plane) test plugs were taken from the whole cores at 32 depths, and for vertical sample cutting at 11 depths. Plug sample locations were chosen by Dr. Susan Howarth and Dr. Joel Walls. Slabbed core photos showing the vertical and horizontal plug locations are included in Appendix A. Horizontal plugs 1 inch in diameter were drilled all the way through the whole core. These 5 to 6 inch long plugs were photographed in white light and X-ray scanned. Photographs were also made of the X-ray images and were combined with the white light photos (AppendixA-A).These photos were used to select the segments of the long plugs to use for the 1 inch long test plugs. Two test plugs (A & B) were then cut from each of the horizontal depths and two plugs (C1 and C2) were taken from each of the vertical depths. The end trims were saved for mineralogical analyses (see plug cutting sketch, Figure 3.1). The solid cylindrical plugs were 1 inch in diameter (+/- 0.002") and 1 inch in length (+ 0.002 /- 0.05"). The ends were cut and ground flat and parallel using a diamond face wheel surface grinder. Grinding was done slowly using compressed air flow to keep the cutting surface cool. Flatness of ends were within 0.001" (0.06 degrees) across the ends of the sample. The sides of the sample were straight within 0.02" when rolled across a flat surface plate. Length and diameter of samples were measured with digital calipers to within 0.001".

After cutting and surface grinding, these samples were labeled with a permanent marker and recorded on the sample tracking forms provided by SNL. The samples were dried in a vacuum oven at 104 degrees C until the weight stabilized to within 0.001 gm over a 24 hour period.

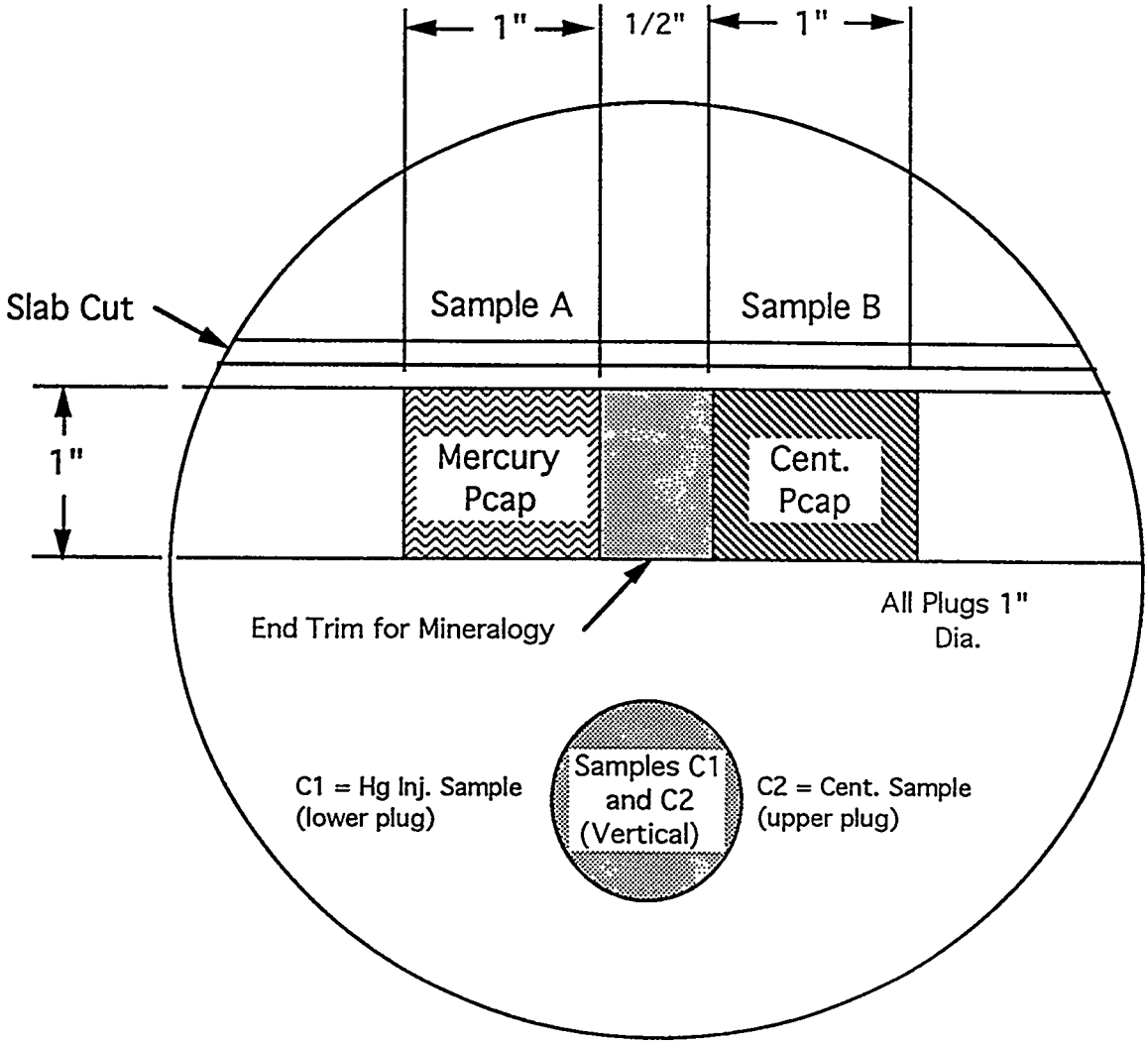

Figure 3.1: Plug Sample Cutting Sketch

3.2 Porosity and Gas Permeability Measurement

Measurement of porosity was done by the pore volume-grain volume method where

$$\text{Porosity} = PV / (PV + GV). \qquad 1$$

This is a measurement of the effective porosity, which will not measure pores that are isolated. Since we want to measure the pore space available for fluid flow, this is the correct porosity measurement method. Pore volume data reported on the 1" samples were taken using the Core

Laboratories CMS 300 system which measures direct pore volume by helium expansion. Grain volume data came from the Autoporosimeter system.

The porosity measurements in the CMS-300 are conducted using an initial pore pressure of 200 psig. The pore pressure drops during the test because the gas expands from the pore volume of the rock to a larger volume equal to the pore volume plus a calibrated reference volume. There is no way to know exactly what the final pore pressure will be, so the software for the CMS-300 predicts arbitrarily that the final pressure will be 100 psi. The software then adjusts the P_{ext} to P_{net} (desired) plus 100 psi. After the pore pressure reaches equilibrium and the pore volume is calculated, the CMS-300 software compares the actual final pore pressure to it's initial prediction of 100 psi. If the actual final pore pressure differs from the predicted value by more than 25 psi, then the software computes a new pore volume which would have been measured at the actual net stress. It does this by using a pore volume compressibility determined from the actual sample, if the sample was tested at multiple confining stresses. This is an iterative process that is fully described in the CMS-300 manual[18], Chapter 4. If the porosity was measured at only one net stress, the computational algorithm uses a default compressibility of 3×10^{-6} psi $^{-1}$. The important point is that the difference between the predicted final pore pressure and the actual final pore pressure is usually less than 50 psi, and this difference causes only minor adjustments to the pore volume.

A test to determine the effect of different drying methods on porosity, as called for in the original procedure, was not done . It was determined that in similar tests performed by other labs, there was no difference in porosity with either method. Also, it was determined from petrographic analysis that these samples contained no measurble clay or other hydration sensitive minerals that should be sensitive to drying methodology.

Permeability measurements to air were made in a steady-state system (Extended Range Autopermeameter System) using a constant upstream pressure. Flow rates were determined with a calibrated low range gas flow meter. The measurements were corrected for Klinkenberg slip effects (where possible) and all measurements were done at ambient temperature conditions. This temperature was recorded before each batch of samples was run.

For the steady state gas permeability measurements, net confining stress (P_{net}) reported is defined as

$$P_{net} = P_{ext} - P_{p,\,ave} \qquad 2$$

where P_{ext} is the external hydrostatic pressure applied to the rubber sleeve surrounding the sample. $P_{p,ave}$ is the average pore pressure, or the pressure of the flowing gas inside the sample measured relative to 1 atmosphere (gauge pressure, typical unit = psig). $P_{p,ave}$ is calculated from the average of the inlet and outlet gas pressure. For example, if the upstream pressure is 200 psig and the downstream pressure is 0 psig then the average pore pressure is 100 psig. The system operator, would then adjust the external confining pressure to P_{net} (desired) plus 100 psi to achieve the proper net stress for the test.

The porosity and permeability measurement procedure on the selected horizontal and vertical plugs (A, B, C1 and C2) was as follows;

1. Cool samples to room temperature in a small closed container with desiccant.
2. Weigh each sample on a digital balance to the nearest 0.0001 gm.
3. Measure grain volume in a Boyle's Law expansion cell with helium (helium pycnometer).
4. Place samples in the computer controlled CMS-300 system and measure porosity at the following net confining stresses: 500 psi (3.45 MPa), 870 psi (6.0 MPa), and 1450 psi (10 MPa).
5. Place samples in the steady state system and measure gas permeability at multiple gas injection pressures. For 1 inch diameter samples, use net confining stresses of 500 psi (3.45 MPa), 870 psi (6.0 MPa), and 1450 psi (10 MPa). Compute Klinkenberg-corrected gas permeability. For 1.5" diameter samples, use P_{net} equal to 400 psi (2.76 MPa), 870 psi (6.0 MPa), and 1450 psi (10 MPa) and do not compute Klinkenberg corrected gas permeability.

3.3 Mercury Capillary Pressure Measurements ("A" and "C2" Samples)

This test involved injecting mercury into the pores of six samples under high pressure. The system measures the volume of mercury injected at each pressure from zero to 50,000 psi. The test is destructive to the sample and the samples are disposed of after the test. The tests were carried out by an automated system that records all data on a computer, and data reduction is performed automatically by software provided by the manufacturer. The mercury injection system in use at Core Labs is the 2-sample Micromeritics Autopore II 9220. This is a standard machine for testing porous ceramics, rocks and other materials.

The test procedure followed for the mercury capillary pressure measurements were as follows.

1. Load dry "A" or "C2" samples into sample holder.
2. Check equilibration criteria values in computer set-up screen. It should be set to the longest allowable time (180 sec).

3. Run auto penetrometer mercury injection routine to 50,000 psi.
4. Remove sample and print out results. Perform data reduction using pore volume from CMS-300 at lowest net stress.

3.4 Centrifuge Capillary Pressure Measurements ("B" and "C1" Samples)

This measurement determines the drainage air-oil capillary pressure of six rock sample to pressures up to about 500 psi. Decane was chosen as the wetting phase because it is available in very pure form, it will not react with water soluble minerals in the samples, and it has a well documented surface tension value of 24 dynes/cm at 25 degrees Celsius[16]. The samples were first fully saturated with decane, then they were placed in a high speed centrifuge with calibrated collection tubes below each sample. As the speed of the centrifuge was increased, decane was displaced by centrifugal force and collected in the tubes.

The volume in each tube was visually read by the operator using a strobe light synchronized to the speed of the spinning rotor. The collection tubes in this experiment had an original volume of 1 cm^3 and were subdivided into 0.025 cm^3 divisions, but are readable to 0.01 cm^3. Because we had already measured the porosity of these samples, we knew that they had about 0.2 cm^3 of pore volume. Therefore to get better volume resolution, small Plexiglas rods whose cross sectional area was about half that of the collection tubes were fabricated . These rods were inserted into the collection tubes as a "ballast volume" to reduce the tube volume by about 50% and improve the volume resolution to about 0.0125/division, readable to 0.005 cm^3. Each tube was calibrated with it's ballast volume in place by spinning it with different amounts of kerosene (kerosene density was established by weighing in NIST certified balance), and then weighing the tube to establish a correlation between the visual scale on the tube and the actual volume of fluid.

The measurement procedure was as follows.

1. Saturate "B" and "C1" samples with decane by placing them in a chamber with a working pressure of at least 2000 psi. Evacuate the chamber to less than 100 microns pressure for 24 hours. Degas the decane with vacuum (less than 0.001 atm.) for at least 4 hours. Flood the chamber with the degassed decane and pressure it to 2000 psi. Leave pressure on samples for 24 hours. All centrifuge capillary samples (B and C1 Samples) were saturated together.
2. Measure the density of the degassed decane. Weigh each sample in air and suspended in the decane.
3. Select the smallest volume collection tubes available and partially pre-fill each one to avoid curvature errors at the bottom of the tube. Weigh the samples and load them into the

centrifuge. Begin the capillary pressure measurement procedure (ambient temperature). Expect high entry pressure to gas and very small volume changes. The equilibrium time between speed changes should be at least 48 hours.

4. Remove and immediately weigh the samples. Collect any loose grains in the centrifuge cup and weigh them. Calculate the final decane saturation by gravimetric and volumetric methods. Transmit data to Rock Physics Associates (RPA) for review. After approval from RPA, then go to step 5.

5. Perform data reduction using the standard Hassler-Brunner[9] method and the alternative Rajan[19] method. Use pore volume from CMS-300 at lowest net stress.

3.5 Mineralogical Analysis

End trims from the ten horizontal sample pairs and five vertical sample pairs were sent to Omni Laboratories in Houston, TX for quantitative X-ray diffraction and thin section point count analysis. This information is presented in Appendix A-B.

4.0 Results and Discussion

4.1 Porosity and Permeability

Porosity of all samples tested is presented in Table 4.1 and ranged from 0.6% to 2.1% at 500 psi net stress. At the next highest net stress (870 psi), porosity measurements could be made on 16 samples. The reduction in porosity from 500 to 870 psi ranged from zero to 12%. Porosity at 1450 psi was only successfully measured on three samples. Porosity, grain density and permeability data for these samples is given in Table 4.1. A plot of the distribution of grain densities is shown in Figure 4.1. Klinkenberg permeability, (K_l) was computed from air permeability measurements at multiple upstream injection pressures. Linear least squares regressions were computed to obtain the slope and intercept of the apparent permeability versus $1/P_{mean}$. K_l was rounded to the nearest +/- 1 X 10^{-6} md. Values of K_l less than 1 X 10^{-5} md were not reported. Plots of Klinkenberg permeability (K_l) versus porosity at 500 psi and 870 psi net stress are given in Figure 4.2. The permeability of the samples at 500 psi net stress ranged from about 4 X 10^{-4} to about 2 X 10^{-3} millidarcy. The permeability of the samples at 850 psi net stress ranged from about 1 X 10^{-4} to about 2 X 10^{-3} millidarcy. The permeability of the samples at 1450 psi net stress ranged from about 5 X 10^{-5} to about 1 X 10^{-3} millidarcy.

4.2 Capillary Pressure Sample Selection

To decide which pairs of samples to use for capillary pressure testing, we looked for two major characteristics; (1) adequate permeability and porosity for testing, and (2) reasonable similarity

between the two samples in each pair as evidenced by the x-ray photos, quantitative XRD, porosity, and permeability data. Based on these criteria, S. Howarth and J. Walls selected the six pairs of samples indicated by asterisks in Table 4.1. After choosing these six samples, axial X-ray CT slices were made at two orientations to get a more detailed picture of the distribution of anhydrite (light) and halite (dark) in each sample. These scans were made with a high energy (420 kV) industrial scanner with a resolution or 0.25 mm. The CT slices for the capillary pressure samples are shown in Figures 4.3 to 4.8. We will refer to the different amounts and distributions of the two major minerals in the discussion of capillary pressure results. More importantly though, is that each sample in a pair is similar to the other, and there does not appear to be any physical damage to the samples on the scale detectable with CT scanning.

4.3 Centrifuge Results

The centrifuge air-decane capillary pressure curves are shown in Figures 4.9 through 4.14. The curves were produced using the Hassler-Brunner method. The initial pressure in each plot is 5 psi and the final pressure is 650 psi. This corresponds to centrifuge rotational speeds from 1720 rpm to 17660 rpm. The starting rotational speed was chosen by the Core Labs based on the experimental procedure which expected high entry pressures relative to most oil and gas reservoir rock. Normally the starting speed would be about 300 RPM to correspond to a pressure of about 1 psi. The ending rotational speed is controlled by the limits of the experimental apparatus.

The Hassler-Brunner results are presented because the critical ratio R_1/R_3 (as shown in Figure 2.3) does not exceed 0.7, a requirement for successful application of this method[9,10,11]. To ensure that errors in this method were small, data reduction was also performed using the Rajan[19] method. The differences between the two in terms of calculated end face saturations were typically less than 1% of pore volume. In these comparisons, the sample pore volume used for data reduction was measured by the CMS-300 at 500 psi net stress, and rounded to the nearest 0.01 cm^3. It should be noted that the fluid volume resolution for this system was about +/- 0.005 cm^3 or about 2.5% of pore volume.

The oil saturation at the lowest capillary pressure of 5 psi varies from about 85% to 95% for the six samples tested. This means that the entry pressure to oil for all samples was less than 5 psi. Final oil saturations at 650 psi ranged from about 11% to 45%. The general appearance of the curves, with the concave downward shape or "knee" at about 80% to 90% liquid saturation suggests a bi-modal or multi-modal pore size distribution. The relatively low value of the final liquid saturation (for all samples except 14) suggests that the samples do not contain a significant amount of microporosity.

4.4 Mercury Injection Results

Mercury injection capillary pressure curves are shown in Figures 4.15 to 4.20. Pore volume for the mercury injection samples was measured by the CMS-300 at 500 psi net confining stress, consistent with the centrifuge pore volumes. The starting pressure for these tests was about 1.5 psi and the final pressure was about 50,000 psi. This provided a more complete capillary pressure curve from 100% wetting phase saturation to final wetting phase saturations which ranged from about 8% to about 23% for the six samples tested. A similar behavior to the centrifuge results in terms of the downward bend in the curve at higher wetting phase saturations was noted. The relatively low final wetting phase saturation is also similar to the centrifuge results. The entry pressure to mercury was defined for these samples by plotting the volume injected versus the injection pressure. There is a sharp break in the slope of this line corresponding to threshold entry pressure. These mercury injection results, converted to the air/brine system, will be discusssed in Section 4.5.

4.5 Comparison and Conversion to Air Water System

Conversion of capillary pressure from one fluid/fluid system to another (i.e. mercury/air to brine/air) is performed using the following equation;

$$P_{c2} = P_{c1}\left(\frac{T_2 \cos\phi_2}{T_1 \cos\phi_1}\right) \qquad (3)$$

where;

P_c = capillary pressure,

T = surface tension, and

ϕ = the contact angle at the fluid/solid interface

subscripts 1 and 2 refer to the different fluid systems.

For the fluids used in this study, we used the values shown in Table 4.5.1[16,21].

Surface Tension and Contact Angle of Experimental Fluid Systems

Fluid System	T (dynes/cm)	ϕ(degrees)
air/decane	24	0
air/brine	72	0
air/Hg	485	140 (180)

The following example shows how air/decane capillary pressure is converted to air/brine using Equation 3.

$$P_{c\,air/brine} = P_{c\,air/decane}\left(\frac{T_{air/brine}\cos\phi_{air/brine}}{T_{air/decane}\cos\phi_{air/decane}}\right) \qquad (4)$$

$$P_{c\,air\,/\,brine} = P_{c\,air\,/\,decane}\left(\frac{72\cos 0}{24\cos 0}\right) = 3\,P_{c\,air\,/\,decane} \qquad (5)$$

This means that to convert air/decane capillary pressures to air/brine we multiply by 3. Similarly, to convert air/Hg to air/brine we divide by 5.16 or 6.74 depending upon whether 140 degrees or 180 degrees respectively is used. The negative sign resulting from the cosine of theta for mercury indicates that the air is the wetting phase and mercury is the non-wetting phase.

Capillary pressure curves for all samples in this project were converted to the air/brine system and are shown in Figures 4.21 through 4.26. The cross-reference between the lab sample numbers used in these figures and the Sandia sample I.D. is in Table 4.1. All capillary pressure samples except 7, 8, 13, and 14 were horizontal plugs. The (A) plots show the comparison using the assumption that theta for air/Hg is 140 degrees, and the (B) plots show the results if 180 degrees is used, as recommended by Good and Mikhail[22]. The effect of assuming contact angle is 140 versus 180 is relatively small, amounting to a difference in converted air-brine capillary pressure of only about 30%. This data does not strongly support one assumption over the other, but for consistency with most literature on the subject, we will focus on the 140 degree contact angle results in this discussion.

For sample pairs 7-8 and 11-12, the wetting phase saturation at 1000 psi equivalent air brine capillary pressure from centrifuge is substantially lower than from mercury injection. The ending saturation from centrifuge is substantially higher than for mercury in samples pairs 13-14 and 23-24. However, the portion of the curve above 50% wetting phase saturation is of greater interest because it is unlikely that water saturation in the Salado formation *in-situ* would ever be less than 50%. In this region, there is remarkably close agreement between the centrifuge and mercury results for all sample pairs except 13-14. Also, we do not expect the curves to match exactly because there are differences between the two samples in each pair as evidenced by the data in Table 4.1 and the CT scans in Figures 4.3 to 4.8. Note that there is no indication in any of this data that the entry pressure to brine ever exceeds about 15 psi. Tabular data for the mercury injection plots is presented in Tables 4.2 to 4.13. Tabular data for the centrifuge capillary pressure is on the plots (Figures 4.9 to 4.14).

The converted brine entry pressure for the samples is considerably lower than would be expected if the samples were tight sandstones with the same permeability. For example, Figure 4.27 shows a plot of entry pressure versus Klinkenberg (intrinsic) permeability for a group of tight gas sands[20], for a compilation of data on oil field rocks[21], and for the MB 139 anhydrite samples in this project.

types of rock are quite different. The thin section results presented in Appendix B show that porosity in the anhydrite sample is so low as to be all but invisible. Porosity in the tight sandstones ranges from about 5 to 15%, and the low permeability is often caused by clay minerals formed in the pores after deposition. The evaporitic nature of these anhydrite samples would suggest that significant differences from shaly clastics could be expected. Therefore, drawing conclusions about the capillary pressure vs. permeability behavior of the anhydrites from experience with sandstones is not recommended.

5.0 Conclusions and Recommendations

Based on these tests, we find several important results concerning porosity, permeability, and capillary pressure in the MB 139 anhydrite samples tested;

1 Porosity ranges from about 0.6 to 2.1 percent and K_a ranges from about 0.026 md to about 0.001 md at 500 psi net stress, as defined by Equation 2.

2 Using Hassler-Brunner versus Rajan data reduction methods for the centrifuge end face saturations make no significant difference, probably because the sample lengths were short enough to keep the ratio of R_1/R_3 below 0.7.

3 Using a contact angle for air/Hg of 180 degrees, as recommended by Good and Mikhail[22], produces converted air/brine capillary pressures that are about 30% lower than if the more commonly assumed angle of 140 degrees is used.

4 Mercury and air/brine capillary pressures match fairly well, especially at the higher wetting phase saturations, and the difference in results between 140 degrees or 180 degrees for contact angle in the air/Hg system is negligible. Based on these six samples, we cannot recommend one contact angle value over the other.

5 Air/brine threshold entry pressures computed from the six Hg injection samples range from about 1 to 4 psi (.007 to 0.028 Mpa). Air/brine threshold entry pressure from the centrifuge tests could not be determined exactly, but the data shows that for all samples the value is less than 15 psi (0.1 MPa).

We recommend that in future work on capillary pressure of the anhydrite, the experimental systems and procedures should be adjusted to more accurately define the low threshold entry pressure

values. For example, centrifuge tests could be started at a lower centrifuge speed and the Hg injection system could be set to measure the range below 1 psi. Also, it would be useful to test some samples using an overburden system to verify the estimated effect of stress on entry pressure.

6.0 References

1 Harbach, F., and H. Nienburg; "Mercury Pressure Porosimetry as an Accessory to the Development of Shaping and Firing Techniques for Dense Ceramic Components," Ceramic Forum International v 64 no. 10, Oct., 1987 p 394-397.

2 Ciftcioglu, M., D. Smith, and S. Ross; "Sintering Studies on Ordered Monodisperse Silica Compacts - Effect of Consolidation," Powder Technology, v 69, No. 2, Feb, 1992, pp 185-193.

3 Gelinas, C., and R. Angens; "Improvement of the Dynamic Water Expulsion Method for Pore Size Distribution Measurements," American Ceramic Society Bulletin, v. 65, No. 9, Sept. 1986, pp 1297-1300.

4 McCullough, J.J., F.W. Albaugh, and P.H. Jones; "Determination of the Interstitial Water Content of Oil and Gas Sand by Laboratory Tests of Core Samples", API Drilling and Production Practice (180), 1944.

5 Thornton, O.F. and D.L. Marshall; "Estimating Interstitial Water by the Capillary Pressure Method," Trans. AIME, Vol. 170, 1947, pp 69-80.

6 Bruce, W.A. and H.G. Welge; "Restored State Method for Determination of Oil in Place and Connate Water," Oil and Gas Journal, Vol. 46, 1947, p 223.

7 Rose, W. and W.A. Bruce; "Evaluation of Capillary Character in Petroleum Reservoir Rock," Trans. AIME Vol. 186, 1949, pp 39-48.

8 Calhoun, J.C, M. Lewis, and R.C. Newman; "Experiments on the Capillary Properties of Porous Solids"; Petr. Trans. AIME, July, 1949, pp 189-196.

9 Hassler, G.L. and E. Brunner; "Measurement of Capillary Pressures in Small Core Samples," Trans., AIME (192), 1945, p 114

10 Christiansen, R.L.; " Geometric Concerns for Accurate Measurement of Capillary Pressure with Centrifuge Methods," SPE Form. Eval., December, 1992, 311-314

11 Melrose, J.C.; "Interpretation of Centrifuge Capillary Pressure Data," The Log Analyst, Jan.-Feb, 1988, pp 40-47.

12 Chen, Zhigang, Huiqing Liu, and Jun Yao; "New Capillary Pressure Models for Parameter Estimation to Interpret Centrifuge Data," SPE paper 24045, presented at the SPE Western Regional Meeting, Bakersfield, CA, March 30- April 1, 1992.

13 Omoregie, Z.S., "Factors Affecting the Equivalency of Different Capillary Pressure Measurement Techniques," SPE paper 15384, presented at the SPE Annual Technical Conference, New Orleans, LA, October 5-8, 1986.

14 Purcell, W.R., Capillary Pressures-Their Measurement Using Mercury Injection and the Calculation of Permeability Therefrom"; Petroleum Trans., AIME, Feb, 1949

15 Melrose, J.C., J.R. Dixon, and J.E. Mallinson, 1991; "Comparison of Different Techniques for Obtaining Capillary Pressure Data in the Low Saturation Region," SPE 22690 presented at the 66th Annual Technical Conference and Exhibition, Dallas, TX, Oct 6-9, 1991.

16 Ward, J.S., and N.R. Morrow; "Capillary Pressure and Gas Relative Permeability of Low Permeability Sandstone," SPE/DOE 13882, presented at the Low Permeability Symposium, Denver, CO, May 19-22, 1985.

17 Walls, J.D. and S. Howarth; "Test Procedures and Quality Assurance Plan: Porosity, Permeability and Capillary Pressure Measurements in Anhydrite Samples from the WIPP," Sandia internal report, May 24, 1993.

18 Core Laboratories; "Operators Manual for CMS-300", by Core Laboratories Inc., Houston, TX, 1988.

19 Rajan, R.R.; "Theoretically Correct Analytical Solution for Calculating Capillary Pressure Curves From Centrifuge Experiments" SPWLA 27th Annual Logging Symposium, Houston, TX, June 9-13, 1986.

20 Walls, J.D., and J.O. Amaefule; "Capillary Pressure and Permeability Relationships in Tight Gas Sands", SPE/DOE 13879, presented at the Low Permeability Gas Reservoirs Symposium, Denver, CO, May, 19-22, 1985.

21 Davies, Peter B., "Evaluation of the Role of Threshold Pressure in Controlling Flow of Waste Generated Gas into Bedded Salt at the Waste Isolation Pilot Plant," Sandia Report Sand90-3246, UC-721, June, 1991.

22 Good, Robert J., and R.S. Mikhail; "The Contact Angle in Mercury Intrusion Porosimetry", Powder Technology, 29, 1981, pp 53-62

Table 4.1: Porosity and Air Permeability at Three Net Confining Stresses

Core Lab ID	Sandia ID	Net Stress psi	Gr. Dens. g/cc	Porosity %	Klinkenberg Perm., md	Cap. Press. Method
1	E1X 10-6 / 4.5A	500	2.637	0.6		
		870				
		1450				
2	E1X 10-6 / 4.5B	500	2.587	0.8	0.000647	
		870		0.7	0.000462	
		1450			0.000278	
3	E1X 10-6 / 5.0A	500	2.489	0.8		
		870				
		1450				
4	E1X 10-6 / 5.0B	500	2.624	0.9	0.001278	
		870		0.9	0.000880	
		1450			0.000646	
5*	E1X 10-6 / 5.25A	500	2.620	0.7	0.000513	Merc. Inject.
		870		0.6	0.000381	
		1450			0.000180	
6*	E1X 10-6 / 5.25B	500	2.617	0.7	0.000581	Centrifuge
		870			0.000297	
		1450			0.000050	
7*	E1X 10-6 / 5.25C1	500	2.953	1.1	0.000948	Merc. Inject.
		870		1.0	0.000549	
		1450				
8*	E1X 10-6 / 5.25C2	500	2.955	1.1	0.000822	Centrifuge
		870		1.0	0.000488	
		1450			0.000138	
9	E1X 10-6 / 5.5A	500	2.848	0.9	0.000535	
		870				
		1450				
10	E1X 10-6 / 5.5B	500	2.943	1.0	0.001083	
		870			0.000176	
		1450				
11*	E1X 10-6 / 5.75A	500	2.888	1.7	0.001804	Merc. Inject.
		870		1.7	0.001559	
		1450		1.6	0.001138	
12*	E1X 10-6 / 5.75B	500	2.923	1.4	0.001364	Centrifuge
		870		1.3	0.001016	
		1450			0.000734	
13*	E1X 10-6 /5.75C1	500	2.960	1.6	0.001622	Merc. Inject.
		870		1.5	0.000308	
		1450		1.5		
14*	E1X 10-6 / 5.75C2	500	2.946	1.2	0.000611	
		870		1.1	0.000311	
		1450			0.000172	
15	E1X 10-7 / 6.25C1	500	2.962	1.0	0.000594	
		870		0.9	0.000128	
		1450			0.000064	

Table 4.1: Porosity and Air Permeability at Three Net Confining Stresses

Lab ID	Sandia ID	(Continued) Net Stress	Gr. Dens.	Porosity	Kl	Cap. Press.
		psi	g/cc	%	md	Method
16	E1X 10-7 / 6.25C2	500	2.961	0.6	0.000439	
		870				
		1450				
17	E1X 11-6 / 4.5A	500	2.628	0.8	0.000407	
		870			0.000337	
		1450			0.000101	
18	E1X 11-6 / 4.5B	500	2.630	1.8		
		870				
		1450				
19	E1X 11-6 / 4.75A	500	2.719	0.9	0.000474	
		870			0.000323	
		1450			0.000101	
20	E1X 11-6 / 4.75B	500	2.795	0.9	0.000393	
		870		0.8		
		1450				
21*	E1X 11-6 / 5.0A	500	2.822	1.1	0.000767	Merc. Inject.
		870		1.0	0.000566	
		1450			0.000265	
22*	E1X 11-6 / 5.0B	500	2.690	1.4	0.001482	Centrifuge
		870		1.3	0.000843	
		1450				
23*	E1X 11-6 / 5.25A	500	2.650	2.1	0.001313	Merc. Inject.
		870			0.000585	
		1450				
24*	E1X 11-6 / 5.25B	500	2.674	1.4	0.001515	Centrifuge
		870		1.4	0.000569	
		1450				
25	E1X 11-6 / 5.25C1	500	2.613	0.9	0.001996	
		870		0.8	0.000563	
		1450			0.000293	
26	E1X 11-6 / 5.25C2	500	2.742	1.6	0.002189	
		870			0.000747	
		1450			0.000333	
27	E1X 11-6 / 5.75A	500	2.750	1.6		
		870		1.4		
		1450		1.2		
28	E1X 11-6 / 5.75B	500	2.906			
		870				
		1450				
29	E1X 11-6 / 5.75C1	500	2.959	0.8		
		870				
		1450				
30	E1X 11-6 / 5.75C2	500	2.961	1.0	0.001458	
		870			0.000590	
		1450				

* Indicates capillary pressure sample

TABLE 4.2
MERCURY INJECTION DATA SUMMARY

Sandia National Laboratories
Waste Isolation Pilot Plant
Core: E1X 10-6

Sample Number 5
File: DAL-93089

Contact Angle = 140

Injection Pressure, psia	Mercury Saturation, fraction	1.0-Mercury Saturation, fraction	Other Laboratory Systems		
			Gas-Water, psia	Gas-Oil, psia	Oil-Water, psia
1.5	0.000	1.000	0.30	0.10	0.17
3.0	0.000	1.000	0.58	0.19	0.33
6.0	0.000	1.000	1.2	0.39	0.67
9.0	0.000	1.000	1.7	0.58	1.0
12	0.040	0.960	2.3	0.77	1.3
18	0.040	0.960	3.5	1.2	2.0
25	0.080	0.920	4.8	1.6	2.8
35	0.080	0.920	6.8	2.3	3.9
45	0.120	0.880	8.7	2.9	5.0
55	0.120	0.880	11	3.5	6.1
75	0.120	0.880	14	4.8	8.4
100	0.120	0.880	19	6.5	11
124	0.160	0.840	24	8.0	14
159	0.160	0.840	31	10	18
181	0.160	0.840	35	12	20
200	0.160	0.840	39	13	22
304	0.200	0.800	59	20	34
398	0.200	0.800	77	26	45
499	0.240	0.760	97	32	56
749	0.320	0.680	145	48	84
997	0.400	0.600	193	64	112
1252	0.440	0.560	243	81	140
1603	0.559	0.441	311	104	179
1996	0.599	0.401	387	129	223
2497	0.599	0.401	484	161	279
3489	0.639	0.361	676	225	390
4255	0.639	0.361	825	275	476
4998	0.679	0.321	968	323	559
6973	0.719	0.281	1351	450	780
9965	0.719	0.281	1931	644	1115
12465	0.759	0.241	2416	805	1395
14950	0.839	0.161	2897	966	1673
19920	0.879	0.121	3860	1287	2229
24925	0.879	0.121	4830	1610	2789
29905	0.879	0.121	5795	1932	3346
34908	0.919	0.081	6765	2255	3906
39861	0.919	0.081	7725	2575	4460
44935	0.919	0.081	8708	2903	5028
49759	0.919	0.081	9643	3214	5567

TABLE 4.3

MERCURY INJECTION DATA SUMMARY

Sandia National Laboratories
Waste Isolation Pilot Plant
Core: E1X 10-6

Sample Number 5
File: DAL-93089

Contact Angle = 180

Injection Pressure, psia	Mercury Saturation, fraction	1.0-Mercury Saturation, fraction	Other Laboratory Systems		
			Gas-Water, psia	Gas-Oil, psia	Oil-Water, psia
1.5	0.000	1.000	0.23	0.08	0.13
3.0	0.000	1.000	0.44	0.15	0.26
6.0	0.000	1.000	0.89	0.30	0.51
9.0	0.000	1.000	1.3	0.44	0.77
12	0.040	0.960	1.8	0.59	1.0
18	0.040	0.960	2.7	0.89	1.5
25	0.080	0.920	3.7	1.2	2.1
35	0.080	0.920	5.2	1.7	3.0
45	0.120	0.880	6.7	2.2	3.8
55	0.120	0.880	8.2	2.7	4.7
75	0.120	0.880	11	3.7	6.4
100	0.120	0.880	15	4.9	8.6
124	0.160	0.840	18	6.2	11
159	0.160	0.840	24	7.9	14
181	0.160	0.840	27	9.0	16
200	0.160	0.840	30	9.9	17
304	0.200	0.800	45	15	26
398	0.200	0.800	59	20	34
499	0.240	0.760	74	25	43
749	0.320	0.680	111	37	64
997	0.400	0.600	148	49	85
1252	0.440	0.560	186	62	107
1603	0.559	0.441	238	79	137
1996	0.599	0.401	296	99	171
2497	0.599	0.401	371	124	214
3489	0.639	0.361	518	173	299
4255	0.639	0.361	632	211	365
4998	0.679	0.321	742	247	428
6973	0.719	0.281	1035	345	598
9965	0.719	0.281	1479	493	854
12465	0.759	0.241	1850	617	1068
14950	0.839	0.161	2219	740	1281
19920	0.879	0.121	2957	986	1707
24925	0.879	0.121	3700	1233	2136
29905	0.879	0.121	4440	1480	2563
34908	0.919	0.081	5182	1727	2992
39861	0.919	0.081	5917	1972	3416
44935	0.919	0.081	6671	2224	3851
49759	0.919	0.081	7387	2462	4265

TABLE 4.4
MERCURY INJECTION DATA SUMMARY

Sandia National Laboratories
Waste Isolation Pilot Plant
Core: E1X 10-6

Sample Number 7
File: DAL-93089

Contact Angle = 140

Injection Pressure, psia	Mercury Saturation, fraction	1.0-Mercury Saturation, fraction	Other Laboratory Systems		
			Gas-Water, psia	Gas-Oil, psia	Oil-Water, psia
1.5	0.000	1.000	0.29	0.10	0.17
3.0	0.000	1.000	0.58	0.19	0.34
6.0	0.000	1.000	1.2	0.39	0.67
9.0	0.000	1.000	1.7	0.58	1.0
12	0.026	0.974	2.3	0.77	1.3
18	0.026	0.974	3.5	1.2	2.0
25	0.052	0.948	4.8	1.6	2.8
35	0.078	0.922	6.8	2.3	3.9
45	0.078	0.922	8.7	2.9	5.0
55	0.078	0.922	11	3.6	6.2
75	0.104	0.896	15	4.9	8.4
101	0.104	0.896	20	6.5	11
126	0.130	0.870	24	8.1	14
161	0.130	0.870	31	10	18
179	0.130	0.870	35	12	20
200	0.130	0.870	39	13	22
300	0.156	0.844	58	19	34
402	0.182	0.818	78	26	45
500	0.208	0.792	97	32	56
753	0.234	0.766	146	49	84
1007	0.260	0.740	195	65	113
1246	0.286	0.714	241	80	139
1598	0.338	0.662	310	103	179
1993	0.390	0.610	386	129	223
2495	0.442	0.558	483	161	279
3493	0.494	0.506	677	226	391
4247	0.546	0.454	823	274	475
4978	0.597	0.403	965	322	557
6985	0.649	0.351	1354	451	782
9976	0.701	0.299	1933	644	1116
12443	0.753	0.247	2411	804	1392
14932	0.805	0.195	2894	965	1671
19941	0.857	0.143	3864	1288	2231
24900	0.857	0.143	4825	1608	2786
29876	0.857	0.143	5790	1930	3343
34873	0.883	0.117	6758	2253	3902
39853	0.883	0.117	7723	2574	4459
44917	0.883	0.117	8705	2902	5026
49965	0.883	0.117	9683	3228	5590

TABLE 4.5
MERCURY INJECTION DATA SUMMARY

Sandia National Laboratories
Waste Isolation Pilot Plant
Core: E1X 10-6

Sample Number 7
File: DAL-93089

Contact Angle = 180

Injection Pressure, psia	Mercury Saturation, fraction	1.0-Mercury Saturation, fraction	Other Laboratory Systems		
			Gas-Water, psia	Gas-Oil, psia	Oil-Water, psia
1.5	0.000	1.000	0.23	0.08	0.13
3.0	0.000	1.000	0.45	0.15	0.26
6.0	0.000	1.000	0.89	0.30	0.51
9.0	0.000	1.000	1.3	0.44	0.77
12	0.026	0.974	1.8	0.59	1.0
18	0.026	0.974	2.7	0.89	1.5
25	0.052	0.948	3.7	1.2	2.1
35	0.078	0.922	5.2	1.7	3.0
45	0.078	0.922	6.7	2.2	3.9
55	0.078	0.922	8.2	2.7	4.7
75	0.104	0.896	11	3.7	6.4
101	0.104	0.896	15	5.0	8.6
126	0.130	0.870	19	6.2	11
161	0.130	0.870	24	7.9	14
179	0.130	0.870	27	8.9	15
200	0.130	0.870	30	9.9	17
300	0.156	0.844	45	15	26
402	0.182	0.818	60	20	34
500	0.208	0.792	74	25	43
753	0.234	0.766	112	37	65
1007	0.260	0.740	149	50	86
1246	0.286	0.714	185	62	107
1598	0.338	0.662	237	79	137
1993	0.390	0.610	296	99	171
2495	0.442	0.558	370	123	214
3493	0.494	0.506	519	173	299
4247	0.546	0.454	631	210	364
4978	0.597	0.403	739	246	427
6985	0.649	0.351	1037	346	599
9976	0.701	0.299	1481	494	855
12443	0.753	0.247	1847	616	1067
14932	0.805	0.195	2217	739	1280
19941	0.857	0.143	2960	987	1709
24900	0.857	0.143	3696	1232	2134
29876	0.857	0.143	4435	1478	2561
34873	0.883	0.117	5177	1726	2989
39853	0.883	0.117	5916	1972	3416
44917	0.883	0.117	6668	2223	3850
49965	0.883	0.117	7417	2472	4282

TABLE 4.6
MERCURY INJECTION DATA SUMMARY

Sandia National Laboratories
Waste Isolation Pilot Plant
Core: E1X 10-6

Sample Number 11
File: DAL-93089

Contact Angle = 140

Injection Pressure, psia	Mercury Saturation, fraction	1.0-Mercury Saturation, fraction	Other Laboratory Systems		
			Gas-Water, psia	Gas-Oil, psia	Oil-Water, psia
1.5	0.000	1.000	0.30	0.10	0.17
3.0	0.000	1.000	0.58	0.19	0.33
6.0	0.000	1.000	1.2	0.39	0.67
9.0	0.000	1.000	1.7	0.58	1.0
12	0.000	1.000	2.3	0.77	1.3
18	0.016	0.984	3.5	1.2	2.0
25	0.016	0.984	4.8	1.6	2.8
35	0.032	0.968	6.8	2.3	3.9
45	0.032	0.968	8.7	2.9	5.0
55	0.032	0.968	11	3.6	6.2
75	0.032	0.968	15	4.8	8.4
100	0.032	0.968	19	6.5	11
125	0.032	0.968	24	8.0	14
159	0.048	0.952	31	10	18
181	0.064	0.936	35	12	20
200	0.079	0.921	39	13	22
304	0.143	0.857	59	20	34
398	0.191	0.809	77	26	45
499	0.207	0.793	97	32	56
749	0.271	0.729	145	48	84
997	0.335	0.665	193	64	112
1251	0.382	0.618	242	81	140
1603	0.430	0.570	311	104	179
1995	0.494	0.506	387	129	223
2497	0.590	0.410	484	161	279
3488	0.590	0.410	676	225	390
4254	0.621	0.379	824	275	476
4997	0.637	0.363	968	323	559
6972	0.669	0.331	1351	450	780
9964	0.701	0.299	1931	644	1115
12464	0.717	0.283	2415	805	1395
14949	0.717	0.283	2897	966	1673
19919	0.733	0.267	3860	1287	2229
24924	0.749	0.251	4830	1610	2789
29904	0.765	0.235	5795	1932	3346
34907	0.765	0.235	6765	2255	3906
39860	0.765	0.235	7725	2575	4460
44934	0.765	0.235	8708	2903	5028
49758	0.765	0.235	9643	3214	5567

TABLE 4.7
MERCURY INJECTION DATA SUMMARY

Sandia National Laboratories
Waste Isolation Pilot Plant
Core: E1X 10-6

Sample Number 11
File: DAL-93089

Contact Angle = 180

Injection Pressure, psia	Mercury Saturation, fraction	1.0-Mercury Saturation, fraction	Other Laboratory Systems		
			Gas-Water, psia	Gas-Oil, psia	Oil-Water, psia
1.5	0.000	1.000	0.23	0.08	0.13
3.0	0.000	1.000	0.44	0.15	0.26
6.0	0.000	1.000	0.89	0.30	0.51
9.0	0.000	1.000	1.3	0.44	0.77
12	0.000	1.000	1.8	0.59	1.0
18	0.016	0.984	2.7	0.89	1.5
25	0.016	0.984	3.7	1.2	2.1
35	0.032	0.968	5.2	1.7	3.0
45	0.032	0.968	6.7	2.2	3.9
55	0.032	0.968	8.2	2.7	4.7
75	0.032	0.968	11	3.7	6.4
100	0.032	0.968	15	5.0	8.6
125	0.032	0.968	18	6.2	11
159	0.048	0.952	24	7.9	14
181	0.064	0.936	27	9.0	16
200	0.079	0.921	30	9.9	17
304	0.143	0.857	45	15	26
398	0.191	0.809	59	20	34
499	0.207	0.793	74	25	43
749	0.271	0.729	111	37	64
997	0.335	0.665	148	49	85
1251	0.382	0.618	186	62	107
1603	0.430	0.570	238	79	137
1995	0.494	0.506	296	99	171
2497	0.590	0.410	371	124	214
3488	0.590	0.410	518	173	299
4254	0.621	0.379	632	211	365
4997	0.637	0.363	742	247	428
6972	0.669	0.331	1035	345	598
9964	0.701	0.299	1479	493	854
12464	0.717	0.283	1850	617	1068
14949	0.717	0.283	2219	740	1281
19919	0.733	0.267	2957	986	1707
24924	0.749	0.251	3700	1233	2136
29904	0.765	0.235	4439	1480	2563
34907	0.765	0.235	5182	1727	2992
39860	0.765	0.235	5917	1972	3416
44934	0.765	0.235	6671	2224	3851
49758	0.765	0.235	7387	2462	4265

TABLE 4.8
MERCURY INJECTION DATA SUMMARY

Sandia National Laboratories
Waste Isolation Pilot Plant
Core: E1X 10-6

Sample Number 13
File: DAL-93089

Contact Angle = 140

Injection Pressure, psia	Mercury Saturation, fraction	1.0-Mercury Saturation, fraction	Other Laboratory Systems		
			Gas-Water, psia	Gas-Oil, psia	Oil-Water, psia
1.5	0.000	1.000	0.29	0.10	0.17
3.0	0.000	1.000	0.58	0.19	0.34
6.0	0.018	0.982	1.2	0.39	0.67
9.0	0.036	0.964	1.7	0.58	1.0
12	0.036	0.964	2.3	0.77	1.3
18	0.036	0.964	3.5	1.2	2.0
25	0.073	0.927	4.8	1.6	2.8
35	0.073	0.927	6.8	2.3	3.9
45	0.073	0.927	8.7	2.9	5.0
55	0.091	0.909	11	3.6	6.2
75	0.091	0.909	15	4.8	8.4
100	0.091	0.909	19	6.4	11
125	0.091	0.909	24	8.1	14
160	0.127	0.873	31	10	18
180	0.145	0.855	35	12	20
200	0.145	0.855	39	13	22
300	0.218	0.782	58	19	34
400	0.236	0.764	77	26	45
498	0.254	0.746	96	32	56
746	0.291	0.709	145	48	84
996	0.345	0.655	193	64	111
1246	0.382	0.618	241	80	139
1593	0.418	0.582	309	103	178
1994	0.509	0.491	386	129	223
2490	0.600	0.400	483	161	279
3493	0.600	0.400	677	226	391
4247	0.600	0.400	823	274	475
4991	0.636	0.364	967	322	558
6972	0.672	0.328	1351	450	780
9972	0.708	0.292	1932	644	1116
12476	0.745	0.255	2418	806	1396
14944	0.799	0.201	2896	965	1672
19933	0.799	0.201	3863	1288	2230
24903	0.836	0.164	4826	1609	2786
29899	0.836	0.164	5794	1931	3345
34832	0.836	0.164	6750	2250	3897
39825	0.854	0.146	7718	2573	4456
44921	0.854	0.146	8705	2902	5026
49791	0.854	0.146	9649	3216	5571

TABLE 4.9
MERCURY INJECTION DATA SUMMARY

Sandia National Laboratories
Waste Isolation Pilot Plant
Core: E1X 10-6

Sample Number 13
File: DAL-93089

Contact Angle = 180

Injection Pressure, psia	Mercury Saturation, fraction	1.0-Mercury Saturation, fraction	Other Laboratory Systems		
			Gas-Water, psia	Gas-Oil, psia	Oil-Water, psia
1.5	0.000	1.000	0.23	0.08	0.13
3.0	0.000	1.000	0.45	0.15	0.26
6.0	0.018	0.982	0.89	0.30	0.51
9.0	0.036	0.964	1.3	0.44	0.77
12	0.036	0.964	1.8	0.59	1.0
18	0.036	0.964	2.7	0.89	1.5
25	0.073	0.927	3.7	1.2	2.1
35	0.073	0.927	5.2	1.7	3.0
45	0.073	0.927	6.7	2.2	3.9
55	0.091	0.909	8.2	2.7	4.7
75	0.091	0.909	11	3.7	6.4
100	0.091	0.909	15	4.9	8.5
125	0.091	0.909	19	6.2	11
160	0.127	0.873	24	7.9	14
180	0.145	0.855	27	8.9	15
200	0.145	0.855	30	9.9	17
300	0.218	0.782	44	15	26
400	0.236	0.764	59	20	34
498	0.254	0.746	74	25	43
746	0.291	0.709	111	37	64
996	0.345	0.655	148	49	85
1246	0.382	0.618	185	62	107
1593	0.418	0.582	236	79	137
1994	0.509	0.491	296	99	171
2490	0.600	0.400	370	123	213
3493	0.600	0.400	519	173	299
4247	0.600	0.400	631	210	364
4991	0.636	0.364	741	247	428
6972	0.672	0.328	1035	345	598
9972	0.708	0.292	1480	493	855
12476	0.745	0.255	1852	617	1069
14944	0.799	0.201	2218	739	1281
19933	0.799	0.201	2959	986	1708
24903	0.836	0.164	3697	1232	2134
29899	0.836	0.164	4439	1480	2563
34832	0.836	0.164	5171	1724	2985
39825	0.854	0.146	5912	1971	3413
44921	0.854	0.146	6669	2223	3850
49791	0.854	0.146	7392	2464	4268

TABLE 4.10
MERCURY INJECTION DATA SUMMARY

Sandia National Laboratories
Waste Isolation Pilot Plant
Core: E1X 11-6

Sample Number 21
File: DAL-93089

Contact Angle = 140

Injection Pressure, psia	Mercury Saturation, fraction	1.0-Mercury Saturation, fraction	Other Laboratory Systems		
			Gas-Water, psia	Gas-Oil, psia	Oil-Water, psia
1.5	0.000	1.000	0.29	0.10	0.17
3.0	0.000	1.000	0.58	0.19	0.34
6.0	0.000	1.000	1.2	0.39	0.67
9.0	0.026	0.974	1.7	0.58	1.0
12	0.026	0.974	2.3	0.77	1.3
18	0.051	0.949	3.5	1.2	2.0
25	0.051	0.949	4.8	1.6	2.8
35	0.051	0.949	6.7	2.2	3.9
45	0.051	0.949	8.7	2.9	5.0
55	0.051	0.949	11	3.6	6.2
75	0.051	0.949	15	4.8	8.4
99	0.077	0.923	19	6.4	11
125	0.077	0.923	24	8.1	14
160	0.077	0.923	31	10	18
180	0.077	0.923	35	12	20
200	0.077	0.923	39	13	22
300	0.127	0.873	58	19	34
400	0.178	0.822	78	26	45
498	0.229	0.771	96	32	56
746	0.357	0.643	145	48	84
996	0.433	0.567	193	64	111
1246	0.484	0.516	241	80	139
1593	0.560	0.440	309	103	178
1994	0.662	0.338	386	129	223
2490	0.662	0.338	483	161	279
3494	0.713	0.287	677	226	391
4248	0.738	0.262	823	274	475
4992	0.738	0.262	967	322	558
6972	0.789	0.211	1351	450	780
9972	0.815	0.185	1932	644	1116
12476	0.840	0.160	2418	806	1396
14944	0.866	0.134	2896	965	1672
19933	0.891	0.109	3863	1288	2230
24909	0.891	0.109	4827	1609	2787
29899	0.891	0.109	5794	1931	3345
34832	0.917	0.083	6750	2250	3897
39826	0.917	0.083	7718	2573	4456
44921	0.917	0.083	8705	2902	5026
49791	0.917	0.083	9649	3216	5571

TABLE 4.11
MERCURY INJECTION DATA SUMMARY

Sandia National Laboratories
Waste Isolation Pilot Plant
Core: E1X 11-6

Sample Number 21
File: DAL-93089

Contact Angle = 180

Injection Pressure, psia	Mercury Saturation, fraction	1.0-Mercury Saturation, fraction	Other Laboratory Systems		
			Gas-Water, psia	Gas-Oil, psia	Oil-Water, psia
1.5	0.000	1.000	0.23	0.08	0.13
3.0	0.000	1.000	0.45	0.15	0.26
6.0	0.000	1.000	0.89	0.30	0.51
9.0	0.026	0.974	1.3	0.44	0.77
12	0.026	0.974	1.8	0.59	1.0
18	0.051	0.949	2.7	0.89	1.5
25	0.051	0.949	3.7	1.2	2.1
35	0.051	0.949	5.2	1.7	3.0
45	0.051	0.949	6.7	2.2	3.8
55	0.051	0.949	8.2	2.7	4.7
75	0.051	0.949	11	3.7	6.4
99	0.077	0.923	15	4.9	8.5
125	0.077	0.923	19	6.2	11
160	0.077	0.923	24	7.9	14
180	0.077	0.923	27	8.9	15
200	0.077	0.923	30	9.9	17
300	0.127	0.873	44	15	26
400	0.178	0.822	59	20	34
498	0.229	0.771	74	25	43
746	0.357	0.643	111	37	64
996	0.433	0.567	148	49	85
1246	0.484	0.516	185	62	107
1593	0.560	0.440	236	79	137
1994	0.662	0.338	296	99	171
2490	0.662	0.338	370	123	213
3494	0.713	0.287	519	173	299
4248	0.738	0.262	631	210	364
4992	0.738	0.262	741	247	428
6972	0.789	0.211	1035	345	598
9972	0.815	0.185	1480	493	855
12476	0.840	0.160	1852	617	1069
14944	0.866	0.134	2218	739	1281
19933	0.891	0.109	2959	986	1708
24909	0.891	0.109	3698	1233	2135
29899	0.891	0.109	4439	1480	2563
34832	0.917	0.083	5171	1724	2985
39826	0.917	0.083	5912	1971	3413
44921	0.917	0.083	6669	2223	3850
49791	0.917	0.083	7392	2464	4268

TABLE 4.12
MERCURY INJECTION DATA SUMMARY

Sandia National Laboratories
Waste Isolation Pilot Plant
Core: E1X 11-6

Sample Number 23
File: DAL-93089

Contact Angle = 140

Injection Pressure, psia	Mercury Saturation, fraction	1.0-Mercury Saturation, fraction	Other Laboratory Systems		
			Gas-Water, psia	Gas-Oil, psia	Oil-Water, psia
1.5	0.000	1.000	0.29	0.10	0.17
3.0	0.000	1.000	0.58	0.19	0.34
6.0	0.000	1.000	1.2	0.39	0.67
9.0	0.025	0.975	1.7	0.58	1.0
12	0.025	0.975	2.3	0.77	1.3
18	0.025	0.975	3.5	1.2	2.0
25	0.037	0.963	4.8	1.6	2.8
35	0.062	0.938	6.8	2.3	3.9
45	0.062	0.938	8.7	2.9	5.0
55	0.062	0.938	11	3.6	6.2
75	0.062	0.938	15	4.9	8.4
101	0.075	0.925	20	6.5	11
125	0.075	0.925	24	8.0	14
161	0.087	0.913	31	10	18
179	0.087	0.913	35	12	20
200	0.099	0.901	39	13	22
300	0.124	0.876	58	19	34
401	0.199	0.801	78	26	45
500	0.261	0.739	97	32	56
753	0.385	0.615	146	49	84
1006	0.484	0.516	195	65	113
1245	0.558	0.442	241	80	139
1597	0.658	0.342	309	103	179
1991	0.732	0.268	386	129	223
2493	0.806	0.194	483	161	279
3491	0.868	0.132	677	226	391
4246	0.881	0.119	823	274	475
4976	0.893	0.107	964	321	557
6984	0.893	0.107	1353	451	781
9974	0.893	0.107	1933	644	1116
12442	0.906	0.094	2411	804	1392
14931	0.906	0.094	2894	965	1671
19940	0.906	0.094	3864	1288	2231
24898	0.918	0.082	4825	1608	2786
29874	0.918	0.082	5789	1930	3343
34871	0.918	0.082	6758	2253	3902
39851	0.918	0.082	7723	2574	4459
44916	0.918	0.082	8704	2901	5025
49963	0.918	0.082	9682	3227	5590

TABLE 4.13
MERCURY INJECTION DATA SUMMARY

Sandia National Laboratories
Waste Isolation Pilot Plant
Core: E1X 11-6

Sample Number 23
File: DAL-93089

Contact Angle = 180

Injection Pressure, psia	Mercury Saturation, fraction	1.0-Mercury Saturation, fraction	Other Laboratory Systems		
			Gas-Water, psia	Gas-Oil, psia	Oil-Water, psia
1.5	0.000	1.000	0.23	0.08	0.13
3.0	0.000	1.000	0.45	0.15	0.26
6.0	0.000	1.000	0.89	0.30	0.51
9.0	0.025	0.975	1.3	0.44	0.77
12	0.025	0.975	1.8	0.59	1.0
18	0.025	0.975	2.7	0.89	1.5
25	0.037	0.963	3.7	1.2	2.1
35	0.062	0.938	5.2	1.7	3.0
45	0.062	0.938	6.7	2.2	3.9
55	0.062	0.938	8.2	2.7	4.7
75	0.062	0.938	11	3.7	6.4
101	0.075	0.925	15	5.0	8.6
125	0.075	0.925	18	6.2	11
161	0.087	0.913	24	7.9	14
179	0.087	0.913	27	8.9	15
200	0.099	0.901	30	9.9	17
300	0.124	0.876	45	15	26
401	0.199	0.801	60	20	34
500	0.261	0.739	74	25	43
753	0.385	0.615	112	37	65
1006	0.484	0.516	149	50	86
1245	0.558	0.442	185	62	107
1597	0.658	0.342	237	79	137
1991	0.732	0.268	296	99	171
2493	0.806	0.194	370	123	214
3491	0.868	0.132	518	173	299
4246	0.881	0.119	630	210	364
4976	0.893	0.107	739	246	427
6984	0.893	0.107	1037	346	599
9974	0.893	0.107	1481	494	855
12442	0.906	0.094	1847	616	1066
14931	0.906	0.094	2217	739	1280
19940	0.906	0.094	2960	987	1709
24898	0.918	0.082	3696	1232	2134
29874	0.918	0.082	4435	1478	2561
34871	0.918	0.082	5177	1726	2989
39851	0.918	0.082	5916	1972	3416
44916	0.918	0.082	6668	2223	3850
49963	0.918	0.082	7417	2472	4282

Figure 4.1: Distribution of Grain Densities in 1 Inch Diameter Sample Set

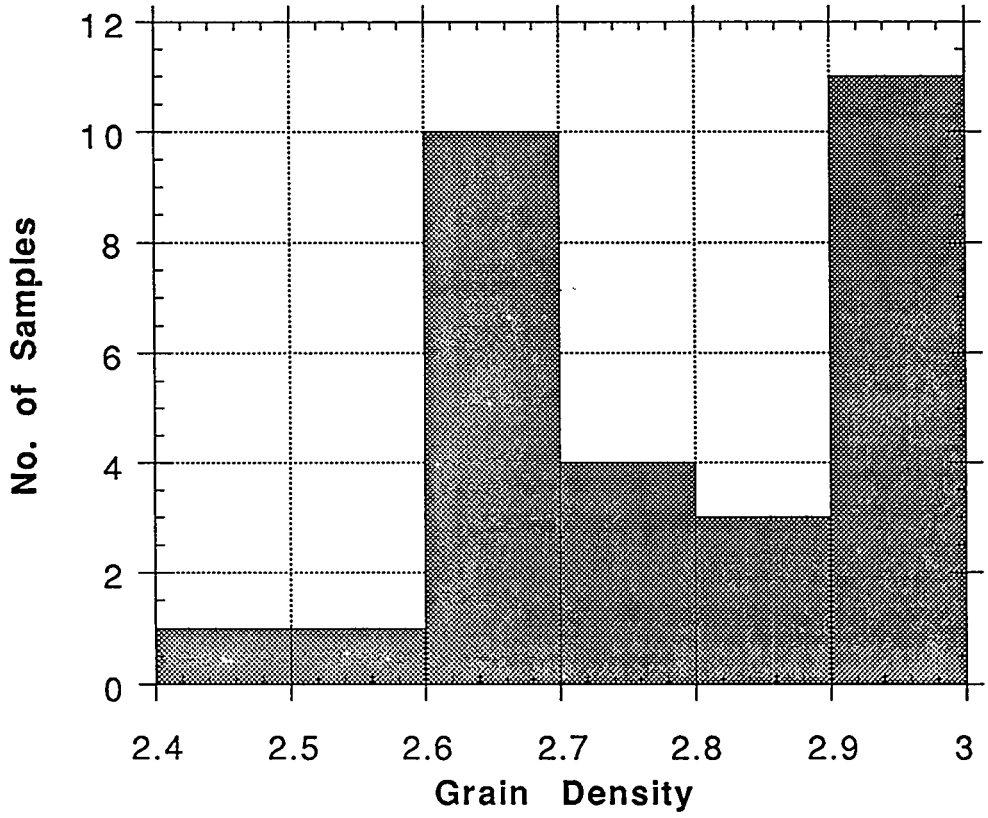

Fig 4.2: Gas Permeability (Kl) vs. Porosity, 1" Samples

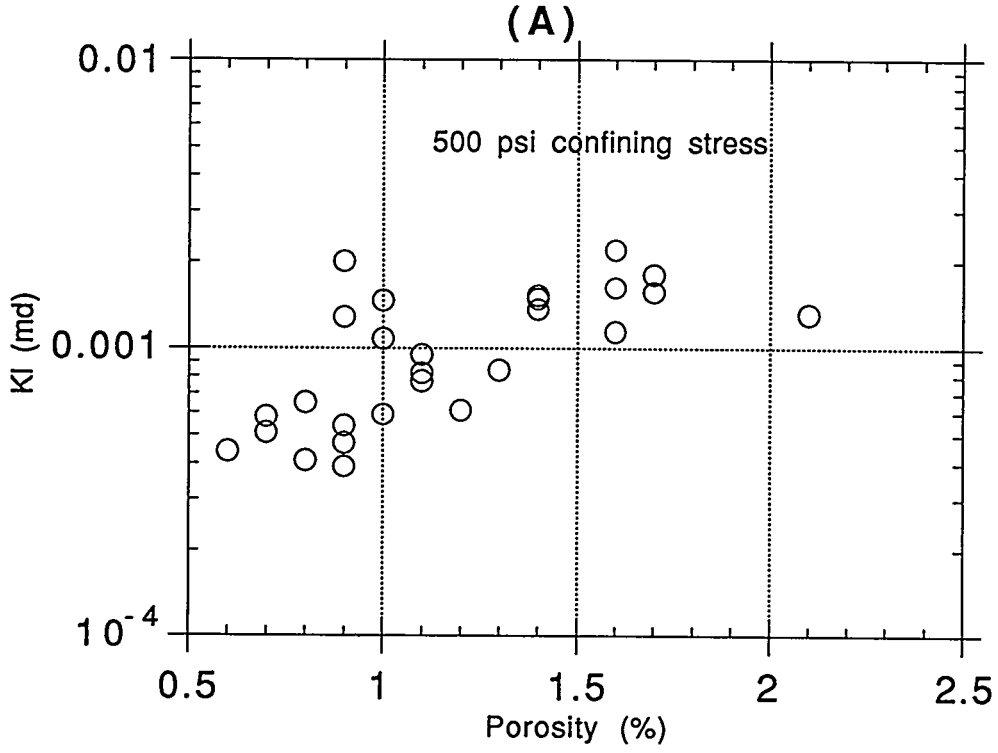

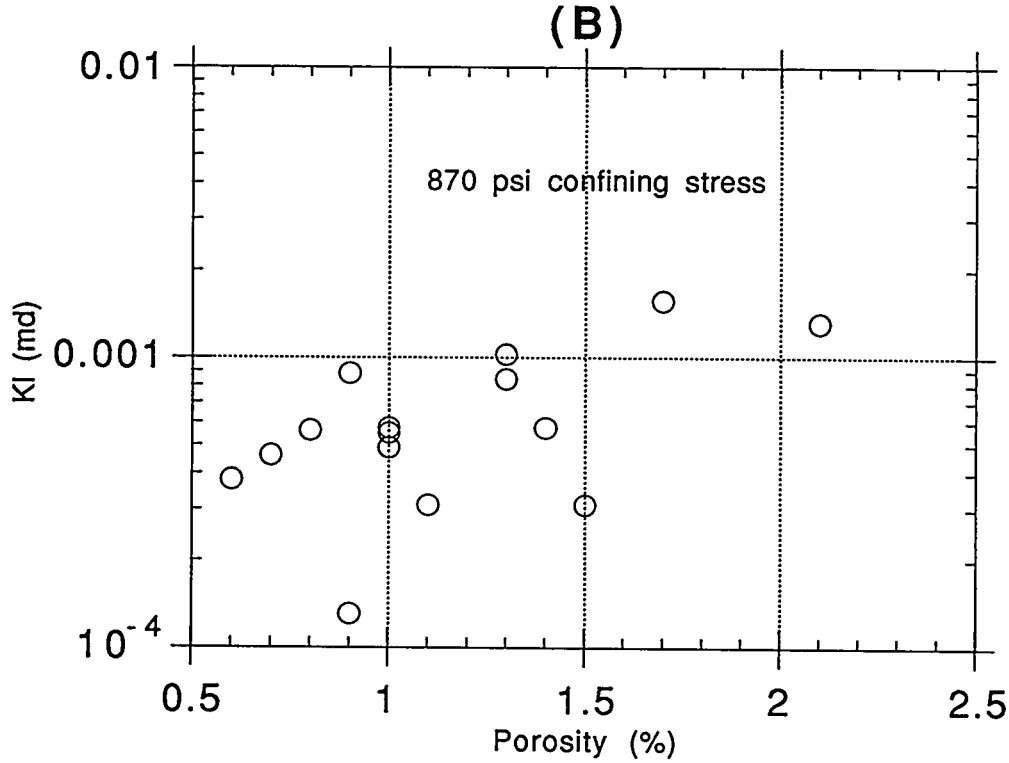

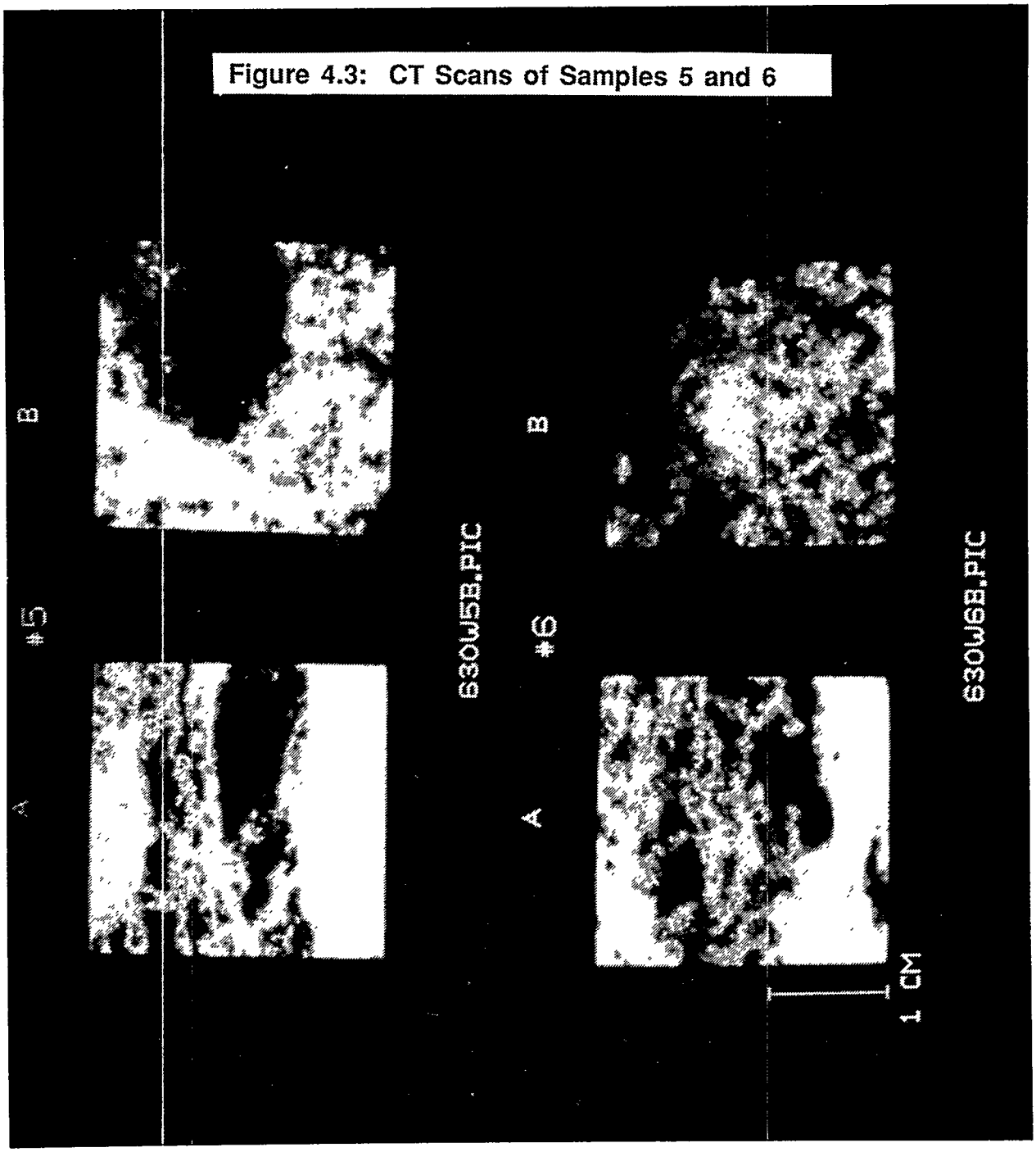

Figure 4.3: CT Scans of Samples 5 and 6

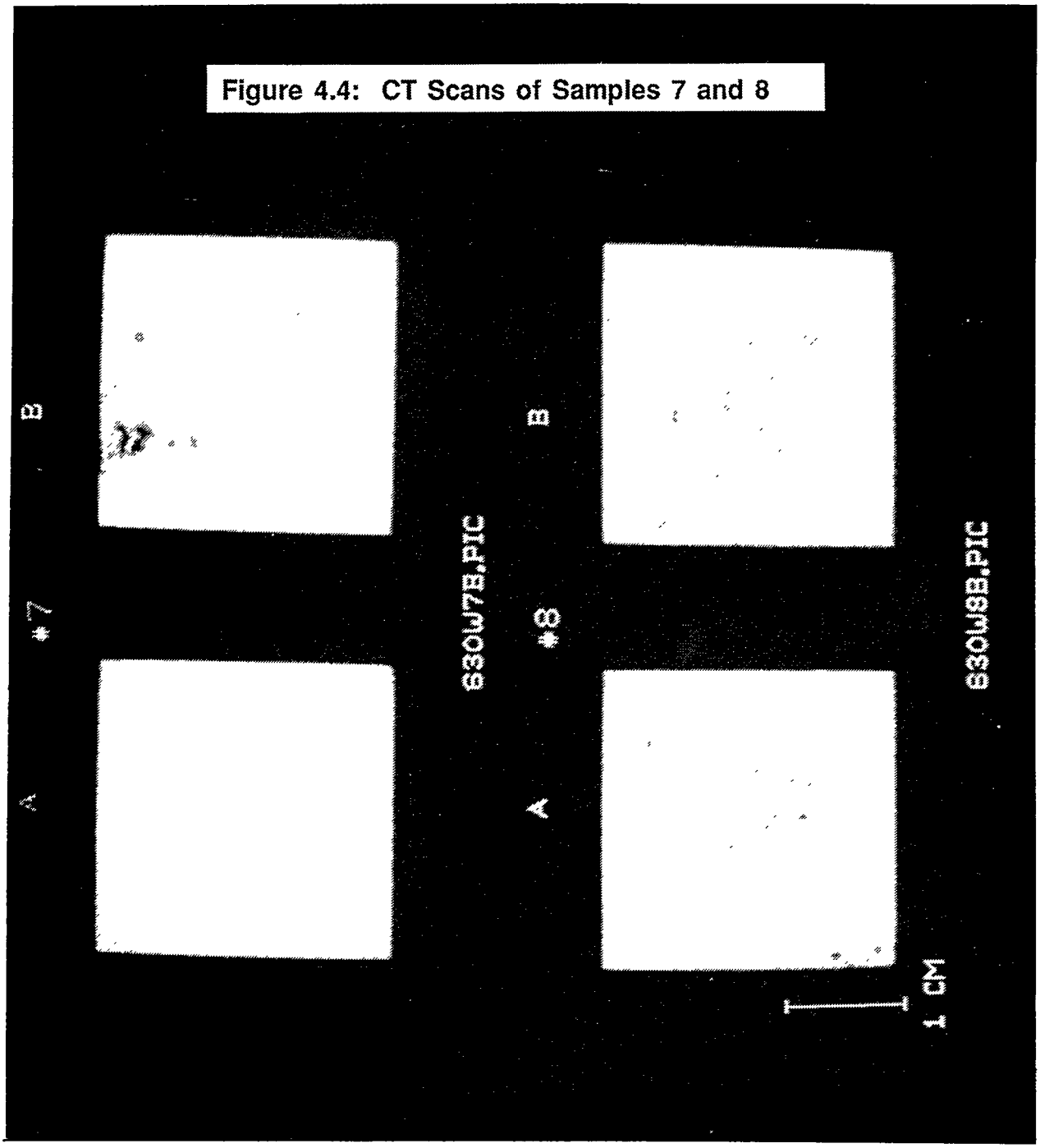

Figure 4.4: CT Scans of Samples 7 and 8

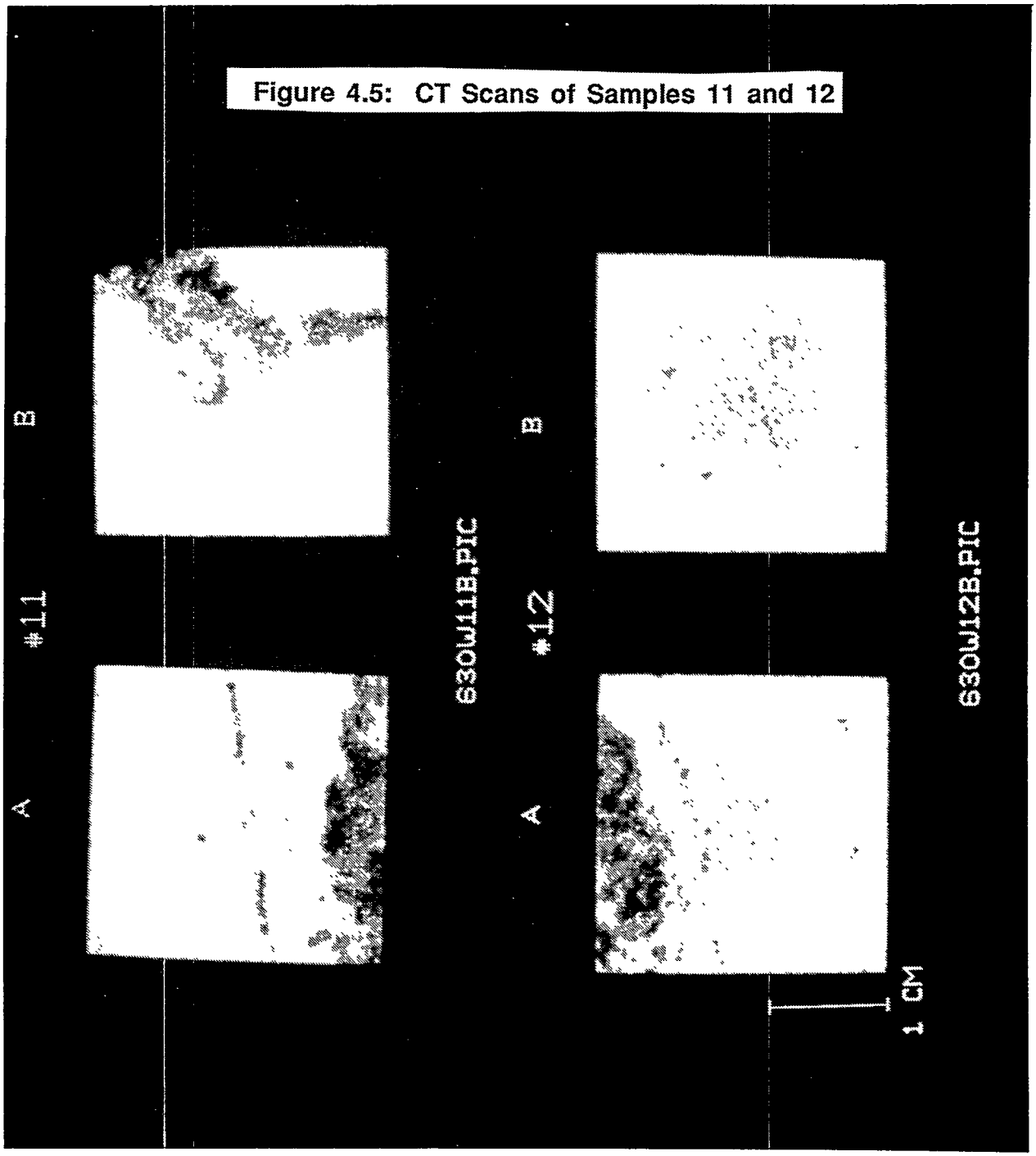

Figure 4.5: CT Scans of Samples 11 and 12

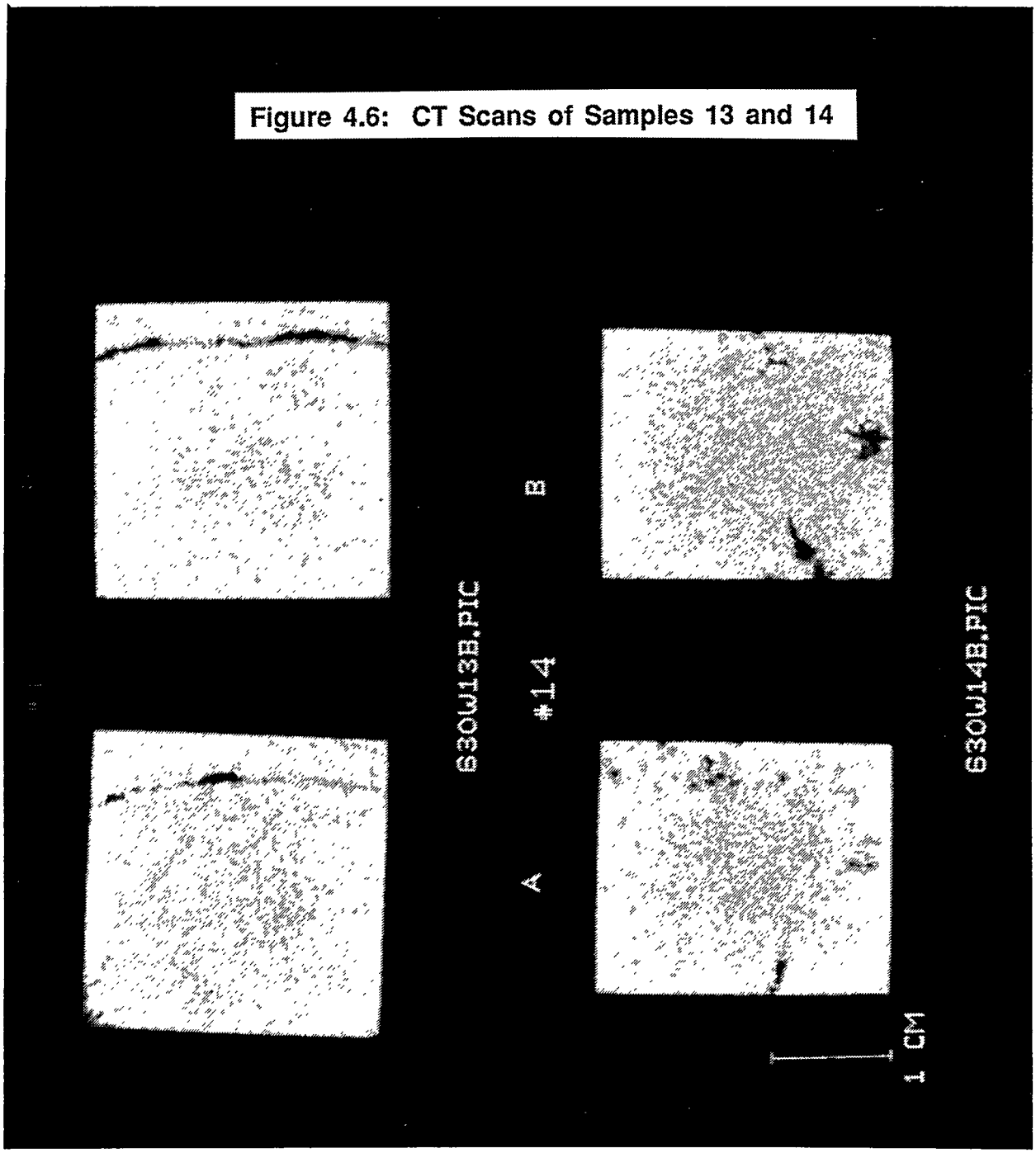
Figure 4.6: CT Scans of Samples 13 and 14
630W13B.PIC
630W14B.PIC
#14
A
B
1 CM

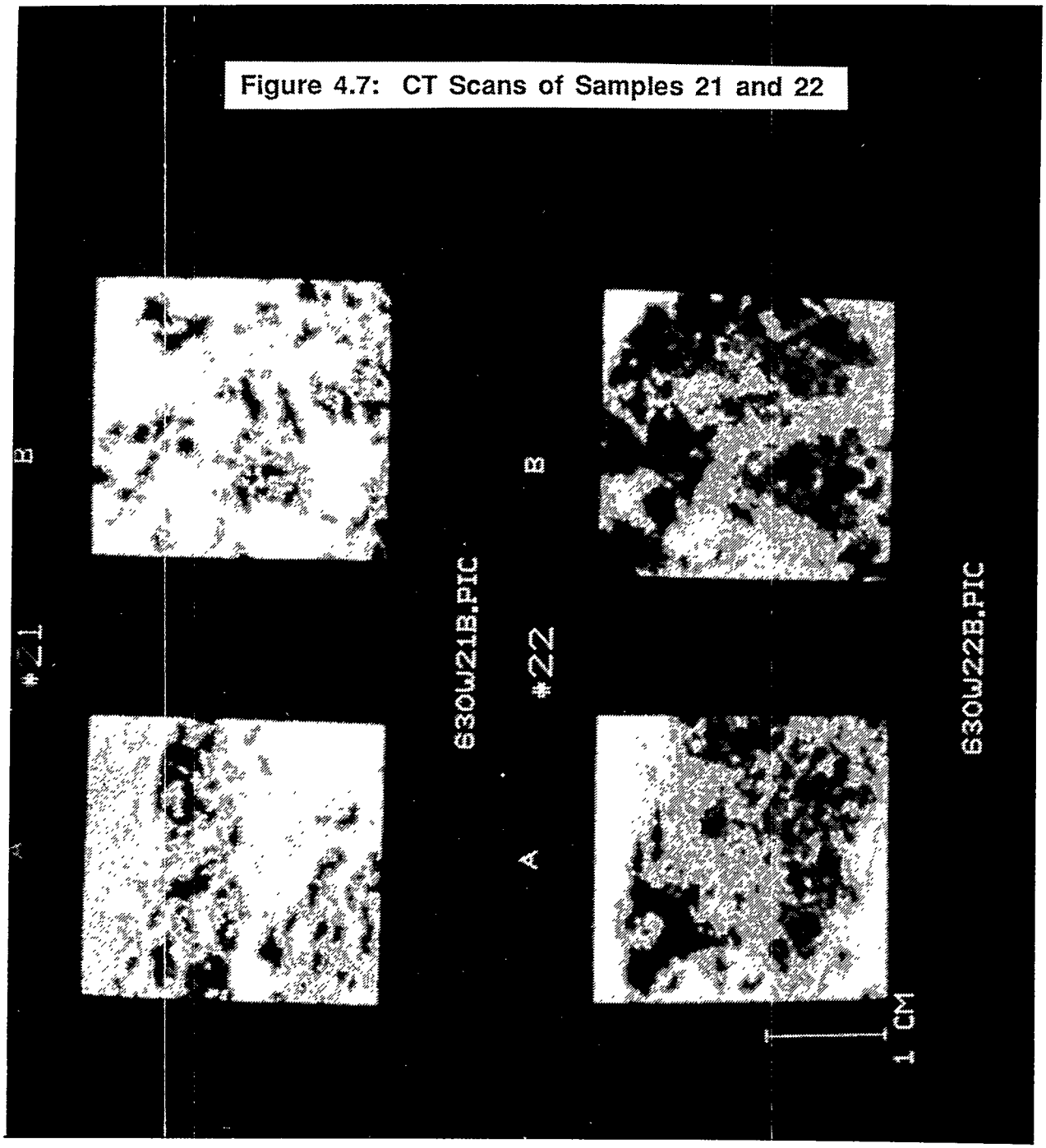

Figure 4.7: CT Scans of Samples 21 and 22

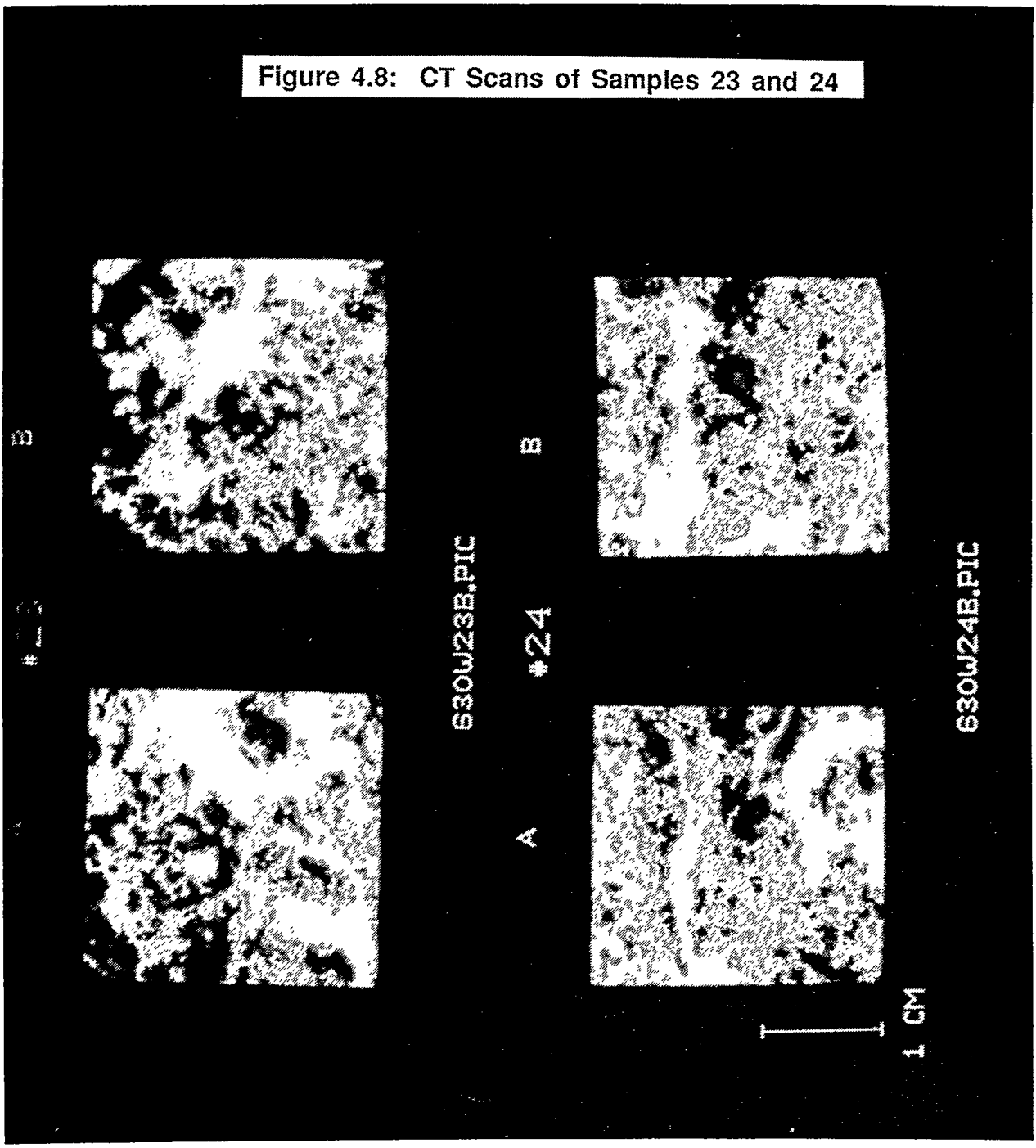

Figure 4.8: CT Scans of Samples 23 and 24

Figure 4.9

GAS-OIL CAPILLARY PRESSURE

Centrifuge Method

Sandia National Laboratories
Waste Isolation Pilot Plant
New Mexico
Core EIX 10-6
Horizontal Plug, B
File: DAL-93089

Sample ID: 6
Initial Oil saturation, fraction: 1.000
Saturant: n-Decane

Capillary Pressure, psi	I-F Oil Saturation, fraction
5	0.874
10	0.794
25	0.791
50	0.674
100	0.525
200	0.400
400	0.300
650	0.244

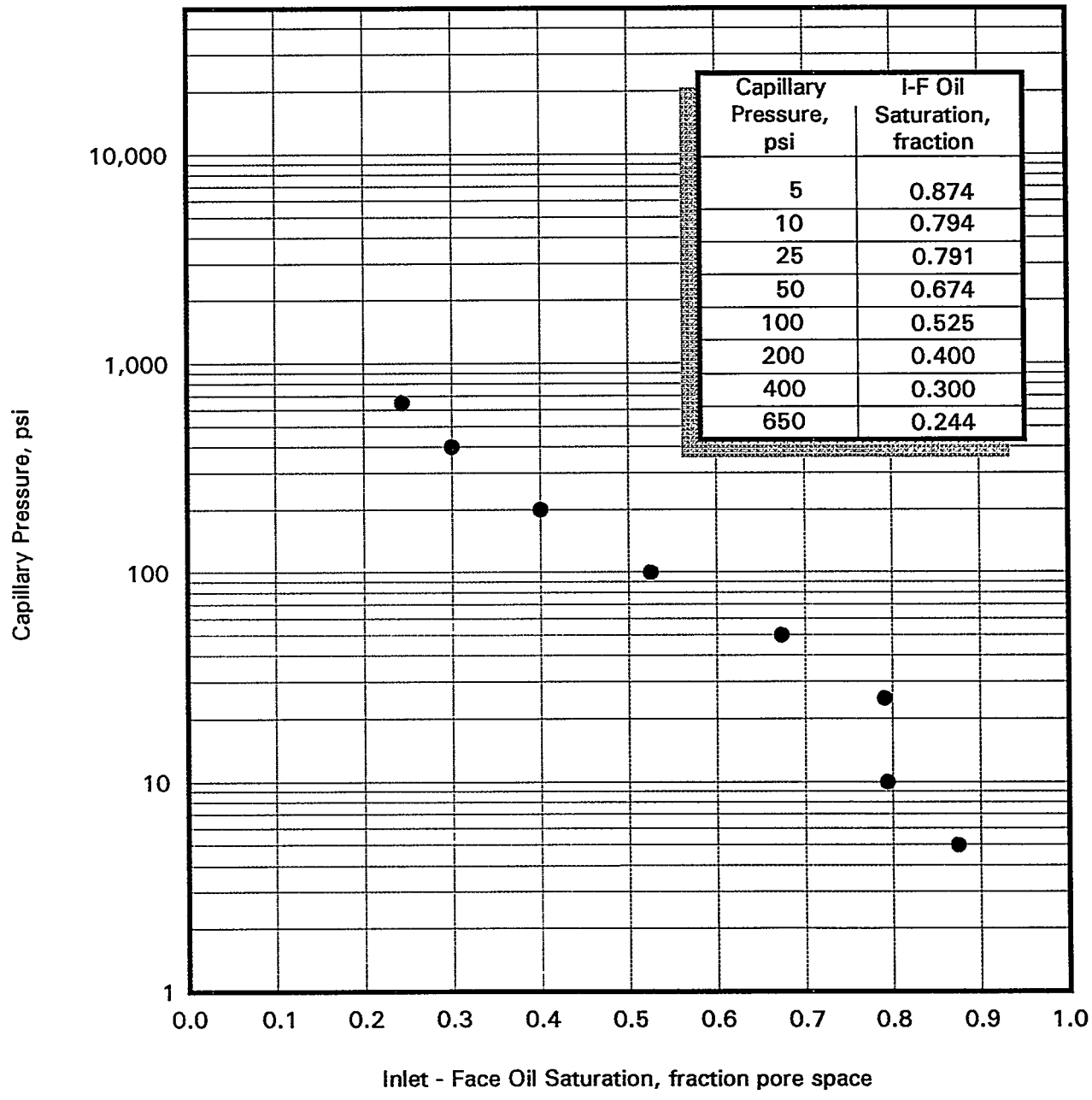

Figure 4.10

GAS-OIL CAPILLARY PRESSURE

Centrifuge Method

Sandia National Laboratories
Waste Isolation Pilot Plant
New Mexico
Core EIX 10-6
Vertical Plug, C2
File: DAL-93089

Sample Number: 8
Initial Oil saturation, fraction: 1.000
Saturant: n-Decane

Capillary Pressure, psi	I-F Oil Saturation, fraction
5	0.869
10	0.864
25	0.846
50	0.805
100	0.683
200	0.321
400	0.178
650	0.107

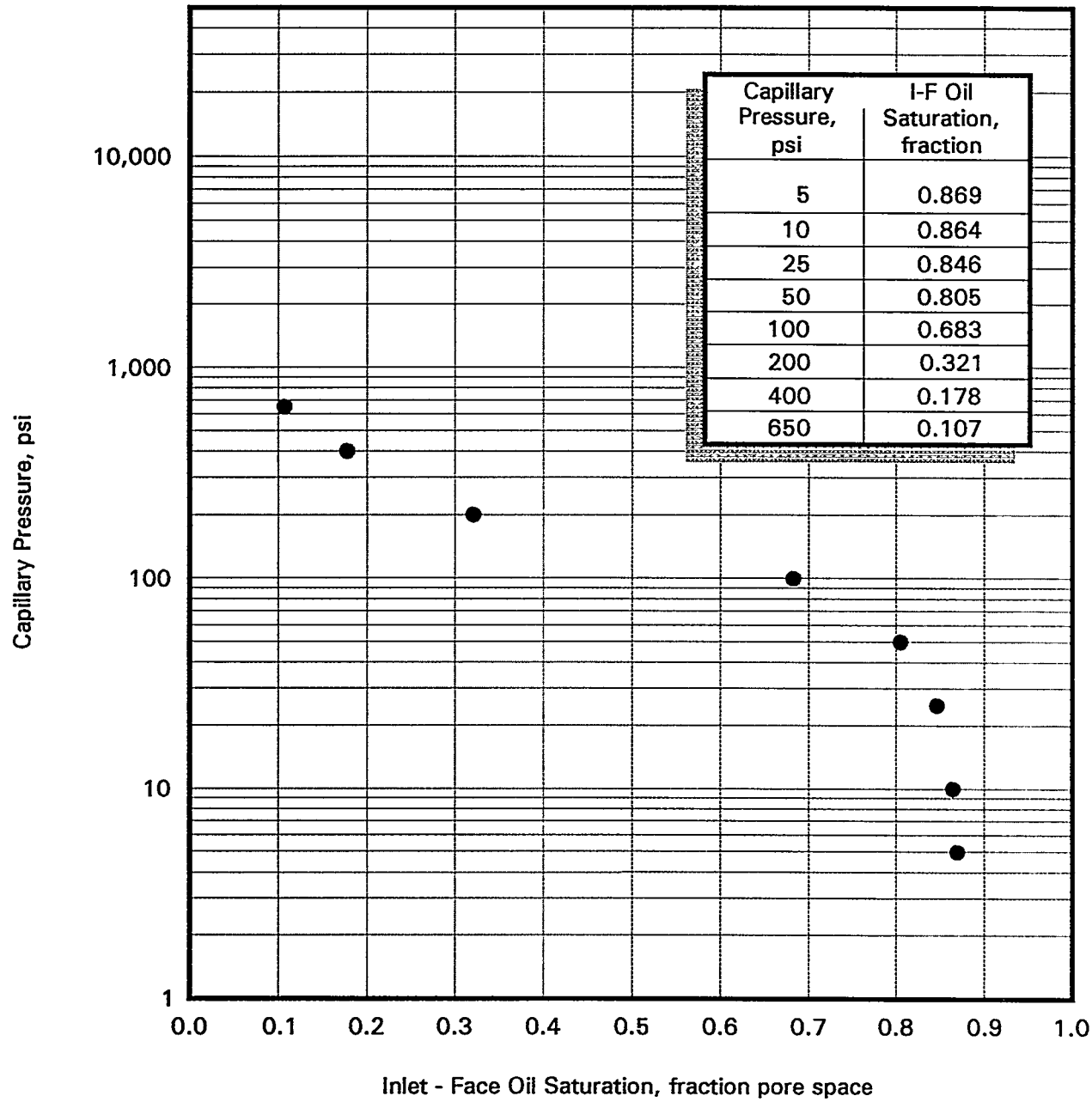

Figure 4.11

GAS-OIL CAPILLARY PRESSURE

Centrifuge Method

Sandia National Laboratories
Waste Isolation Pilot Plant
New Mexico
Core EIX 10-6
Horizontal Plug, B
File: DAL-93089

Sample ID: 12
Initial Oil saturation, fraction: 1.000
Saturant: n-Decane

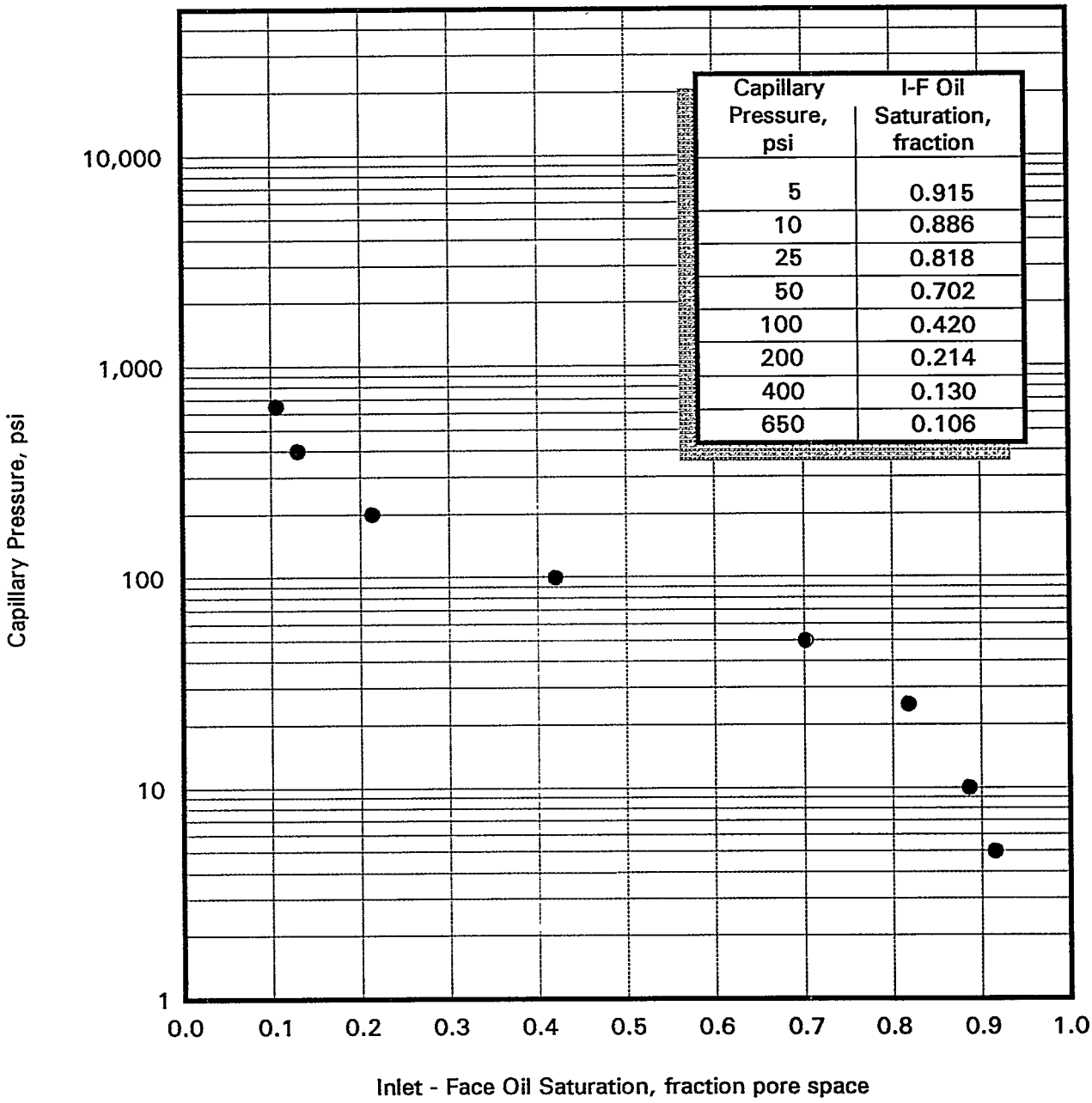

Capillary Pressure, psi	I-F Oil Saturation, fraction
5	0.915
10	0.886
25	0.818
50	0.702
100	0.420
200	0.214
400	0.130
650	0.106

Figure 4.12

GAS-OIL CAPILLARY PRESSURE

Centrifuge Method

Sandia National Laboratories
Waste Isolation Pilot Plant
New Mexico
Core EIX 10-6
Vertical Plug, C2
File: DAL-93089

Sample ID: 14
Initial Oil saturation, fraction: 1.000
Saturant: n-Decane

Capillary Pressure, psi	I-F Oil Saturation, fraction
5	0.852
10	0.851
25	0.845
50	0.823
100	0.736
200	0.486
400	0.451
650	0.445

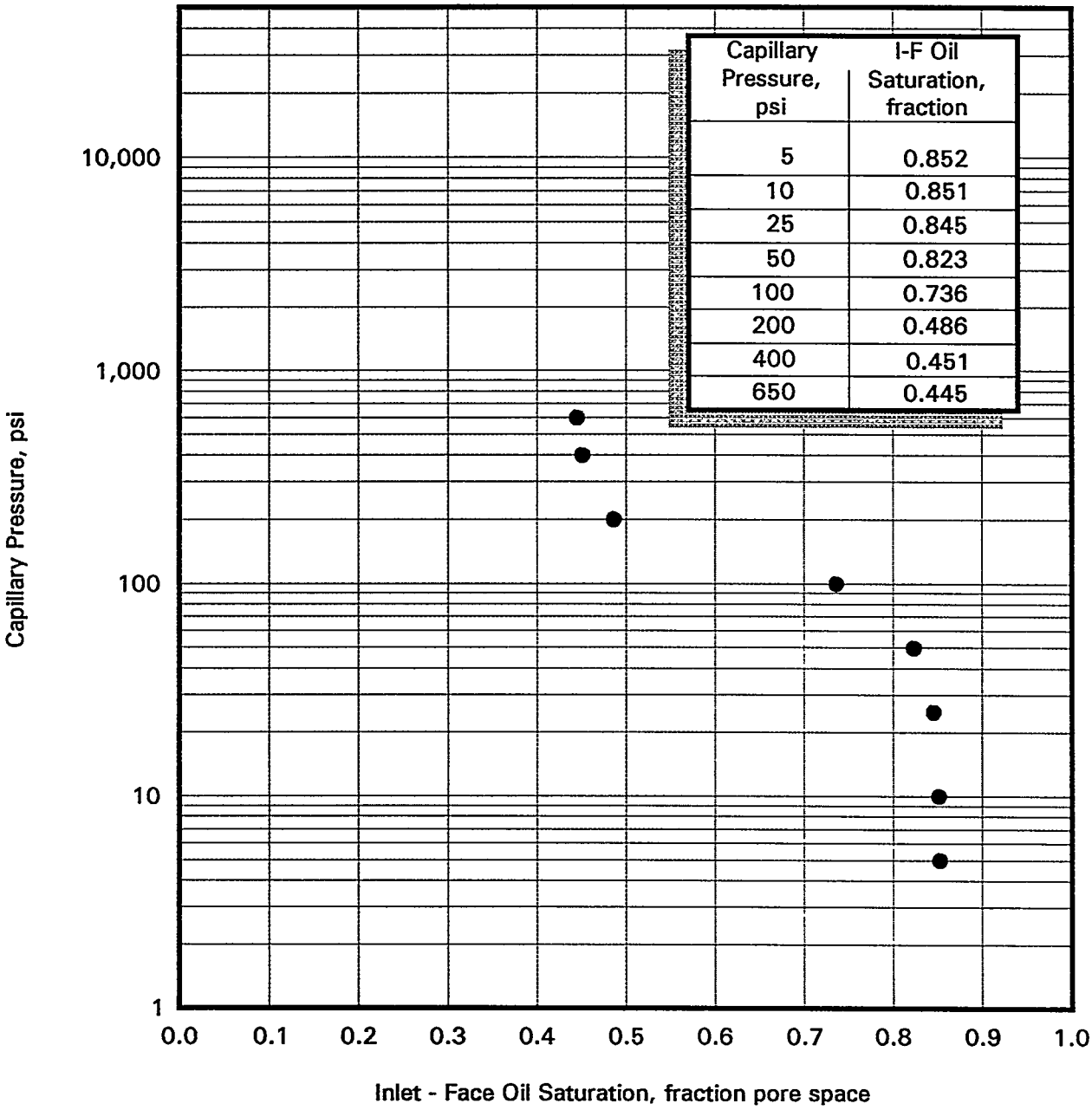

Figure 4.13

GAS-OIL CAPILLARY PRESSURE

Centrifuge Method

Sandia National Laboratories
Waste Isolation Pilot Plant
New Mexico
Core EIX 11-6
Horizontal Plug, B
File: DAL-93089

Sample ID: 22
Initial Oil saturation, fraction: 1.000
Saturant: n-Decane

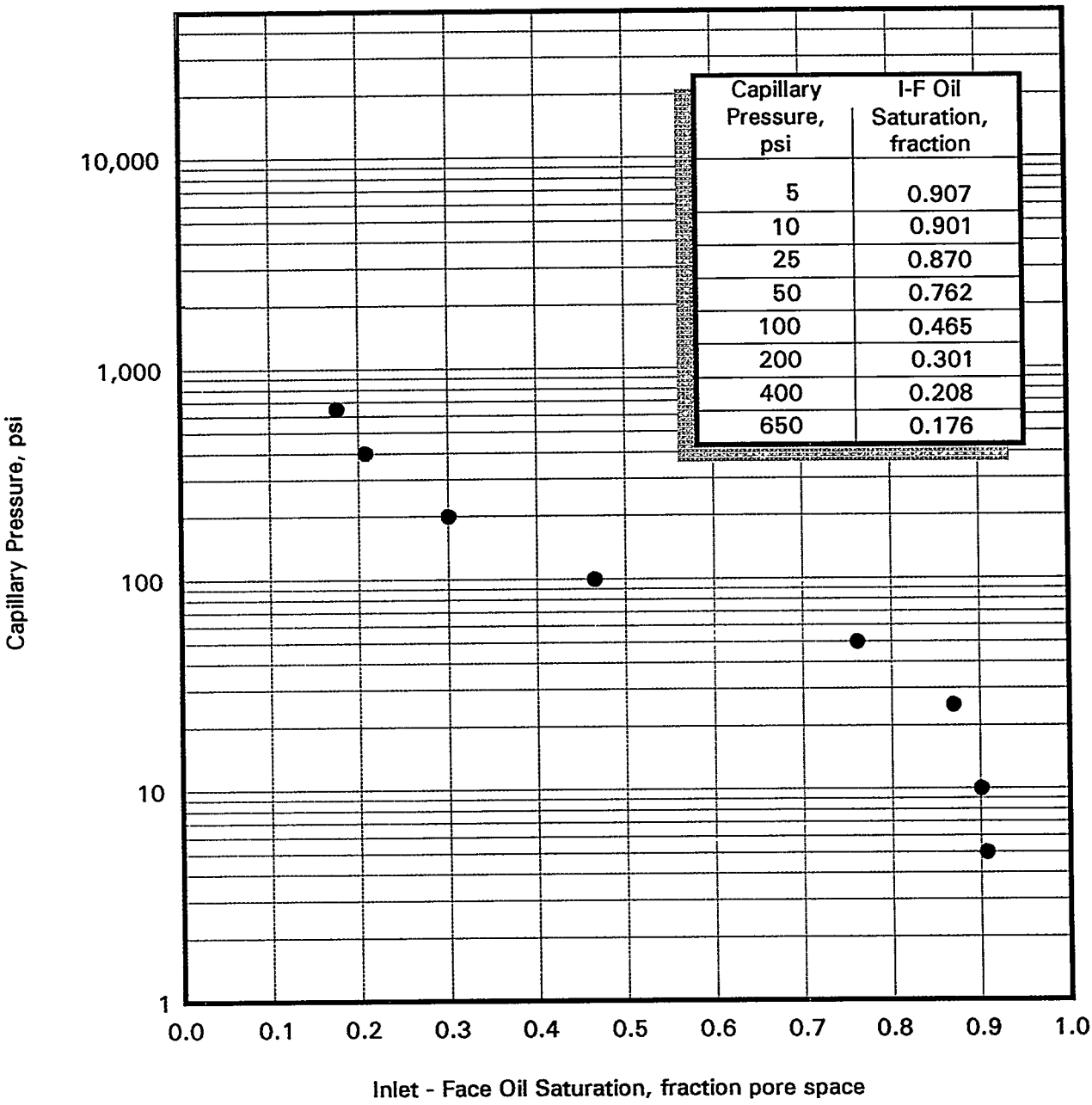

Capillary Pressure, psi	I-F Oil Saturation, fraction
5	0.907
10	0.901
25	0.870
50	0.762
100	0.465
200	0.301
400	0.208
650	0.176

Figure 4.14

GAS-OIL CAPILLARY PRESSURE

Centrifuge Method

Sandia National Laboratories
Waste Isolation Pilot Plant
New Mexico
Core EIX 11-6
Horizontal Plug, B
File: DAL-93089

Sample ID: 24
Initial Oil saturation, fraction: 1.000
Saturant: n-Decane

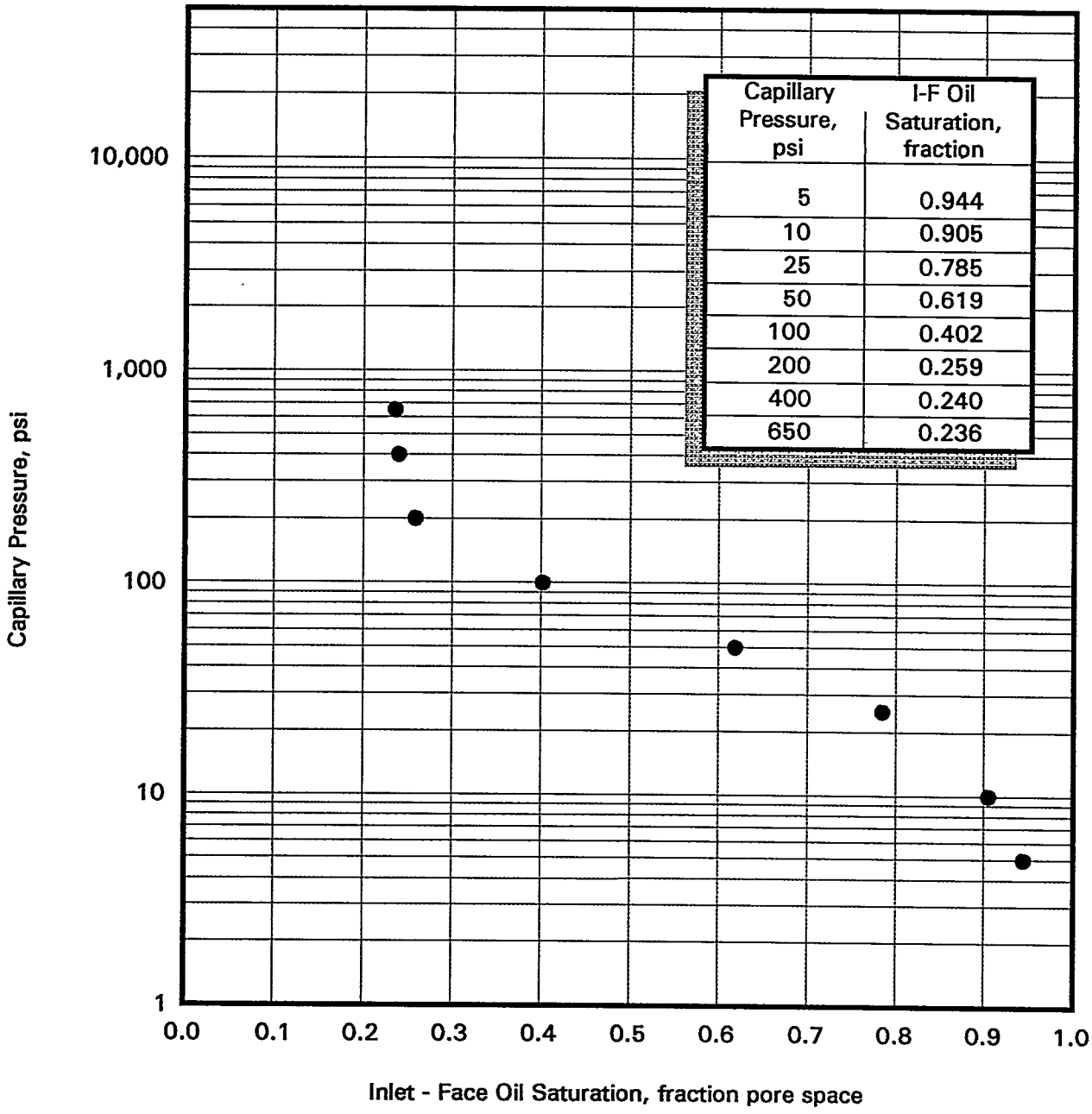

Capillary Pressure, psi	I-F Oil Saturation, fraction
5	0.944
10	0.905
25	0.785
50	0.619
100	0.402
200	0.259
400	0.240
650	0.236

Figure 4.15

MERCURY INJECTION

Sandia National Laboratories
Waste Isolation Pilot Plant
Core: E1X 10-6
File: DAL-93089

Sample Number: 5

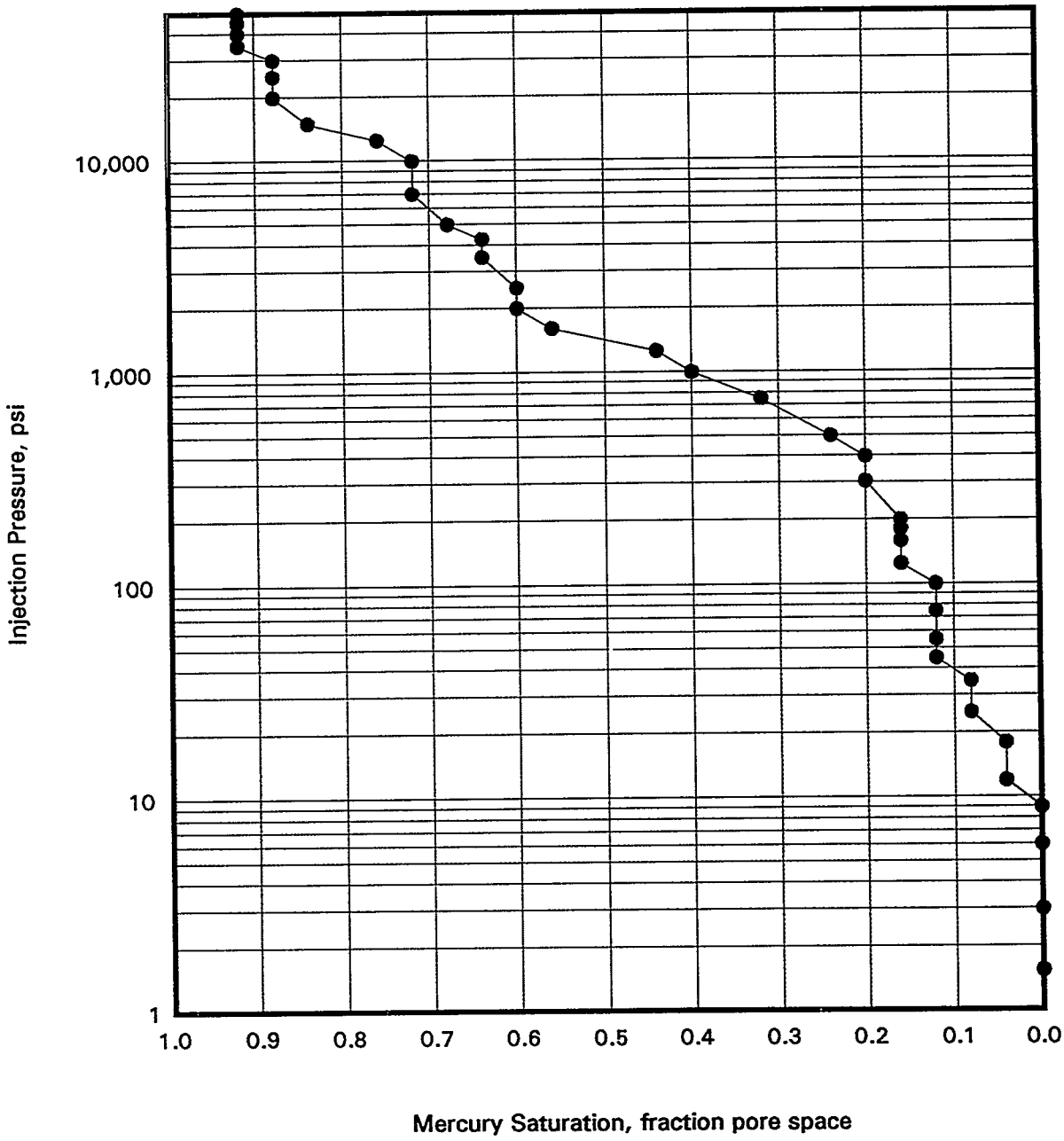

Figure 4.16

MERCURY INJECTION

Sandia National Laboratories
Waste Isolation Pilot Plant
Core: E1X 10-6
File: DAL-93089

Sample Number: 7

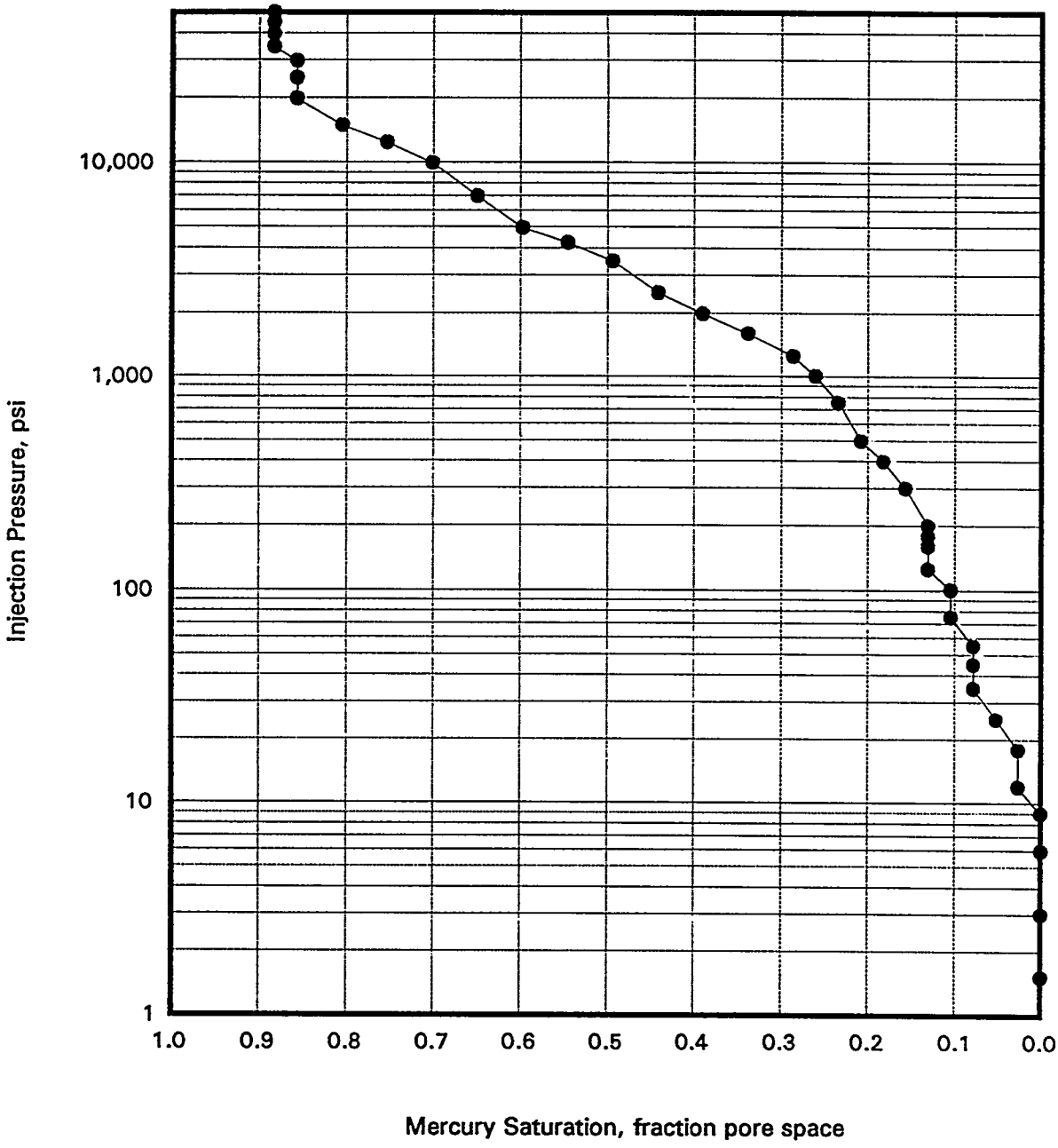

Figure 4.17

MERCURY INJECTION

Sandia National Laboratories
Waste Isolation Pilot Plant
Core: E1X 10-6
File: DAL-93089

Sample Number: 11

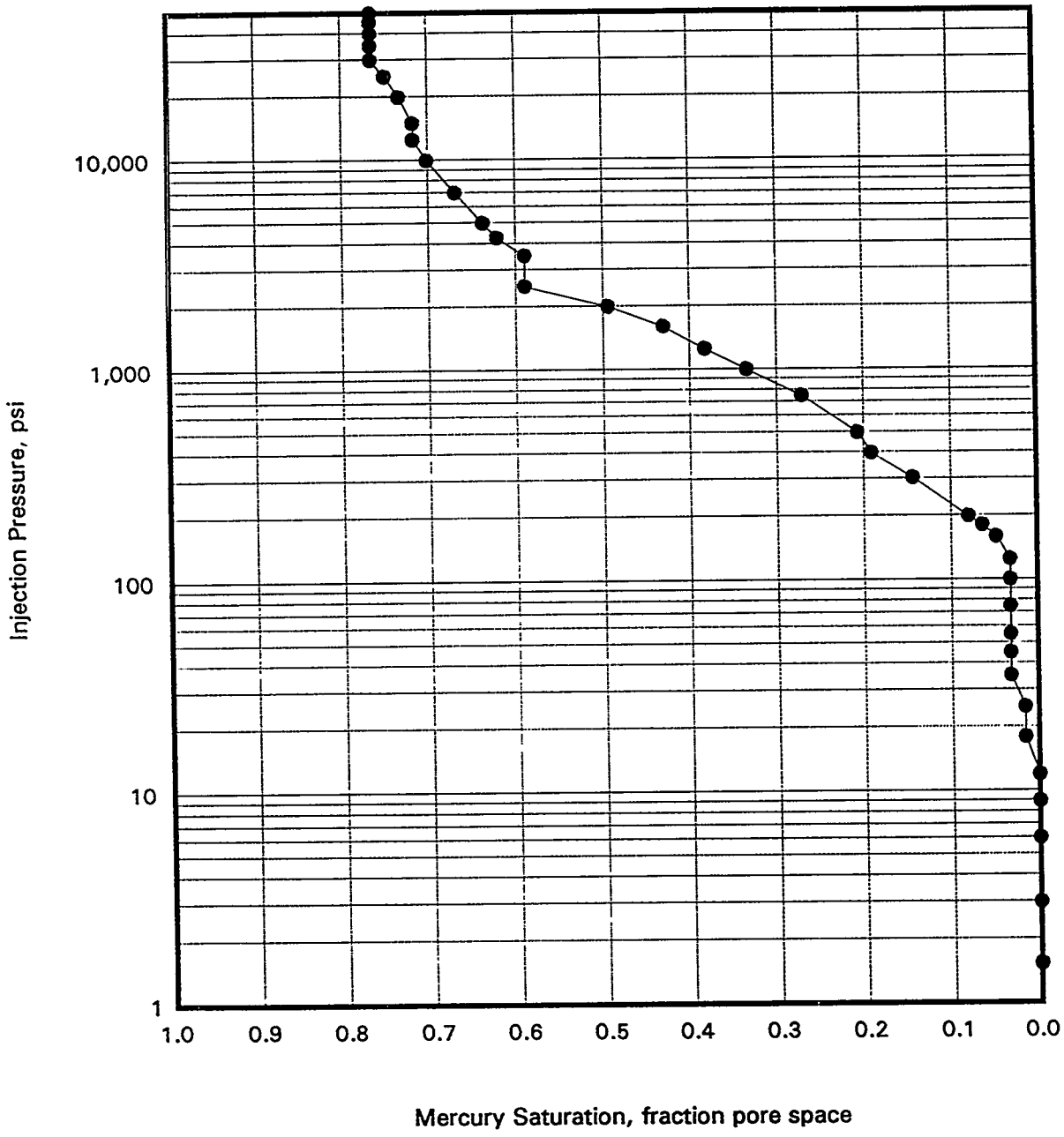

Figure 4.18

MERCURY INJECTION

Sandia National Laboratories
Waste Isolation Pilot Plant
Core: E1X 10-6
File: DAL-93089

Sample Number: 13

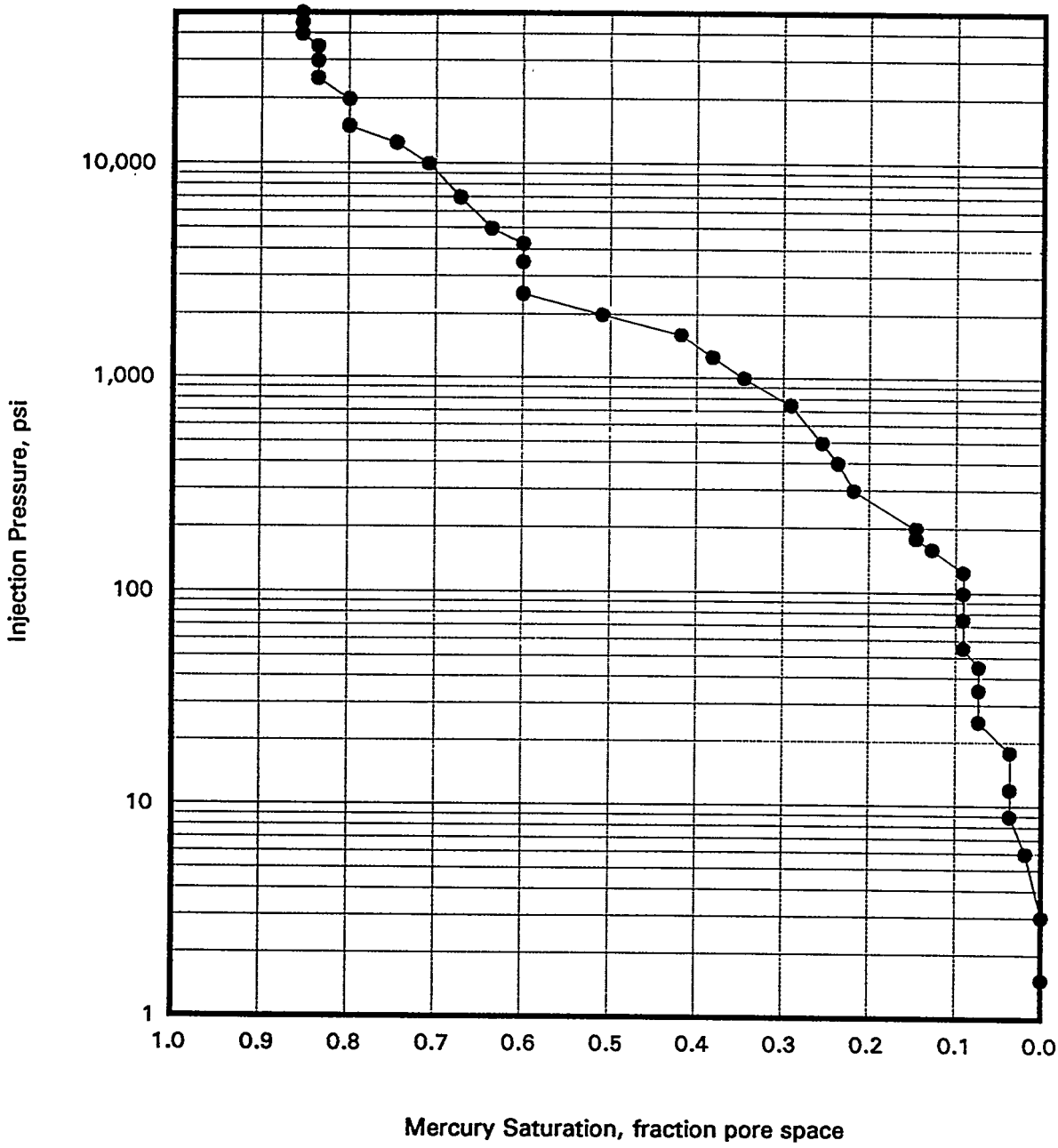

Figure 4.19

MERCURY INJECTION

Sandia National Laboratories
Waste Isolation Pilot Plant
Core: E1X 10-6
File: DAL-93089

Sample Number: 21

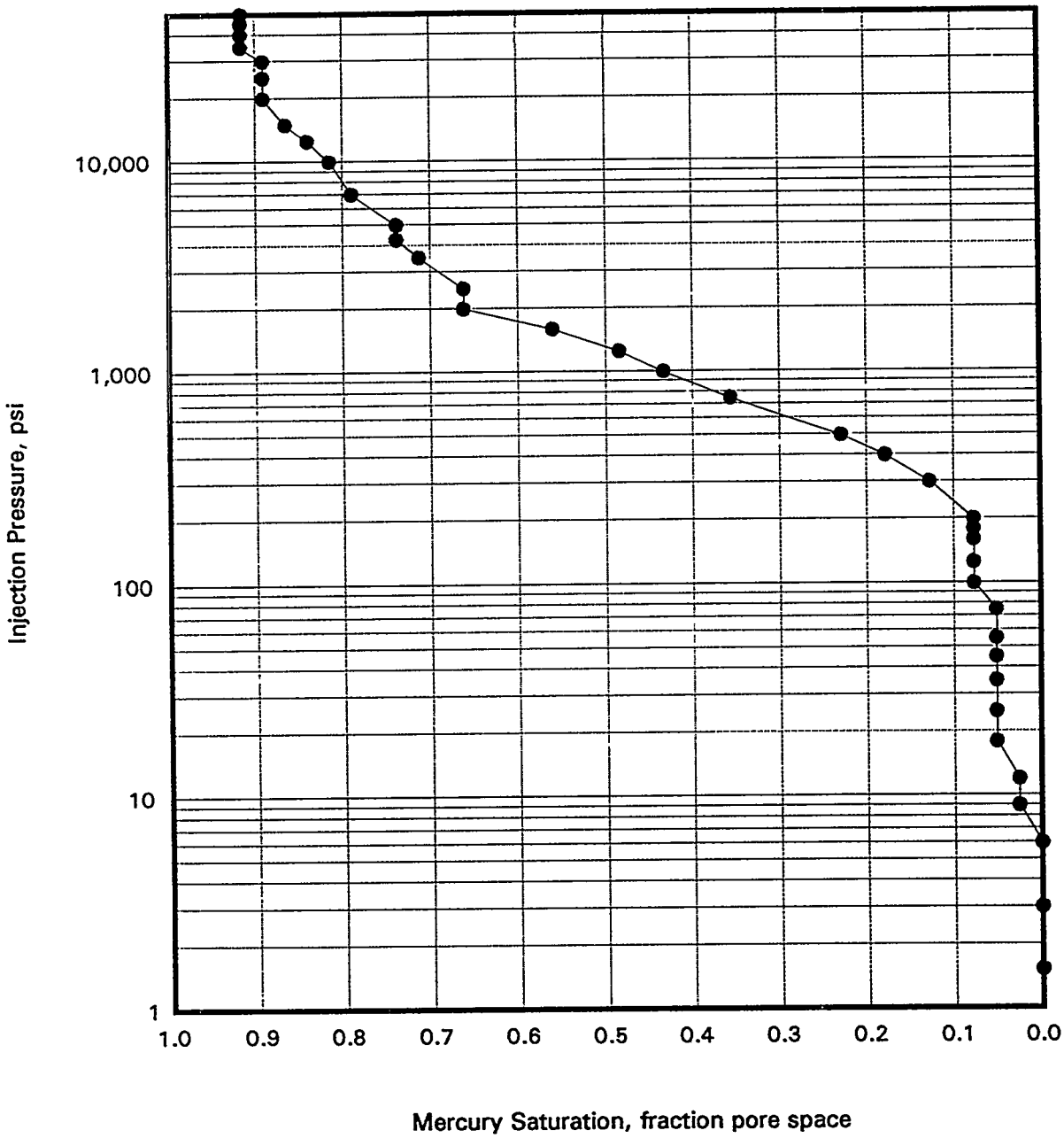

Figure 4.20

MERCURY INJECTION

Sandia National Laboratories
Waste Isolation Pilot Plant
Core: E1X 10-6
File: DAL-93089

Sample Number: 23

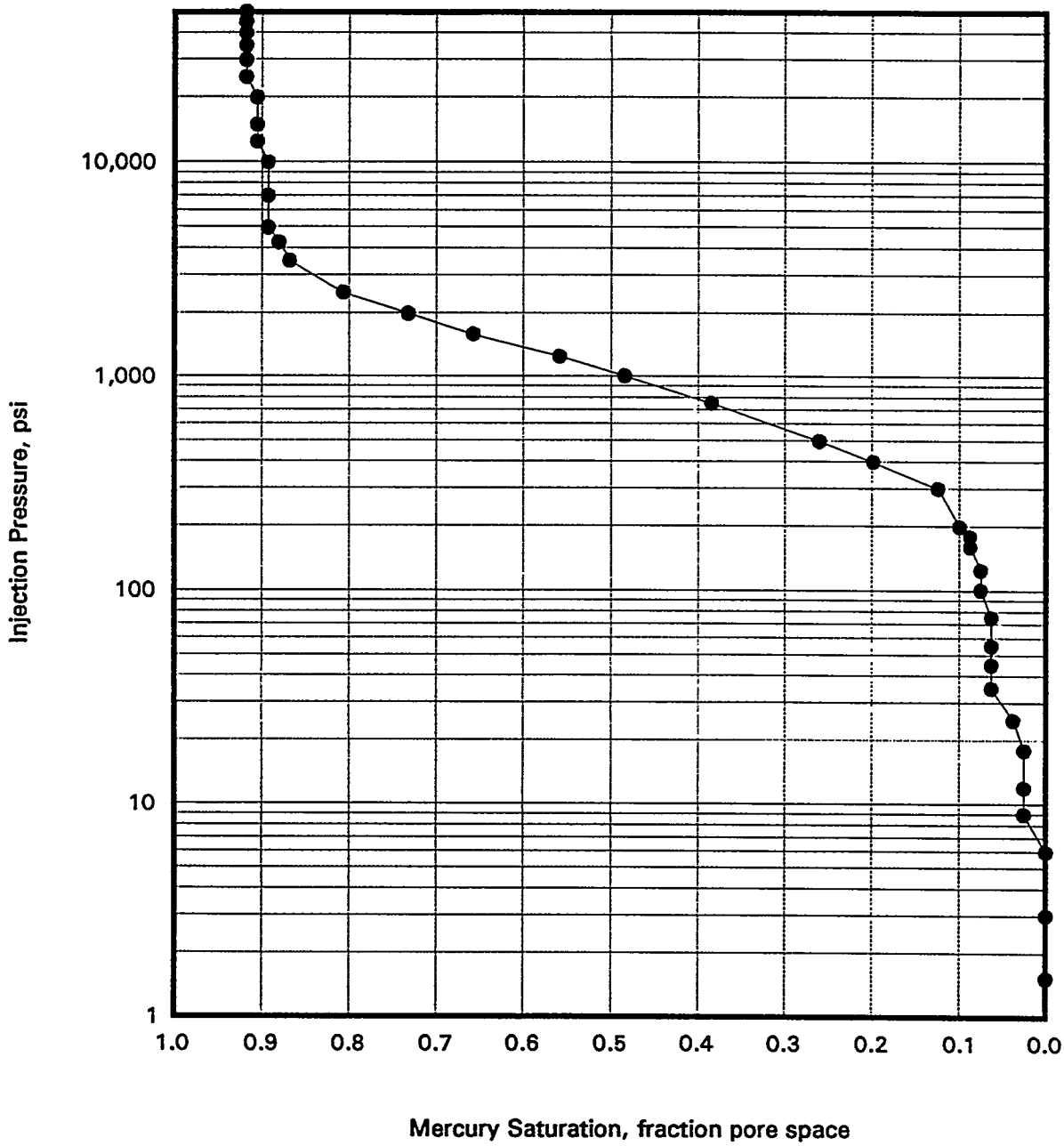

Figure 4.21
Samples 5 and 6
Comparison of Converted Hg and Cent. Air/Water Pcap Data

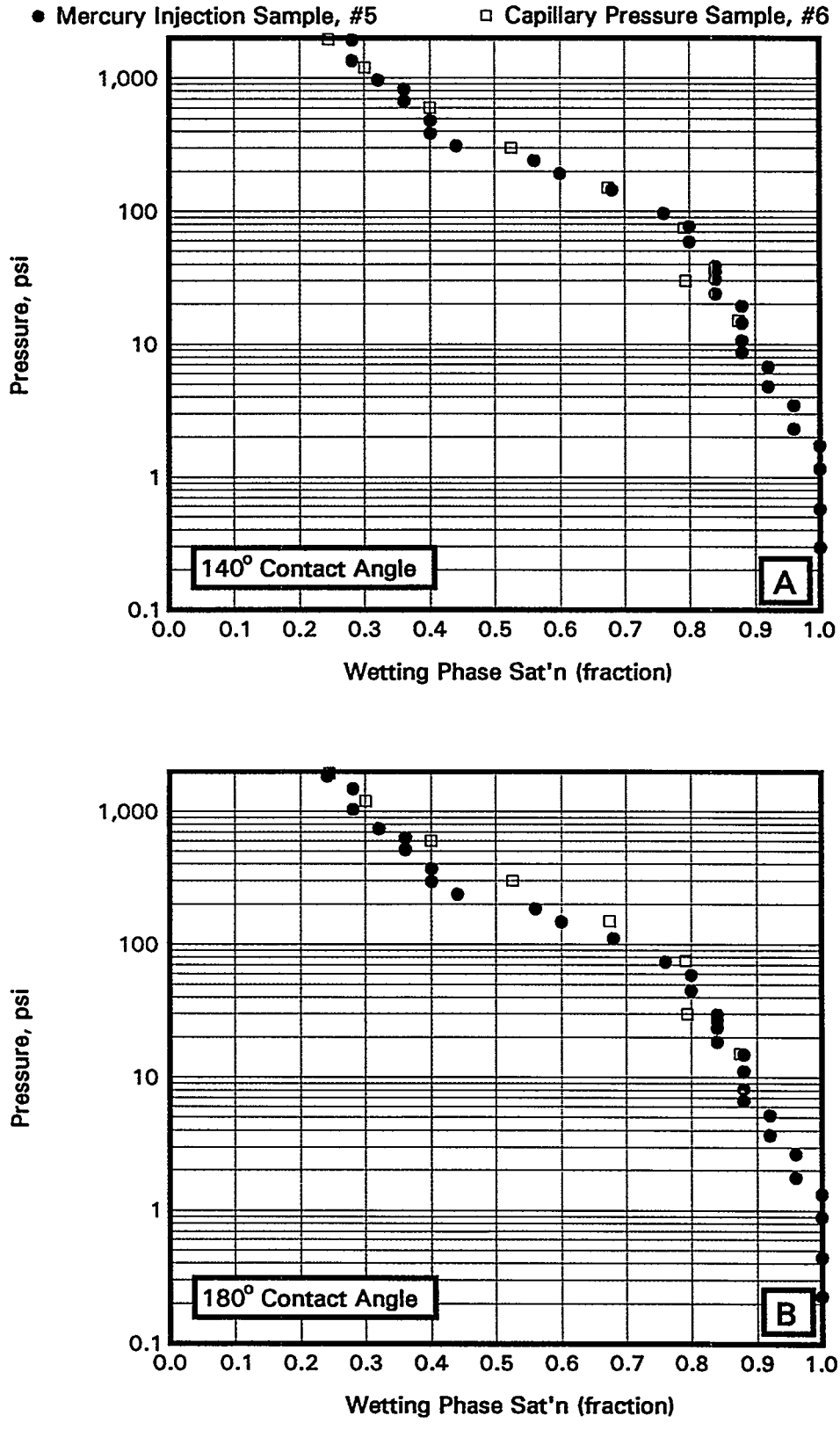

Figure 4.22
Samples 7 and 8
Comparison of Converted Hg and Cent. Air/Water Pcap Data

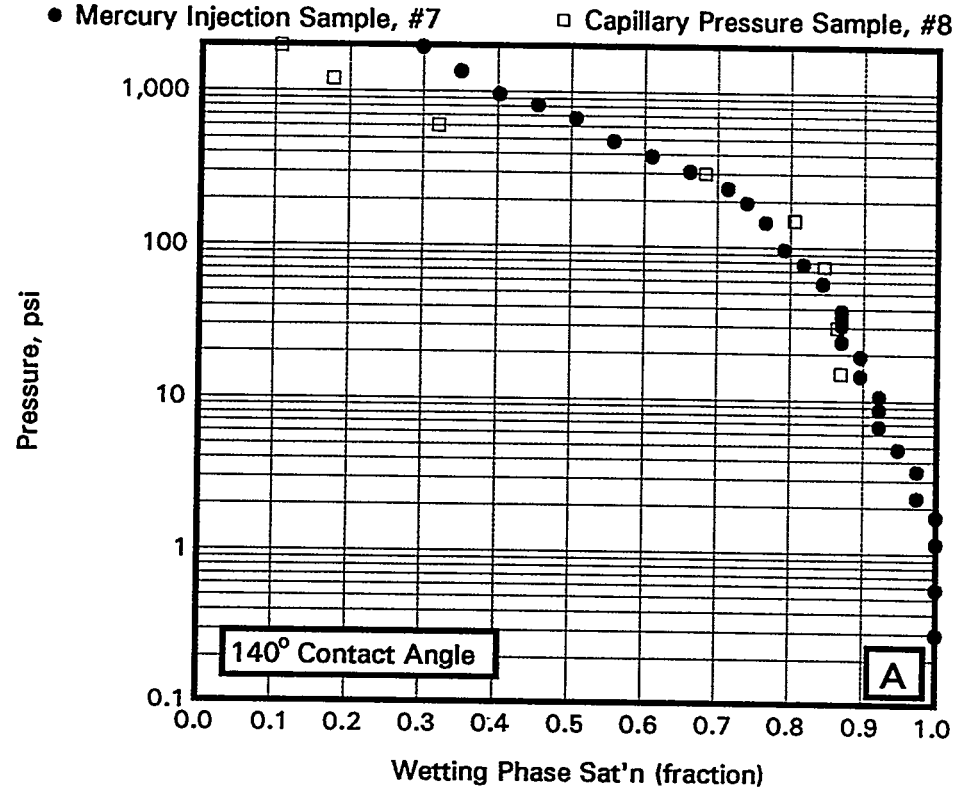

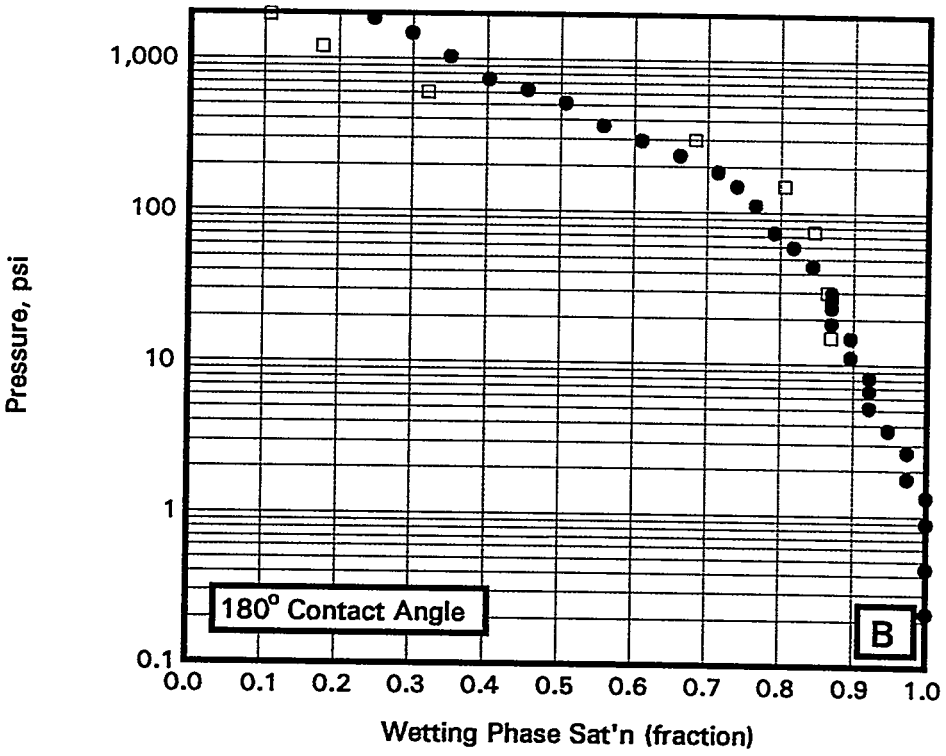

Figure 4.23
Samples 11 and 12
Comparison of Converted Hg and Cent. Air/Water Pcap Data

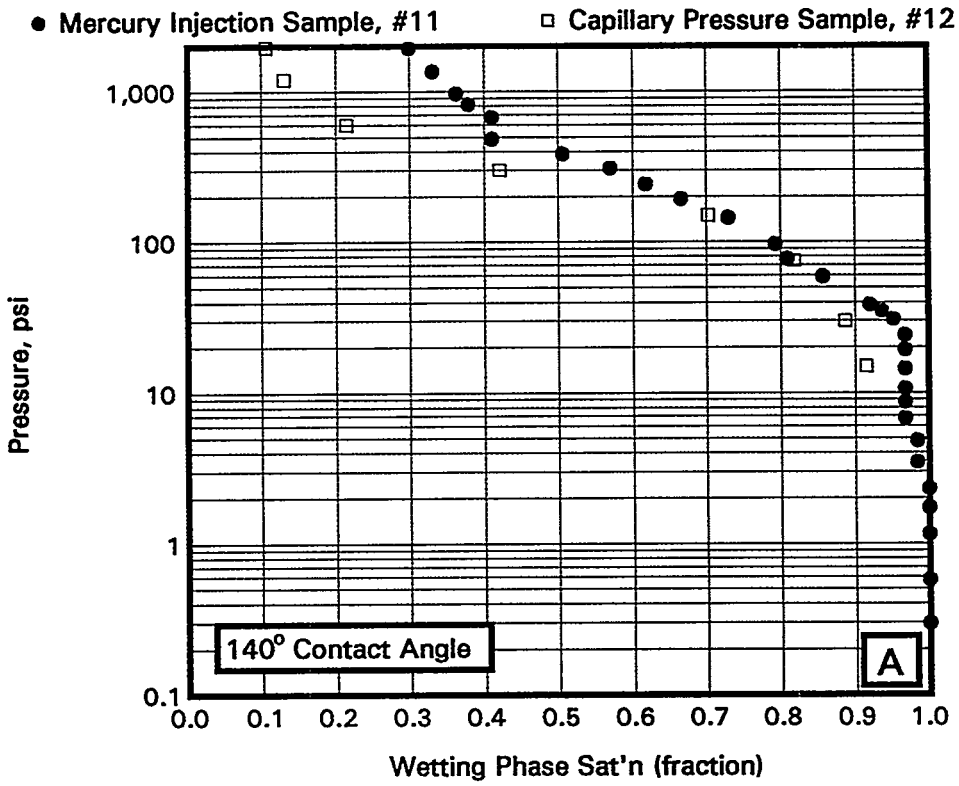

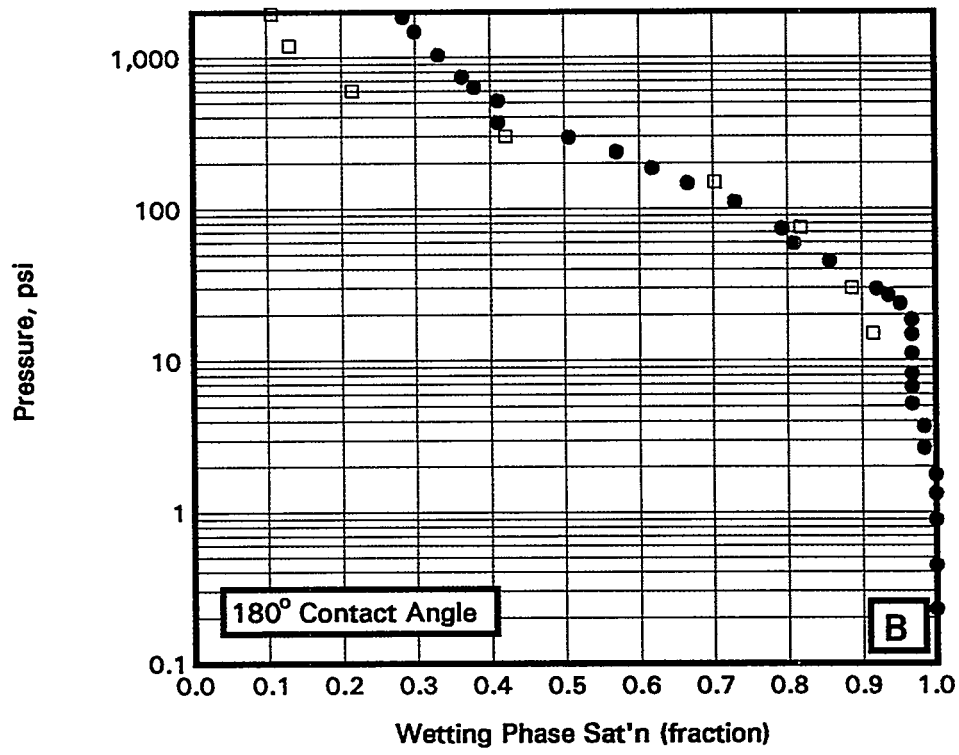

Figure 4.24
Samples 13 and 14
Comparison of Converted Hg and Cent. Air/Water Pcap Data

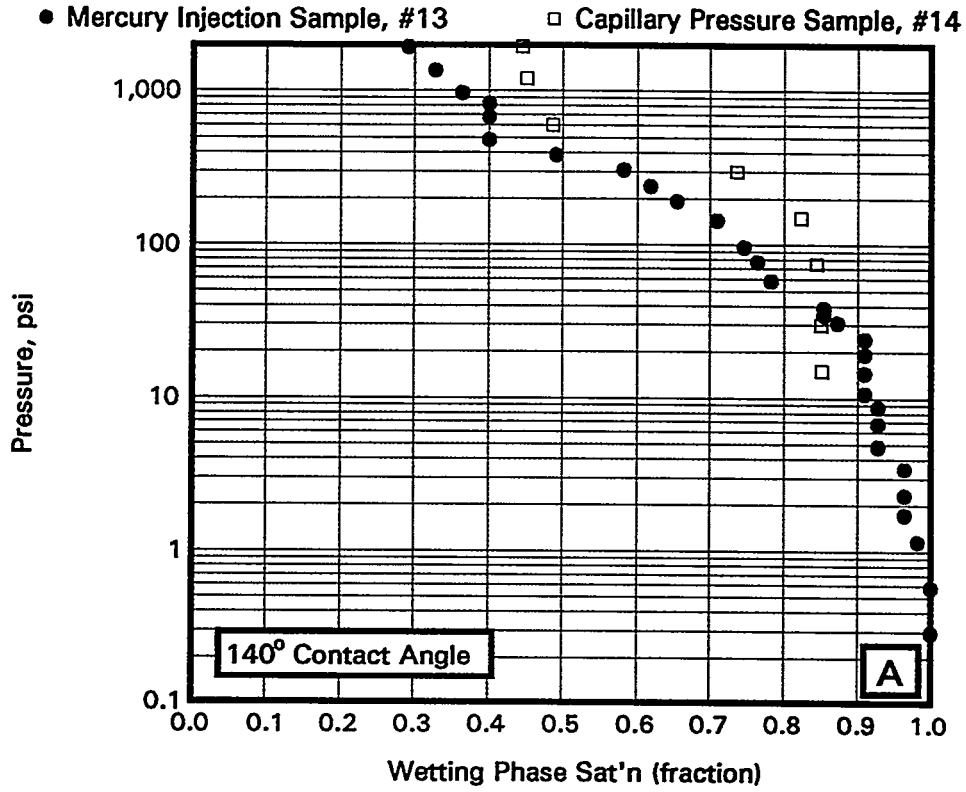

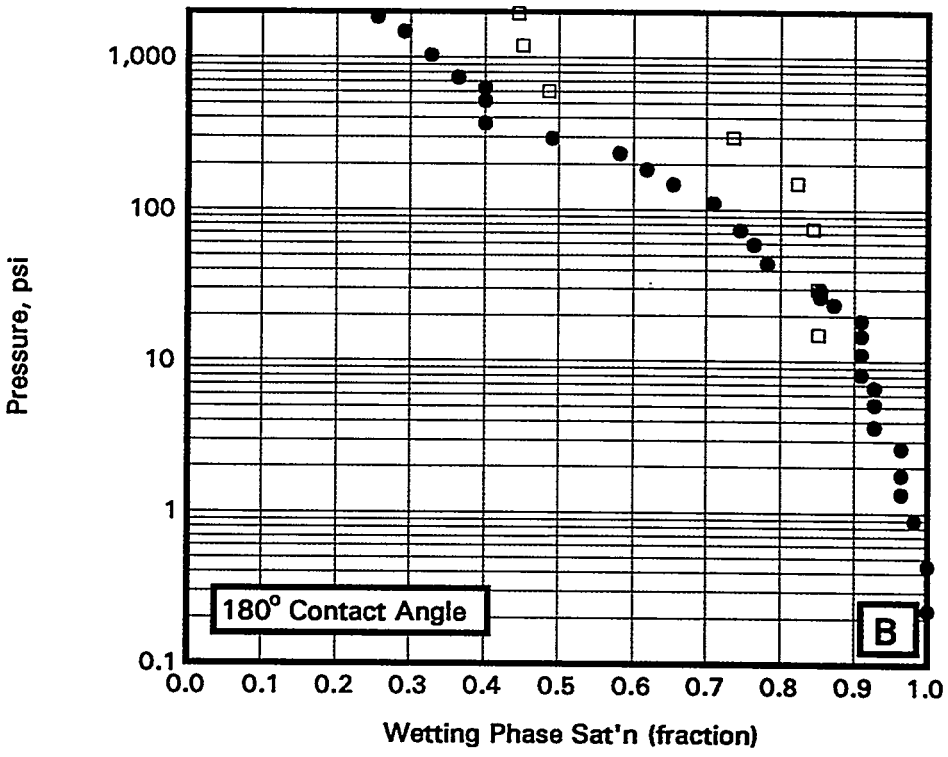

Figure 4.25
Samples 21 and 22
Comparison of Converted Hg and Cent. Air/Water Pcap Data

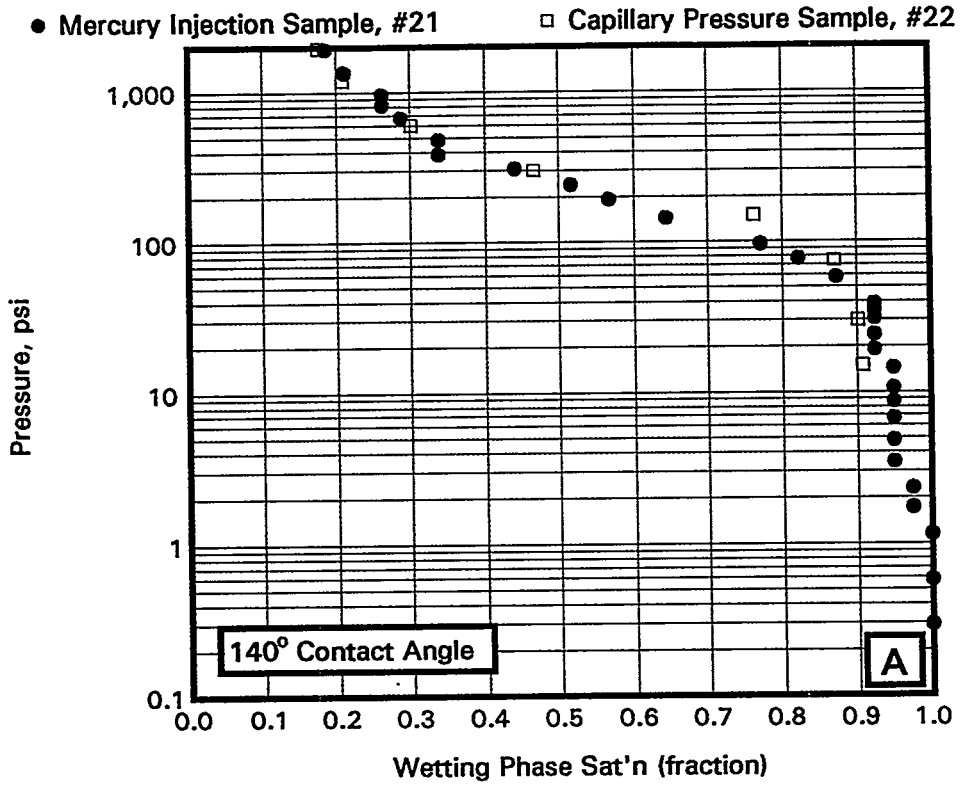

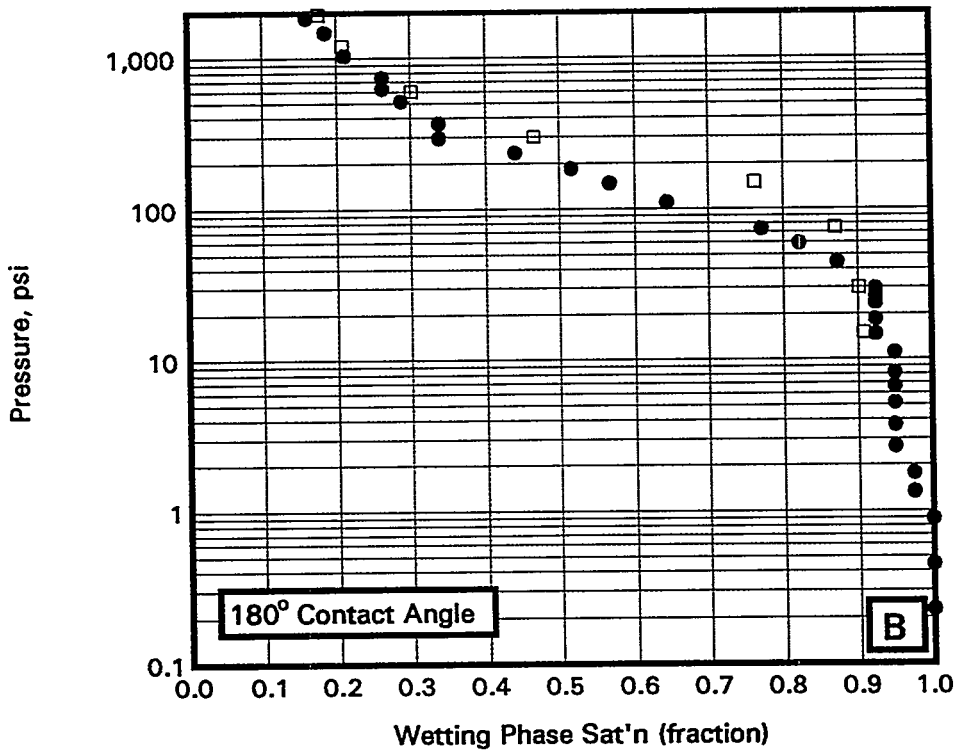

Figure 4.26
Samples 23 and 24
Comparison of Converted Hg and Cent. Air/Water Pcap Data

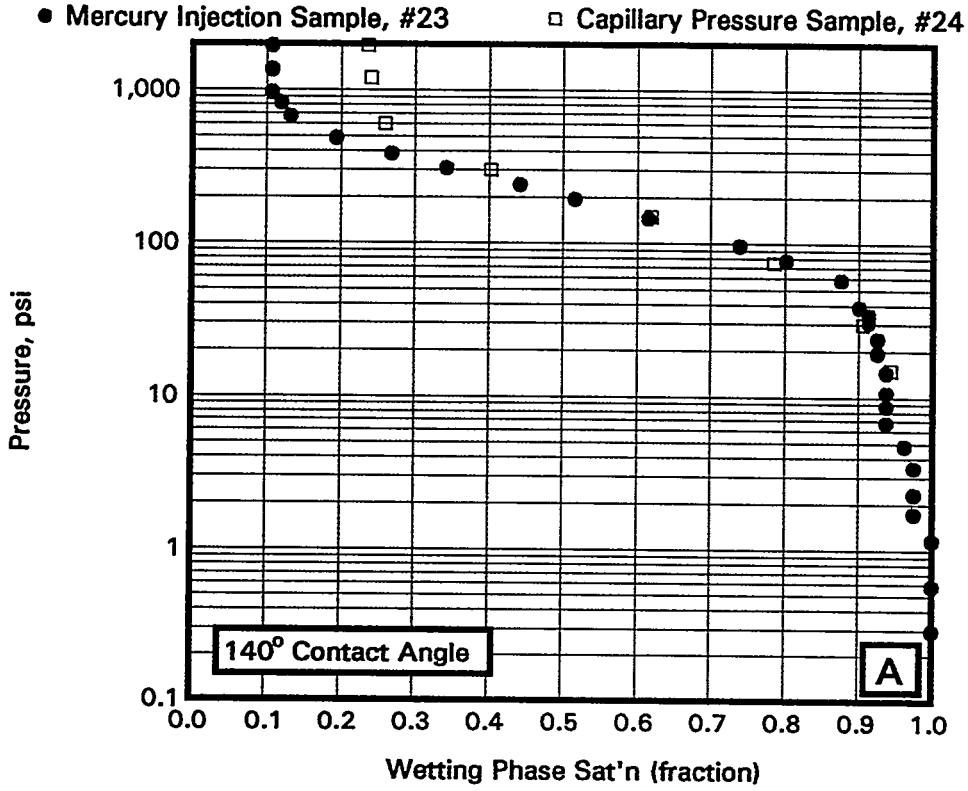

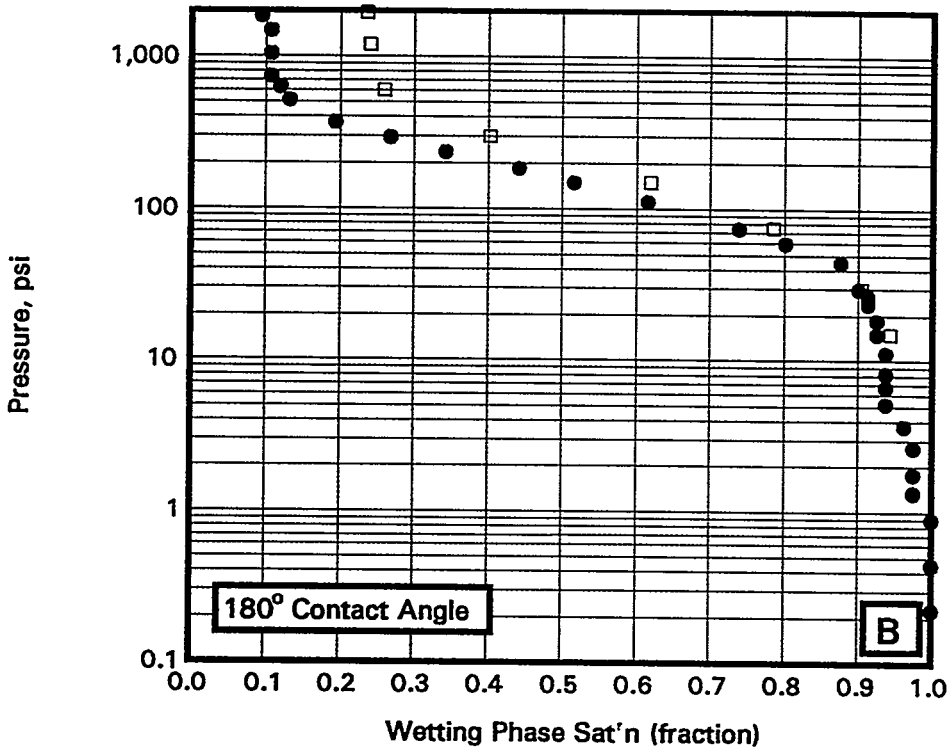

Figure 4.27: Equivalent Air-Brine Entry Pressure vs. Klinkenberg Permeability for Tight Sand Samples (Ref. 19), Davies (Ref. 20) and MB 139

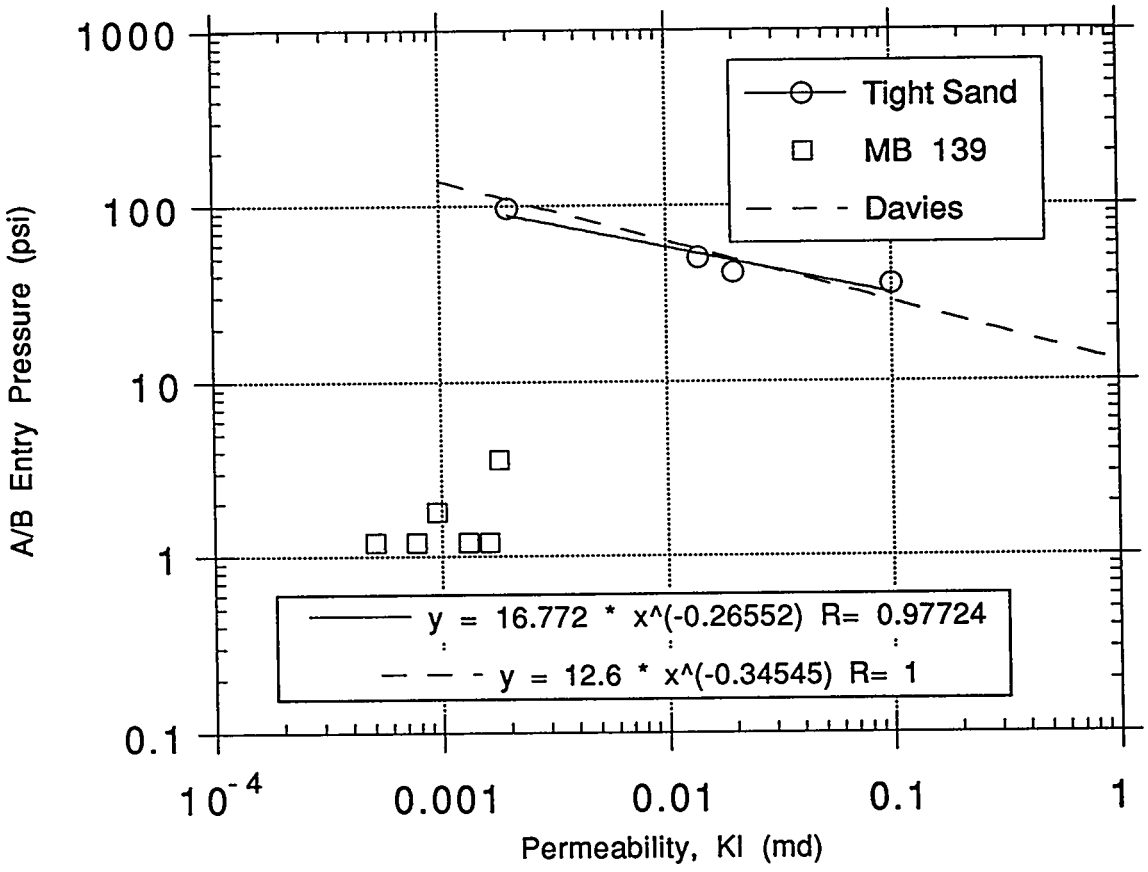

Appendix A-A.
Appendix A of Appendix A [Data Report: Rock Physics Associates (Core Laboratories)]


SANDIA NATIONAL LABORATORIES

SANDIA NATIONAL LABORATORIES

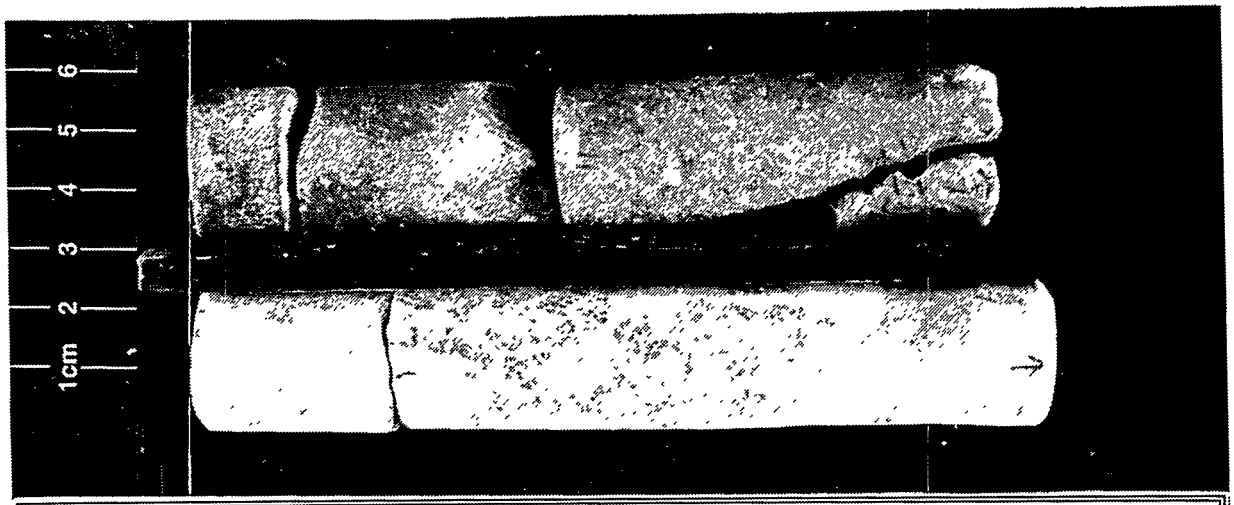

E1X 11 - 6	E1X 11 - 6
HORIZONTAL 4.25 FT.	HORIZONTAL 4.50 FT. 0°

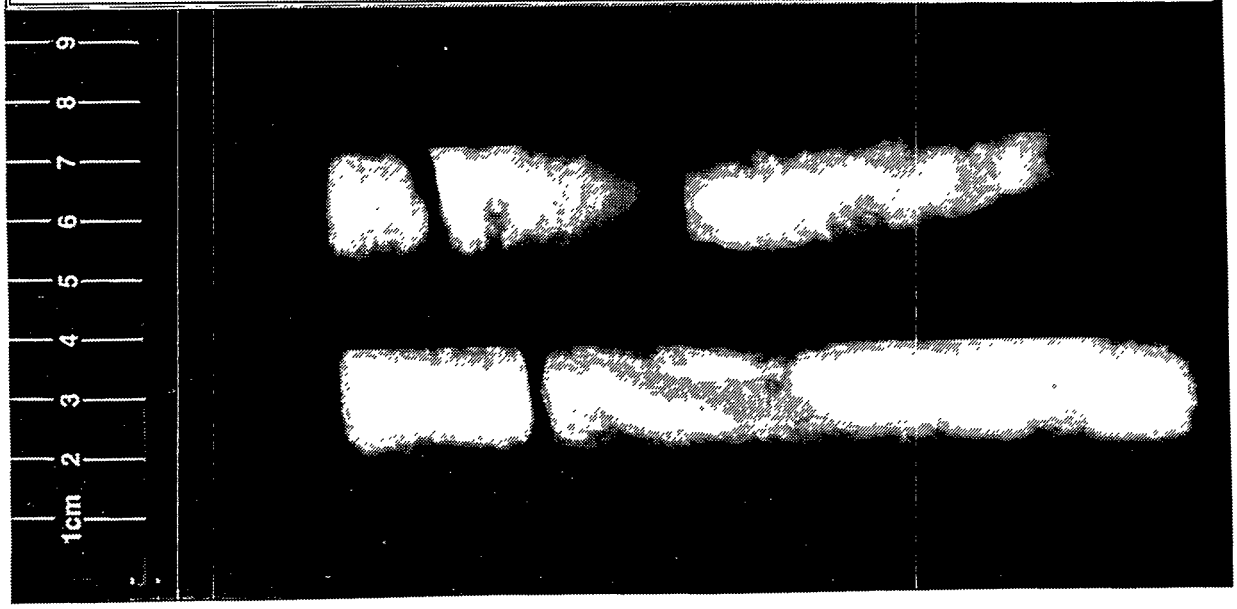

CORE LABORATORIES

SANDIA NATIONAL LABORATORIES

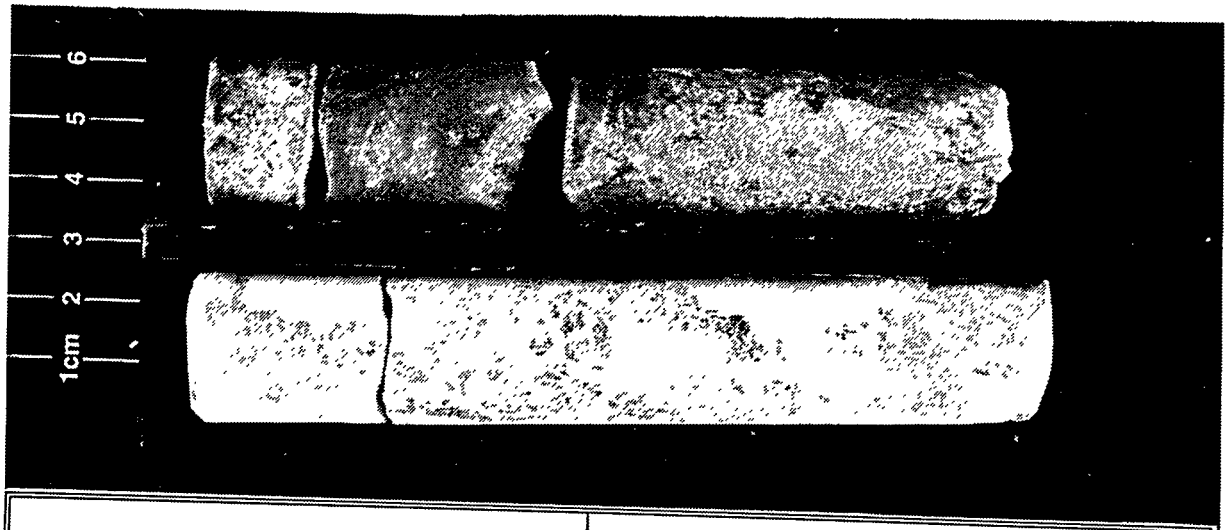

E1X 11 - 6	E1X 11 - 6
HORIZONTAL 4.25 FT.	HORIZONTAL 4.50 FT. 90°

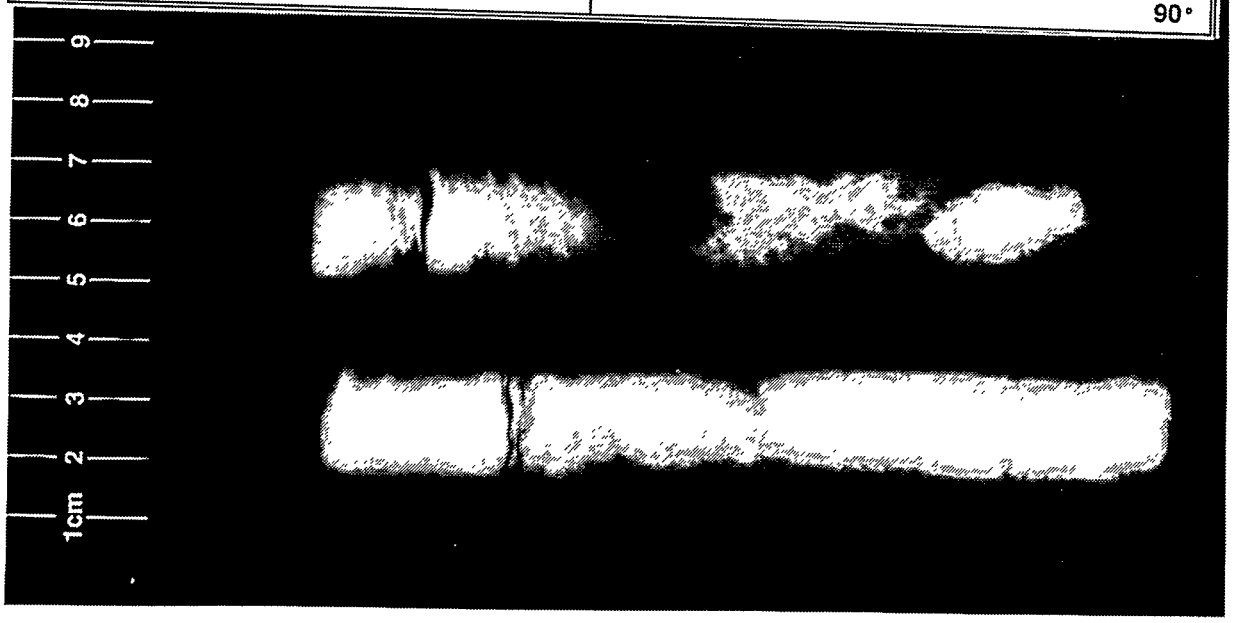

CORE LABORATORIES

SANDIA NATIONAL LABORATORIES

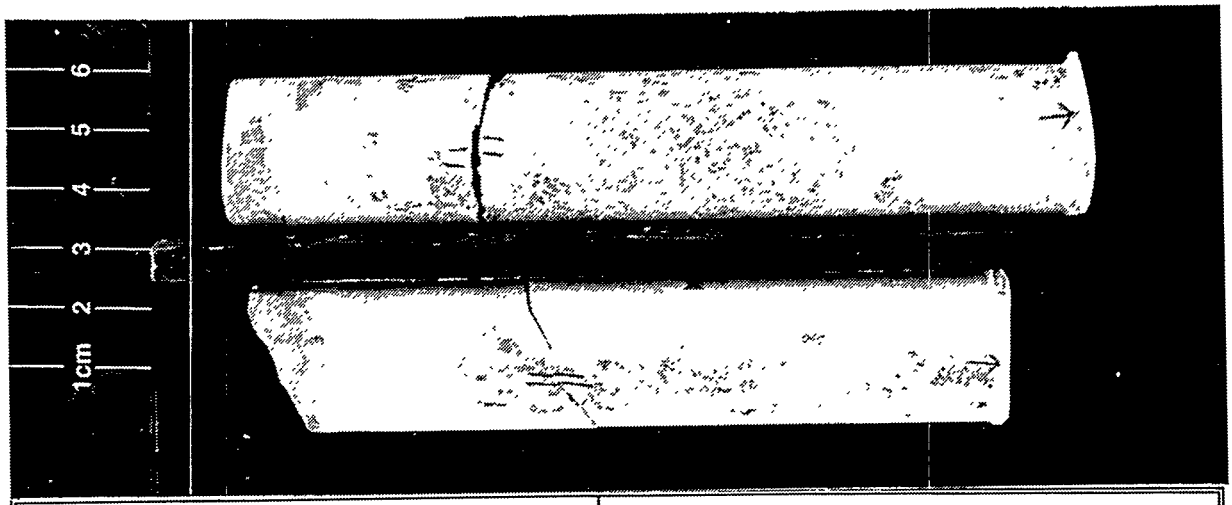

E1X 11 - 6	E1X 11 - 6
HORIZONTAL 4.75 FT.	HORIZONTAL 5.0 FT. 0°

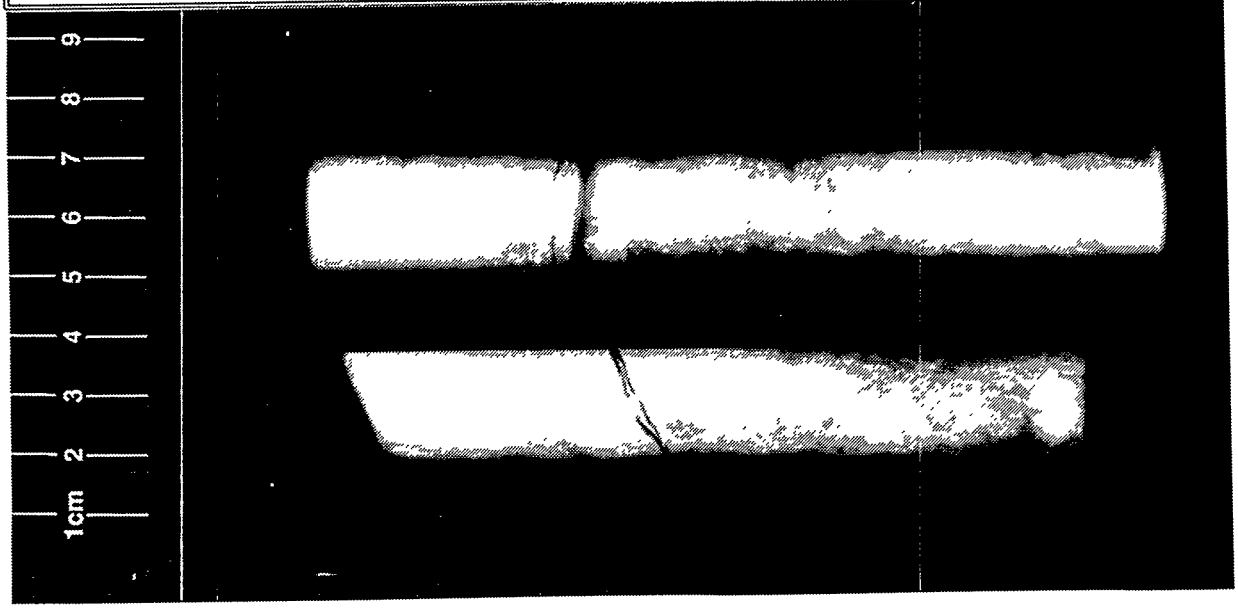

CORE LABORATORIES

SANDIA NATIONAL LABORATORIES

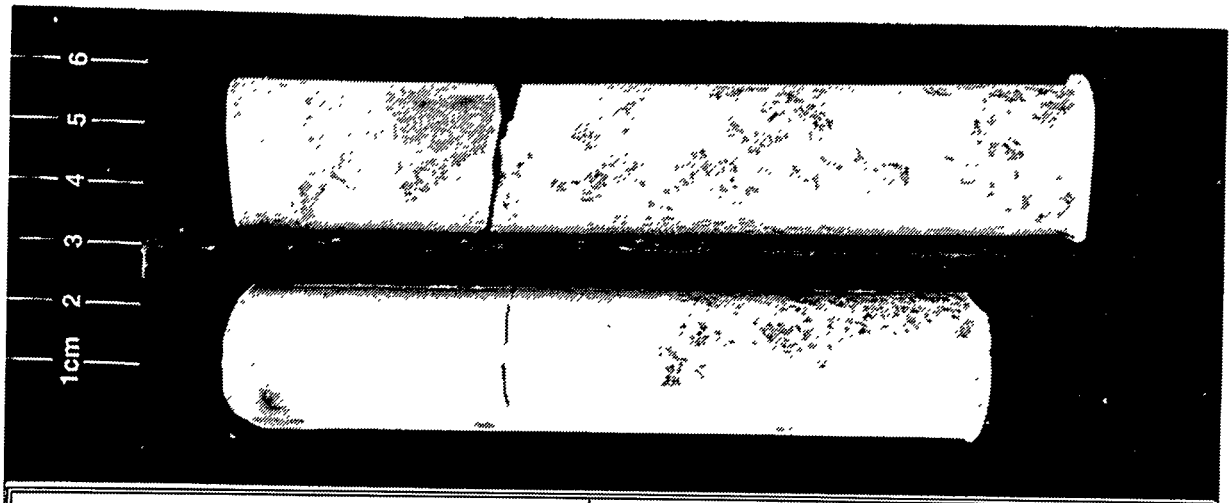

E1X 11 - 6	E1X 11 - 6
HORIZONTAL 4.75 FT.	HORIZONTAL 5.0 FT. 90°

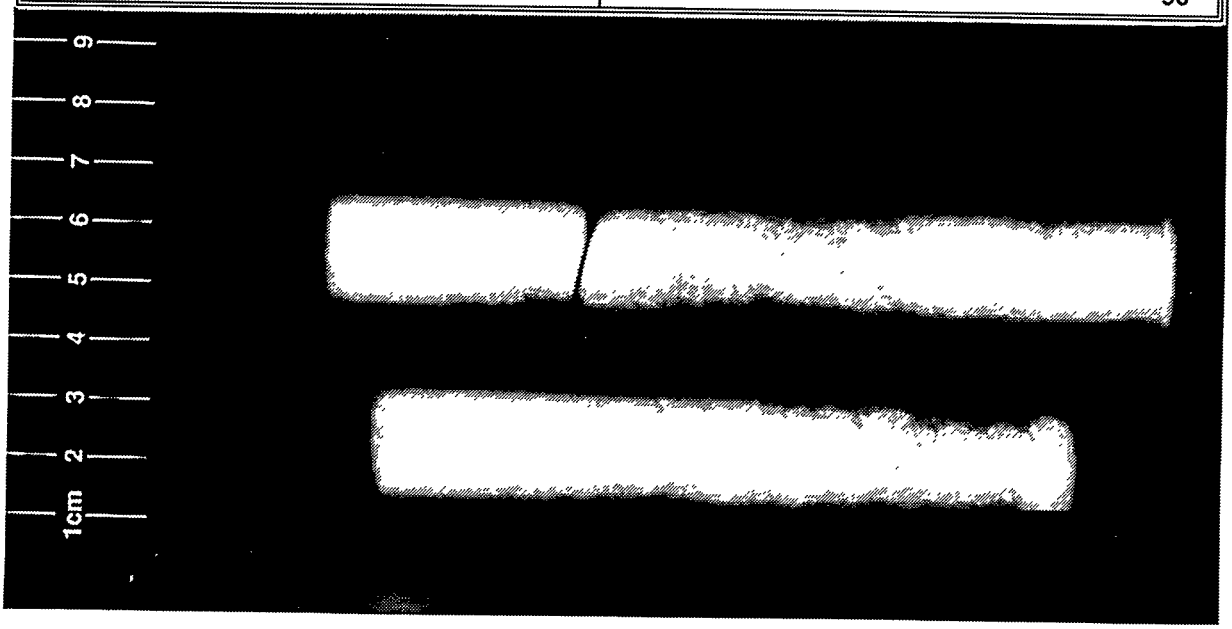

CORE LABORATORIES

SANDIA NATIONAL LABORATORIES

E1X 11 - 6	E1X 11 - 6
HORIZONTAL 5.25 FT.	HORIZONTAL 5.50 FT. 90°

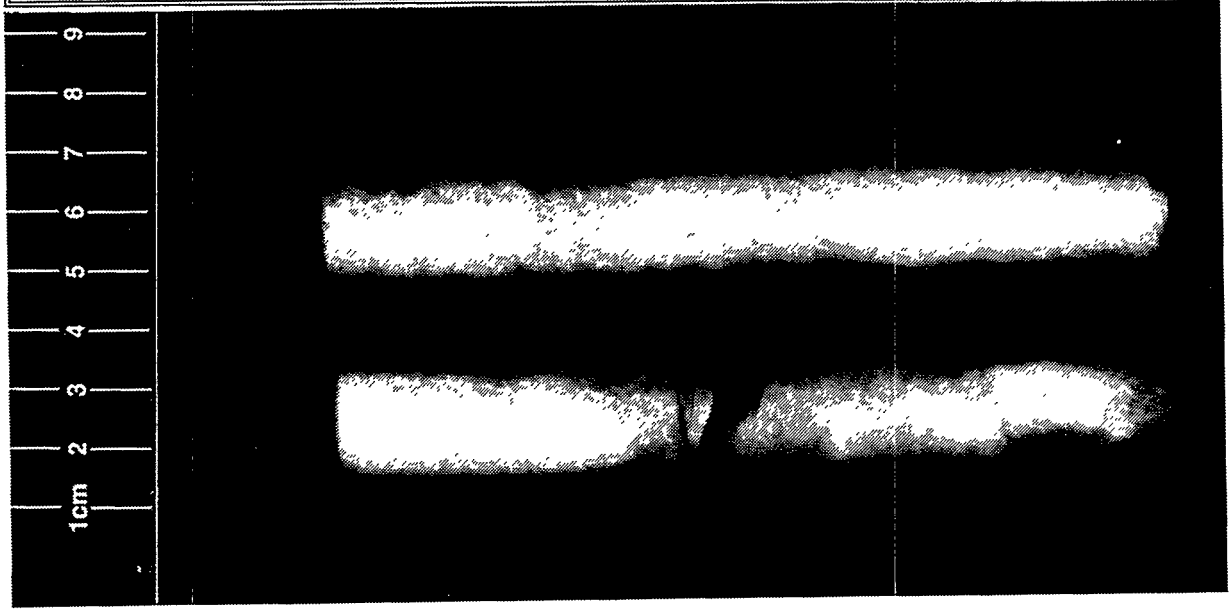

CORE LABORATORIES

SANDIA NATIONAL LABORATORIES

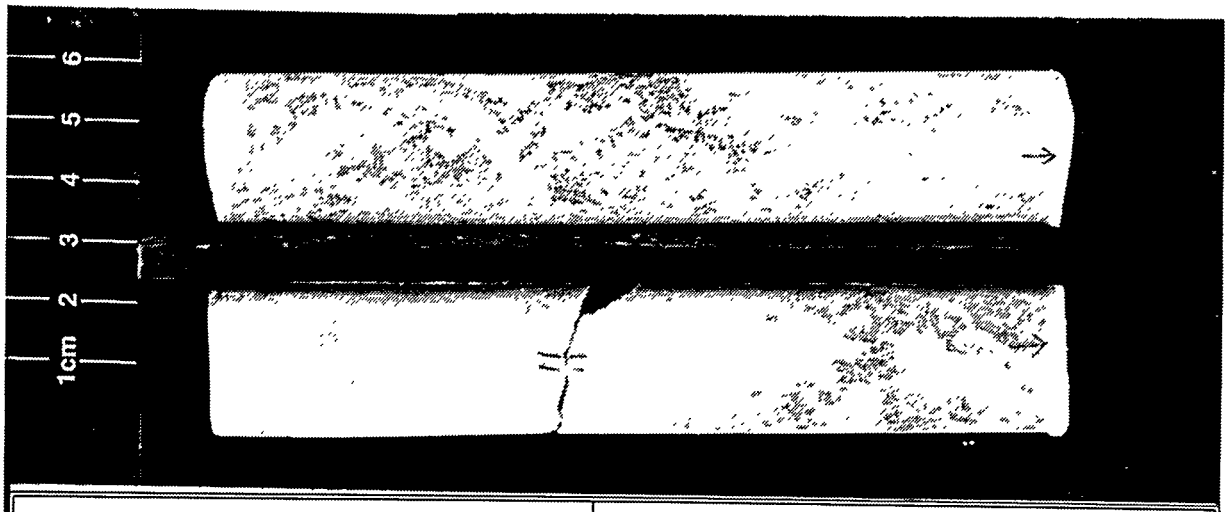

E1X 11 - 6	E1X 11 - 6
HORIZONTAL 5.25 FT.	HORIZONTAL 5.50 FT. 0°

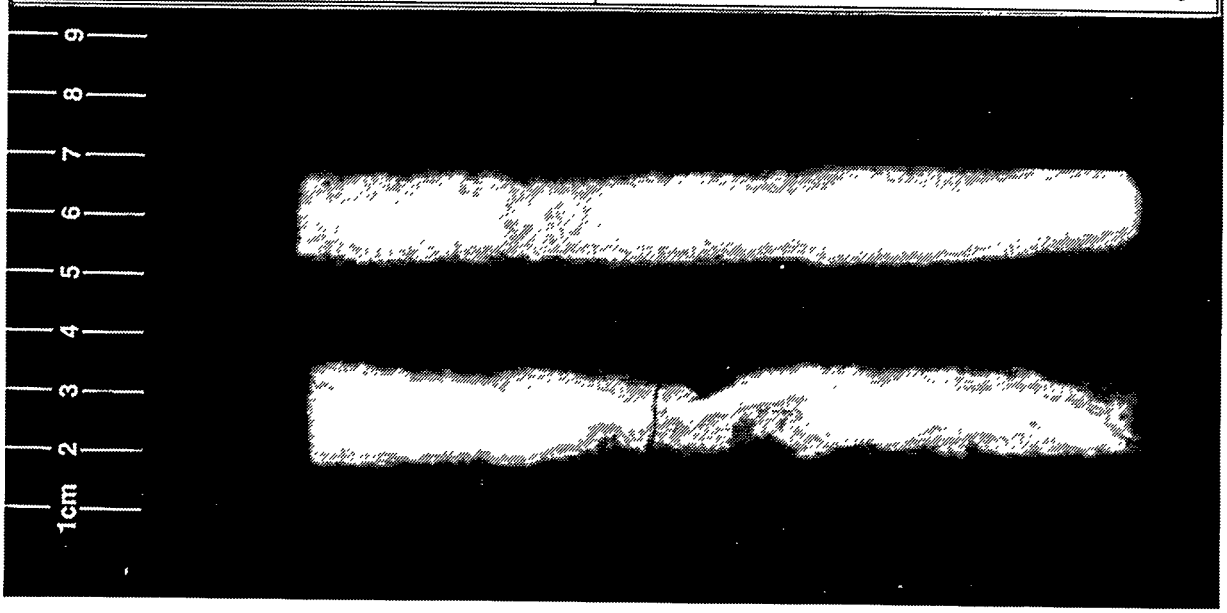

SANDIA NATIONAL LABORATORIES

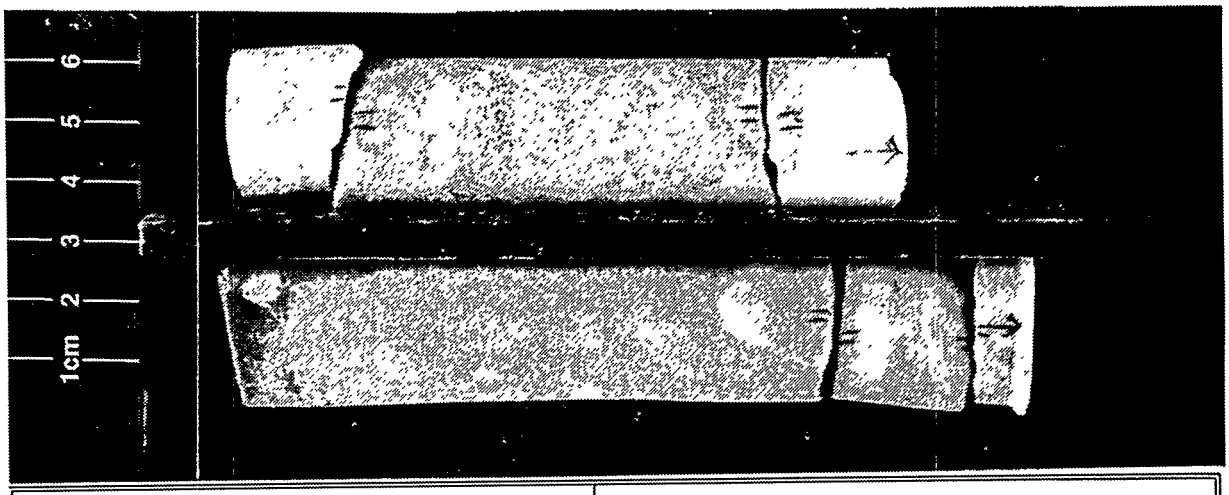

E1X 11 - 6	E1X 11 - 6
VERTICAL 5.25 FT.	VERTICAL 5.75 FT. 0°

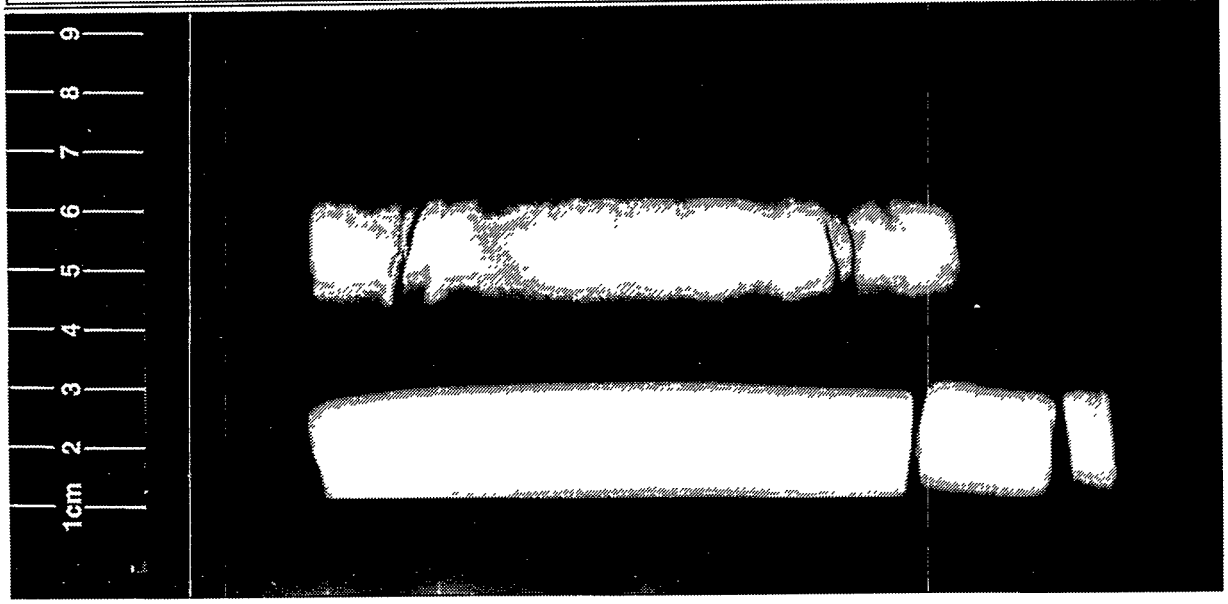

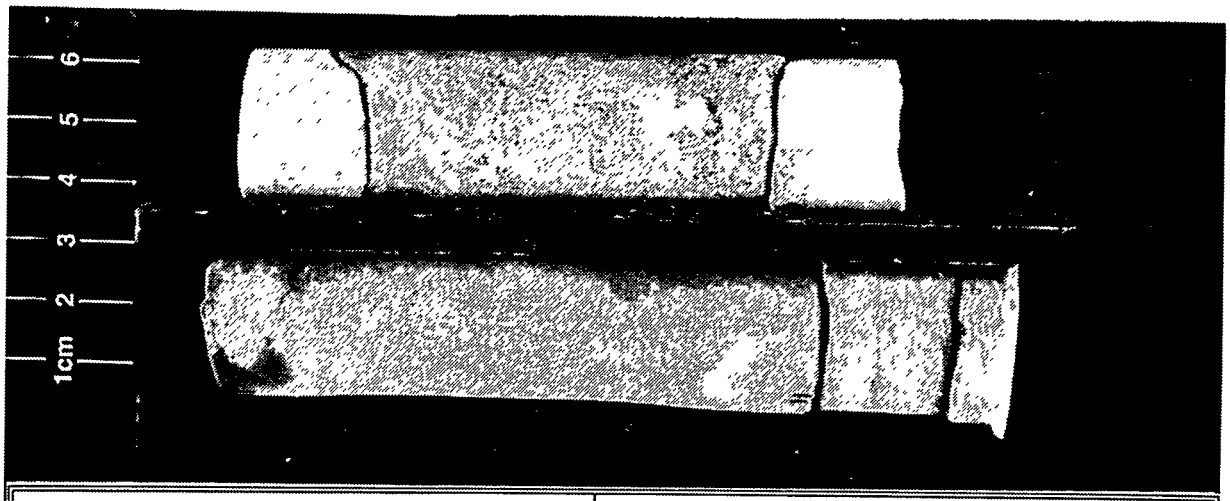

E1X 11 - 6	E1X 11 - 6
VERTICAL 5.25 FT.	VERTICAL 5.75 FT. 90°

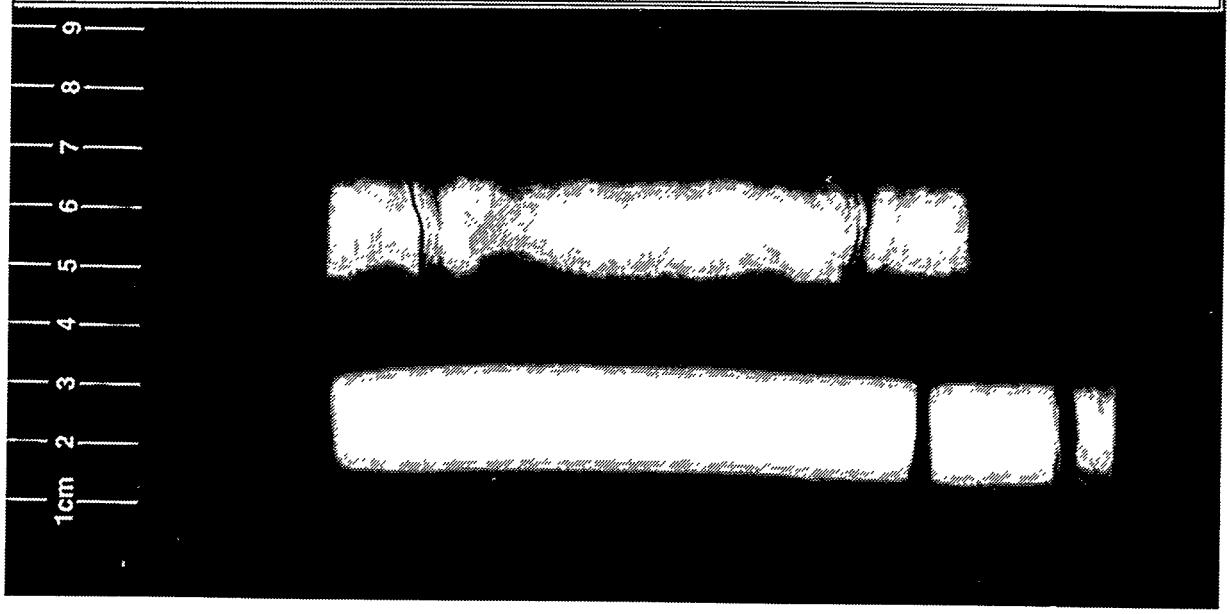

CORE LABORATORIES

SANDIA NATIONAL LABORATORIES

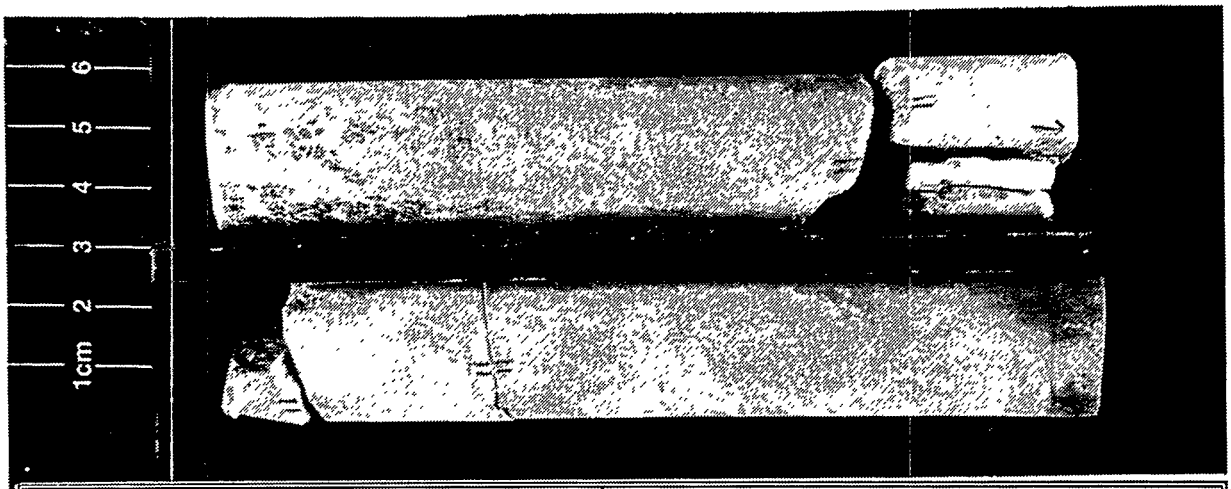

E1X 11 - 6	E1X 11 - 6
HORIZONTAL 5.75 FT.	HORIZONTAL 6.0 FT. 0°

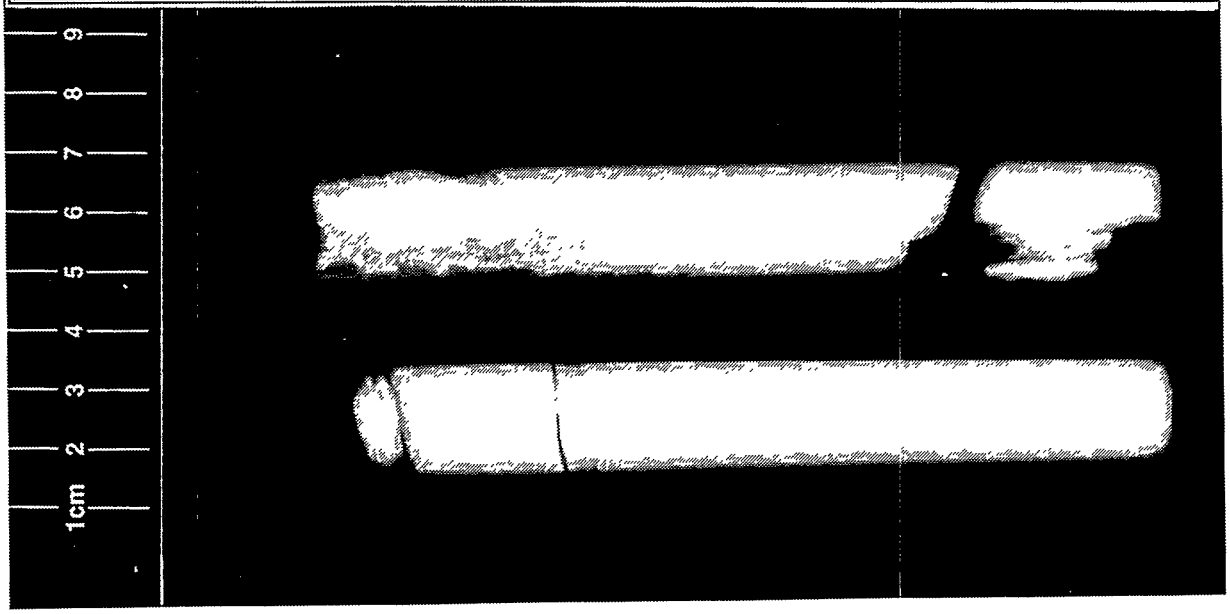

CORE LABORATORIES

SANDIA NATIONAL LABORATORIES

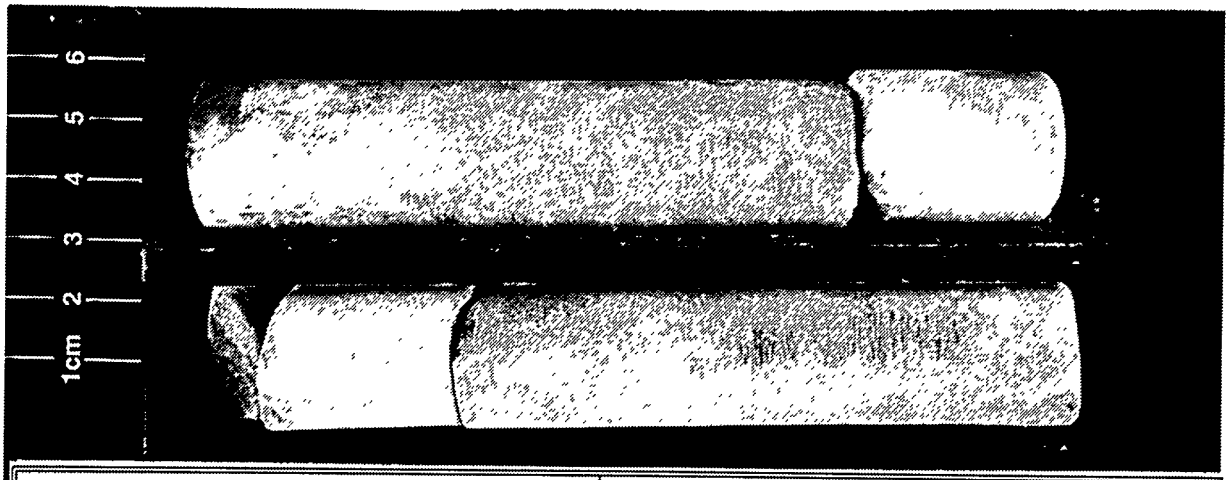

E1X 11 - 6	E1X 11 - 6
HORIZONTAL 5.75 FT.	HORIZONTAL 6.0 FT. 90°

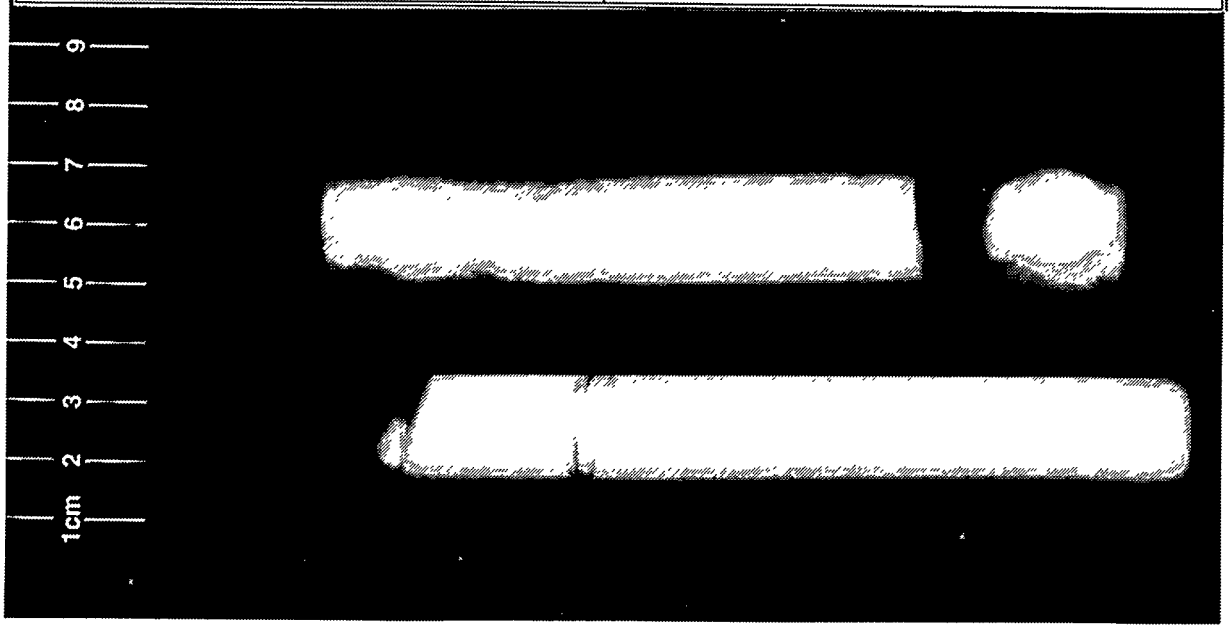

CORE LABORATORIES

SANDIA NATIONAL LABORATORIES

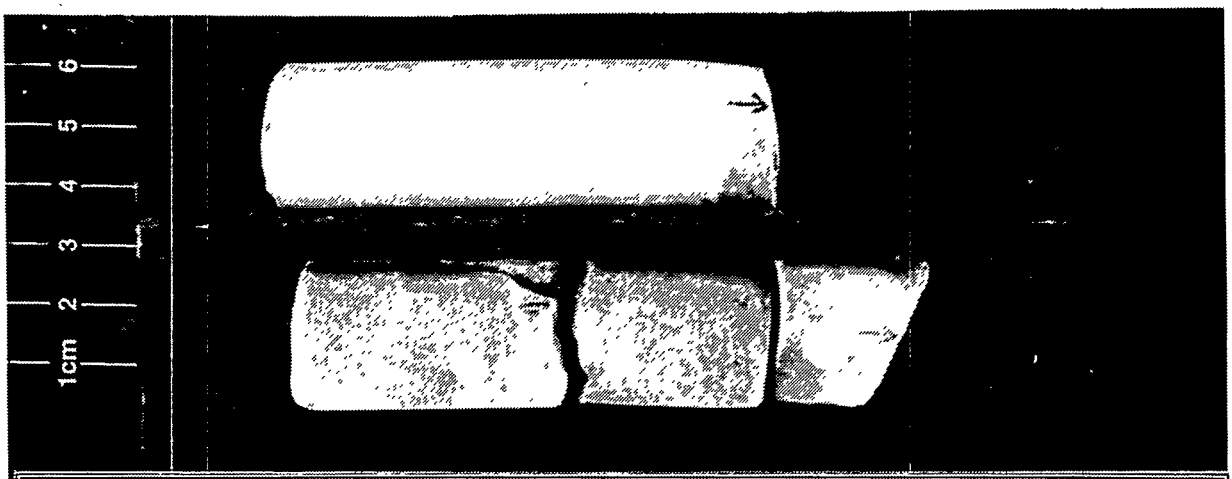

E1X 10 - 7	E1X 11 - 6
VERTICAL 6.25 FT.	VERTICAL 4.75 FT. 0°

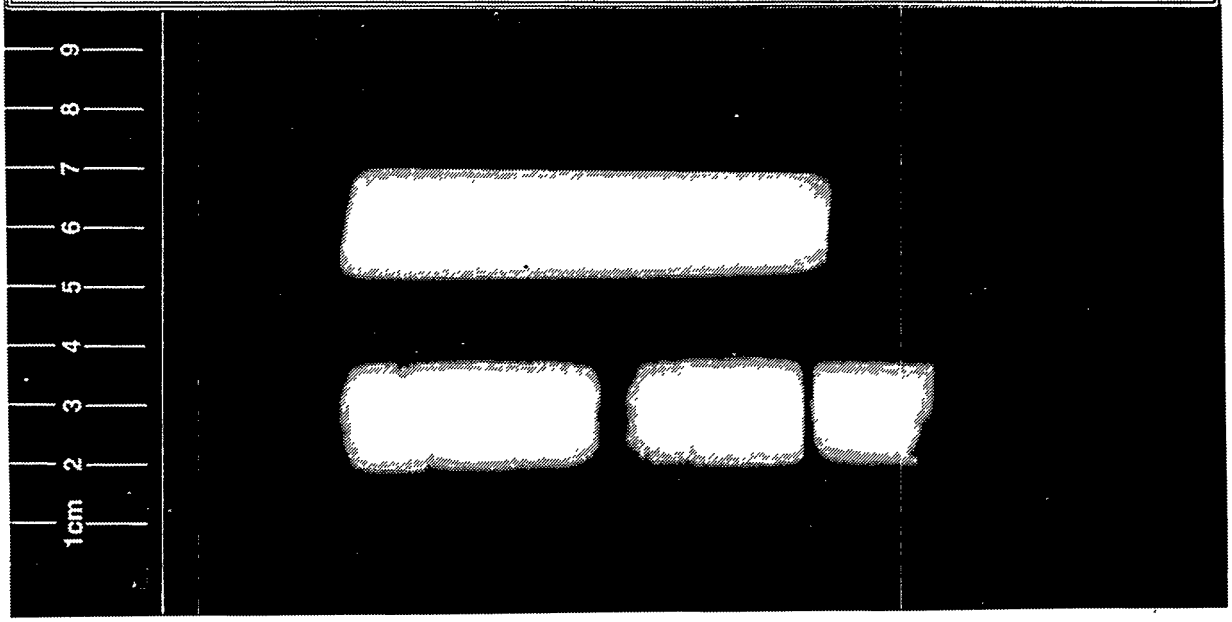

CORE LABORATORIES

SANDIA NATIONAL LABORATORIES

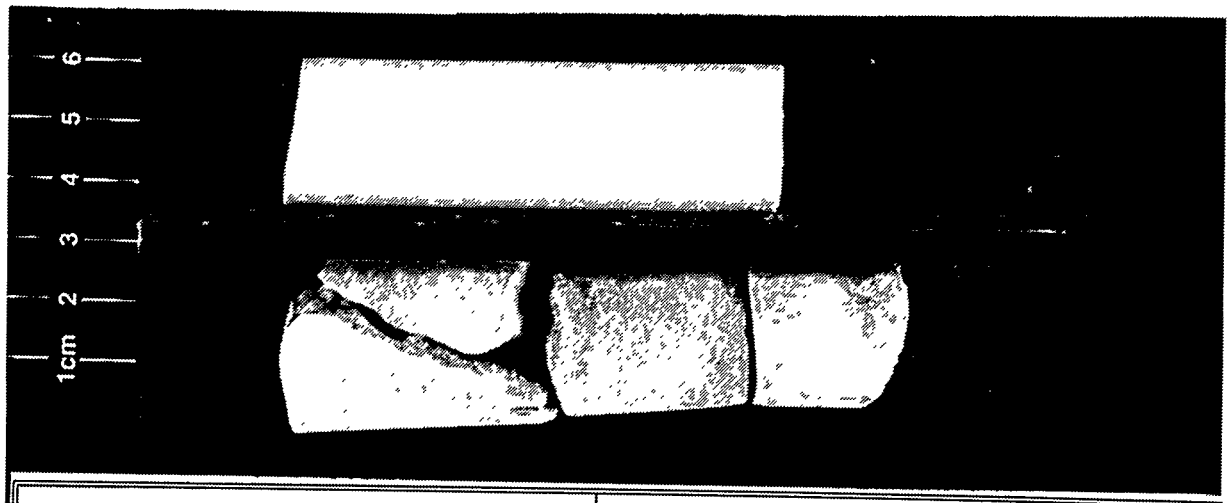

E1X 10 - 7	E1X 11 - 6
VERTICAL 6.25 FT.	VERTICAL 4.75 FT. 90°

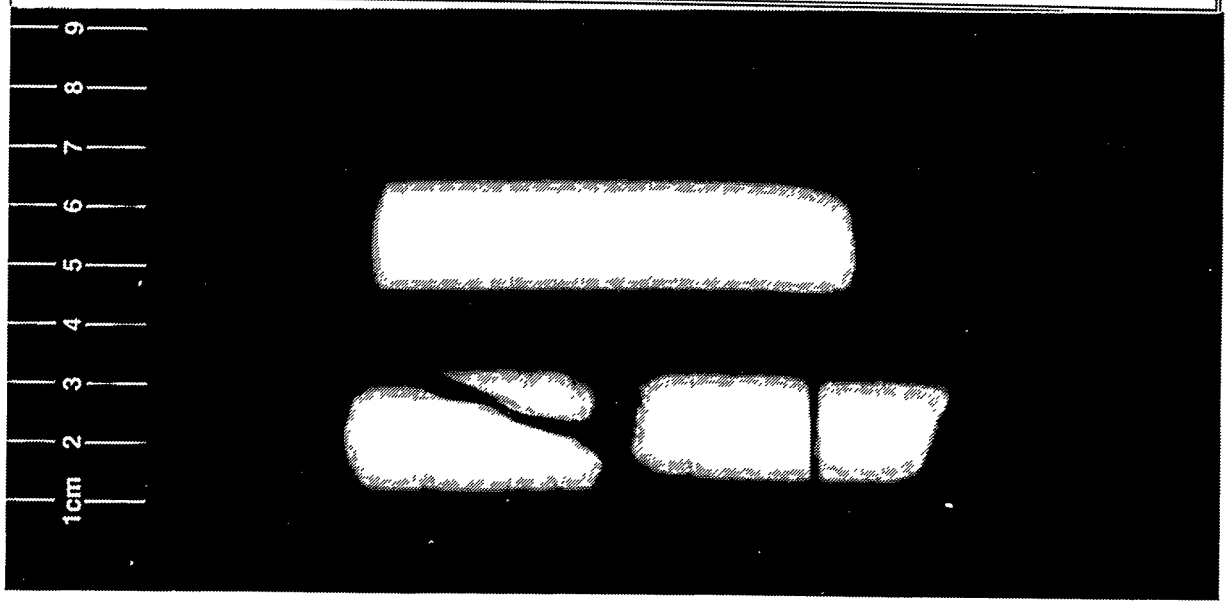

CORE LABORATORIES

SANDIA NATIONAL LABORATORIES

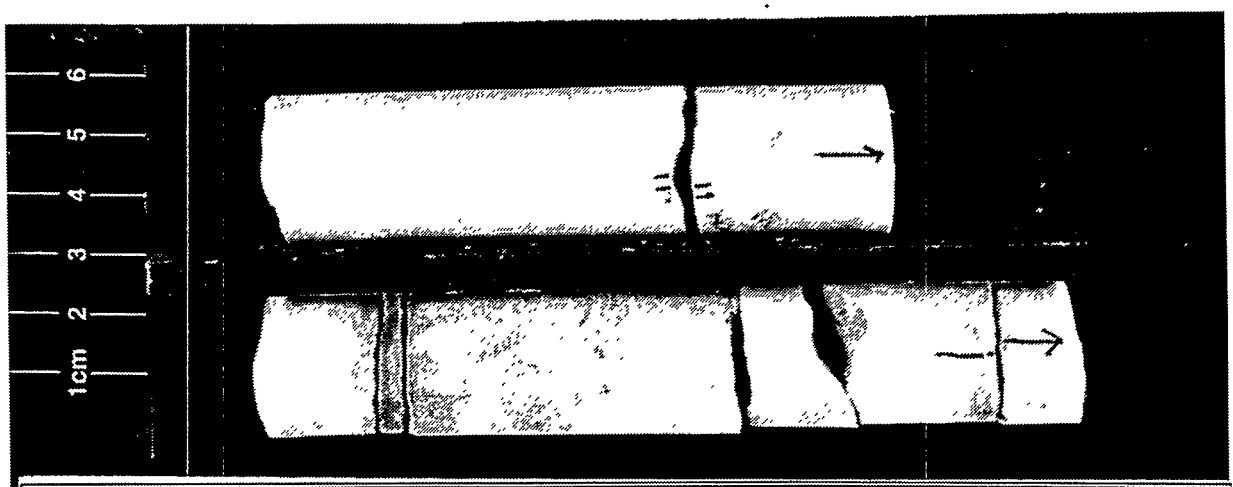

E1X 10 - 6	E1X 10 - 6
VERTICAL 5.25 FT.	VERTICAL 5.75 FT. 0°

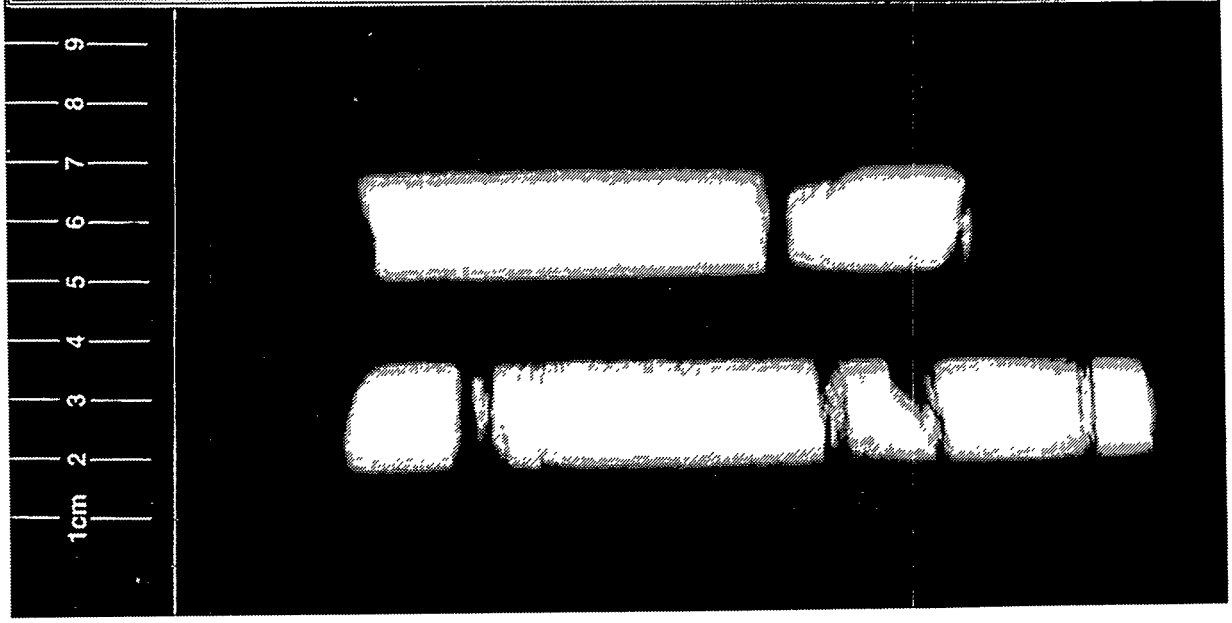

CORE LABORATORIES

SANDIA NATIONAL LABORATORIES

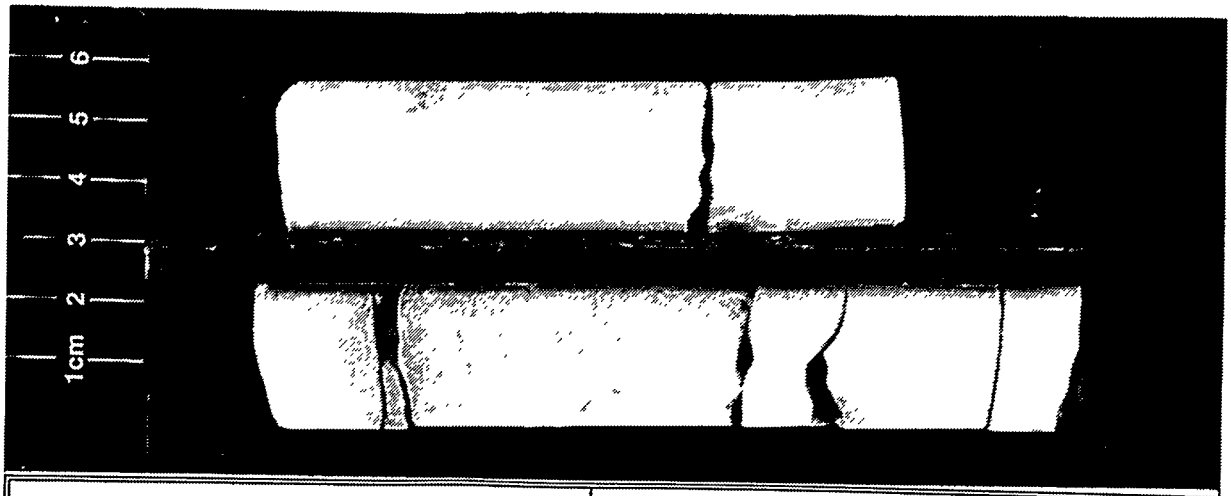

E1X 10 - 6	E1X 10 - 6
VERTICAL 5.25 FT.	VERTICAL 5.75 FT. 90°

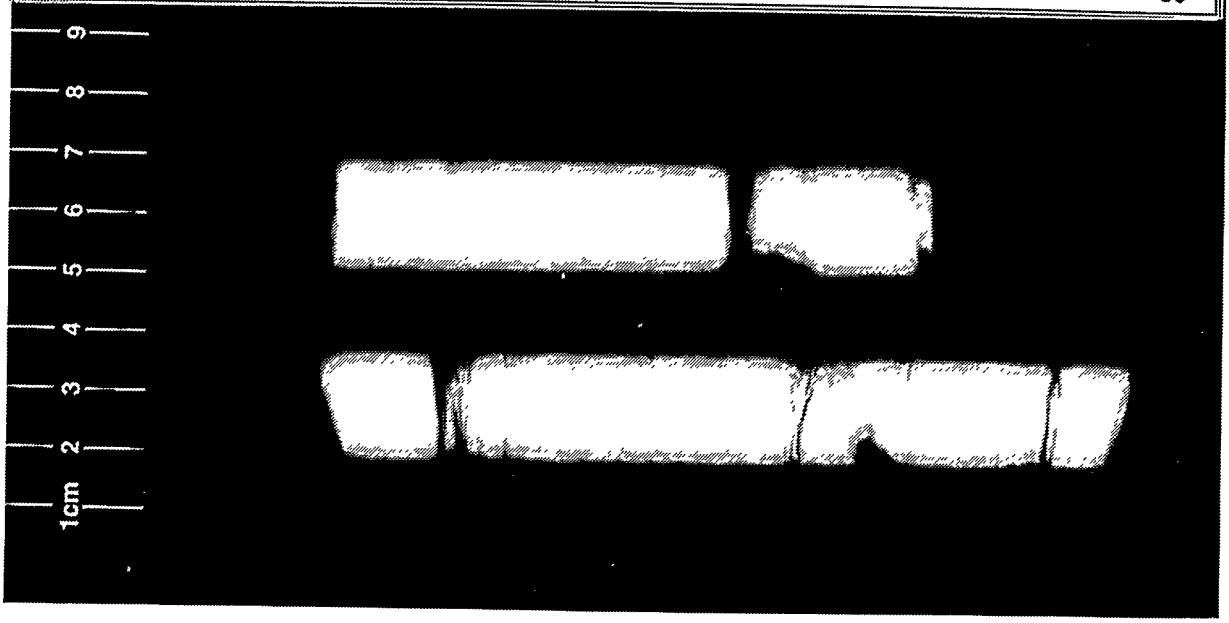

CORE LABORATORIES

SANDIA NATIONAL LABORATORIES

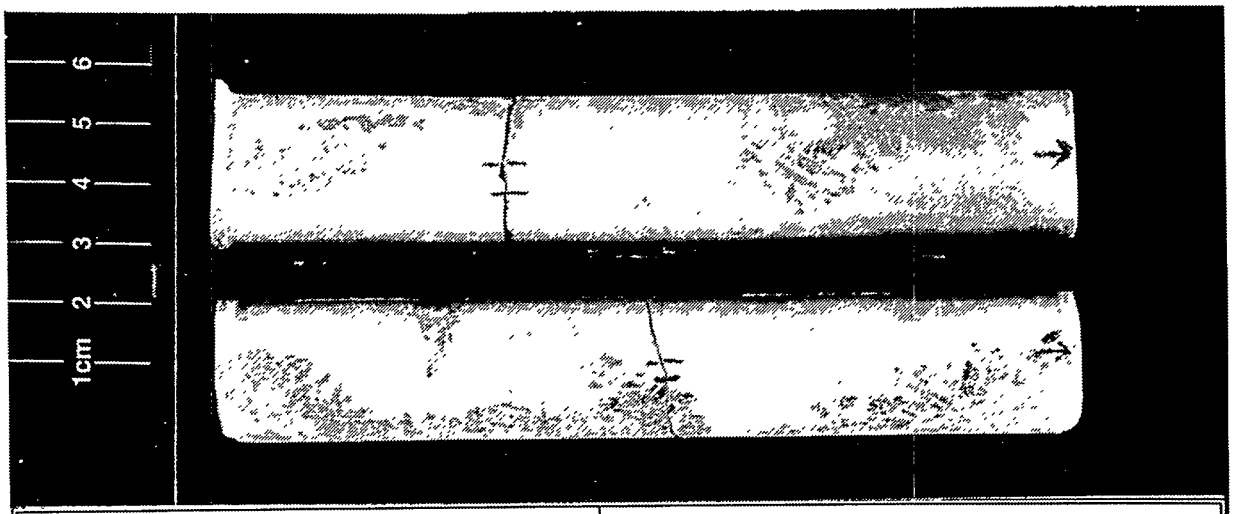

E1X 10 - 6	E1X 10 - 6
HORIZONTAL 5.50 FT.	HORIZONTAL 5.75 FT. 0°

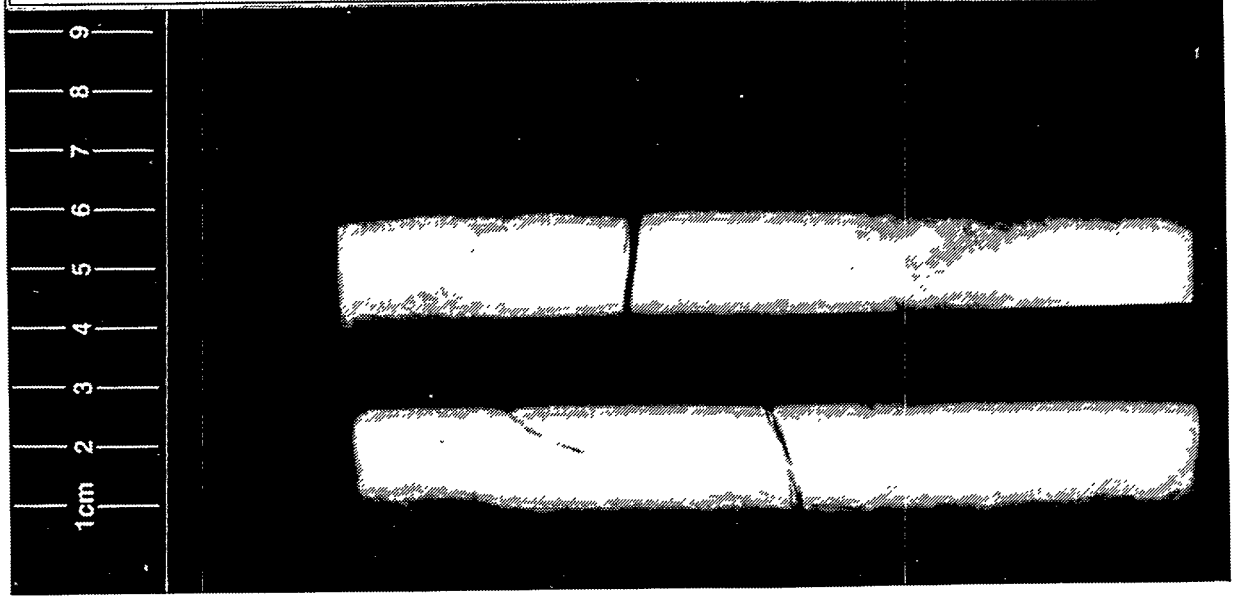

CORE LABORATORIES

SANDIA NATIONAL LABORATORIES

E1X 10 - 6	E1X 10 - 6
HORIZONTAL 5.50 FT.	HORIZONTAL 5.75 FT. 90°

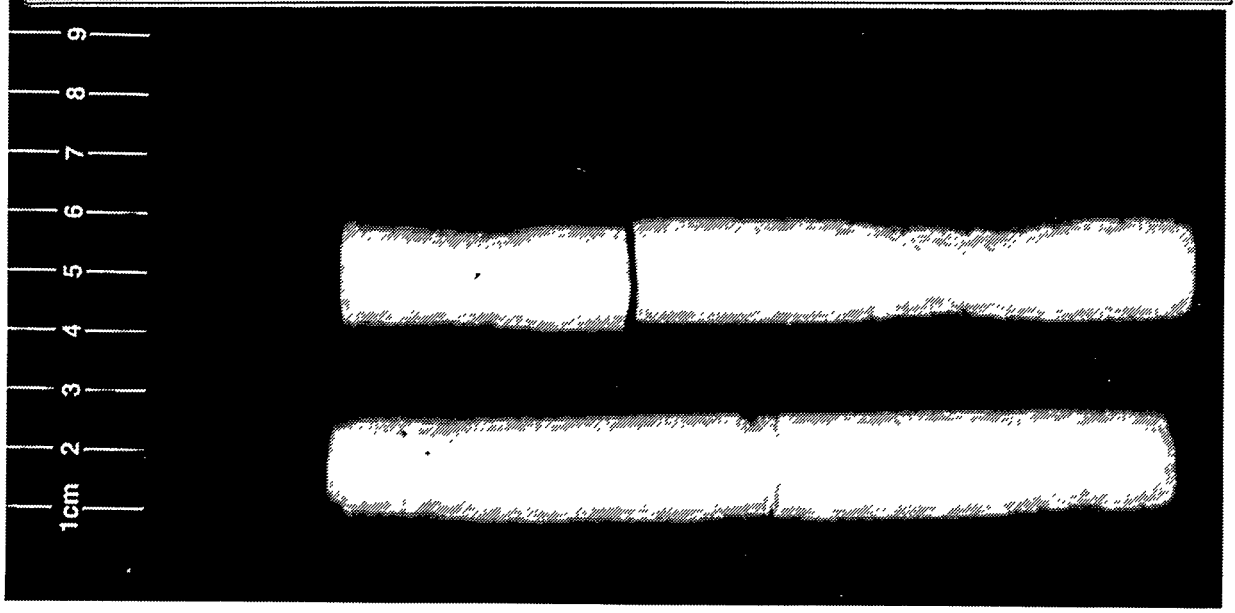

CORE LABORATORIES

SANDIA NATIONAL LABORATORIES

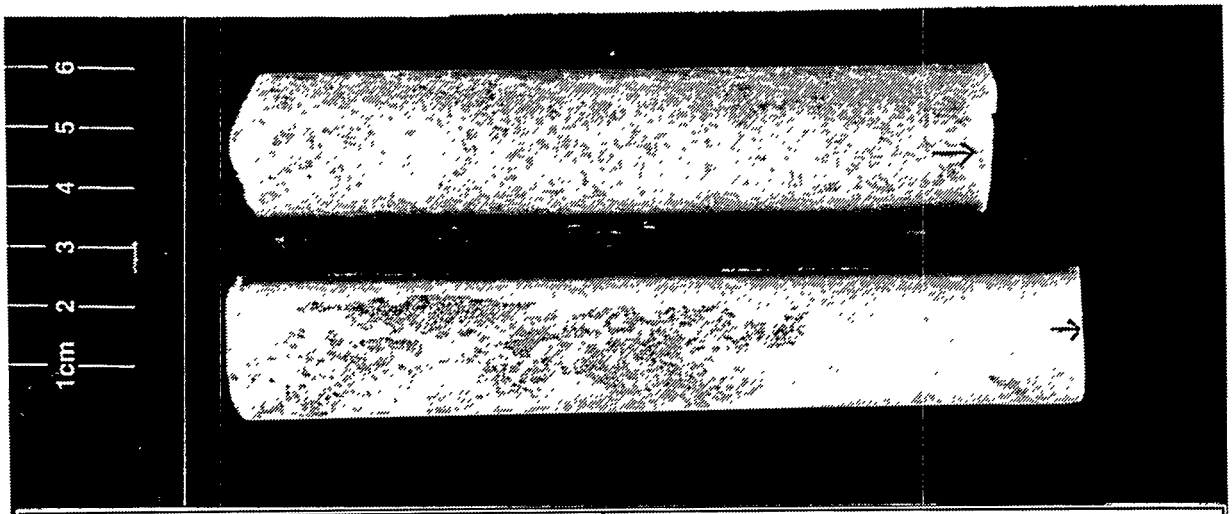

E1X 10 - 6	E1X 10 - 6
HORIZONTAL 5.0 FT.	HORIZONTAL 5.25 FT. 0°

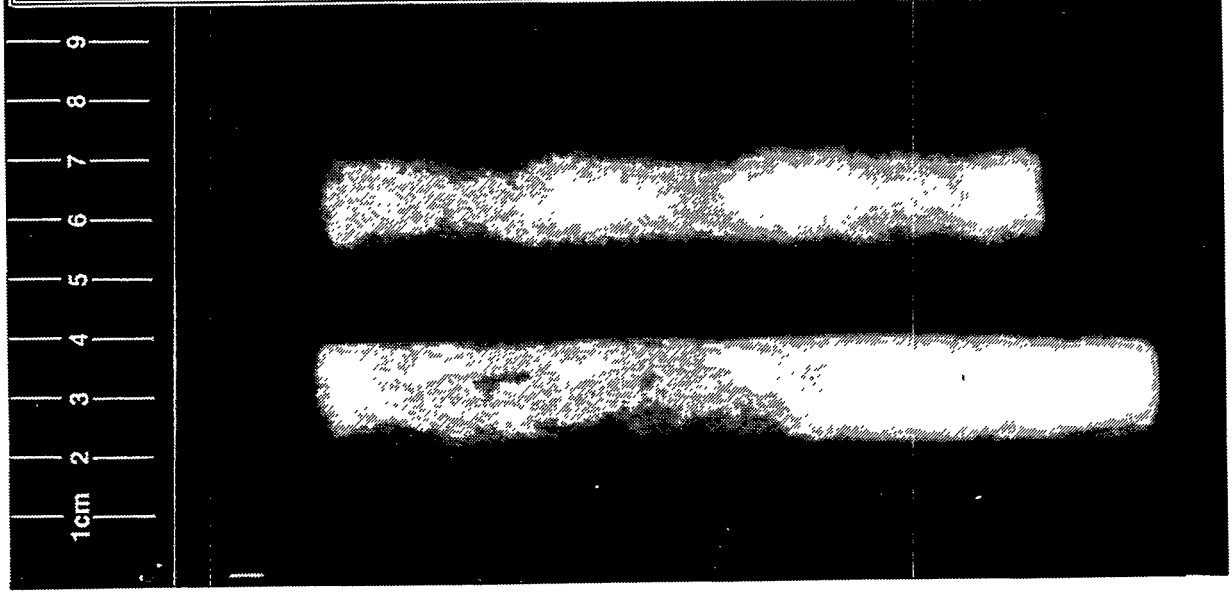

CORE LABORATORIES

SANDIA NATIONAL LABORATORIES

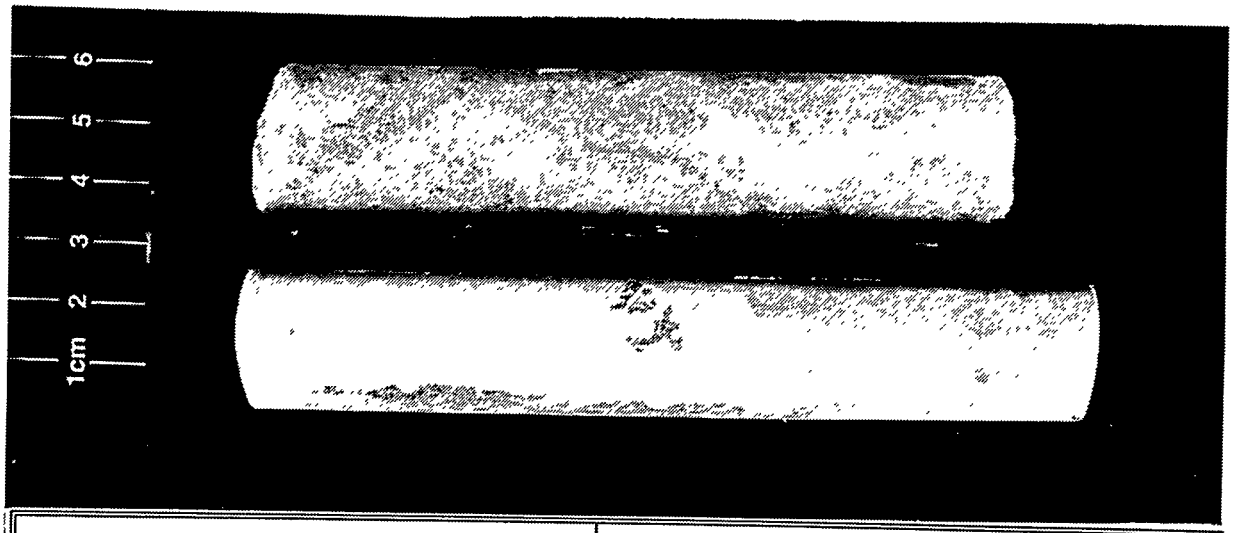

E1X 10 - 6	E1X 10 - 6
HORIZONTAL 5.0 FT.	HORIZONTAL 5.25 FT. 90°

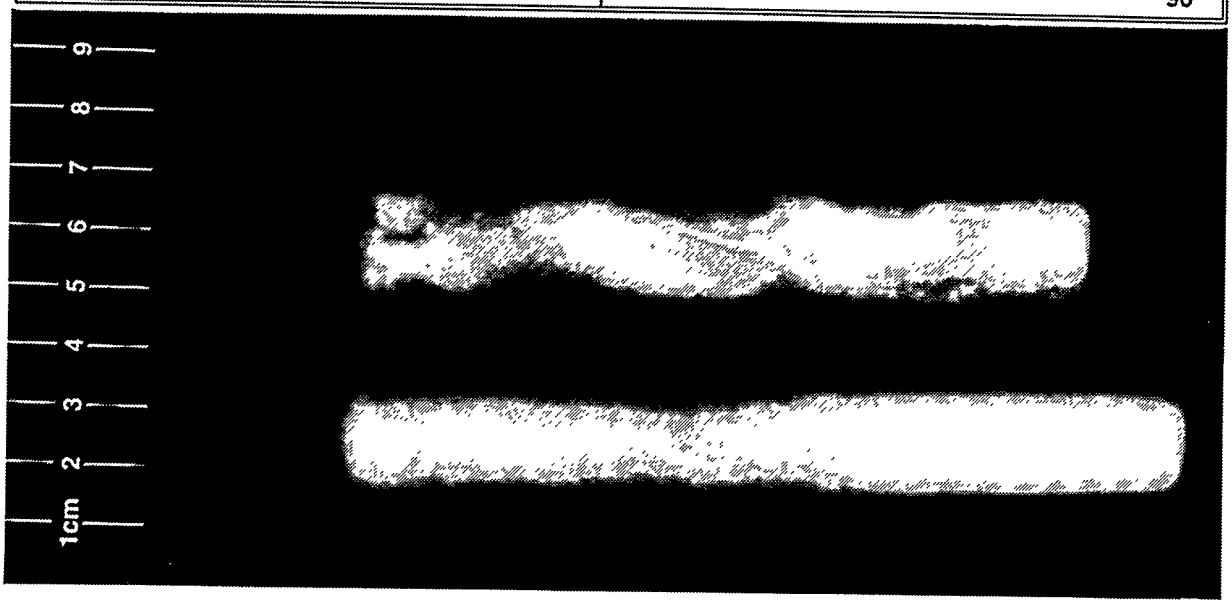

CORE LABORATORIES

Western Atlas International

SANDIA NATIONAL LABORATORIES

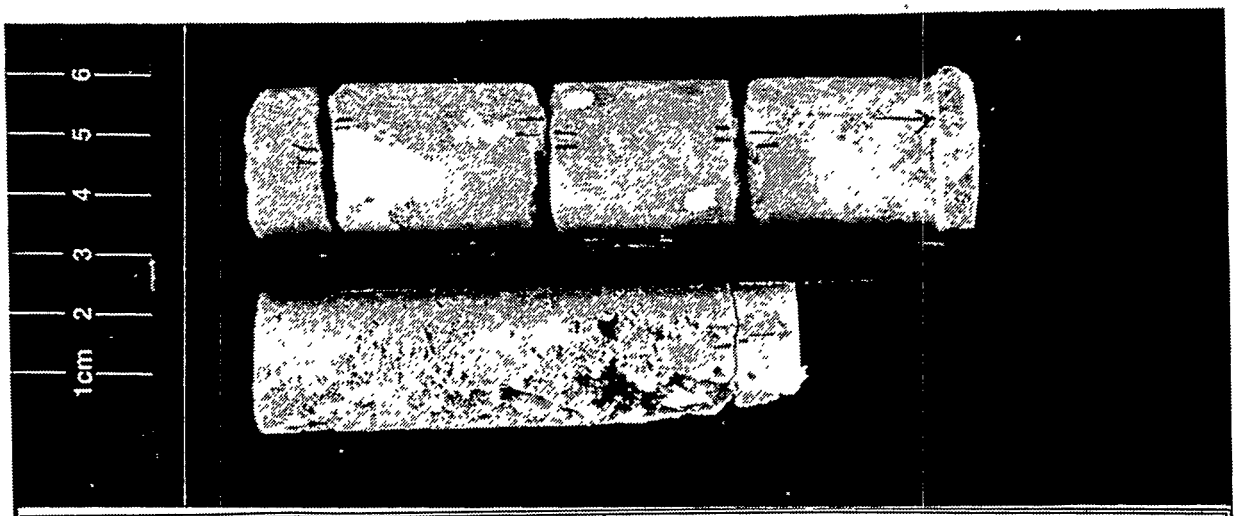

E1X 10 - 6	E1X 10 - 6
HORIZONTAL 4.50 FT.	HORIZONTAL 4.75 FT. 0°

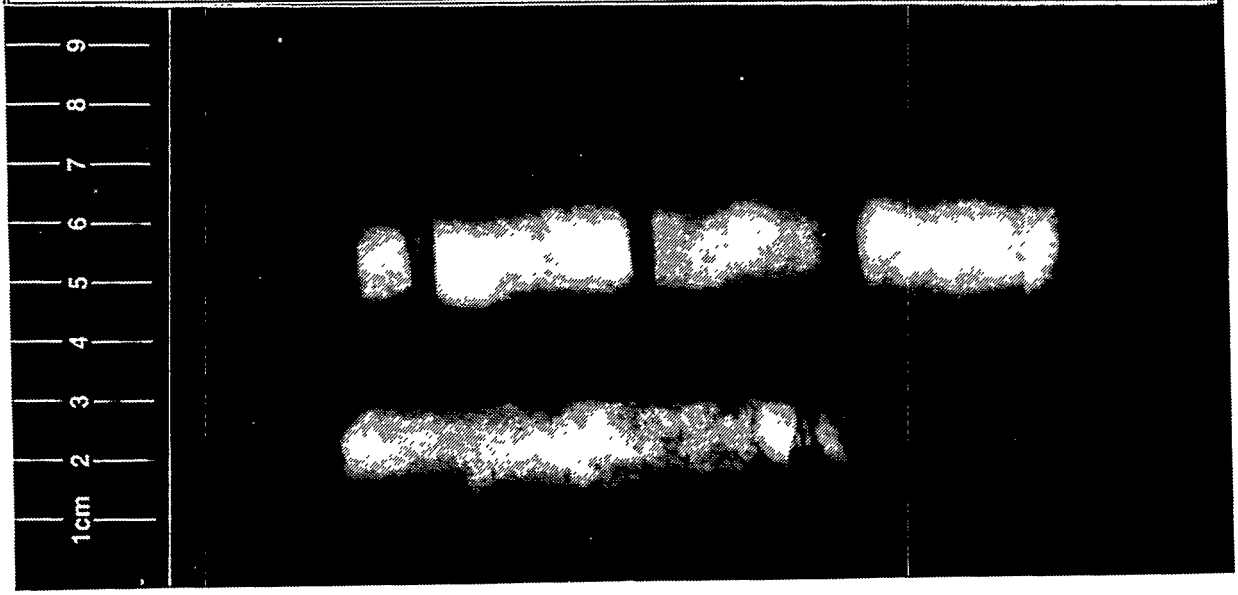

SANDIA NATIONAL LABORATORIES

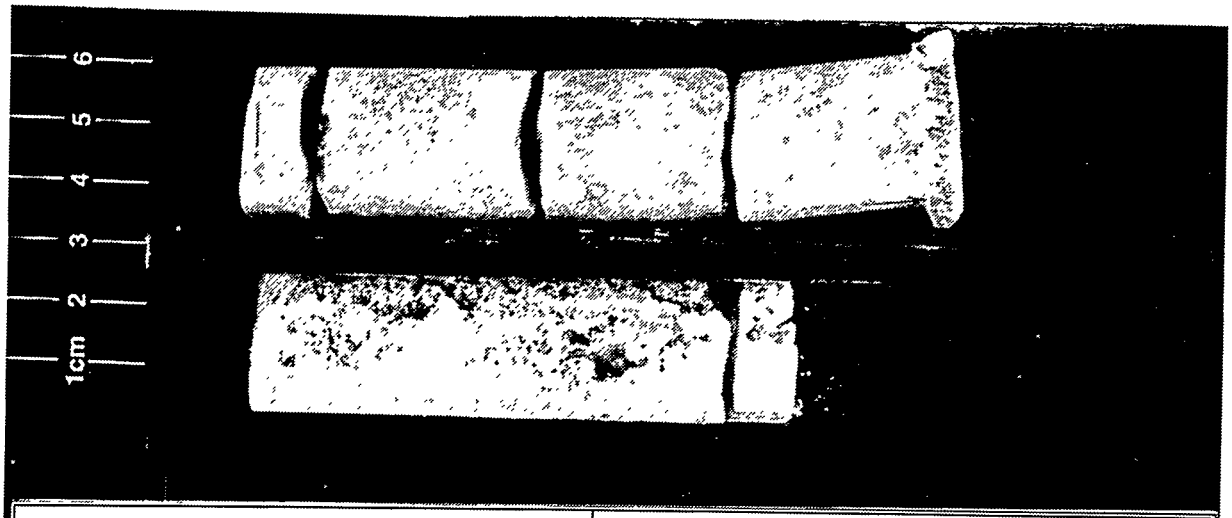

E1X 10 - 6	E1X 10 - 6
HORIZONTAL 4.50 FT.	HORIZONTAL 4.75 FT. 90°

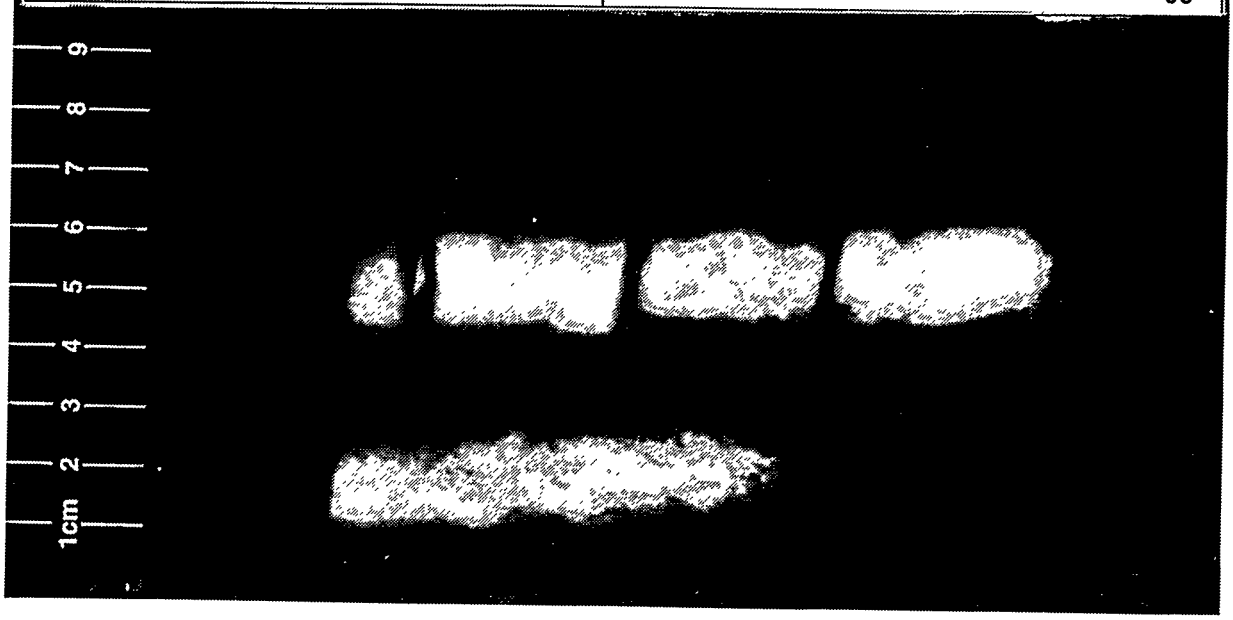

SANDIA NATIONAL LABORATORIES

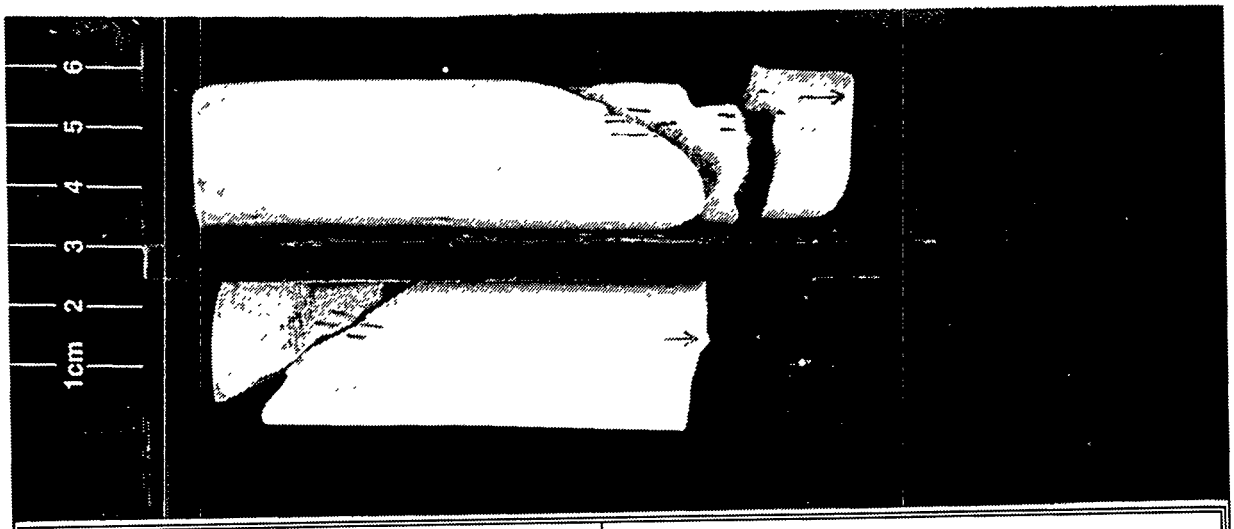

E1X 10 - 7	E1X 10 - 7
HORIZONTAL 6.0 FT.	HORIZONTAL 6.25 FT. 0°

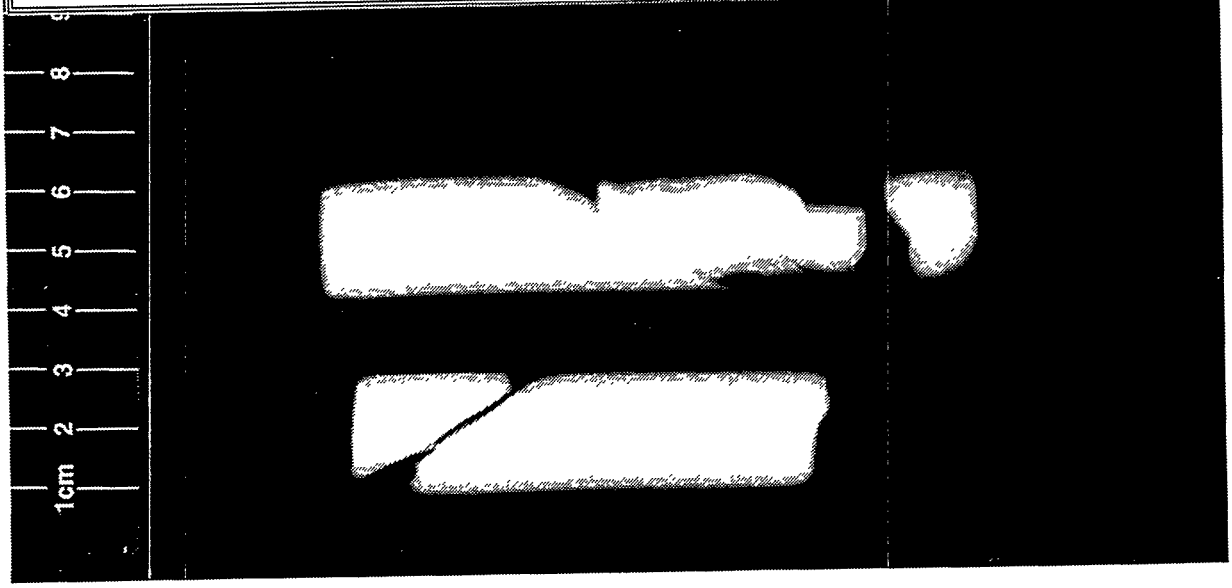

CORE LABORATORIES

SANDIA NATIONAL LABORATORIES

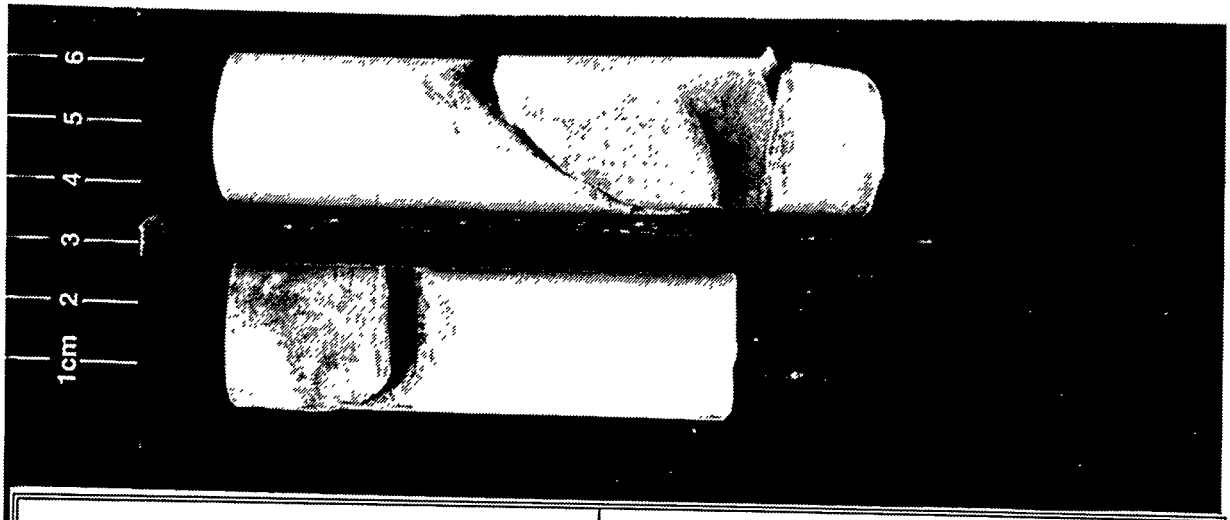

E1X 10 - 7	E1X 10 - 7
HORIZONTAL 6.0 FT.	HORIZONTAL 6.25 FT. 90°

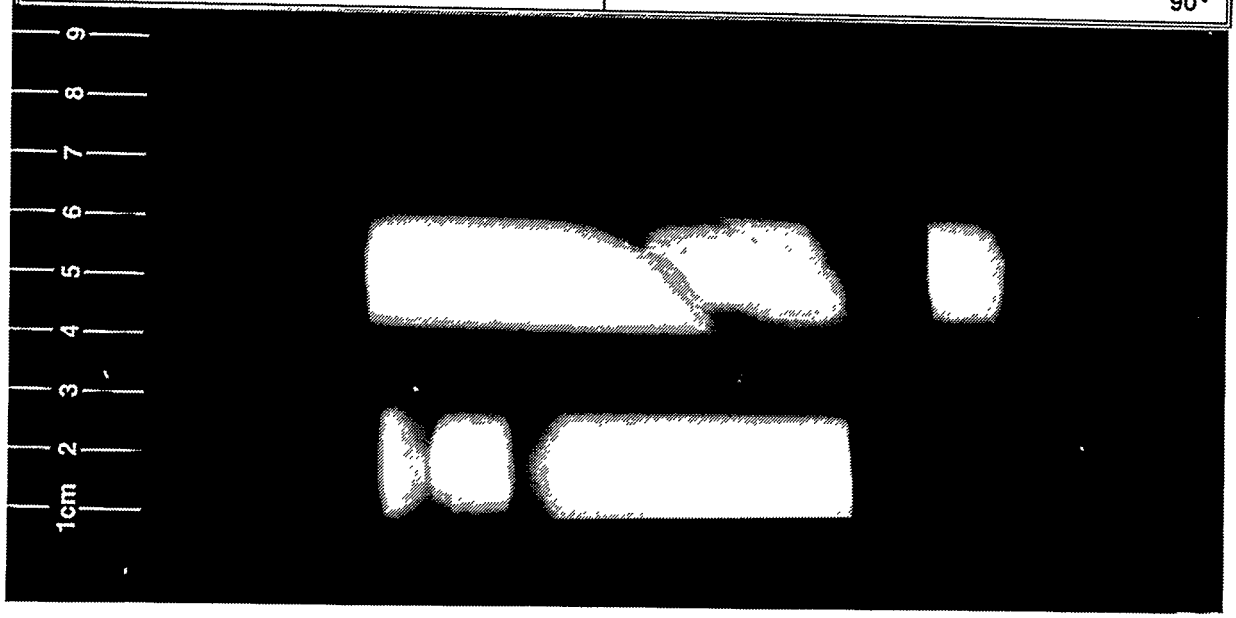

Appendix A-B.
Appendix B of Appendix A [Data Report: Rock Physics Associates (Core Laboratories)]

PETROGRAPHIC STUDY
FOR
ROCK PHYSICS ASSOCIATES
WASTE ISOLATION PILOT PLANT

OMNI Laboratories, Inc.

(713) 862-2400
6955 Portwest Drive • Suite 100 • Houston, Texas 77024-8018

August 2, 1993

Dr. Joel Walls
Rock Physics Associates
4320 Stevens Creek Boulevard
Suite #282
San Jose, California 95129

SUBJECT: Petrographic Study
Waste Isolation Pilot Plant
File No: G-2016

Dear Dr. Walls,

The following final report presents the results of a Petrographic Study, which includes thin section analysis and X-ray diffraction analysis (XRD), performed on fifteen (15) core plug end trim samples from the above referenced well. Included in this report are the analytical data, interpretations of results, and photomicrographs with descriptions. Two (2) copies of this report with photomicrographs are provided, as well as 2 xerox copies.

It has been a pleasure to provide this study for Rock Physics Associates. Feel free to contact us if you have any questions concerning this report or if we can be of further service.

Sincerely,

OMNI LABORATORIES

Michael Dixon
Manager, Geologic Services

Monte C. Manske
Senior Geologist

SUMMARY OF PETROGRAPHIC RESULTS

A Petrographic Study was performed on fifteen (15) core plug end trim samples. Included with this Petrographic Study are both thin section analysis and X-ray diffraction (XRD) analysis.

These samples are all evaporitic. Samples consist of a limited mineralogic suite of halite, anhydrite, gypsum, magnesite, and clay. Anhydrite, present in all samples, is the most common mineral. Halite is also very common and occurs in most samples, in some cases nearly as abundant as anhydrite. Magnesite occurs in low amounts in all samples. Gypsum and clay are trace components of most samples. Some iron oxide staining is evident in certain thin sections, but was not quantified.

INTRODUCTION

Thin section petrography and X-ray diffraction (XRD) analyses were performed on 15 core plug end trim samples from the referenced well. Table 1 outlines the sample designations and analyses performed.

TABLE 1

SAMPLE NUMBERS AND PETROGRAPHIC ANALYSES PERFORMED

SAMPLE DESIGNATION (EIX)	SAMPLE # (OMNI)	THIN SECTION (TS)	X-RAY DIFFRACTION (XRD)
10-6 H-4.50'	01	X	X
10-6 H-5.00'	02	X	X
10-6 H-5.25'	03	X	X
10-6 V-5.25'	04	X	X
10-6 H-5.50'	05	X	X
10-6 H-5.75'	06	X	X
10-6 V-5.75'	07	X	X
10-7 V-6.25'	08	X	X
11-6 H-4.50'	09	X	X
11-6 H-4.75'	10	X	X
11-6 H-5.00'	11	X	X
11-6 H-5.25'	12	X	X
11-6 V-5.25'	13	X	X
11-6 H-5.75'	14	X	X
11-6 V-5.75'	15	X	X

The objective of the petrographic analyses was to characterize the lithology and mineralogy in the evaporite interval.

PETROGRAPHIC RESULTS

The following sections briefly characterize the samples with respect to rock fabric, texture, and composition. Specific information on individual samples is provided in the Appendices and Photomicrographs with Captions sections.

Rock Fabric, Texture, and Composition

The samples are massive to "felted", and some show slight subparallel alignment. The principal mineral component, anhydrite (54-99% by weight from XRD), consists of densely packed laths. Areas of anhydrite are commonly separated by semi-circular patches of halite. Halite (trace-46% by weight from XRD) appears isotropic in thin section but is identified by its cubic cleavage, mineral/fluid inclusions, and rare negative crystals. Inclusions in halite are normally undefined dusty clusters. In some cases they are identifiable as magnesite, and occasionally they are aligned in linear aggregates or "trails". Coarser laths of anhydrite, and rare gypsum (0%-trace), occur near the contacts with halite. Magnesite (trace-4% by weight from XRD) is a magnesium carbonate mineral with very high birefringence found associated with both the anhydrite and halite (mainly with anhydrite). It exists as very small, rhombohedral crystals within the rock groundmass. Detrital clay (0%-trace) occurs in stringers in most samples. Crystal size of the anhydrite varies slightly throughout the sample interval. Crystal size is commonly 10-40 microns within the dense portions of the samples, and there is no significant variation between the samples, except in the last sample. Sample EIX 11-6 V-5.75' contains coarser crystals (40-100 microns) throughout. In all samples containing halite, anhydrite crystal size increases dramatically to greater than 500 microns near the halite zones. Coarse gypsum crystals are also present near the halite.

APPENDIX A-B.1

ANALYTICAL PROCEDURES

Sample Preparation

Core plug end trim samples were first separated into two fractions, one for X-ray diffraction analysis and one for thin sectioning. The thin section samples were cut of standard size (to fit a 27 mm by 46 mm glass slide) and thickness (0.03 mm). Samples were cut in oil, or dry whenever possible, to prevent the loss of water soluble phases.

Approximately 4 grams of each X-ray Diffraction sample was first ground in a Brinkmann Retsch MM-2 mortar to attain proper particle size. Samples were then loaded into bulk sample holders for X-ray Diffraction scanning.

Methods

Thin section samples were analyzed on a Nikon polarizing microscope with a Swift automatic point-count attachment stage and box. Three hundred (300) points were counted per thin section, and the percent of each mineral species present was derived. Later, thin section photography was performed with an attached 35 mm camera assembly.

The portions of the samples subjected to X-ray Diffraction analysis were scanned on a Philips XRD unit. The scan range was 2 degrees to 70 degrees two theta. The resultant "patterns" were then analyzed to determine mineralogy.

APPENDIX A-B.2

X-RAY DIFFRACTION DATA

OMNI LABORATORIES, INC.
AUTO X-RAY DIFFRACTION
(WEIGHT%)

ROCK PHYSICS ASSOCIATES
WASTE ISOLATION PILOT PLANT

FILE NO: G-2016
DATE : 7-28-93

SAMPLE	CLAYS					CARBONATES		OTHER MINERALS							TOTALS		
NUMBER*	KAOLINITE	CHLORITE	ILLITE	SMECTITE	TOTAL	CALCITE	MAGNESITE	QUARTZ	PLAG.	K-SPAR	CELESTITE	GYPSUM	ANHYDRITE	HALITE	CLAYS	CARB.	OTHER
01	0	0	0	0	TR	0	TR	0	0	0	0	0	80	20	TR	TR	100
02	0	0	0	0	TR	0	1	0	0	0	0	0	73	26	TR	1	99
03	0	0	0	0	TR	0	TR	0	0	0	0	0	56	44	TR	TR	100
04	0	0	0	0	TR	0	TR	0	0	0	0	TR	99	1	TR	TR	100
05	0	0	0	0	TR	0	1	0	0	0	0	0	92	7	TR	1	99
06	0	0	0	0	TR	0	3	0	0	0	0	0	93	4	TR	3	97
07	0	0	0	0	TR	0	TR	0	0	0	0	0	97	3	TR	TR	100
08	0	0	0	0	TR	0	4	0	0	0	0	0	96	TR	TR	4	96
09	0	0	0	0	TR	0	TR	0	0	0	0	0	54	46	TR	TR	100
10	0	0	0	0	0	0	TR	0	0	0	0	0	68	32	0	TR	100
11	0	0	0	0	TR	0	4	0	0	0	0	0	66	30	TR	4	96
12	0	0	0	0	TR	0	2	0	0	0	0	0	54	44	TR	2	98
13	0	0	0	0	TR	0	3	0	0	0	0	TR	69	28	TR	3	97
14	0	0	0	0	TR	0	TR	0	0	0	0	0	85	15	TR	TR	100
15	0	0	0	0	0	0	TR	0	0	0	0	0	99	1	0	TR	100
AVERAGE	0	0	0	0	TR	0	1	0	0	0	0	TR	79	20	TR	1	99

* Corresponding original sample designations are shown on Table 1.

APPENDIX A-B.3

THIN SECTION POINT-COUNT ANALYSIS

AND

THIN SECTION PHOTOMICROGRAPHS

ROCK PHYSICS ASSOCIATES
WASTE ISOLATION PILOT PLANT
Thin Section Modal Analysis

SAMPLE:	EIX 10–6 H–4.50'	EIX 10–6 H–5.00'	EIX 10–6 H–5.25'	EIX 10–6 V–5.25'
Rock Name:	Evaporite	Evaporite	Evaporite	Evaporite
FRAMEWORK GRAINS				
Quartz	0	0	0	0
Monocrystalline	0	0	0	0
Polycrystalline	0	0	0	0
Feldspar	0	0	0	0
K–feldspar	0	0	0	0
Plagioclase	0	0	0	0
Lithic Fragments	0	0	0	0
Plutonic	0	0	0	0
Volcanic	0	0	0	0
Metamorphic	0	0	0	0
Chert	0	0	0	0
Mudstone	0	0	0	0
Accessory Grains	0	0	0	0
Muscovite	0	0	0	0
Biotite	0	0	0	0
Heavy Minerals	0	0	0	0
ENVIRON. INDICATORS				
Organic Materials	0	0	0	0
Glauconite	0	0	0	0
Calcareous Frag.	0	0	0	0
CLAY MATRIX	tr	tr	tr	tr
AUTHIGENIC CEMENT	100	100	100	100
Clay	0	0	0	0
Quartz Overgrowths	0	0	0	0
Gypsum	tr	tr	tr	tr
Anhydrite	82	72	67	99
Halite	16	26	30	1
Calcite	0	0	0	0
Ankerite	0	0	0	0
Magnesite	2	2	3	tr
Pyrite	0	0	0	0
POROSITY	0	0	0	0
Primary	0	0	0	0
Secondary	0	0	0	0
Microscopic	0	0	0	0
TOTALS	100	100	100	100

ROCK PHYSICS ASSOCIATES
WASTE ISOLATION PILOT PLANT
Thin Section Modal Analysis

SAMPLE:	EIX 10–6 H–5.50'	EIX 10–6 H–5.75'	EIX 10–6 V–5.75'	EIX 10–7 V–6.25'
Rock Name:	Evaporite	Evaporite	Evaporite	Evaporite
FRAMEWORK GRAINS				
Quartz	0	0	0	0
Monocrystalline	0	0	0	0
Polycrystalline	0	0	0	0
Feldspar	0	0	0	0
K–feldspar	0	0	0	0
Plagioclase	0	0	0	0
Lithic Fragments	0	0	0	0
Plutonic	0	0	0	0
Volcanic	0	0	0	0
Metamorphic	0	0	0	0
Chert	0	0	0	0
Mudstone	0	0	0	0
Accessory Grains	0	0	0	0
Muscovite	0	0	0	0
Biotite	0	0	0	0
Heavy Minerals	0	0	0	0
ENVIRON. INDICATORS				
Organic Materials	0	0	0	0
Glauconite	0	0	0	0
Calcareous Frag.	0	0	0	0
CLAY MATRIX	tr	tr	tr	tr
AUTHIGENIC CEMENT	100	100	100	100
Clay	0	0	0	0
Quartz Overgrowths	0	0	0	0
Gypsum	tr	0	tr	0
Anhydrite	93	95	82	100
Halite	2	0	15	0
Calcite	0	0	0	0
Ankerite	0	0	0	0
Magnesite	5	5	3	tr
Pyrite	0	0	0	0
POROSITY	0	0	0	0
Primary	0	0	0	0
Secondary	0	0	0	0
Microscopic	0	0	0	0
TOTALS	100	100	100	100

ROCK PHYSICS ASSOCIATES
WASTE ISOLATION PILOT PLANT
Thin Section Modal Analysis

SAMPLE:	EIX 11-6 H-4.50'	EIX 11-6 H-4.75'	EIX 11-6 H-5.00'	EIX 11-6 H-5.25'
Rock Name:	Evaporite	Evaporite	Evaporite	Evaporite
FRAMEWORK GRAINS				
Quartz	0	0	0	0
Monocrystalline	0	0	0	0
Polycrystalline	0	0	0	0
Feldspar	0	0	0	0
K-feldspar	0	0	0	0
Plagioclase	0	0	0	0
Lithic Fragments	0	0	0	0
Plutonic	0	0	0	0
Volcanic	0	0	0	0
Metamorphic	0	0	0	0
Chert	0	0	0	0
Mudstone	0	0	0	0
Accessory Grains	0	0	0	0
Muscovite	0	0	0	0
Biotite	0	0	0	0
Heavy Minerals	0	0	0	0
ENVIRON. INDICATORS				
Organic Materials	0	0	0	0
Glauconite	0	0	0	0
Calcareous Frag.	0	0	0	0
CLAY MATRIX	tr	0	tr	tr
AUTHIGENIC CEMENT	100	100	100	100
Clay	0	0	0	0
Quartz Overgrowths	0	0	0	0
Gypsum	tr	1	tr	tr
Anhydrite	60	71	64	69
Halite	37	26	30	26
Calcite	0	0	0	0
Ankerite	0	0	0	0
Magnesite	3	2	6	5
Pyrite	0	0	0	0
POROSITY	0	0	0	0
Primary	0	0	0	0
Secondary	0	0	0	0
Microscopic	0	0	0	0
TOTALS	100	100	100	100

ROCK PHYSICS ASSOCIATES
WASTE ISOLATION PILOT PLANT
Thin Section Modal Analysis

SAMPLE:	EIX 11-6 V-5.25'	EIX 11-6 H-5.75'	EIX 11-6 V-5.75'
Rock Name:	Evaporite	Evaporite	Evaporite
FRAMEWORK GRAINS			
Quartz	0	0	0
Monocrystalline	0	0	0
Polycrystalline	0	0	0
Feldspar	0	0	0
K-feldspar	0	0	0
Plagioclase	0	0	0
Lithic Fragments	0	0	0
Plutonic	0	0	0
Volcanic	0	0	0
Metamorphic	0	0	0
Chert	0	0	0
Mudstone	0	0	0
Accessory Grains	0	0	0
Muscovite	0	0	0
Biotite	0	0	0
Heavy Minerals	0	0	0
ENVIRON. INDICATORS			
Organic Materials	0	0	0
Glauconite	0	0	0
Calcareous Frag.	0	0	0
CLAY MATRIX	tr	tr	0
AUTHIGENIC CEMENT	100	100	100
Clay	0	0	0
Quartz Overgrowths	0	0	0
Gypsum	tr	tr	0
Anhydrite	83	44	100
Halite	12	56	0
Calcite	0	0	0
Ankerite	0	0	0
Magnesite	5	tr	tr
Pyrite	0	0	0
POROSITY	0	0	0
Primary	0	0	0
Secondary	0	0	0
Microscopic	0	0	0
TOTALS	100	100	100

SAMPLE NUMBER: EIX 10-6 H-4.50'

PLATE 1A

This low magnification photomicrograph displays an evaporite rock consisting mainly of anhydrite (tan) and halite (white, center). Anhydrite crystals are generally fine (area of C4) to coarse (H6) near the halite. Magnesite is a patchy carbonate mineral present.

Magnification: 40X

SAMPLE NUMBER: EIX 10-6 H-4.50'

PLATE 1B

The high magnification view documents the relationship of the three main minerals in this sample. Halite (center) appears white, and in this sample shows little evidence of cleavage or inclusions. Tiny rhombs of magnesite (A10) rim the halite/anhydrite contact. Relatively large anhydrite crystal laths (H9) are found bordering the halite.

Magnification: 100X

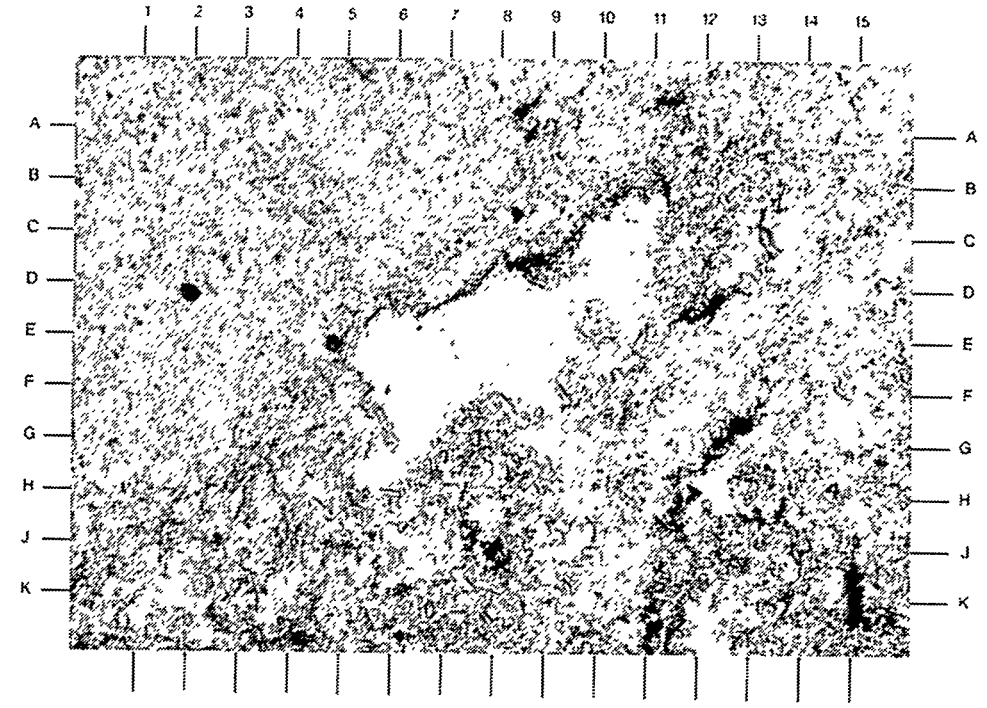
1 2 3 4 5 6 7 8 9 10 11 12 13 14 15
A B C D E F G H J K

A

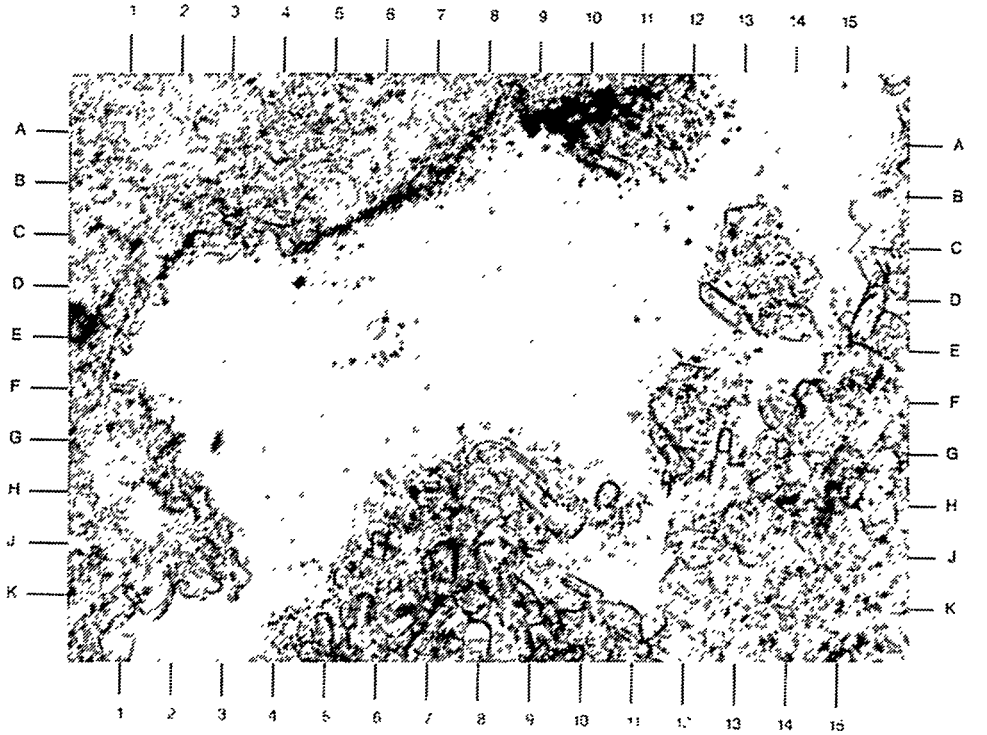
1 2 3 4 5 6 7 8 9 10 11 12 13 14 15
A B C D E F G H J K

B

Rock Physics Associates
Waste Isolation Pilot Plant

File No. G-2016

SAMPLE NUMBER: EIX 10-6 H-5.00'

PLATE 2A

The low magnification survey view shows a representative section of this evaporite. Halite (white, left of center) is common. Magnesite is found associated with both the halite (G7) and anhydrite (E13). Large anhydrite laths (K7,C5), and occasional gypsum laths, protrude into the halite.

Magnification: 40X

SAMPLE NUMBER: EIX 10-6 H-5.00'

PLATE 2B

The high magnification view demonstrates the interrelationship of all three major mineral phases. Magnesite is composed of small, dark brown, rhombohedral crystals (H6) contained within, in this case, the halite. Halite shows evidence of inclusion zoning (diagonal from A2.5 to D4). Anhydrite is composed of densely-packed, lathlike, bladed crystals (B15,D-E11.5).

Magnification: 100X

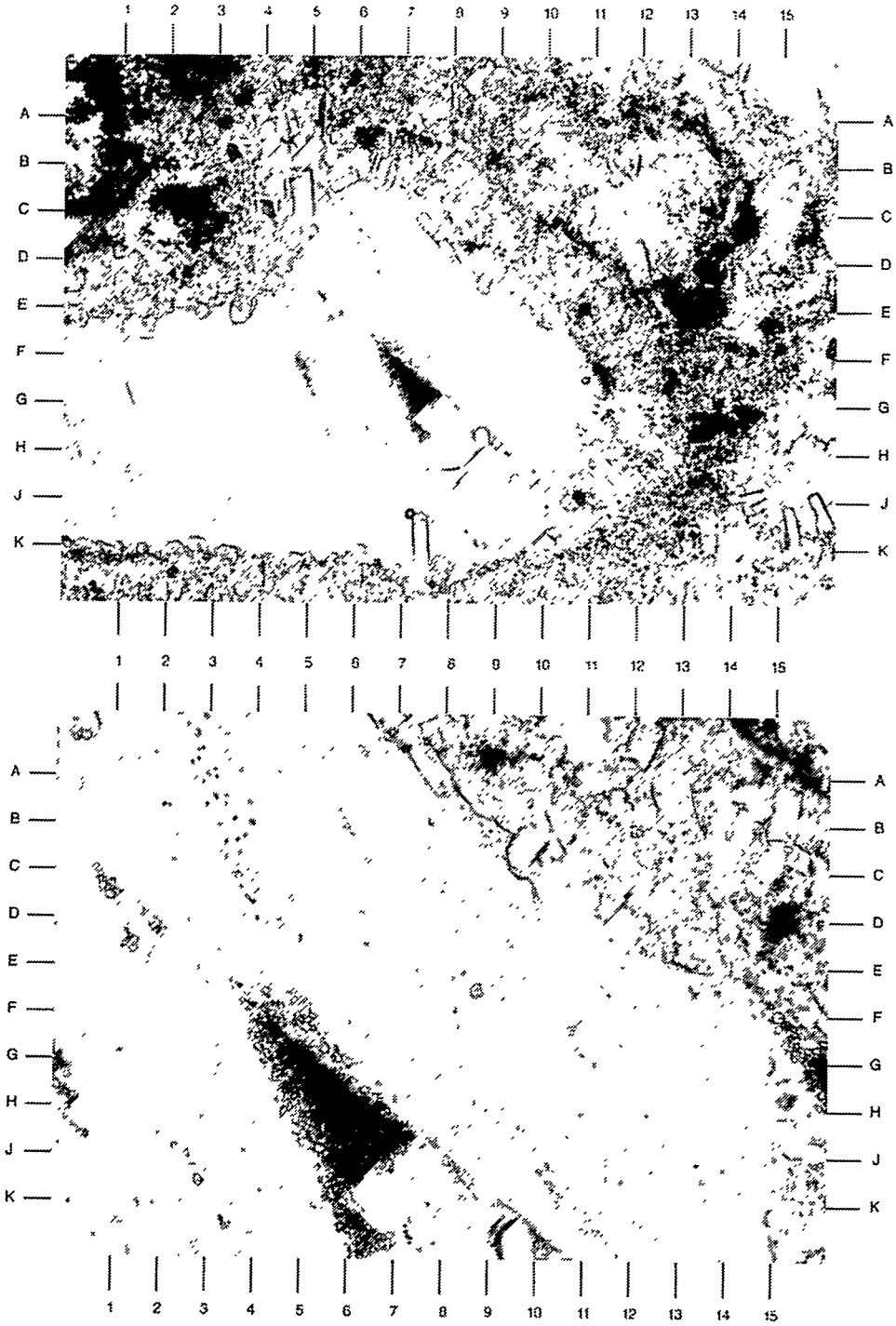
1 2 3 4 5 6 7 8 9 10 11 12 13 14 15
A B C D E F G H J K
A
1 2 3 4 5 6 7 8 9 10 11 12 13 14 15
A B C D E F G H J K
B

Rock Physics Associates
Waste Isolation Pilot Plant

File No. G-2016

SAMPLE NUMBER: EIX 10-6 H-5.25'

PLATE 3A

The low magnification photomicrograph depicts the complex intergrowth relationship of halite (white) and anhydrite (tan). Original bedding may be defined by clayey zones (subvertical brown streaks at J1,G4). This rock contains 56% anhydrite and 44% halite (weight percent by XRD).

Magnification: 40X

SAMPLE NUMBER: EIX 10-6 H-5.25'

PLATE 3B

In this high magnification photomicrograph, anhydrite laths (B3.5) appear to float in later-forming halite. Magnesite (D13.5) is a trace component that nonetheless occurs with frequency in scattered patches. The halite in this view shows no evidence of zoning or cleavage.

Magnification: 100X

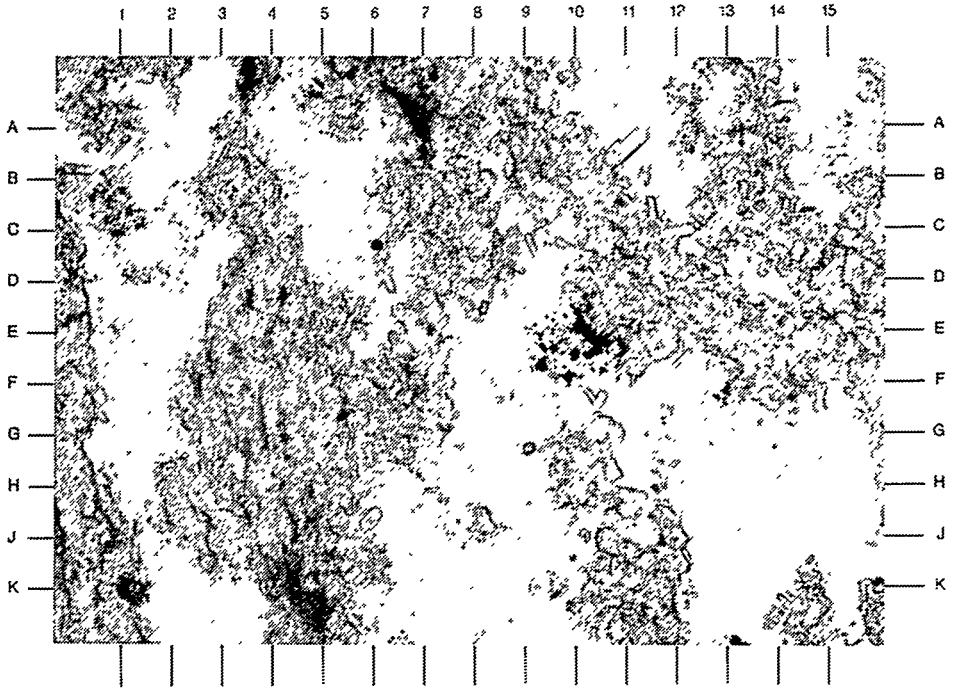
1 2 3 4 5 6 7 8 9 10 11 12 13 14 15
A B C D E F G H J K

A

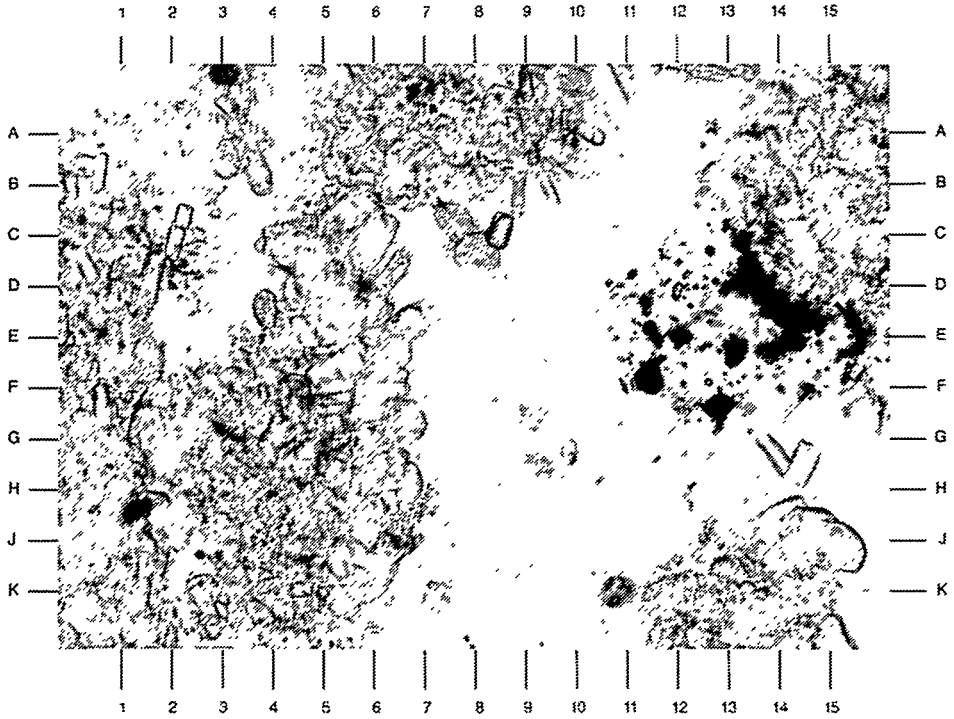
1 2 3 4 5 6 7 8 9 10 11 12 13 14 15
A B C D E F G H J K

B

Rock Physics Associates
Waste Isolation Pilot Plant

File No. G-2016

SAMPLE NUMBER: EIX 10-6 V-5.25'

PLATE 4A

This survey view shows an evaporitic rock composed mainly of anhydrite. Impurities include clay with possible iron oxides (light brown, H1) and magnesite (dark brown, J12.5).

Magnification: 40X

SAMPLE NUMBER: EIX 10-6 V-5.25'

PLATE 4B

This high magnification view depicts the dense intergrowth of individual anhydrite crystals. No visible porosity exists. Magnesite (D7.5) is patchy.

Magnification: 100X

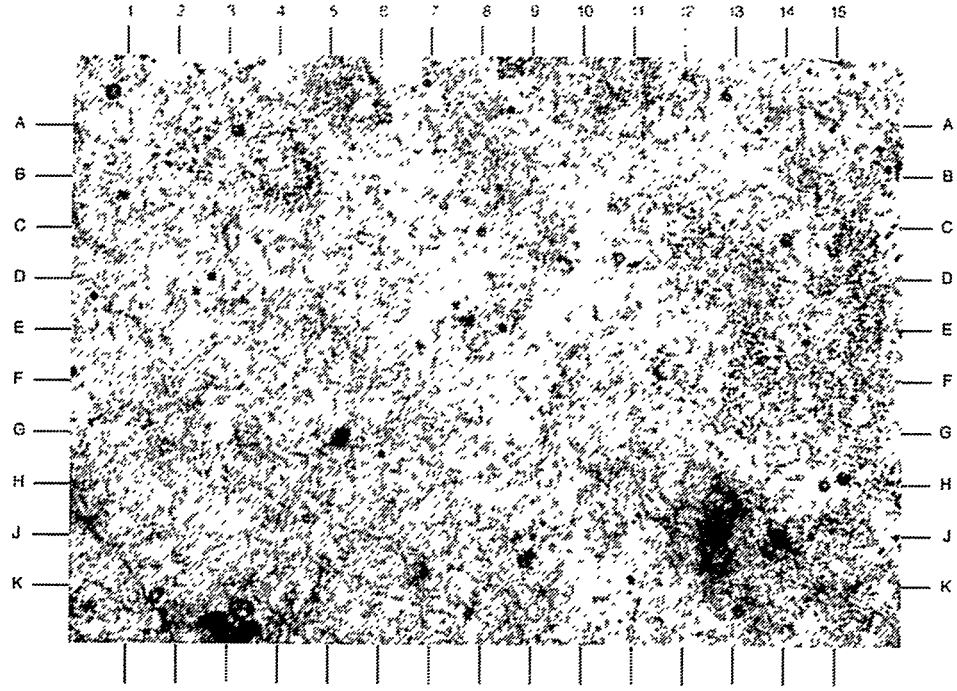
1 2 3 4 5 6 7 8 9 10 11 12 13 14 15
A B C D E F G H J K

A

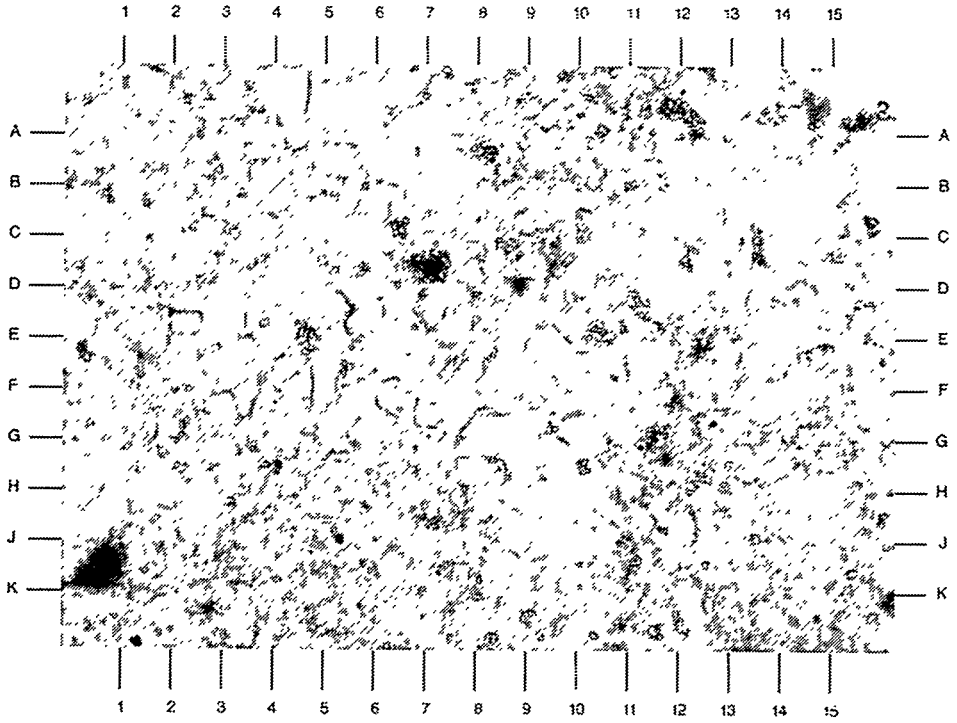
1 2 3 4 5 6 7 8 9 10 11 12 13 14 15
A B C D E F G H J K

B

Rock Physics Associates
Waste Isolation Pilot Plant

File No. G-2016

SAMPLE NUMBER: EIX 10-6 H-5.50'

PLATE 5A

The survey photomicrograph illustrates a massive anhydrite rock. Clay exists in subparallel stringers (left side of photo around D1 and D4). Magnesite occurs in large scattered patches (F10,A12).

Magnification: 40X

SAMPLE NUMBER: EIX 10-6 H-5.50'

PLATE 5B

The same features are highlighted in the high magnification view. Anhydrite (light) is the main mineral component. Magnesite (H12) is a common accessory mineral made up of tiny individual carbonate rhombs, and is patchy in occurrence. Original depositional orientation is probably defined by clayey zones (around E3).

Magnification: 100X

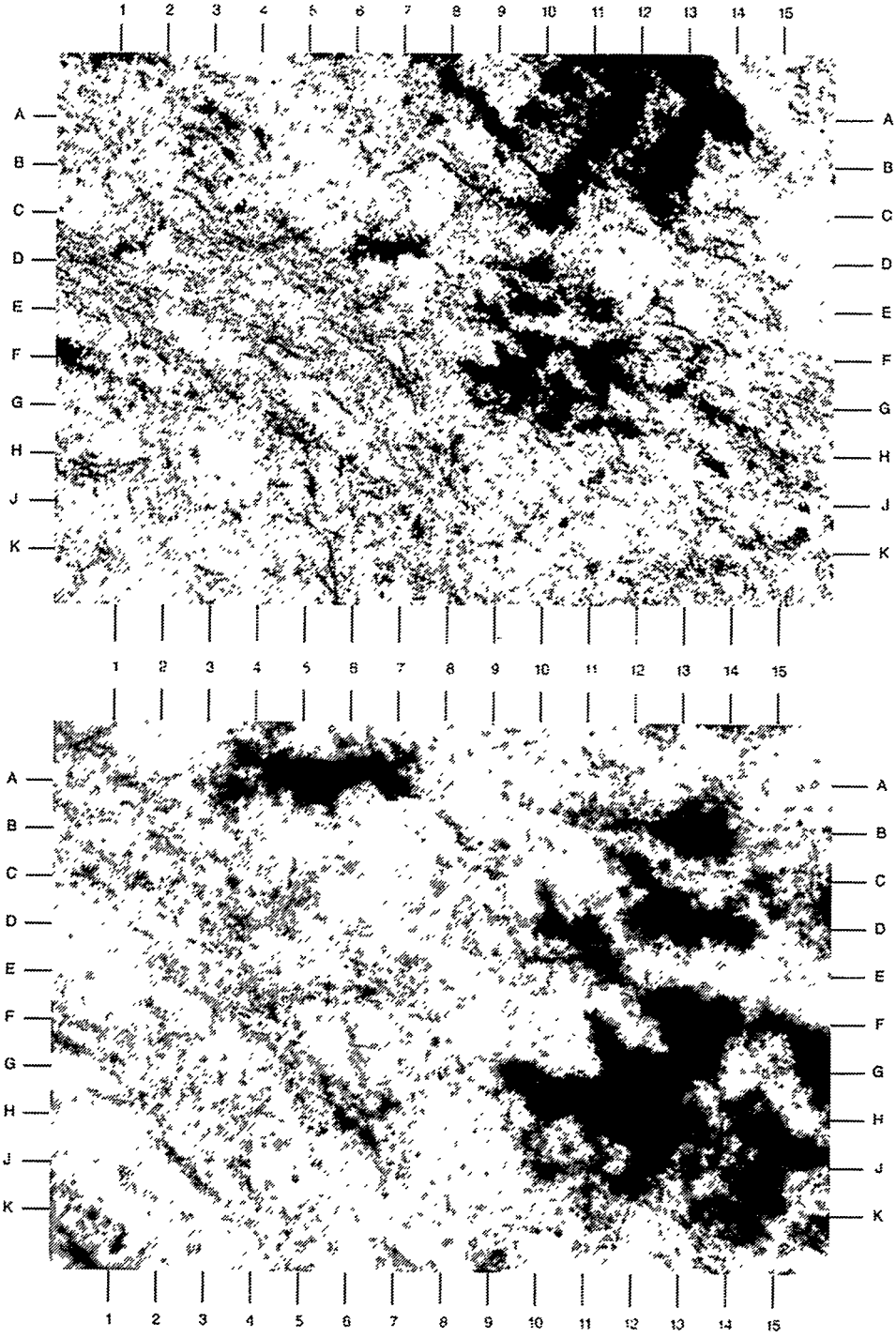
1 2 3 4 5 6 7 8 9 10 11 12 13 14 15
A B C D E F G H J K
A

1 2 3 4 5 6 7 8 9 10 11 12 13 14 15
A B C D E F G H J K
B

SAMPLE NUMBER: EIX 10-6 H-5.75'

PLATE 6A

The low magnification photomicrograph displays a fine-grained anhydritic rock with magnesite replacement. Individual laths of anhydrite are interwoven into a felted massive fabric. Clayey streaks (G6.5) trend subparallel. Magnesite (C3) tends to follow this same general orientation.

Magnification: 40X

SAMPLE NUMBER: EIX 10-6 H-5.75'

PLATE 6B

This photomicrograph illustrates the fine-grained texture of the anhydrite crystals (area of C5), as well as the relationship of the anhydrite to two other mineral phases. Clay (J5) occurs in stringers, probably along with organic material. Magnesite (G5) is, in the case of this sample, associated with the stringers.

Magnification: 100X

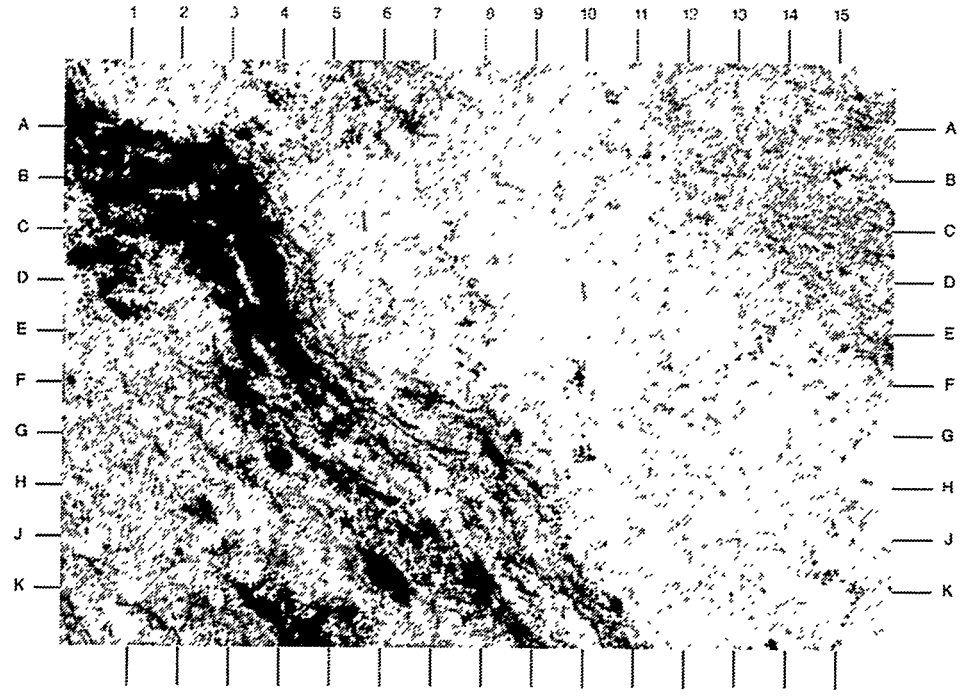
1 2 3 4 5 6 7 8 9 10 11 12 13 14 15
A B C D E F G H J K

A

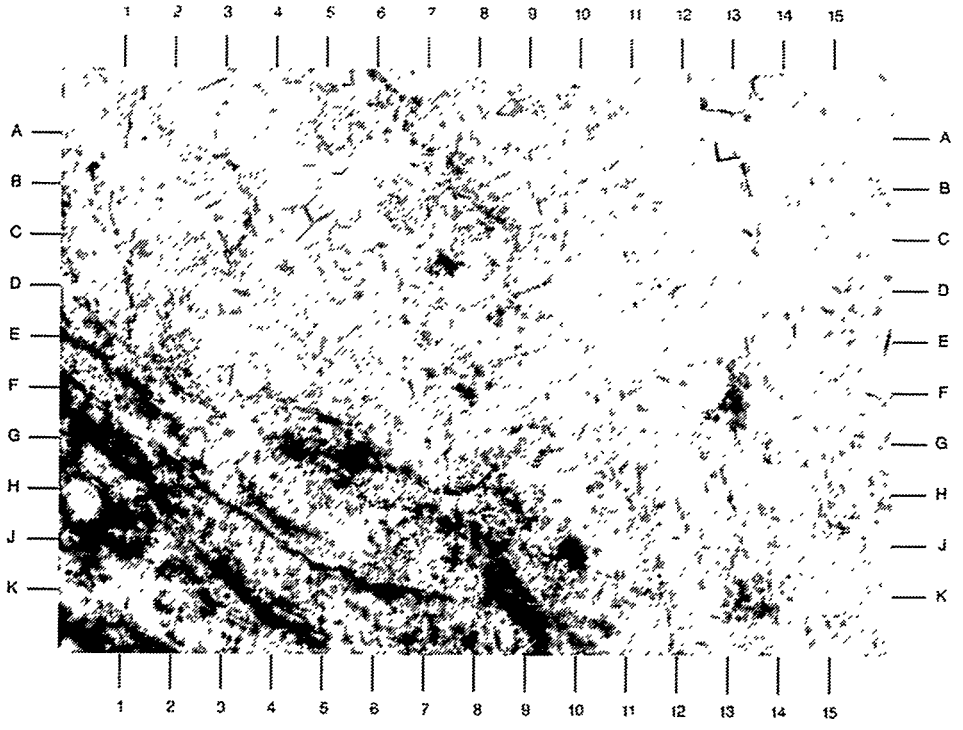
1 2 3 4 5 6 7 8 9 10 11 12 13 14 15
A B C D E F G H J K

B

SAMPLE NUMBER: EIX 10-6 V-5.75'

PLATE 7A

The sample depicted in this low magnification photomicrograph actually contains 97% anhydrite and 3% halite, by weight from XRD. However, this field of view shows substantially more halite (white). In some cases the halite is obviously surrounding anhydrite laths (K7.5). Magnesite is associated with both halite and anhydrite. Two large magnesite patches are evident at E5.5 and H12.5. Two stages of anhydrite growth are detected in this sample. The common, massive anhydrite (area of H2) contrasts sharply with the blady anhydrite growing perpendicular to the halite (diagonally across photo from C1 to J5.5).

Magnification: 40X

SAMPLE NUMBER: EIX 10-6 V-5.75'

PLATE 7B

The three major mineral components are depicted in this high magnification view. Halite (white) is nearly free of inclusions (some are evident at F10) and obvious cleavage. Magnesite (B2) appears massive but is composed of thousands of individual rhombs. Anhydrite (C11) is coarser near the halite boundary.

Magnification: 100X

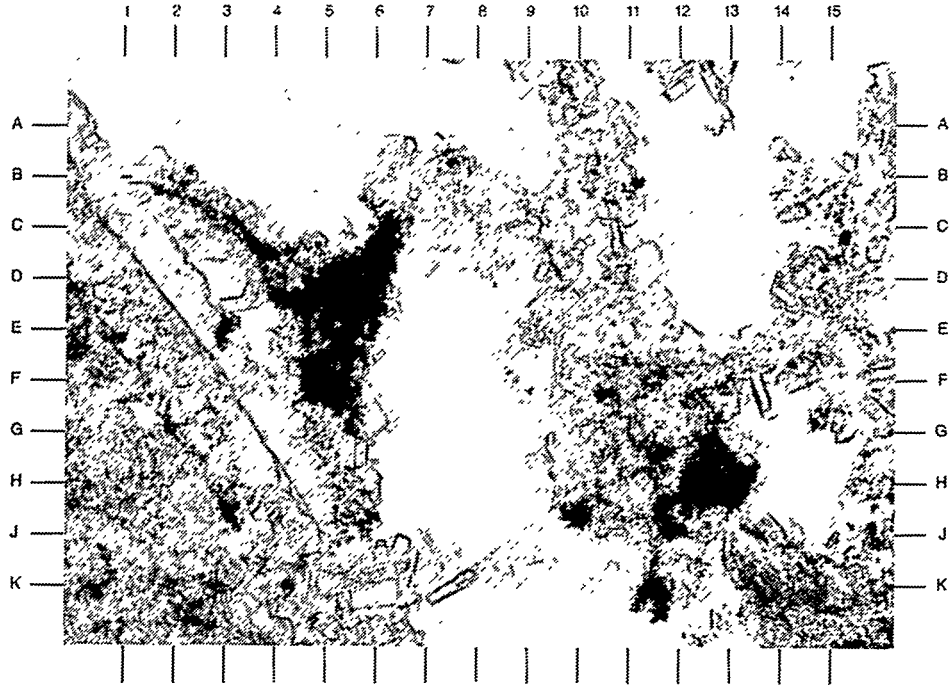
1 2 3 4 5 6 7 8 9 10 11 12 13 14 15
A B C D E F G H J K

A

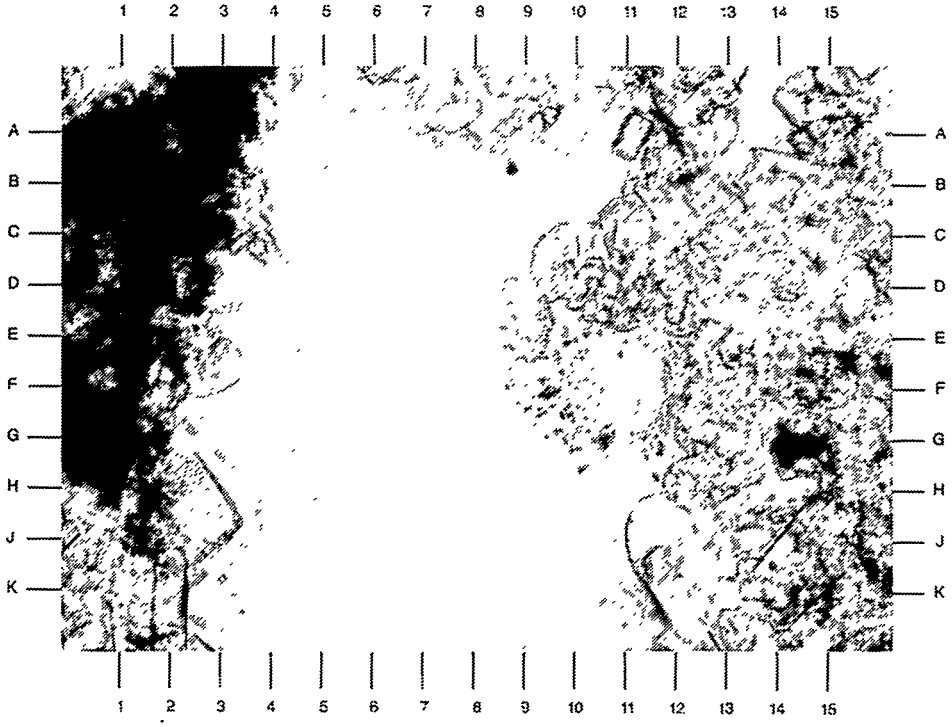
1 2 3 4 5 6 7 8 9 10 11 12 13 14 15
A B C D E F G H J K

B

Rock Physics Associates
Waste Isolation Pilot Plant

File No. G-2016

SAMPLE NUMBER: EIX 10-7 V-6.25'

PLATE 8A

The survey photomicrograph depicts massive anhydrite completely void of intercrystalline porosity. Occasional brownish flecks (G12,D9,J5.5) represent clay and magnesite.

Magnification: 40X

SAMPLE NUMBER: EIX 10-7 V-6.25'

PLATE 8B

The high magnification view demonstrates the complete, dense intergrowth of individual laths of anhydrite (G8). Clay and possible organics exist in faintly defined, narrow zones (D6-K6).

Magnification: 100X

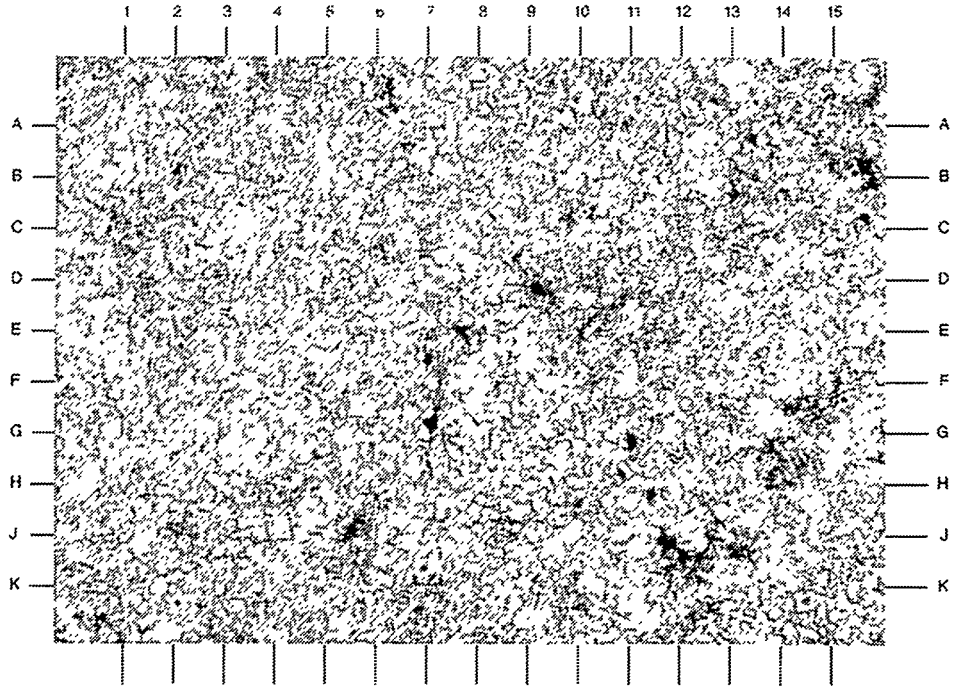
1 2 3 4 5 6 7 8 9 10 11 12 13 14 15
A B C D E F G H J K

A

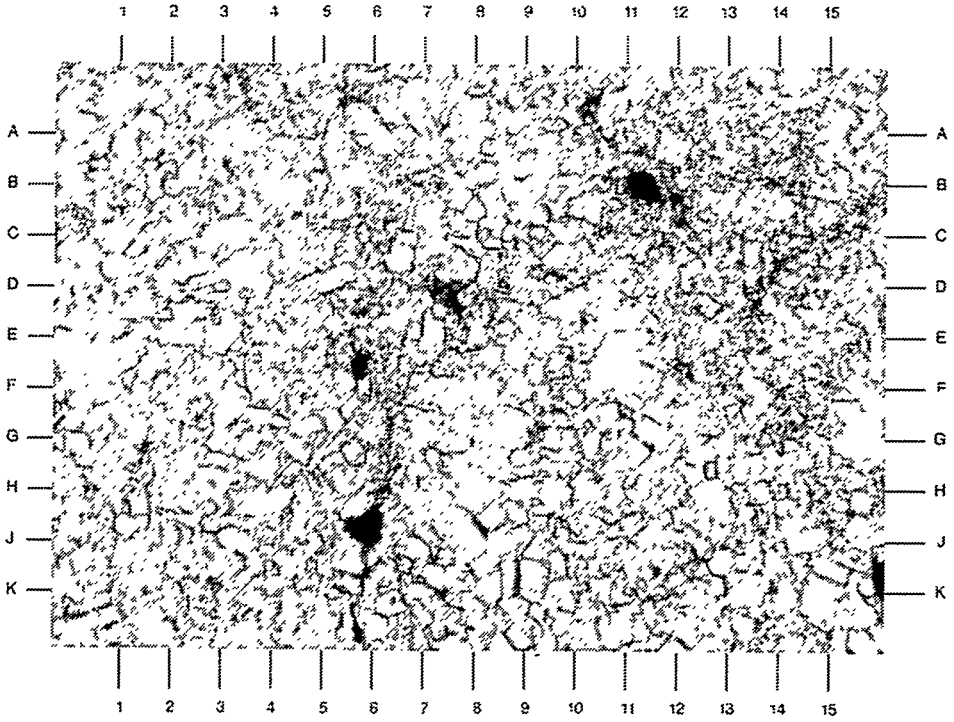
1 2 3 4 5 6 7 8 9 10 11 12 13 14 15
A B C D E F G H J K

B

Rock Physics Associates
Waste Isolation Pilot Plant

File No. G-2016

SAMPLE NUMBER: EIX 11-6 H-4.50'

PLATE 9A

The low magnification photomicrograph demonstrates the mineral associations present in this sequence of evaporites. Clay stringers (C2) occur within the fine anhydrite groundmass. Halite (B12) shows some cleavage (K14) and inclusion zoning (above A15). Iron oxide (D9.5) is unusually common in this sample, and appears to stain anhydrite. Magnesite, in its common cluster form, K4), occurs sporadically. Some zoning of inclusions (D10,E8) within the halite has occurred.

Magnification: 40X

SAMPLE NUMBER: EIX 11-6 H-4.50'

PLATE 9B

The high magnification view demonstrates the nature of the halite. Some zoning of inclusions (D10,E8) has occurred. In other areas, anhydrite crystals (E3.5,B8,K6) are surrounded by later halite.

Magnification: 100X

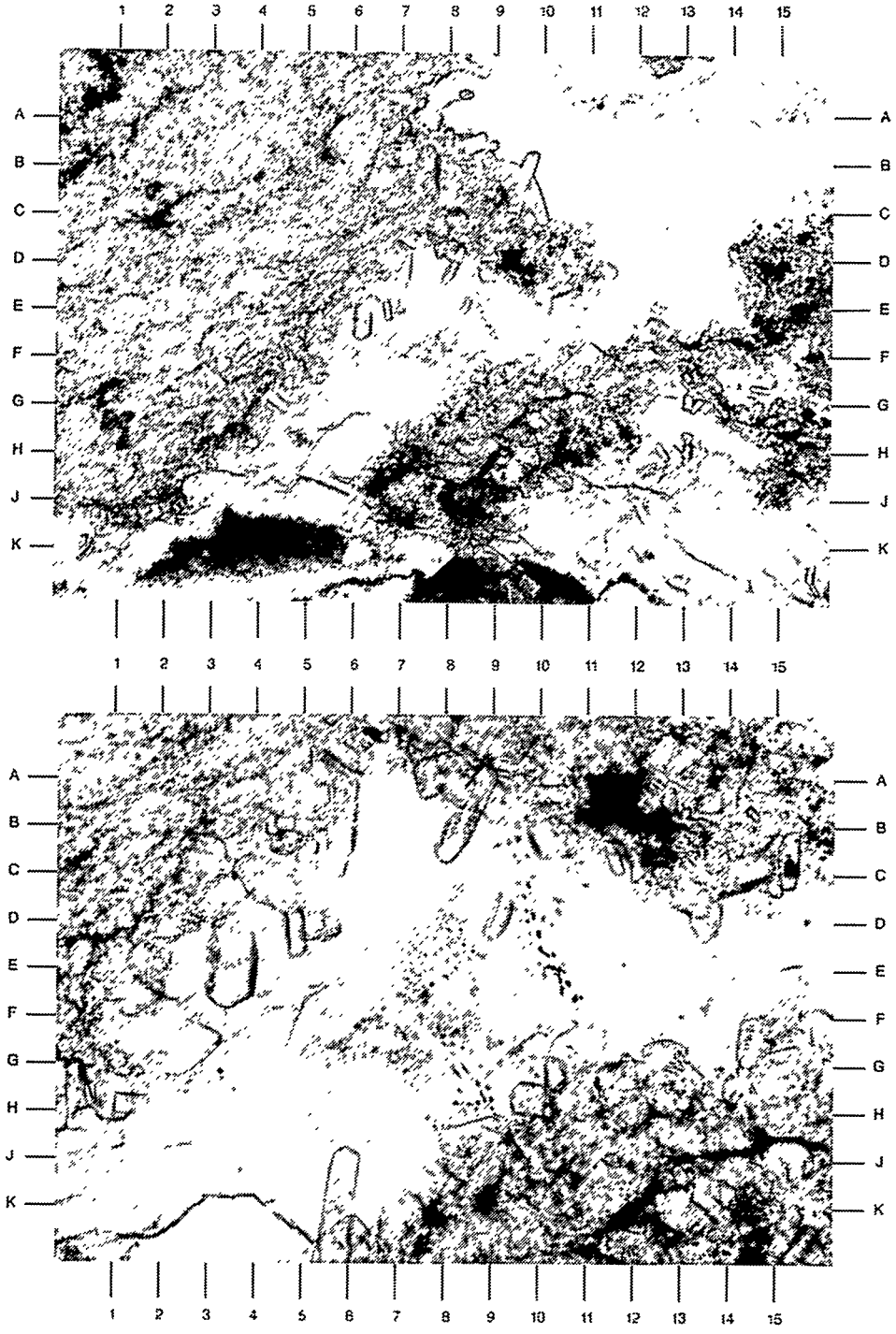
1 2 3 4 5 6 7 8 9 10 11 12 13 14 15
A B C D E F G H J K
A

1 2 3 4 5 6 7 8 9 10 11 12 13 14 15
A B C D E F G H J K
B

Rock Physics Associates
Waste Isolation Pilot Plant

File No. G-2016

SAMPLE NUMBER: EIX 11-6 H-4.75'

PLATE 10A

The complex interrelationship of the various evaporite/carbonate mineral phases is evident in this low magnification field of view. Note the irregular borders (H6) between anhydrite (tan) and halite (white). Magnesite (D3) is patchy and irregular.

Magnification: 40X

SAMPLE NUMBER: EIX 11-6 H-4.75'

PLATE 10B

The high magnification view shows details of halite in this sample. Some inclusion trails (E11 to G8) are quite regular; others (beak-like area defined by endpoints C12 and H14) are highly irregular. Large anhydrite laths (lower left of photo) are partially surrounded by halite.

Magnification: 100X

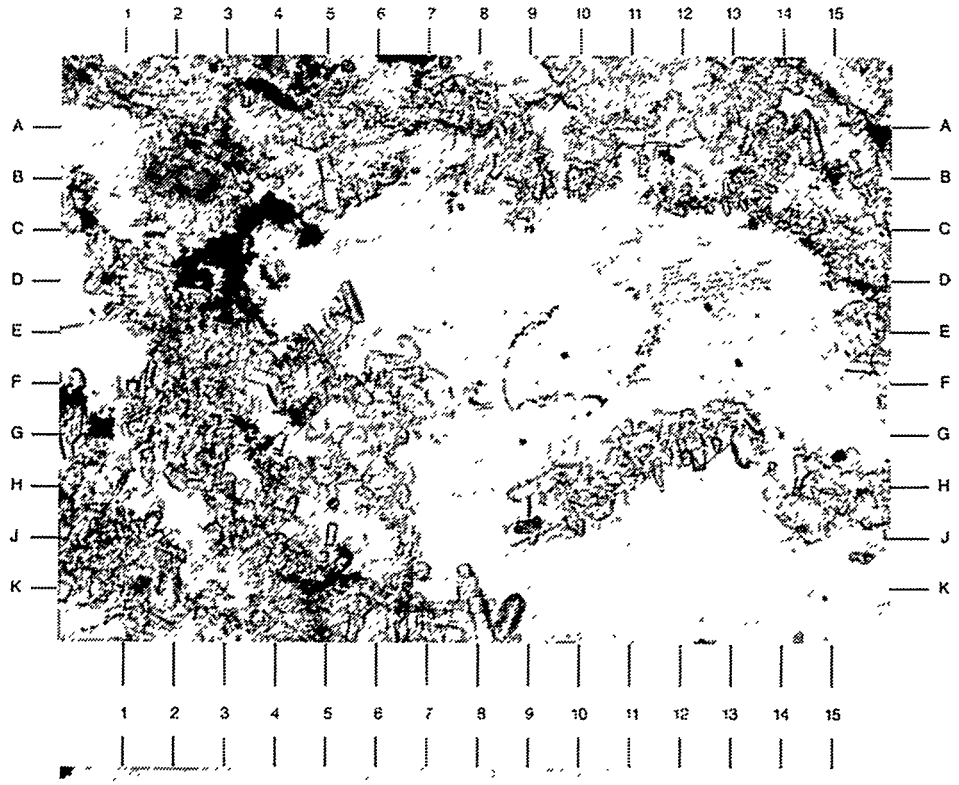
1 2 3 4 5 6 7 8 9 10 11 12 13 14 15
A B C D E F G H J K

A

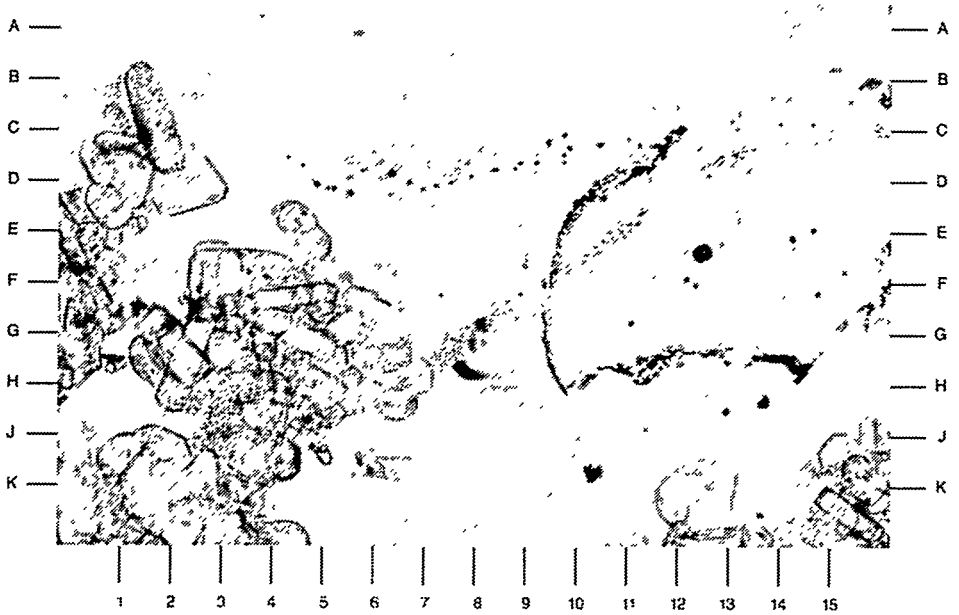
1 2 3 4 5 6 7 8 9 10 11 12 13 14 15
A B C D E F G H J K

B

Rock Physics Associates
Waste Isolation Pilot Plant

File No. G-2016

SAMPLE NUMBER: EIX 11-6 H-5.00'

PLATE 11A

The low magnification view of this sample shows a more distinct boundary separating halite and anhydrite, than that of the previous sample. The halite/anhydrite contact (E8.5) is also marked by the presence of the carbonate mineral magnesite (J9). Individual crystals within the anhydrite (tan) are small, with the exception of those in one area (G9). The halite is marked by well-defined inclusion zones (across photo at B-C,D,E-F,G,and J).

Magnification: 40X

SAMPLE NUMBER: EIX 11-6 H-5.00'

PLATE 11B

The high magnification view of the evaporite shows many of the above features in more detail. Fine-grained anhydrite crystals (C15), coarser anhydrite crystals (F14), and magnesite (H7.5) are clearly noted. Also evident is a clayey streak (diagonally across photo from B13 to K10). The well-defined, parallel, inclusion zones are obvious (B,C,F,J).

Magnification: 100X

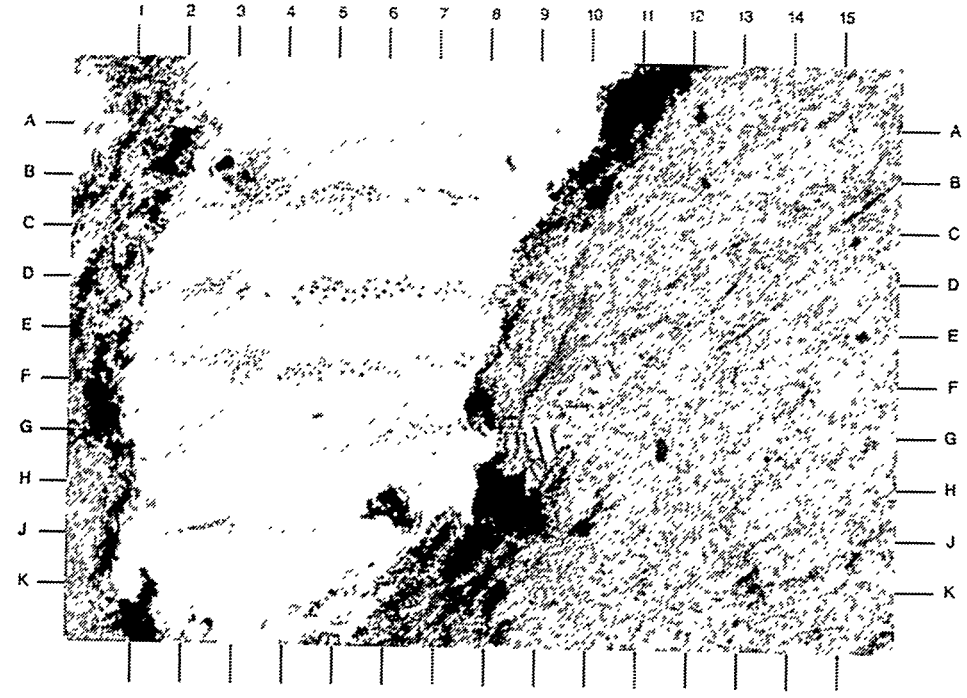
1 2 3 4 5 6 7 8 9 10 11 12 13 14 15
A B C D E F G H J K

A

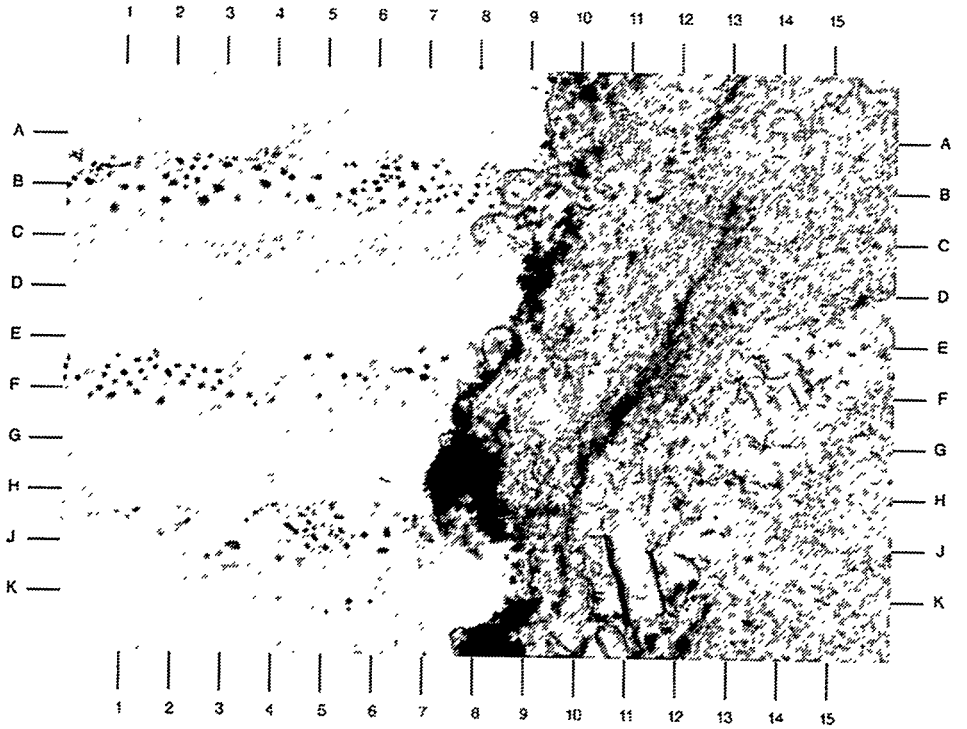
1 2 3 4 5 6 7 8 9 10 11 12 13 14 15
A B C D E F G H J K

B

Rock Physics Associates
Waste Isolation Pilot Plant

File No. G-2016

SAMPLE NUMBER: EIX 11-6 H-5.25'

PLATE 12A

This low magnification survey photomicrograph demonstrates the mottled relationship of the two major mineral species present, halite (white) and anhydrite (tan). Magnesite (F3.5) and detrital clay (D-E14) are also present. Most anhydrite laths are very small (area of A-B7); some, however, are much larger (C-D5).

Magnification: 40X

SAMPLE NUMBER: EIX 11-6 H-5.25'

PLATE 12B

The high magnification view of the center of photo "A" demonstrates the complex boundaries present between the halite and anhydrite. The halite in this sample contains dusty inclusions (C-D8.5) with no preferred orientation. Anhydrite laths (G12) are much coarser, where partially surrounded by halite.

Magnification: 100X

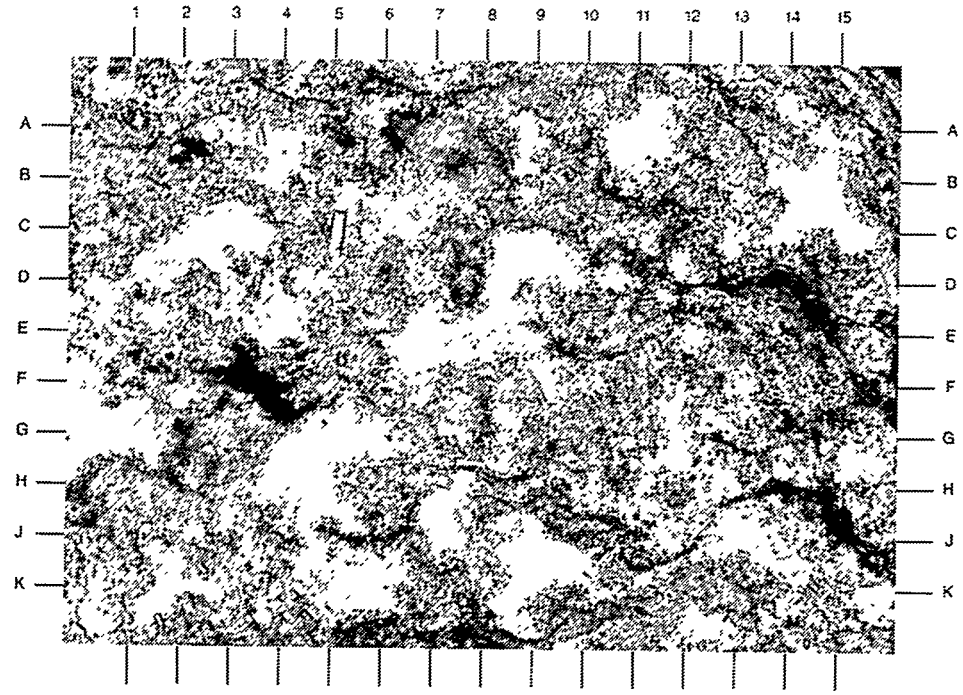
1 2 3 4 5 6 7 8 9 10 11 12 13 14 15
A B C D E F G H J K

A

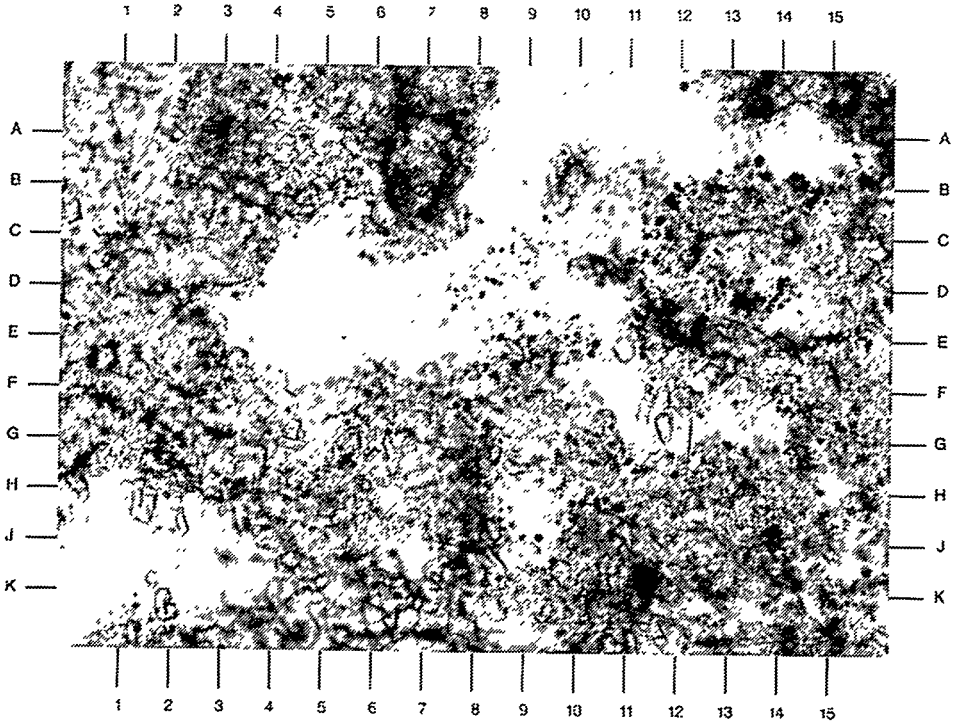
1 2 3 4 5 6 7 8 9 10 11 12 13 14 15
A B C D E F G H J K

B

Rock Physics Associates
Waste Isolation Pilot Plant

File No. G-2016

SAMPLE NUMBER: EIX 11-6 V-5.25'

PLATE 13A

This survey photomicrograph shows four different minerals present in this evaporite rock. Anhydrite (tan) is massive and fine- (area of D11) to coarse- grained (J7). Halite (white, E7.5) occurs in scattered patches. Magnesite (J2.5) is quite rare, as is detrital clay (above A1) which exists in stringers.

Magnification: 40X

SAMPLE NUMBER: EIX 11-6 V-5.25'

PLATE 13B

This high magnification photomicrograph details an inclusion trail (diagonally from D6 to H10) within the halite. Some iron oxide staining (J4) is present, and is associated with the anhydrite.

Magnification: 100X

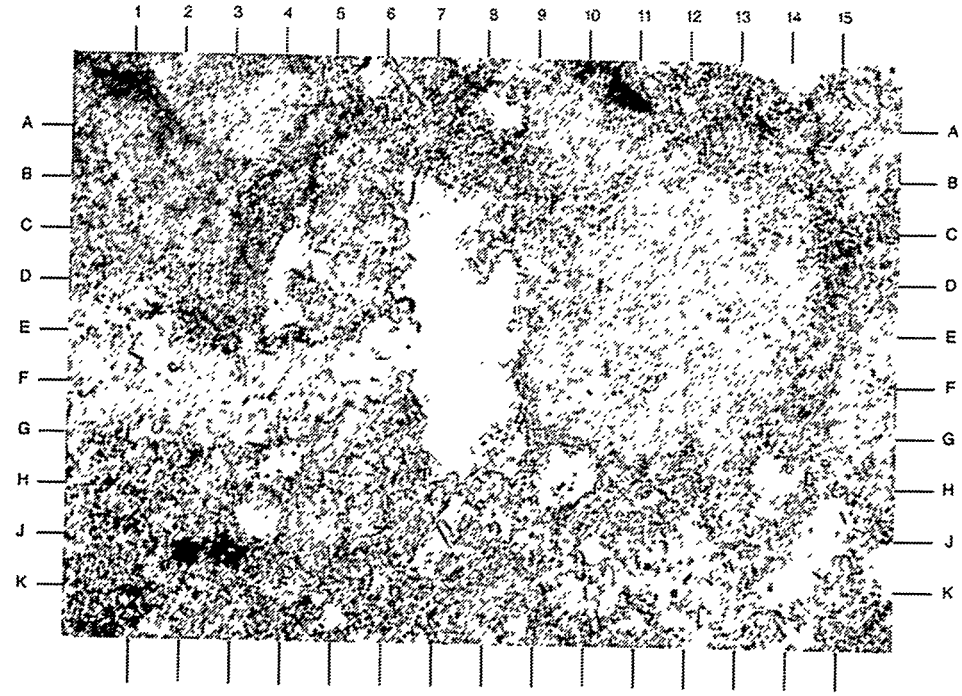
1 2 3 4 5 6 7 8 9 10 11 12 13 14 15
A B C D E F G H J K

A

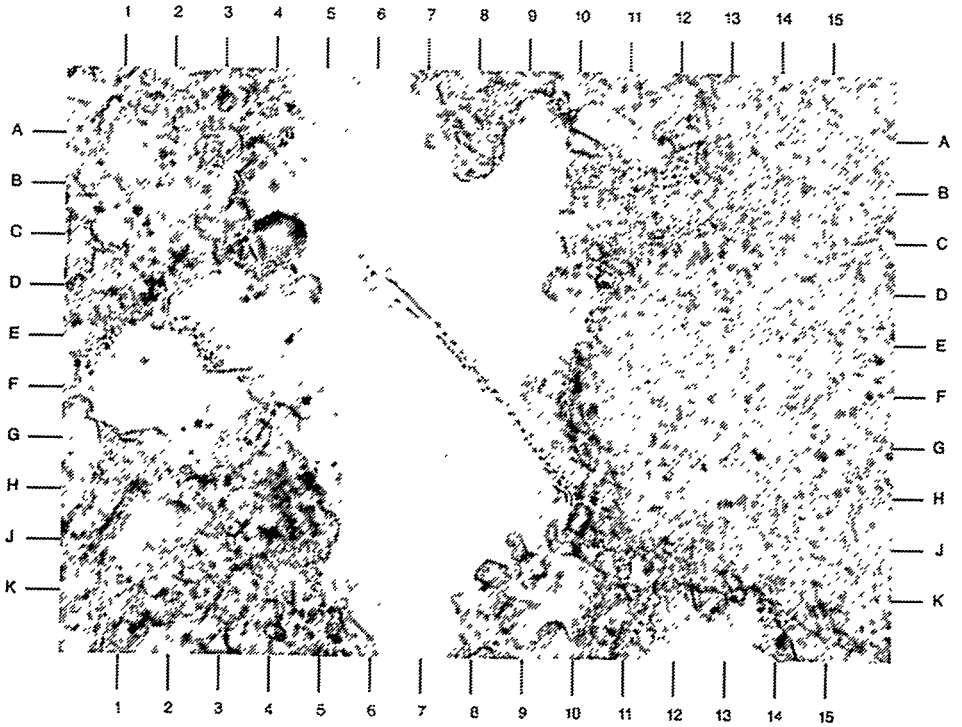
1 2 3 4 5 6 7 8 9 10 11 12 13 14 15
A B C D E F G H J K

B

Rock Physics Associates
Waste Isolation Pilot Plant

File No. G-2016

SAMPLE NUMBER: EIX 11-6 H-5.75'

PLATE 14A

This low magnification photomicrograph illustrates the mineral associations within this evaporite. Clay and organic material form subparallel stringers (brown, lower left) and are relatively abundant in this sample. Anhydrite (tan) and halite (white) make up the bulk of the rock. Anhydrite is massive and fine-grained, although coarser anhydrite (A13) is found in association with halite. Halite has common unoriented inclusions (D-E14).

Magnification: 40X

SAMPLE NUMBER: EIX 11-6 H-5.75'

PLATE 14B

This expanded-view photomicrograph of the center of photo "A" illustrates the detail of the dusty inclusions within the halite. Different types of inclusions, including probable magnesite (C5.5) appear randomly scattered. Clay (K8.5,K13)is detrital in origin; some is iron oxide stained (i.e. K8.5).

Magnification: 100X

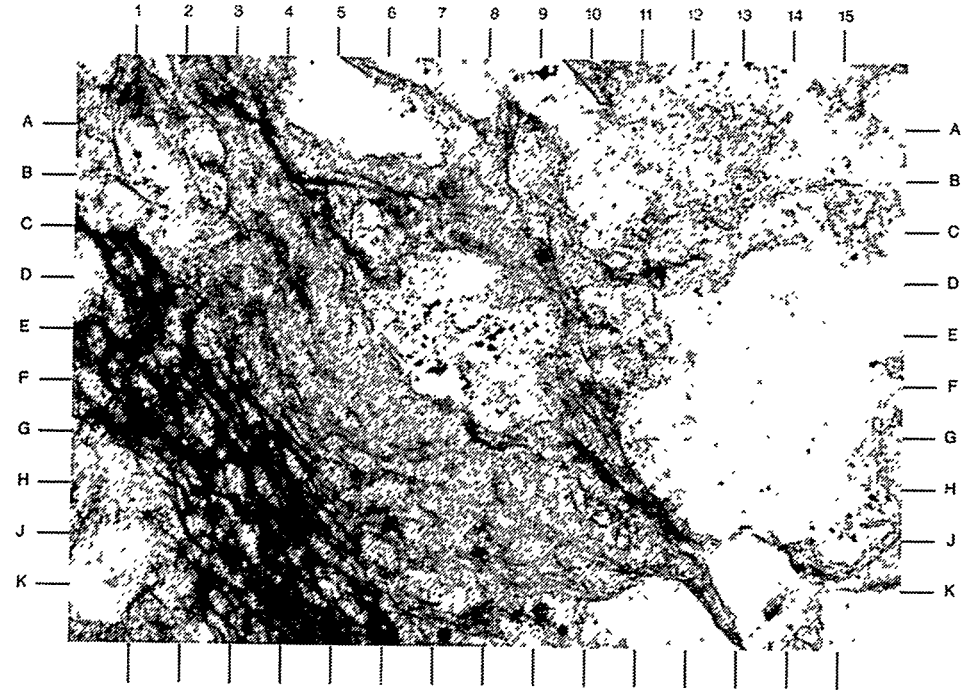
1 2 3 4 5 6 7 8 9 10 11 12 13 14 15
A B C D E F G H J K

A

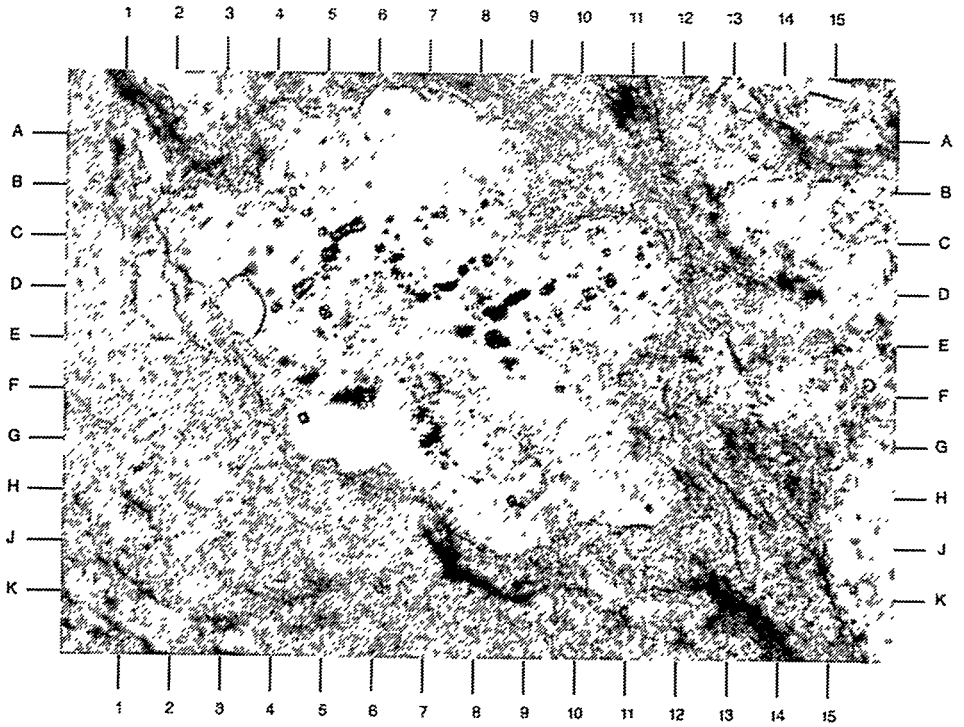
1 2 3 4 5 6 7 8 9 10 11 12 13 14 15
A B C D E F G H J K

B

Rock Physics Associates
Waste Isolation Pilot Plant

File No. G-2016

SAMPLE NUMBER: EIX 11-6 V-5.75'

PLATE 15A

The rock depicted in this low magnification view is a massive anhydrite. An unusual feature of this anhydrite is its coarser-grained texture when compared with that in other samples. Note this coarser crystal size, especially in the upper left and lower right of the photo. Some clay with organics and possible iron oxide (H8,H10,F12,J6) is evident as well.

Magnification: 40X

SAMPLE NUMBER: EIX 11-6 V-5.75'

PLATE 15B

The anhydrite crystal size variation is even more evident under high magnification (center of photo "A"). Note the intergrown, almost "feltic" texture of the coarser crystals (area of C5). The finer anhydrite (lower part of photo) shows more iron oxide staining (brown-red). A cluster of magnesite rhombs is visible at F12.

Magnification: 100X

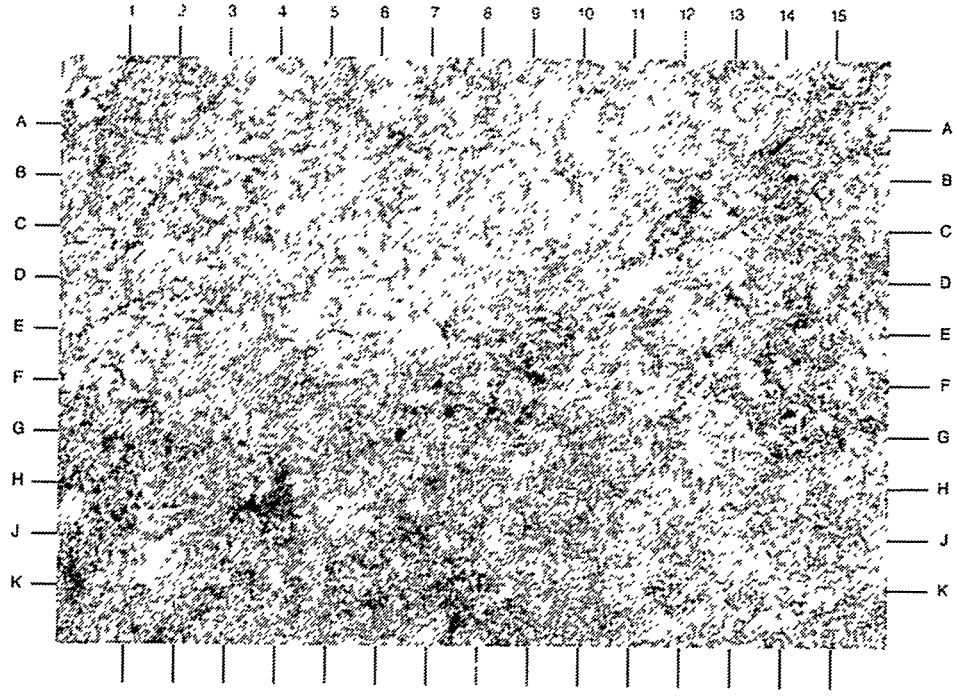
1 2 3 4 5 6 7 8 9 10 11 12 13 14 15
A B C D E F G H J K

A

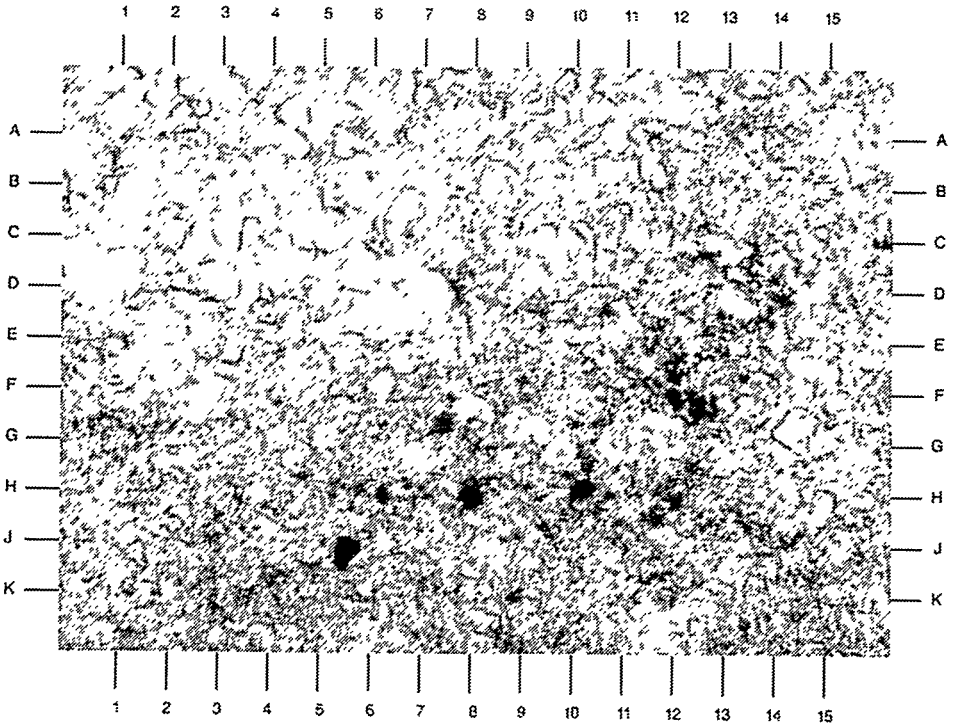
1 2 3 4 5 6 7 8 9 10 11 12 13 14 15
A B C D E F G H J K

B

Appendix A-C.
Appendix C of Appendix A [Data Report: Rock Physics Associates (Core Laboratories)]

Western Atlas International
A Litton/Dresser Company

CORE LABORATORIES

BASIC ROCK PROPERTIES

Waste Isolation Pilot Plant

FINAL REPORT

PREPARED FOR:
SANDIA NATIONAL LABORATORIES
P.O. Box 5800
Albuquerque, NM 87185

PREPARED BY:
CORE LABORATORIES
1875 Monetary Lane
Carrollton, Texas 75006
(214) 466-2673

January 24, 1994
File: DAL-93089

Western Atlas International

CORE LABORATORIES

January 24, 1994

Sandia National Laboratories
P.O. Box 5800
Albuquerque, New Mexico 87185

Attn: Dr. Susan Howarth

Subject: Basic Rock Properties
Waste Isolation Pilot Plant
File: DAL-93089

Dr. Howarth:

Following are the final results of basic rock properties determinations on selected core material from the subject well. Testing was performed following the procedures dated October 8, 1993 provided by Sandia National Laboratories.

We appreciate the opportunity to have been of service to Sandia National Laboratories. If we may be of further assistance, please telephone (214) 466-2673.

Thank you,

Marilyn P. Black
Supervisor, Petrophysics

Dallas Advanced Technology Center
1875 Monetary Drive, Carrollton, Texas 75006-7012, (214) 466-2673, Telex 163166, CORDAL UT, Fax (214) 323-3930

Sandia National Laboratories
File: DAL-93089

TABLE OF CONTENTS

SECTION 1

LABORATORY PROCEDURES

Sandia National Laboratories
File: DAL-93089

LABORATORY PROCEDURES

Equipment Calibrations

The calipers used in this study were calibrated against certified gauge blocks traceable to NIST (National Institute of Standards and Technology) standards.

The test balance used for this project reads to 0.0001 grams. The digital balance was calibrated within the last twelve months by an authorized representative of the manufacturer. Prior to this project, the balances were checked against a set of secondary weight standards.

All pressure transducers and the mass flowmeter in the AutoPermeameter™, which was modified to provide extended range values, were calibrated prior to this project. The lower limit of the AutoPermeameter™ was set to 0.0001 millidarcys (md). A standard set of calibrated billets were used to calibrate the helium AutoPorosimeter™ prior to testing.

Calibration documentation is included as an appendix to this report.

Sample Preparation

Eight core plugs, 1.5" in diameter, were drilled using a light refined mineral oil (Isopar-L) as the bit lubricant and coolant. Although the plugs were trimmed to the longest length possible, given sample quality no sample exceeded 1 2/3 inches. Two samples were too chipped for further analysis. The samples were dried to stable weights in a vacuum oven at 220°F, then cooled to room temperature in a small closed container with desiccant prior to basic property determinations.

Basic Properties

The sample dry weights were recorded to the nearest 0.0001 gram. Length and diameter measurements were made using digital calipers. The recorded value of each dimension was determined from an average of 10 caliper measurements. Each sample was placed into a matrix cup and the AutoPorosimeter™ used to inject helium from reference cells of known volume and pressure. Grain volume was determined using Boyle's law of gas expansion. Grain density values were calculated for each sample.

Each sample was then loaded into a hydrostatic coreholder for determination of

permeability to helium and pore volume at 400, 870, and 1450 psi net confining pressure. At each pressure, helium was injected into the sample from reference cells of known volume and initial pressure. Pore volume was calculated using Boyle's law. Allowing ample time for the helium in place to exit the sample, the sample was again charged with helium and, using the modified AutoPermeameter™, steady-state permeability values were determined after a 3 to 5 minute stabilization period. Permeability to helium was calculated as follows:

$$K\,(md) = \frac{2000 * 14.696 * P2 * \mu * Qa * L}{A * (P1^2 - P2^2)} \qquad (1)$$

where:

2000	=	Conversion factor
14.696	=	Barometric pressure, psi
μ	=	Viscosity of helium, 72°F
Qa	=	Flow rate to helium, cc/second
L	=	Sample length, cm
A	=	Sample area, cm^2
P1	=	Upstream pressure, psia
P2	=	Downstream pressure, psia

Basic properties results are presented in tabular format on the following page.

Sandia National Laboratories
File: DAL-93089

BASIC ROCK PROPERTIES

Extended Range Values

Sample ID	Sample Depth	Net OB, psig	P1, psia	P2, psia	Qa, cc/sec	Area, cm2	Length, cm	Permeability to Helium, md	1/Pm, Atm	Bulk Volume, cc	Grain Volume, cc	Pore Volume, cc	Porosity, percent	Sample Weight, gm	Grain Density, gm/cc
EX 10-5	4.00 - 4.2	400	232	14.651	0.091	11.5	3.568	0.0044625	0.119	40.767	40.376	0.3908	0.96	103.8442	2.572
		870	322.93	14.653	0.07	11.5	3.568	0.0017685	0.087	40.682		0.3061	0.75		
		1450	400.62	14.654	0.051	11.5	3.568	0.0008432	0.071	40.621		0.2449	0.60		
EX 10-6	4.50 - 5.1	400	277.77	14.637	0.065	11.3	3.047 ~~3.801~~	0.0023862	0.101	79.967	79.278	0.6889	0.86	213.3797	2.692
		870	276.77	14.637	0.053	11.3	~~3.801~~	0.0019487	0.101	79.946		0.6684	0.84		
		1450	373.75	14.641	0.04	11.3	~~3.801~~	0.0008042	0.076	79.885		0.6070	0.76		
EX 10-5	4.25 - 4.5	400	226.82	14.386	0.331	11.3	2.054	0.0096913	0.122	23.282	23.098	0.1837	0.79	59.1268	2.560
		870	229.82	14.381	0.182	11.3	2.054	0.0051877	0.120	23.271		0.1726	0.74		
		1450	232.33	14.384	0.095	11.3	2.054	0.0026499	0.119	23.256		0.1576	0.68		
EX 10-7	5.75 - 5.9	400	218.77	14.378	0.244	11.3	4.108	0.0153952	0.126	46.517	44.470	2.0465	4.40	130.0600	2.925
		870	219.03	14.381	0.216	11.3	4.108	0.0135987	0.126	46.436		1.9664	4.23		
		1450	219.53	14.384	0.171	11.3	4.108	0.0107183	0.126	46.419		1.9493	4.20		

Sandia National Laboratories
File: DAL-93089

BASIC ROCK PROPERTIES

Extended Range Values

Sample ID	Sample Depth	Net OB, psig	P1, psia	P2, psia	Qa, cc/sec	Area, cm2	Length, cm	Permeability to Helium, md	1/Pm, Atm	Bulk Volume, cc	Grain Volume, cc	Pore Volume, cc	Porosity, percent	Sample Weight, gm	Grain Density, gm/cc
EX 11-5	2.70 - 3.4	400	231.54	14.387	0.116	11.3	2.615	0.0041511	0.120	29.564	29.309	0.2548	0.86	76.3734	2.606
		870	231.09	14.389	0.076	11.3	2.615	0.0027343	0.120	29.507		0.1980	0.67		
		1450	230.94	14.388	0.051	11.3	2.615	0.0018204	0.120	29.503		0.1941	0.66		
EX 11-6	3.80	400	219.78	14.383	0.265	11.3	3.159	0.0127091	0.126	35.8	35.618	0.1817	0.51	90.7512	2.548
		870	216.97	14.383	0.14	11.3	3.159	0.0068903	0.127	35.783		0.1646	0.46		
		1450	217.68	14.385	0.057	11.3	3.159	0.0027974	0.127	35.765		0.1466	0.41		

SECTION 2

APPENDIX
A-C.1
CALIBRATIONS

Dec 29,1993 1:27 PM

Description: Calibration of low range flow meter
X-Y Table Size: 41 Active Points: 41

X Variable: Voltage

Xmin:	0.0195	Xmax:	1.67	Xrange:	1.6505
Xmean:	0.5471341463	Xstd:	0.4962067173	Xmedian:	0.403
X@Ymin:	0.02	X@Ymax:	1.67	X@Yrange:	1.65
Xav@Ymax:	1.6275	X@50Y:	0.826376352	Xlt@50Y:	0
Xrt@50Y:	0	X@25Y:	0.44925	X@75Y:	1.43
Xwavemin:	0.0652083333	Xwavemax:	1.6275	Xwaverng:	3.1245833333

Y Variable: Rate, cc's/sec

Ymin:	0.008	Ymax:	0.86	Yrange:	0.852
Ymean:	0.281195122	Ystd:	0.2570742324	Ymedian:	0.206
Y@Xmin:	0.008	Y@Xmax:	0.86	Y@Xrange:	0.852

35 Eqn 64 y=(a+bx+cx2) r=0.9999626919

	Coefficient	Std Error	T(Coef/Err)	95% Confidence Limits	
a	-0.001706727	0.000497417	-3.431179833	-0.002713541	-0.000699914
b	0.5153059743	0.0017051914	302.19832747	0.5118545244	0.5187574241
c	0.0017798469	0.0010476571	1.6988830455	-0.000340699	0.0039003926

Curve-Fit Std Error: 0.001611009953397

Source	Sum of Squares	DF	Mean Square	F
Regr	2.64338782	2	1.32169391	509254
Error	9.86234167e-005	38	2.59535307e-006	
Total	2.64348644	40		

Calibration of low range flow meter
Page 1

#	X-Value	Y-Value	Y-Predict	95% Confidence Intvl	
1	0.0195	0.008	0.00834242	0.00738751	0.00929732
2	0.02	0.008	0.0086001	0.0076465	0.00955371
3	0.046	0.023	0.02200111	0.02111215	0.02289008
4	0.0466	0.023	0.0223104	0.02142286	0.02319794
5	0.0635	0.032	0.03102238	0.03017388	0.03187088
6	0.064	0.032	0.03128015	0.03043276	0.03212753
7	0.0647	0.033	0.03164102	0.0307952	0.03248684
8	0.0793	0.04	0.03916823	0.03835406	0.0399824
9	0.0793	0.039	0.03916823	0.03835406	0.0399824
10	0.0806	0.035	0.0398385	0.03902706	0.04064994
11	0.109	0.054	0.05448277	0.05372716	0.05523838
12	0.11	0.055	0.05499847	0.05424469	0.05575225
13	0.197	0.1	0.09987762	0.09924526	0.10050999
14	0.197	0.099	0.09987762	0.09924526	0.10050999
15	0.1975	0.099	0.10013563	0.09950373	0.10076752
16	0.304	0.156	0.15511078	0.15452336	0.15569819
17	0.308	0.157	0.15717636	0.15658865	0.15776406
18	0.309	0.158	0.15769276	0.15710496	0.15828056
19	0.4	0.206	0.20470044	0.20407954	0.20532134
20	0.402	0.206	0.2057339	0.20511186	0.20635595
21	0.403	0.206	0.20625064	0.20562803	0.20687326
22	0.497	0.256	0.25483998	0.25415483	0.25552513
23	0.497	0.255	0.25483998	0.25415483	0.25552513
24	0.497	0.255	0.25483998	0.25415483	0.25552513
25	0.597	0.307	0.30656529	0.30581209	0.3073185
26	0.597	0.307	0.30656529	0.30581209	0.3073185
27	0.599	0.309	0.30760016	0.30684571	0.30835462
28	0.69	0.357	0.35470178	0.35389731	0.35550625
29	0.692	0.354	0.35573731	0.35493191	0.35654271
30	0.692	0.354	0.35573731	0.35493191	0.35654271
31	0.799	0.412	0.411159	0.41031551	0.4120025
32	0.8005	0.411	0.41193623	0.41109236	0.4127801
33	0.986	0.508	0.50811532	0.50725215	0.50897849
34	0.988	0.51	0.50915296	0.50828978	0.51001614
35	0.991	0.507	0.51070945	0.50984626	0.51157264
36	1.25	0.645	0.64520675	0.64430482	0.64610869
37	1.25	0.645	0.64520675	0.64430482	0.64610869
38	1.61	0.833	0.83254943	0.83106327	0.83403559
39	1.61	0.833	0.83254943	0.83106327	0.83403559
40	1.62	0.842	0.83775998	0.83624546	0.83927451
41	1.67	0.86	0.86381807	0.86215248	0.86548365

Calibration 12/29/93 JAK/RIA

of

500 psi Guage (Helium) Pressure

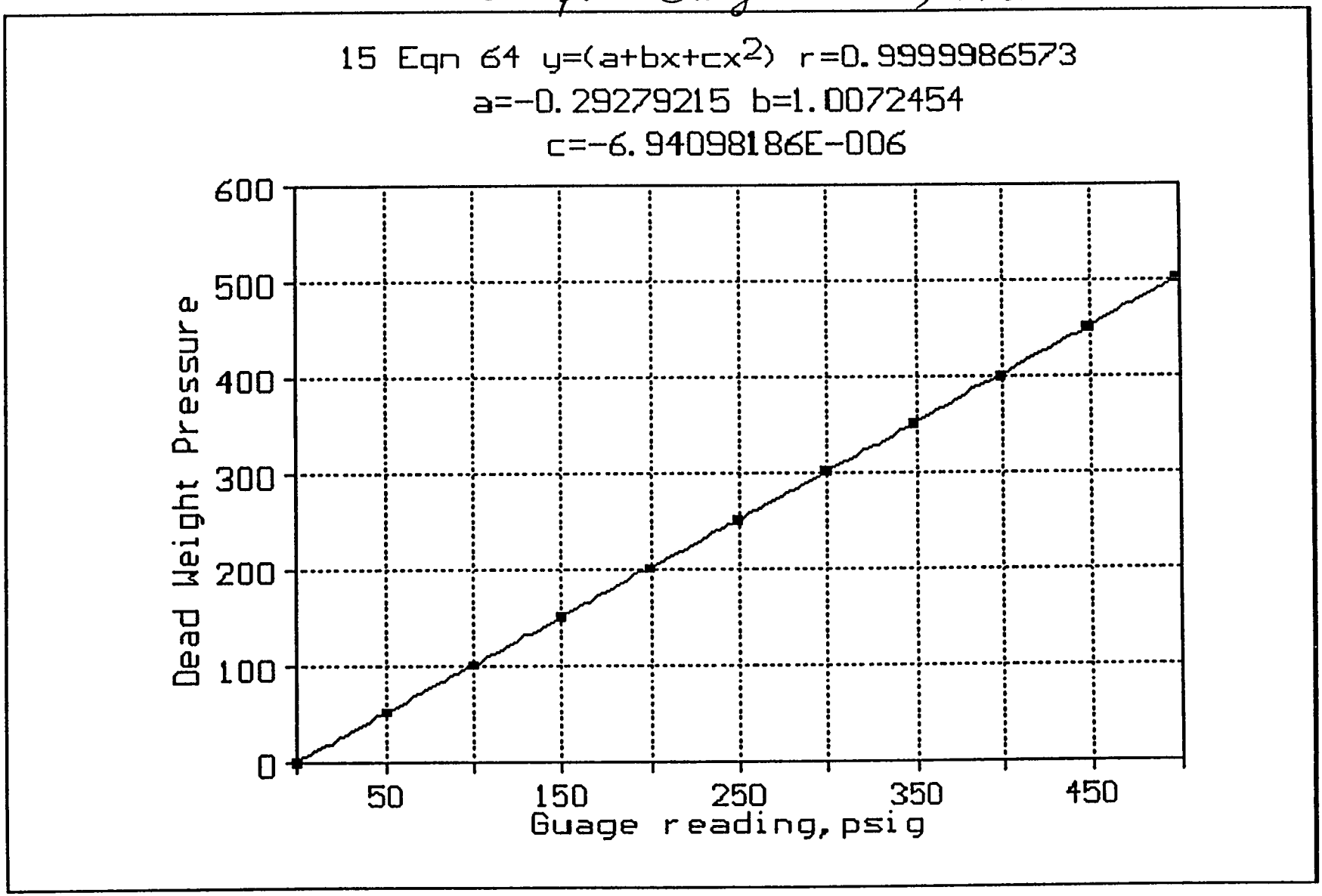

Jan 4,1994 10:14 AM

Description: Calibration of low range flow meter
X-Y Table Size: 10 Active Points: 10

X Variable: Voltage

Xmin:	0.0183	Xmax:	0.939	Xrange:	0.9207
Xmean:	0.36466	Xstd:	0.3555943044	Xmedian:	0.2545
X@Ymin:	0.0183	X@Ymax:	0.933	X@Yrange:	0.9147
Xav@Ymax:	0.936	X@50Y:	0.5267812836	Xlt@50Y:	0
Xrt@50Y:	0	X@25Y:	0.2411974498	X@75Y:	0.73375
Xwavemin:	0.0183	Xwavemax:	0.933	Xwaverng:	1.8294

Y Variable: Rate,cc's/sec

Ymin:	0.0042	Ymax:	0.468	Yrange:	0.4638
Ymean:	0.18085	Ystd:	0.1788639784	Ymedian:	0.12675
Y@Xmin:	0.0042	Y@Xmax:	0.468	Y@Xrange:	0.4638

46 Eqn 64 y=(a+bx+cx2) r=0.9999476886

	Coefficient	Std Error	T(Coef/Err)	95% Confidence Limits	
a	-0.00308274	0.0008701821	-3.54263823	-0.005148497	-0.001016983
b	0.507905247	0.005338892	95.133081582	0.4952310549	0.520579439
c	-0.005186764	0.0054385014	-0.953712055	-0.018097423	0.0077238942

Curve-Fit Std Error: 0.001466875254761

Source	Sum of Squares	DF	Mean Square	F
Regr	0.287915843	2	0.143957921	66903.56
Error	1.50620611e-005	7	2.15172301e-006	
Total	0.287930905	9		

Calibration of low range flow meter
Page 1

#	X-Value	Y-Value	Y-Predict	95% Confidence Intvl	
1	0.0183	0.0042	0.00621019	0.00430902	0.00811136
2	0.0256	0.0096	0.00991623	0.00807568	0.01175679
3	0.0537	0.0254	0.02417681	0.02254044	0.02581319
4	0.105	0.0508	0.05019013	0.04879385	0.05158641
5	0.199	0.0988	0.097785	0.0963985	0.09917151
6	0.31	0.1547	0.15386944	0.15217458	0.1555643
7	0.531	0.265	0.26515248	0.26314924	0.26715572
8	0.532	0.264	0.26565487	0.26365191	0.26765783
9	0.933	0.468	0.46627783	0.46385968	0.46869599
10	0.939	0.468	0.46926701	0.46680086	0.47173316

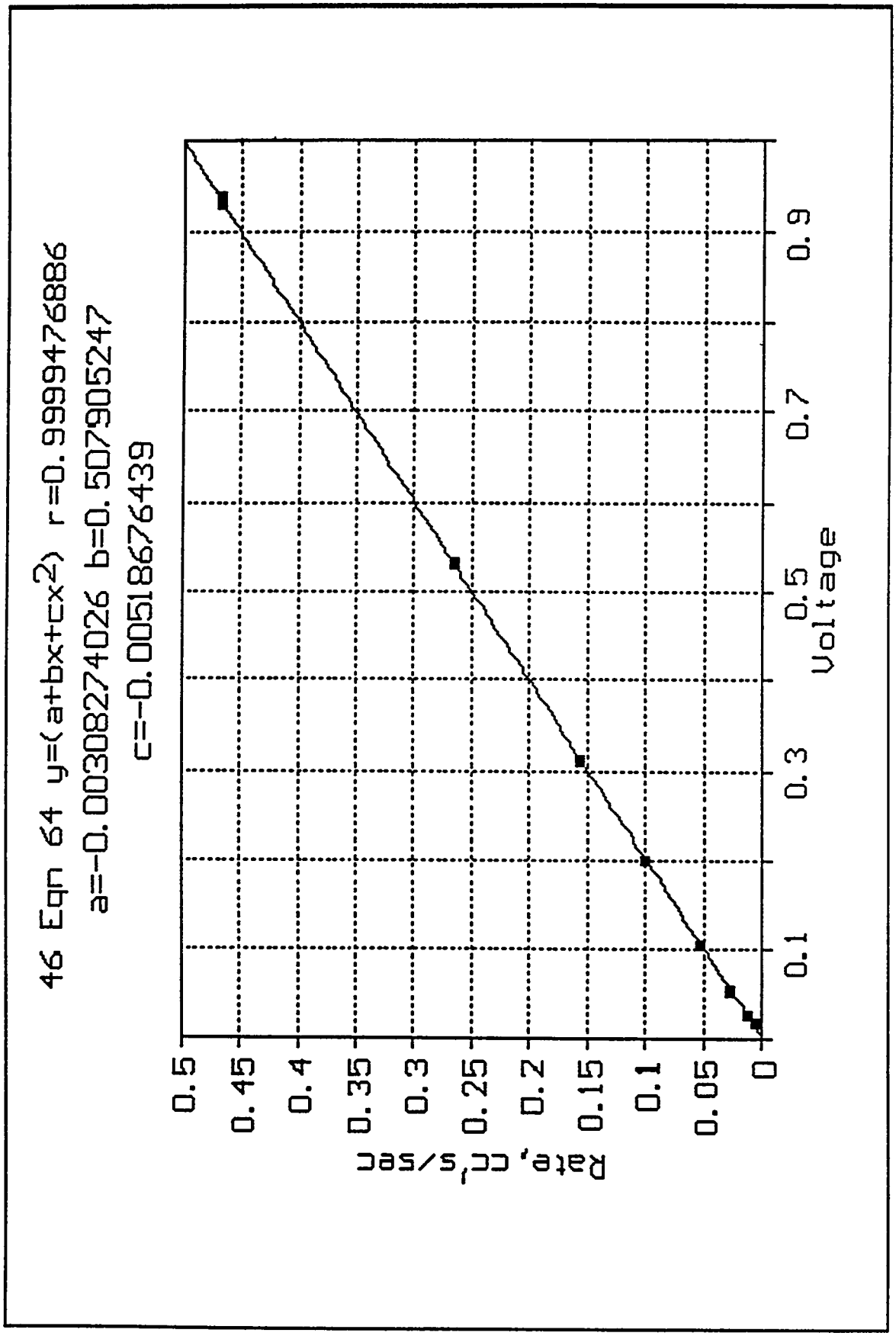
46 Eqn 64 y=(a+bx+cx^2) r=0.9999476886
a=-0.0030827402 6 b=0.5079052 47
c=-0.0051867643 9
Rate, CC's/sec
Voltage
0.5
0.45
0.4
0.35
0.3
0.25
0.2
0.15
0.1
0.05
0
0.1
0.3
0.5
0.7
0.9

Jan 5,1994 3:40 PM

Description: 500pis Guage Calibration
X-Y Table Size: 11 Active Points: 11

X Variable: Guage reading,psig

Xmin:	0	Xmax:	498.5	Xrange:	498.5
Xmean:	249.09090909	Xstd:	165.20579109	Xmedian:	248.75
X@Ymin:	0	X@Ymax:	498.5	X@Yrange:	498.5
Xav@Ymax:	498.5	X@50Y:	248.75	Xlt@50Y:	0
Xrt@50Y:	0	X@25Y:	124.765625	X@75Y:	373.5
Xwavemin:	0	Xwavemax:	498.5	Xwaverng:	997

Y Variable: Dead Weight Pressure

Ymin:	0	Ymax:	500	Yrange:	500
Ymean:	250	Ystd:	165.83123952	Ymedian:	250
Y@Xmin:	0	Y@Xmax:	500	Y@Xrange:	500

15 Eqn 64 y=(a+bx+cx2) r=0.9999986573

	Coefficient	Std Error	T(Coef/Err)	95% Confidence Limits	
a	-0.29279215	0.1637898374	-1.787608771	-0.671810845	0.0862265447
b	1.0072453999	0.0015277072	659.31835415	1.0037102014	1.0107805985
c	-6.941e-006	2.95099e-006	-2.352084236	-1.377e-005	-1.1222e-007

Curve-Fit Std Error: 0.21483810289

Source	Sum of Squares	DF	Mean Square	F
Regr	274999.631	2	137499.815	2979062
Error	0.369243284	8	0.0461554105	
Total	275000	10		

500pis Guage Calibration
Page 1

#	X-Value	Y-Value	Y-Predict	95% Confidence Intvl	
1	0	0	-0.2927921	-0.6718108	0.08622654
2	50	50	50.0521254	49.7899743	50.3142765
3	100	100	100.362338	100.155228	100.569448
4	149.5	150	150.135262	149.930963	150.339562
5	199.25	200	200.125293	199.906378	200.344207
6	248.75	250	249.830017	249.603796	250.056238
7	298.5	300	299.751503	299.532283	299.970723
8	348.5	350	349.889232	349.684617	350.093847
9	398.5	400	399.992256	399.784924	400.199588
10	448.5	450	450.060576	449.798295	450.322857
11	498.5	500	500.09419	499.715175	500.473205

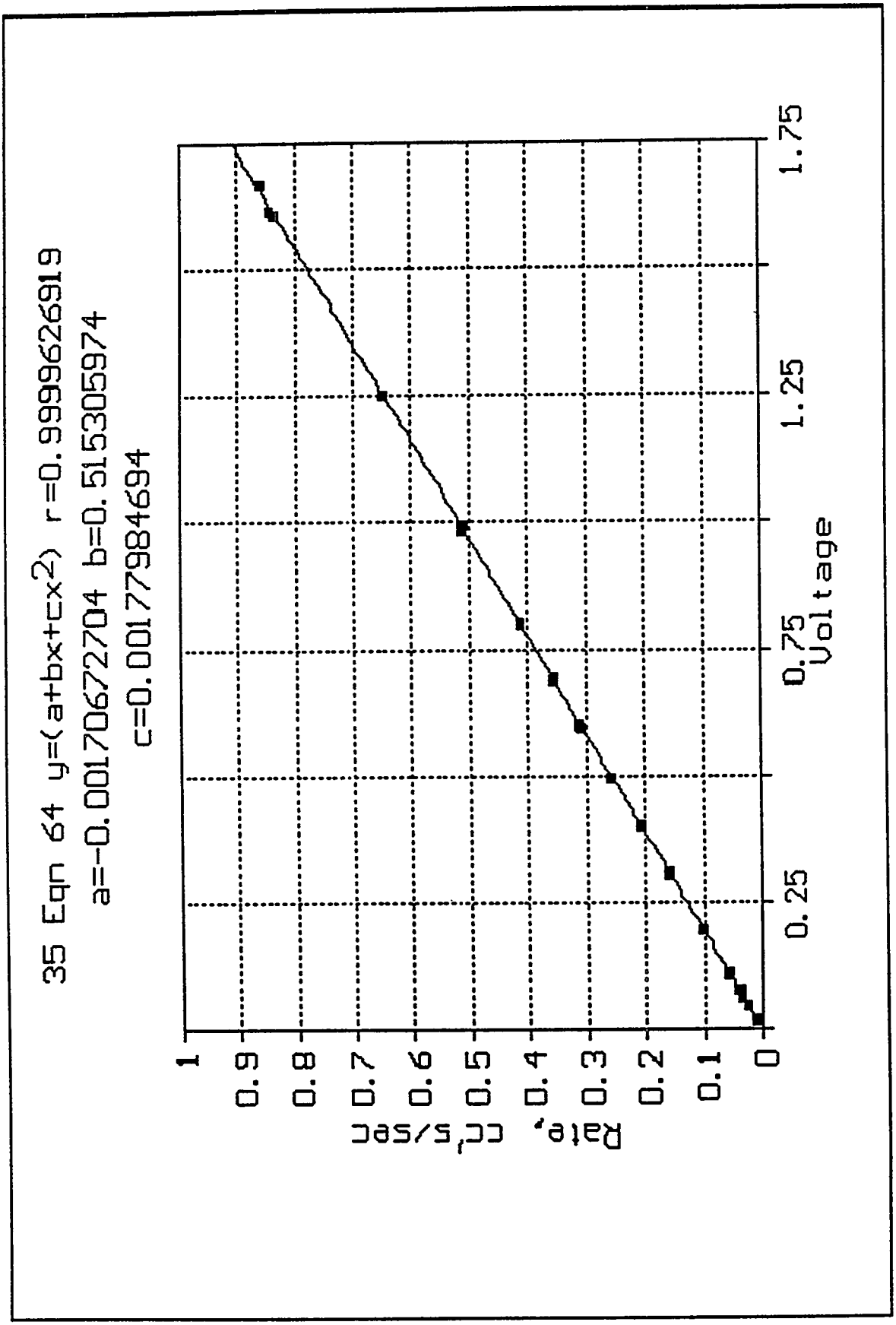
35 Eqn 64 y=(a+bx+cx^2) r=0.9999626919
a=-0.0017067272704 b=0.5153059974
c=0.0017779846694
Rate, CC's/sec
Voltage
0
0.1
0.2
0.3
0.4
0.5
0.6
0.7
0.8
0.9
1
0.25
0.75
1.25
1.75

Jan 6,1994 7:54 AM

Description: Recalibration @ 14.3601 Pb
X-Y Table Size: 6 Active Points: 6

X Variable: Voltage

Xmin:	0.0134	Xmax:	0.221	Xrange:	0.2076
Xmean:	0.0801333333	Xstd:	0.0767259973	Xmedian:	0.05675
X@Ymin:	0.0134	X@Ymax:	0.221	X@Yrange:	0.2076
Xav@Ymax:	0.221	X@50Y:	0.1267811111	Xlt@50Y:	0
Xrt@50Y:	0	X@25Y:	0.0587410639	X@75Y:	0.1913153337
Xwavemin:	0.0134	Xwavemax:	0.221	Xwaverng:	0.4152

Y Variable: Rate, cc's/sec

Ymin:	0.0008	Ymax:	0.1128	Yrange:	0.112
Ymean:	0.03725	Ystd:	0.0410825876	Ymedian:	0.0268
Y@Xmin:	0.0008	Y@Xmax:	0.1128	Y@Xrange:	0.112

53 Eqn 64 y=(a+bx+cx2) r=0.9980941858

	Coefficient	Std Error	T(Coef/Err)	95% Confidence Limits	
a	-0.00574819	0.0023016858	-2.49738265	-0.013018843	0.0015224623
b	0.5389838926	0.0567495106	9.4975954308	0.3597213843	0.718246401
c	-0.016984578	0.2311745348	-0.073470802	-0.747227474	0.7132583175

Curve-Fit Std Error: 0.002315380855453

Source	Sum of Squares	DF	Mean Square	F
Regr	0.00842281203	2	0.00421140602	785.5652
Error	1.60829655e-005	3	5.36098851e-006	
Total	0.008438895	5		

Recalibration @ 14.3601 Pb
Page 1

#	X-Value		Y-Value		Y-Predict	95% Confidence Intvl	
1	0.0134	.001	0.0008	.001	0.00147114	-0.0039246	0.00686685
2	0.0269	.008	0.0075	.009	0.00873819	0.00468925	0.01278712
3	0.0403	.018	0.0177	.016	0.01594528	0.01250702	0.01938353
4	0.0732	.036	0.0359	.034	0.03361442	0.02926302	0.03796583
5	0.106	.049	0.0488	.051	0.05119326	0.04562369	0.05676284
6	0.221	.113	0.1128	.113	0.11253771	0.10524415	0.11983126

Calibration of Low Range Mass Flow Meter (to Helium)

Calibration 1/6/94

Morning

Pb = 14.3601

29.23 01

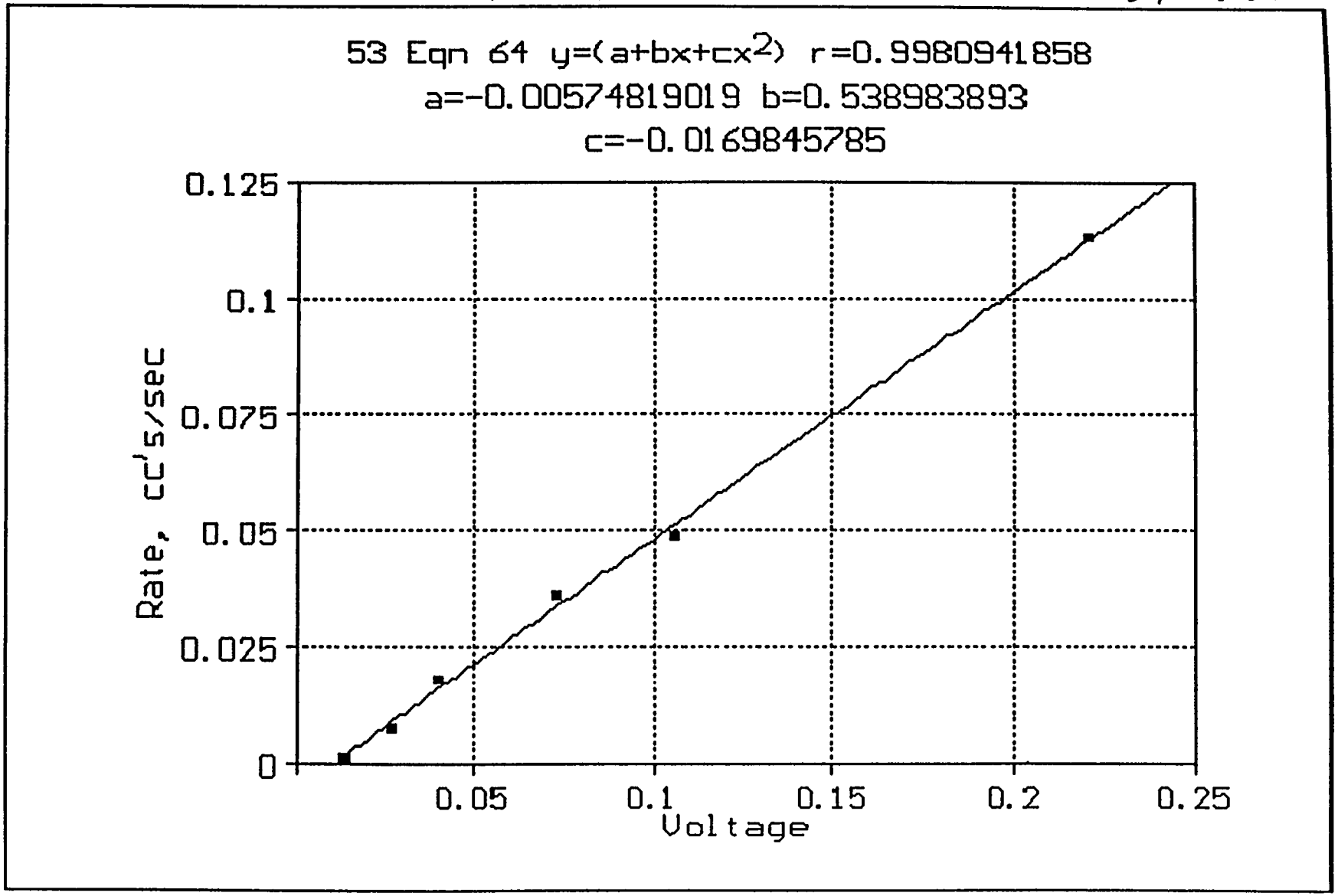

1" and 1½" Calibration Ck (Caliper)

DATE: 12/20/93 TECH: JAK

JOB#: 93085

SAMPLE ID	CALIP.EV CC	HG.EV CC	WEIGHT GMS.	AREA SQCM	LENGTH CM	DIAMETER CM	P
1S	12.879	0.000	~~98.857~~	5.067	3.540	3.540	0
2S	103.057	0.000	~~789.596~~	20.287	5.085	5.085	0
1-2	40.868	0.000	103.851	11.455	3.565	3.569	0
10-5D	23.295	0.000	59.130	11.343 11.347	2.054	3.901	0
1-6	79.961	0.000	213.811	11.351 11.347	7.047	7.051	0
10-7	46.490	0.000	130.088	11.518 11.317	5.1?6	5.?9?	0
11-5	25.658	0.000	76.377	11.342 11.34	2.515	3.500	0
11-6	35.851	0.000	90.756	11.350 11.347	3.15?	3.5?1	0

5/8

WIPP
UC721 - DISTRIBUTION LIST
SAND94-0472

Federal Agencies

US Department of Energy (4)
Office of Civilian Radioactive Waste Mgmt.
Attn: Deputy Director, RW-2
Acting Director, RW-10
Office of Human Resources & Admin.
Director, RW-30
Office of Program Mgmt. & Integ.
Director, RW-40
Office of Waste Accept., Stor., & Tran.
Forrestal Building
Washington, DC 20585

Attn: Project Director
Yucca Mountain Site Characterization Office
Director, RW-3
Office of Quality Assurance
P.O. Box 30307
Las Vegas, NV 89036-0307

US Department of Energy
Albuquerque Operations Office
Attn: National Atomic Museum Library
P.O. Box 5400
Albuquerque, NM 87185-5400

US Department of Energy
Research & Waste Management Division
Attn: Director
P.O. Box E
Oak Ridge, TN 37831

US Department of Energy (5)
Carlsbad Area Office
Attn: G. Dials
D. Galbraith
M. McFadden
R. Lark
J. A. Mewhinney
P.O. Box 3090
Carlsbad, NM 88221-3090

US Department of Energy
Office of Environmental Restoration and
Waste Management
Attn: M Frei, EM-30
Forrestal Building
Washington, DC 20585-0002

US Department of Energy (3)
Office of Environmental Restoration and
Waste Management
Attn: J. Juri, EM-34, Trevion II
Washington, DC 20585-0002

US Department of Energy
Office of Environmental Restoration and
Waste Management
Attn: S. Schneider, EM-342, Trevion II
Washington, DC 20585-0002

US Department of Energy (2)
Office of Environment, Safety & Health
Attn: C. Borgstrom, EH-25
R. Pelletier, EH-231
Washington, DC 20585

US Department of Energy (2)
Idaho Operations Office
Fuel Processing & Waste Mgmt. Division
785 DOE Place
Idaho Falls, ID 83402

US Environmental Protection Agency (2)
Radiation Protection Programs
Attn: M. Oge
ANR-460
Washington, DC 20460

Boards

Defense Nuclear Facilities Safety Board
Attn: D. Winters
625 Indiana Ave. NW, Suite 700
Washington, DC 20004

Nuclear Waste Technical Review Board (2)
Attn: Chairman
J. L. Cohon
1100 Wilson Blvd., Suite 910
Arlington, VA 22209-2297

State Agencies

Attorney General of New Mexico
P.O. Drawer 1508
Santa Fe, NM 87504-1508

Environmental Evaluation Group (3)
Attn: Library
7007 Wyoming NE
Suite F-2
Albuquerque, NM 87109

NM Environment Department (3)
Secretary of the Environment
Attn: Mark Weidler
1190 St. Francis Drive
Santa Fe, NM 87503-0968

NM Bureau of Mines & Mineral Resources
Socorro, NM 87801

Laboratories/Corporations

Battelle Pacific Northwest Laboratories
Battelle Blvd.
Richland, WA 99352

INTERA, Inc.
Attn: G. A. Freeze
1650 University Blvd. NE, Suite 300
Albuquerque, NM 87102

INTERA, Inc.
Attn: J. F. Pickens
6850 Austin Center Blvd., Suite 300
Austin, TX 78731

Los Alamos National Laboratory
Attn: B. Erdal, INC-12
P.O. Box 1663
Los Alamos, NM 87544

RE/SPEC, Inc.
Attn: A. Robb
4775 Indian School NE, Suite 300
Albuquerque, NM 87110-3927

RE/SPEC, Inc.
Attn: J. L. Ratigan
P. O. Box 725
Rapid City. SD 57709

Tech Reps, Inc. (3)
Attn: J. Chapman (1)
Loretta Robledo (2)
5000 Marble NE, Suite 222
Albuquerque, NM 87110

Westinghouse Electric Corporation (5)
Attn: Library
J. Epstein
J. Lee
B. A. Howard
R. Kehrman
P.O. Box 2078
Carlsbad, NM 88221

S. Cohen & Associates
Attn: Bill Thurber
1355 Beverly Road
McLean, VA 22101

Rock Physics Associates
Attn: J. Walls
4320 Steven Creek Blvd., Ste 282
San Jose, CA 95129

National Academy of Sciences, WIPP Panel

Howard Adler
Oxyrase, Incorporated
7327 Oak Ridge Highway
Knoxville, TN 37931

Tom Kiess
Board of Radioactive Waste Management
GF456
2101 Constitution Ave.
Washington, DC 20418

Rodney C. Ewing
Department of Geology
University of New Mexico
Albuquerque, NM 87131

Charles Fairhurst
Department of Civil and Mineral Engineering
University of Minnesota
500 Pillsbury Dr. SE
Minneapolis, MN 55455-0220

B. John Garrick
PLG Incorporated
4590 MacArthur Blvd., Suite 400
Newport Beach, CA 92660-2027

Leonard F. Konikow
US Geological Survey
431 National Center
Reston, VA 22092

Carl A. Anderson, Director
Board of Radioactive Waste Management
National Research Council
HA 456
2101 Constitution Ave. NW
Washington, DC 20418

Christopher G. Whipple
ICF Kaiser Engineers
1800 Harrison St., 7th Floor
Oakland, CA 94612-3430

John O. Blomeke
720 Clubhouse Way
Knoxville, TN 37909

Sue B. Clark
University of Georgia
Savannah River Ecology Lab
P.O. Drawer E
Aiken, SC 29802

Konrad B. Krauskopf
Department of Geology
Stanford University
Stanford, CA 94305-2115

Della Roy
Pennsylvania State University
217 Materials Research Lab
Hastings Road
University Park, PA 16802

David A. Waite
CH_2 M Hill
P.O. Box 91500
Bellevue, WA 98009-2050

Thomas A. Zordon
Zordan Associates, Inc.
3807 Edinburg Drive
Murrysville, PA 15668

Universities

University of New Mexico
Geology Department
Attn: Library
141 Northrop Hall
Albuquerque, NM 87131

Libraries

Thomas Brannigan Library
Attn: D. Dresp
106 W. Hadley St.
Las Cruces, NM 88001

Government Publications Department
Zimmerman Library
University of New Mexico
Albuquerque, NM 87131

New Mexico Junior College
Pannell Library
Attn: R. Hill
Lovington Highway
Hobbs, NM 88240

New Mexico State Library
Attn: N. McCallan
325 Don Gaspar
Santa Fe, NM 87503

New Mexico Tech
Martin Speere Memorial Library
Campus Street
Socorro, NM 87810

WIPP Public Reading Room
Carlsbad Public Library
101 S. Halagueno St.
Carlsbad, NM 88220

Foreign Addresses

Atomic Energy of Canada, Ltd.
Whiteshell Laboratories
Attn: B. Goodwin
Pinawa, Manitoba, CANADA R0E 1L0

Francois Chenevier (2)
ANDRA
Route de Panorama Robert Schumann
B. P. 38
92266 Fontenay-aux-Roses, Cedex
FRANCE

Claude Sombret
Centre d'Etudes Nucleaires de la Vallee Rhone
CEN/VALRHO
S.D.H.A. B.P. 171
30205 Bagnols-Sur-Ceze
FRANCE

Commissariat a L'Energie Atomique
Attn: D. Alexandre
Centre d'Etudes de Cadarache
13108 Saint Paul Lez Durance Cedex
FRANCE

Bundesanstalt fur Geowissenschaften und Rohstoffe
Attn: M. Langer
Postfach 510 153
D-30631 Hannover
GERMANY

Bundesministerium fur Forschung und Technologie
Postfach 200 706
5300 Bonn 2
GERMANY

Institut fur Tieflagerung
Attn: K. Kuhn
Theodor-Heuss-Strasse 4
D-3300 Braunschweig
GERMANY

Gesellschaft fur Anlagen und Reaktorsicherheit (GRS)
Attn: B. Baltes
Schwertnergasse 1
D-50667 Cologne
GERMANY

Shingo Tashiro
Japan Atomic Energy Research Institute
Tokai-Mura, Ibaraki-Ken, 319-11
JAPAN

Netherlands Energy Research Foundation ECN
Attn: J. Prij
3 Westerduinweg
P.O. Box 1
1755 ZG Petten
THE NETHERLANDS

Svensk Karnbransleforsorjning AB
Attn: F. Karlsson
Project KBS (Karnbranslesakerhet)
Box 5864
S-102 48 Stockholm
SWEDEN

Nationale Genossenschaft fur die Lagerung Radioaktiver Abfalle (2)
Attn: S. Vomvoris
P. Zuidema
Hardstrasse 73
CH-5430 Wettingen
SWITZERLAND

AEA Technology
Attn: J. H. Rees
D5W/29 Culham Laboratory
Abington, Oxfordshire OX14 3DB
UNITED KINGDOM

AEA Technology
Attn: W. R. Rodwell
044/A31 Winfrith Technical Centre
Dorchester, Dorset DT2 8DH
UNITED KINGDOM

AEA Technology
Attn: J. E. Tinson
B4244 Harwell Laboratory
Didcot, Oxfordshire OX11 ORA
UNITED KINGDOM

Internal

MS	Org.	
1324	6115	P. B. Davies
1324	6115	T. L. Christian-Frear (5)
1324	6115	C. Boney
1324	6115	R. L. Beauheim
1324	6115	S. W. Webb
1320	6831	E. J. Nowak
1322	6121	J. R. Tillerson
1328	6849	D. R. Anderson
1328	6848	H. N. Jow
1335	6801	M. Chu
1335	6801	S. M. Howarth (15)
1341	6832	J. T. Holmes
1395	6800	L. Shephard
1395	6821	M. Marietta
0751	6117	L. S. Costin
0751	6117	N. S. Brodsky
0751	6117	J. T. Fredrich
0751	6117	D. J. Holcomb

0751	6117	D. H. Zeuch
0705	6116	D. J. Borns
1330	6811	K. Hart (2)
1330	4415	NWM Library (20)
9018	8940-2	Central Technical Files
0899	4414	Technical Library (5)
0619	12690	Review and Approval Desk (2), For DOE/OSTI

*U.S. GOVERNMENT PRINTING OFFICE 1997-0-573-030/20047